Bioanalysis: Advanced Materials, Methods, and Devices
Series Editor: Tuan Vo-Dinh

Steen J. Madsen *Editor*

Optical Methods and Instrumentation in Brain Imaging and Therapy

Springer

Bioanalysis

Advanced Materials, Methods, and Devices

Series Editor

Tuan Vo-Dinh
Fitzpatrick Institute for Photonics
Duke University
Durham, NC, USA

For further volumes:
http://www.springer.com/series/8091

Steen J. Madsen
Editor

Optical Methods and Instrumentation in Brain Imaging and Therapy

Springer

Editor
Steen J. Madsen
Department of Health Physics
and Diagnostic Sciences
University of Nevada, Las Vegas
NV, USA

ISBN 978-1-4614-4977-5 ISBN 978-1-4614-4978-2 (eBook)
DOI 10.1007/978-1-4614-4978-2
Springer New York Heidelberg Dordrecht London

Library of Congress Control Number: 2012952098

© Springer Science+Business Media New York 2013
This work is subject to copyright. All rights are reserved by the Publisher, whether the whole or part of the material is concerned, specifically the rights of translation, reprinting, reuse of illustrations, recitation, broadcasting, reproduction on microfilms or in any other physical way, and transmission or information storage and retrieval, electronic adaptation, computer software, or by similar or dissimilar methodology now known or hereafter developed. Exempted from this legal reservation are brief excerpts in connection with reviews or scholarly analysis or material supplied specifically for the purpose of being entered and executed on a computer system, for exclusive use by the purchaser of the work. Duplication of this publication or parts thereof is permitted only under the provisions of the Copyright Law of the Publisher's location, in its current version, and permission for use must always be obtained from Springer. Permissions for use may be obtained through RightsLink at the Copyright Clearance Center. Violations are liable to prosecution under the respective Copyright Law.
The use of general descriptive names, registered names, trademarks, service marks, etc. in this publication does not imply, even in the absence of a specific statement, that such names are exempt from the relevant protective laws and regulations and therefore free for general use.
While the advice and information in this book are believed to be true and accurate at the date of publication, neither the authors nor the editors nor the publisher can accept any legal responsibility for any errors or omissions that may be made. The publisher makes no warranty, express or implied, with respect to the material contained herein.

Printed on acid-free paper

Springer is part of Springer Science+Business Media (www.springer.com)

Preface

Therapeutic applications of lasers in the brain date back to the mid-1960s when a low power ruby laser was used to debulk a malignant glioma. Although no improvement in patient survival was observed, the procedure demonstrated the potential of lasers in neurosurgical applications. The development of continuous wave lasers such as the CO_2 laser provided the rationale for larger clinical studies since accurate cutting and vaporization of brain tissue was now possible. Throughout the 1970s and into the mid-1980s, a number of clinical studies focused on the utility of the CO_2 laser for tumor debulking. Although these studies demonstrated the utility of the CO_2 laser in surgical resection, it had a number of limitations that made it difficult to integrate into the surgical suite and therefore it failed to replace traditional resection techniques using ultrasound aspirators, and bipolar and loop cautery.

In addition to tumor debulking, vessel coagulation is a commonly performed neurosurgical procedure. The use of the Nd:YAG laser ($\lambda = 1.064\ \mu\text{m}$) for photocoagulation in neurosurgical applications dates to the late 1970s. Although hemoglobin is highly absorbing at 1.064 μm, this wavelength is also scattered by brain tissue which makes it difficult to confine the beam to the treatment volume thereby jeopardizing adjacent normal structures. This limitation has prevented the widespread use of the Nd:YAG laser in neurosurgical applications.

Presently, the laser has a rather limited role in therapeutic applications in the brain. In contrast, there has been a steady growth in diagnostic laser-based approaches for brain imaging and spectroscopy. This has been driven primarily by the development of small, user-friendly, and inexpensive diode lasers that can easily be integrated into the clinical setting. Other factors include the development of instrumentation and mathematical models that have facilitated rapid and noninvasive imaging and spectroscopy.

The first demonstration of in vivo diffuse optical measurements in the brain can be traced to Franz Jobsis who, in 1977, used near infrared light to measure hemoglobin and cytochrome c oxidase in felines and humans. Since then, a number of near infrared laser-based spectroscopic and imaging approaches have been developed. These techniques, collectively referred to as near infrared spectroscopy

(NIRS), diffuse optical spectroscopy (DOS), or diffuse optical tomography (DOT), are reviewed in Chaps. 2, 3, and 4. The history and applications of DOS are emphasized in Chap. 2 while Chap. 3 focuses on the theory and instrumentation. These themes are continued in Chap. 4 which also provides a specific example of an in vivo application of DOT for brain imaging.

Newer brain imaging approaches are presented in Chaps. 5, 6, and 7. These include laser speckle imaging (Chap. 5), photoacoustic imaging and spectroscopy (Chap. 6), and optical coherence tomography (OCT: Chap. 7). Laser speckle imaging is ideally suited for real-time imaging of cerebral blood flow. The instrumentation is relatively simple and can easily be integrated into existing neurosurgical microscopes. The utility of this imaging technique has already been verified in pilot clinical studies. Both photoacoustic imaging and OCT have demonstrated their potential for brain imaging and spectroscopy in animal models and, in the case of OCT, its clinical feasibility for imaging cerebral vessels has been shown in human subjects. Although no clinical trials have been performed to date, real-time photoacoustic imaging of cortical hemodynamics has been demonstrated in rodents and the ability of this modality to image through relatively thick skulls suggests that it could be useful in human neonatal brain imaging.

ALA-based fluorescence-guided resection (FGR: Chap. 8) has proven effective in maximizing the extent of surgical resection of high-grade gliomas as evidenced from increased progression-free survival. The technique has received regulatory approval in Europe and is currently being evaluated in clinical trials in the USA. Compared to other imaging techniques (MRI, PET) for resection guidance, FGR compares favorably: it is cost-effective and does not impede the surgical procedure.

The remaining Chaps. 9, 10, and 11 focus on promising laser-based therapeutics for the treatment of brain tumors. The most developed of these is photodynamic therapy (PDT: Chap. 9) which has been the subject of a number of clinical trials since the early 1980s. Results are somewhat mixed: some studies show a positive correlation between survival and light dose while others do not. Very high light doses seem to be particularly effective and additional trials are required in order to validate this treatment option for high-grade glioma patients. Ongoing efforts are aimed in part towards optimizing light delivery protocols for maximum PDT effect. Additionally, the combined use of FGR and PDT is intriguing as it has the potential to reduce the tumor burden substantially.

Laser interstitial thermotherapy (LITT) of brain tumors has been the subject of numerous preclinical studies dating back to the early 1990s. The results of recent clinical trials suggest that LITT may be an effective therapy for patients who fail radiation therapy; however, the technique is only suitable for relatively small focal lesions which would preclude its use for invasive tumors such as high-grade gliomas. An interesting variant of LITT is the use of near infrared absorbing nanoparticles for thermal destruction of brain lesions. This approach, termed photothermal therapy (PTT) is the subject of Chap. 10. Gold-silica nanoshells have proven to be especially effective both in vitro and in vivo. A particularly interesting approach for enhancing tumor specificity is the use of macrophages as delivery vehicles for nanoparticles. This theme is explored further in Chap. 11.

Chapter 11 reviews recent developments in optical therapeutics including PTT and photochemical internalization (PCI). These techniques may prove useful in the treatment of high-grade gliomas. Specifically, recent findings illustrating the potential of PCI for the delivery of chemotherapeutic agents and tumor suppressor genes are presented as are specific examples of nanoshell-mediated PTT.

Finally, returning to the beginning, knowledge of the optical properties of the brain are essential in both diagnostic and therapeutic applications, and as such, Chap. 1 provides an updated summary along with a discussion of the commonly used techniques for their determination.

In closing, the book is not intended as an exhaustive review of optical-based diagnostic and therapeutic approaches in the brain, indeed, much has been left out. Rather, the emphasis is on techniques that appear promising and have already been (or will soon be) evaluated in the clinic.

Las Vegas, NV USA Steen J. Madsen

Contents

1 Optical Properties of Brain Tissue 1
Steen J. Madsen and Brian C. Wilson

2 History of Diffuse Optical Spectroscopy of Human Tissue 23
Theodore J. Huppert

3 Diffuse Optical Tomography for Brain Imaging: Continuous Wave Instrumentation and Linear Analysis Methods 57
Paolo Giacometti and Solomon G. Diamond

4 Diffuse Optical Tomography for Brain Imaging: Theory 87
Zhen Yuan and Huabei Jiang

5 Laser Speckle Imaging of Cerebral Blood Flow 117
Lisa M. Richards, Erica L. Towle, Douglas J. Fox, and Andrew K. Dunn

6 Photoacoustic Tomography of the Brain 137
Jun Xia and Lihong V. Wang

7 Optical Coherence Tomography for Brain Imaging 157
Gangjun Liu and Zhongping Chen

8 Delineating Normal from Diseased Brain by Aminolevulinic Acid-Induced Fluorescence 173
Herbert Stepp and Walter Stummer

9 Intracranial Photodynamic Therapy 207
Brian C. Wilson and Steen J. Madsen

10 Nanoparticle-Mediated Photothermal Therapy of Brain Tumors 235
Amani R. Makkouk and Steen J. Madsen

11 Photo-activated Cancer Therapy: Potential for Treatment of Brain Tumors 253
Henry Hirschberg

Index 273

Contributors

Zhongping Chen Department of Biomedical Engineering, University of California, Irvine, CA, USA

Solomon G. Diamond Thayer School of Engineering, Dartmouth College, Hanover, NH, Germany

Andrew K. Dunn Department of Biomedical Engineering, The University of Texas at Austin, Austin, TX, USA

Douglas J. Fox NeuroTexas Institute, St. David's Hospital, Austin, TX, USA

Paolo Giacometti Thayer School of Engineering, Dartmouth College, Hanover, NH, Germany

Henry Hirschberg Beckman Laser Institute, University of California, Irvine, CA, USA

Theodore J. Huppert Department of Radiology and Bioengineering, University of Pittsburgh, Pittsburgh, PA, USA

Huabei Jiang Department of Biomedical Engineering, University of Florida, Gainesville, FL, USA

Gangjun Liu Department of Biomedical Engineering, Beckman Laser Institute, University of California, Irvine, CA, USA

Steen J. Madsen Department of Health Physics and Diagnostic Sciences, University of Nevada, Las Vegas, NV, USA

Amani R. Makkouk Interdisciplinary Graduate Program in Immunology, University of Iowa, Iowa City, IA, USA

Lisa M. Richards Department of Biomedical Engineering, The University of Texas at Austin, Austin, TX, USA

Herbert Stepp Laser-Forschungslabor, Klinikum der Universitaet Muenchen, Munich, Germany

Walter Stummer Universitaetsklinikum Muenster, Muenster, Germany

Erica L. Towle Department of Biomedical Engineering, The University of Texas at Austin, Austin, TX, USA

Lihong V. Wang Department of Biomedical Engineering, Washington University, St. Louis, MO, USA

Brian C. Wilson Department of Medical Biophysics, University of Toronto/ Ontario Cancer Institute, Toronto, ON, Canada

Jun Xia Department of Biomedical Engineering, Washington University, St. Louis, MO, USA

Zhen Yuan Department of Biomedical Engineering, University of Florida, Gainesville, FL, USA

Chapter 1
Optical Properties of Brain Tissue

Steen J. Madsen and Brian C. Wilson

1.1 Introduction

Knowledge of the propagation and distribution of light in tissues is critical to enable interpretation and quantification in diagnostic applications and to maximize efficacy and minimize collateral damage in therapeutic applications. The latter is especially relevant for therapeutic applications in the brain, where damage to eloquent areas can result in severe morbidity. Like other tissues that scatter and absorb light, the brain is optically turbid, so that light propagation can be described using the radiation transport equation (RTE), also known as the Boltzmann transport equation [1]. Solution of the RTE requires knowledge of the fundamental optical properties of tissues: the absorption coefficient, the scattering coefficient, and the scattering anisotropy. Once the tissue optical properties are known, the transport equation can be used to calculate the light distribution (fluence rate) at any point for a given source specification [2]. In the vast majority of cases, analytical solutions to the transport equation do not exist, thus necessitating the use of approximate methods.

1.2 Light Transport in Tissue

1.2.1 Radiation Transport Equation

If the wave properties of light are ignored (e.g., polarization and diffraction), then light photons propagating in biological tissues can be considered as neutral

---

S.J. Madsen (✉)
Department of Health Physics and Diagnostic Sciences, University of Nevada,
Las Vegas, NV, USA
e-mail: steen.madsen@unlv.edu

B.C. Wilson
Ontario Cancer Institute/University of Toronto, Toronto, ON, Canada

S.J. Madsen (ed.), *Optical Methods and Instrumentation in Brain Imaging and Therapy*, Bioanalysis: Advanced Materials, Methods, and Devices 3,
DOI 10.1007/978-1-4614-4978-2_1, © Springer Science+Business Media New York 2013

particles, analogous to neutrons in a nuclear reactor. The fundamental quantity of interest in the RTE is the energy radiance, $L(r, \mathbf{\Omega})$, which is the radiant power transported at location $\mathbf{r}$ in a given direction $\mathbf{\Omega}$ per unit solid angle per unit area perpendicular to that direction [W m^{-2} sr^{-1}]. The integral of the radiance over 4π solid angle is called the energy fluence rate, $E_0(\mathbf{r})$, which has units of W m^{-2}. The fluence rate is an important quantity in a number of applications, including photodynamic therapy dosimetry [2, 3]. Key parameters include the absorption coefficient, μ_a, and the differential scattering coefficient, $\mu_s(\mathbf{\Omega}' \rightarrow \mathbf{\Omega})$, where $\mathbf{\Omega}'$ and $\mathbf{\Omega}$ are the propagation directions before and after elastic scattering. The total scattering coefficient, μ_s, is obtained by integrating the differential scattering coefficient over all final directions. Since all the interaction coefficients may be functions of position, the time-dependent RTE can be expressed as [3]

$$\begin{aligned}\frac{1}{v}\frac{\partial}{\partial t}L(\boldsymbol{r},\Omega,t) + \Omega\cdot\nabla L(\boldsymbol{r},\Omega,t) + [\mu_a(\boldsymbol{r}) + \mu_s(\boldsymbol{r})]L(\boldsymbol{r},\Omega,t) \\ = \int_{4\pi} L(\boldsymbol{r},\Omega',t)\mu_s(\boldsymbol{r},\Omega' \rightarrow \Omega)\mathrm{d}\Omega' + S(\boldsymbol{r},\Omega,t)\end{aligned} \tag{1.1}$$

where $S(\mathbf{r}, \mathbf{\Omega}, t)$ is a source term and v is the speed of light in tissue. Once the optical properties of the tissue are known, (1.1) can be used to calculate the fluence rate at any position for a specific source configuration.

1.2.2 Solution to the Transport Equation

Exact solutions to the RTE exist for only a few limiting cases. For example, Chandrasekhar [4] has solved the case of a homogeneous, semi-infinite, isotropically scattering medium irradiated with a collimated beam of infinite extent, while Rybicki [5] has solved the RTE in a similar medium irradiated with a narrow collimated beam. A number of numerical techniques, including the discrete ordinates approach [6], have been attempted and methods suitable for a simple slab geometry have been summarized by van de Hulst [7].

The most commonly used numerical technique for solving the RTE is Monte Carlo (MC) modeling. The algorithms used in MC simulations are relatively straightforward and codes for simulating light propagation in tissues are widely available (e.g., [8]). MC simulations record the history of individual photons, and parameters such as the distance between interactions and the scattering angle are sampled from appropriate probability distributions [9]. The fluence can be estimated from the number of photon interactions recorded in each volume element, and the accuracy depends on the total number of photon histories. Although MC modeling can be used to simulate light propagation under realistic conditions (variety of light sources, multiple tissue types, and complex geometries), simulations can be computationally intensive, since they typically require millions of photon histories to obtain adequate signal-to-noise ratio in the calculated values. Presently, MC modeling is used primarily to check the accuracy of more rapid approximate methods.

1.2.3 Approximate Solutions to the Transport Equation

1.2.3.1 The Diffusion Approximation

Under the assumption that the radiance is only weakly direction dependent (i.e., linearly anisotropic), the integro-differential equation (1.1) can be expressed as a partial differential equation that can be solved using standard techniques. In terms of the fluence rate, $E_0(\mathbf{r})$, the diffusion equation can be expressed as [3]

$$\frac{1}{v}\frac{\partial}{\partial t}E_0(\boldsymbol{r},t) - \nabla\cdot[3(1-g(\boldsymbol{r}))\mu_\mathrm{s}(\boldsymbol{r})]^{-1}\nabla E_0(\boldsymbol{r},t) + \mu_\mathrm{a}(\boldsymbol{r})E_0(\boldsymbol{r},t) = S(\boldsymbol{r},t) \quad (1.2)$$

where $g(\mathbf{r})$ is the scattering anisotropy parameter (equal to the expectation value of the cosine of the polar scattering angle). The value of g varies from -1 to 1: $g = 0$ corresponds to isotroptic scattering, while values of 1 and -1 correspond to total forward and backward scattering, respectively. Light scattering in most tissues is highly forwardly directed (i.e., $g > 0.9$), thus requiring several scattering events to randomize the direction of light propagation. To account for this, a reduced (or transport) scattering coefficient has been defined: $\mu_\mathrm{s}' = \mu_\mathrm{s}(1-g)$. The diffusion approximation is valid only in highly scattering media (i.e., $\mu_\mathrm{s}' > {\sim}10\ \mu_\mathrm{a}$) and if the point of interest is far from sources or boundaries. Analytic solutions to the diffusion equation exist for very simple conditions (optically homogeneous tissue) and geometries (infinite, semi-infinite, and slab) [10]. In these situations, the diffusion approximation can be used to calculate the fluence rate to an accuracy of around 10% [3].

1.2.3.2 Kubelka–Munk Model

This 2-flux model describes the propagation of a uniform, diffuse irradiance in a one-dimensional isotropic slab with no reflection at the boundaries [11, 12]. It is assumed that the slab is illuminated by a Lambertian source and that the radiance remains isotropic with depth. Under these conditions, the inward, i, and outward, j, fluxes can be expressed by the coupled equations: [2]

$$-\,\mathrm{d}i = -(S+K)i\mathrm{d}x + Sj\,\mathrm{d}x \quad (1.3)$$

$$\mathrm{d}j = -(S+K)j\mathrm{d}x + Si\,\mathrm{d}x \quad (1.4)$$

where dx is the thickness of an elemental layer of the slab, and S and K are the Kubelka-Munk scattering and absorption coefficients, respectively. It should be noted that K and S are not equivalent to the absorption and scattering coefficients of diffusion theory: K dx is the fraction of incident flux absorbed by a layer illuminated by a Lambertian source, while S dx is the fraction scattered into the backward hemisphere. Due to the simplicity of the Kubelka–Munk model, it has been used for measuring the optical properties of tissues, particularly in layered models, but the underlying assumptions of isotropic scattering, matched boundaries, and diffuse irradiance are unrealistic for many light–tissue applications.

1.2.3.3 Inverse Adding-Doubling Method

The inverse adding doubling (IAD) method is a numerical solution to the one-dimensional RTE that is applicable to homogeneous turbid slabs with any optical thickness, albedo, or phase function [13–15]. The method is a reversal of the usual procedure of calculating reflection and transmission from optical properties, hence the term "inverse." "Adding-doubling" refers to the numerical method used to solve the RTE. The IAD method begins with an initial guess of the optical properties of the sample. The reflection and transmission are then calculated using the adding-doubling method. The calculated values are compared with the measured reflection and transmission. This procedure is repeated until a match is obtained. The set of optical properties resulting in reflection and transmission values matching the measured values is assumed to be the optical properties of the sample The IAD approach has a number of advantages over other methods, including increased speed and accuracy and a high degree of flexibility in modeling turbid samples with intermediate albedos, mismatched boundary conditions, and anisotropic scattering [13]. The accuracy of the technique can be improved simply by increasing the computation time: errors of less than 3% are readily achievable. Since both anisotropic phase functions and Fresnel reflection at boundaries are readily accounted for, the IAD approach is ideally suited to measurements involving biological tissues placed between glass slides, and it has been used to determine the optical properties of a number of tissues, including the brain. Since this technique applies only to uniformly illuminated homogenous slabs, it is difficult to envision its use for in vivo determination of optical properties.

1.3 Optical Property Measurements

A wide variety of methods have been employed to measure the optical properties of biological tissues, including the brain [16, 17]. Early attempts were generally very invasive, requiring excised tissue specimens. However, with the advent of time- and frequency-domain techniques in the early 1990s, in situ optical measurements have become possible, paving the way for minimally invasive or noninvasive techniques suitable for clinical use.

In general, the optical properties of tissues can be divided into two classes: fundamental and derived. Fundamental optical properties include the absorption and scattering coefficients, scattering phase function, the mean cosine of scatter, the transport scattering coefficient, the total attenuation coefficient, μ_t, (sum of absorption and scattering coefficients) and its inverse, the mean free path, and the albedo, a (the ratio of the scattering coefficient to the total attenuation coefficient). Derived optical properties can be considered as descriptors of different aspects of the spatial distribution of light in bulk tissue, and may be expressed in terms of the fundamental coefficients using various propagation models. They include the local and total diffuse reflectance and transmittance, the effective attenuation coefficient, $\mu_{\mathrm{eff}} = [3\mu_a\,(\mu_a + \mu_s')]^{0.5}$, and its inverse, the effective penetration depth, δ.

Experimental techniques for measuring the fundamental optical properties can be divided into two categories: indirect and direct [18]. Indirect methods are based on in vitro or in vivo measurements in bulk tissue. The fundamental parameters can then be deduced by applying one or more light propagation models. Direct methods involve the use of tissue samples that are sufficiently thin that multiple photon scattering is negligible. The fundamental optical properties can then be determined directly from measurements of the fractional light absorbance in the sample, or of the light flux scattered by the sample. In terms of modeling, the only assumption made in this case is that light propagation can be described by the RTE.

1.3.1 Direct Methods

These methods require tissue samples sufficiently thin such that single scattering dominates. For example, in soft tissues at 630 nm, if $\mu_s = 40\ \mathrm{mm}^{-1}$, this implies that the sample should be less than about 25 μm thick in order to ensure that single scattering events dominate the signal. Samples are typically mounted in a cuvette or supported between microscope slide covers. Different light irradiation and detection geometries are then used depending on the particular fundamental property to be measured. Measurement of the total attenuation coefficient can be accomplished using a setup of the type illustrated in Fig. 1.1a [19]. A well collimated light beam is incident on the tissue sample, and the directly transmitted (primary) light is measured by a detection method insensitive to scattered radiation. For a sample of thickness x, if the incident and detected fluence rates (Ψ_o and Ψ, respectively) are known, then the total attenuation coefficient is given by

$$\mu_t = \frac{\frac{1}{x}\ln \Psi_o}{\Psi} \tag{1.5}$$

Figure 1.1b illustrates the goniometer method used to measure the scattering phase function [20–23]. The sample is held between glass slides and immersed in a cylindrical water tank to minimize distortions in the measured phase function caused by refraction at the tissue boundaries. The detector is rotated around the sample and the signal is measured as a function of angle. A microscope-based

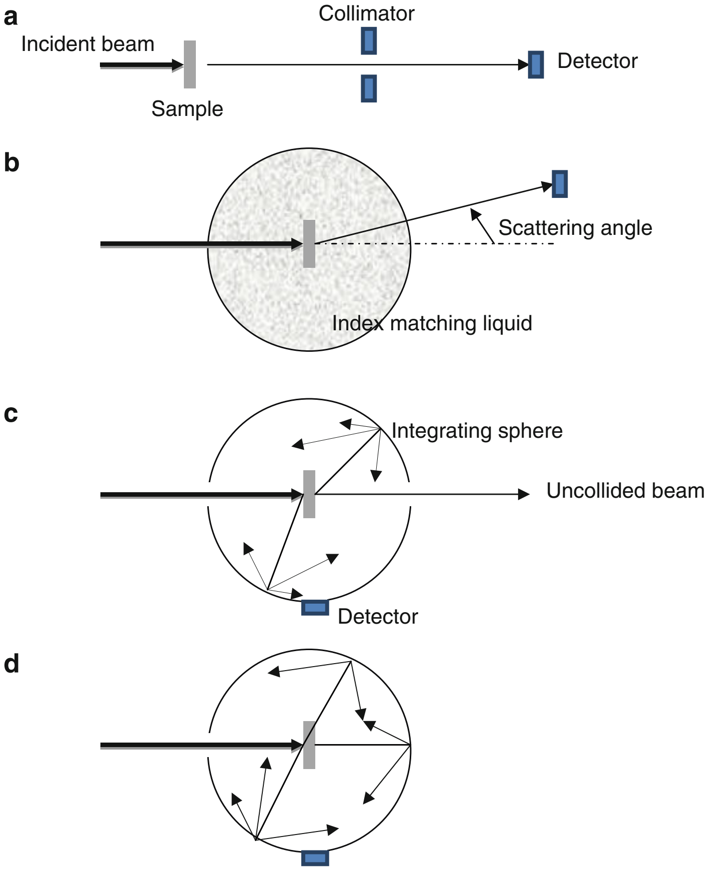

Fig. 1.1 Methods for the direct measurement of fundamental optical properties of a tissue. (**a**) Measurement of the total attenuation coefficient. (**b**) Measurement of the scattering phase function. (**c**) Measurement of the scattering coefficient using an integrating sphere with its interior surface coated with Spectralon, MgO, or $BaSO_4$ which has nearly 100 % diffuse reflectance over the entire optical spectrum. (**d**) Measurement of the absorption coefficient using an integrating sphere

system for measurements of scattering from small tissue volumes has also been described by Popp et al. [24].

Measurement of the scattering coefficient using an integrating sphere technique is illustrated in Fig. 1.1c. The detector signal is measured with the sample present (S_s) and without the sample (S_o). For an optically thin sample of thickness x, the scattering coefficient is given by

$$\mu_s = \frac{1}{x}\frac{S_s}{S_o} \tag{1.6}$$

The absorption coefficient can also be measured with an integrating sphere (Fig. 1.1d). Measurements are made of the signal with the sample (S_a) and without the sample (S_o), but in this case S_a includes both the scattered and directly transmitted radiation. The difference between S_a and S_o is due only to absorption; thus, the absorption coefficient is given by [19]

$$\mu_a = \frac{1}{x} \frac{S_o - S_a}{S_o} \tag{1.7}$$

Although direct methods are model independent, they are problematic due to complications associated with obtaining sufficiently thin samples. Procedures such as freezing and mechanical grinding of tissue are commonly used to obtain thin samples but these may result in measurement bias (e.g., loss of blood and cell lysis) compared with the values in intact tissues.

1.3.2 Indirect Methods

Due to the limitations associated with direct methods, many investigators have pursued indirect methods to derive the optical properties of tissue. Sample preparation is relatively simple since optically thin samples are not required and there is the possibility of performing noninvasive in vivo measurements.

Indirect methods may be divided into three categories: [18] (1) external, in which detectors are located outside the tissue volume, (2) internal, in which detector probes are located within the tissue, and (3) pertubative methods, in which external or internal measurements are made after the addition to the tissue of some substance of known optical properties. Clearly, in a clinical situation, external methods are preferred since they are noninvasive.

There are three main classes of external techniques: photothermal, photoacoustic, and radiometric. The discussion here will be confined to radiometric techniques since photothermal methods are limited to surface applications (e.g., measurement of the optical properties of skin lesions), and photoacoustic techniques combine both optical and ultrasonic modalities. In general, six different types of radiometric measurements can be made: reflectance or transmittance, total or local fluence, and steady-state or time-resolved (i.e., sensitive to the photon propagation time through tissue following picosecond laser pulse irradiation). Photon propagation time-dependent measurements may also be made in the frequency domain: while conceptually similar to time-resolved methods, the instrumentation is vastly different and in most cases simpler and cheaper to implement. Most studies have focused on measurements of diffuse reflectance where the measurable quantities are R, $R(t)$, $R(\rho)$, and R (ρ,t) (or R (ρ,ω) in the frequency domain). These quantities correspond to the total and local reflectance under steady-state and time-dependent conditions. The source–detector separation is denoted by ρ. Since both the diffuse reflectance and transmittance depend strongly on the tissue optical properties, their measurement may yield the fundamental optical properties if an appropriate model of light propagation is applied.

Typically, such models have assumed optically homogeneous tissues or very simple layered structures, and simple tissue and irradiation geometries.

Although indirect methods may be clinically appealing in that they offer the potential for noninvasive in vivo measurements, there are numerous complications. For example, the particular model used in deriving the optical properties can be quite complicated due to the fact that the irradiation and detection geometries must be accounted for in both cases. The validity of the model may also be suspect in some cases. In general, the simpler models are accurate only over a limited range of optical properties and geometries. The lack of analytic inverse solutions may also pose problems, that is, the models usually predict the behavior of the derived parameters given the fundamental properties, and only the simplest yield analytic expressions for the inverse task of calculating the fundamental properties from measurements of the derived parameters. Therefore, it is necessary to iterate between the required fundamental properties and the derived data to obtain a best-fit solution.

A potential problem with all indirect methods is that the derived data are usually restricted, that is, it is unlikely that the fluence rate and/or reflectance will be measured at all points in or out of the irradiated tissue. Thus, it may not be possible to derive all the fundamental values from the measured data. Furthermore, van de Hulst [25] has shown that the particular value of any derived parameter may result from different combinations of the fundamental properties—the so-called Similarity Principle, which can lead to ambiguity in the calculated values [18].

1.4 Optical Properties of Brain Tissue

The optical properties of various brain tissues from a number of species are summarized in Tables 1.1 and 1.2. In addition to the fundamental optical properties, the optical penetration depth (the tissue depth over which the light fluence is attenuated by 63%) is included in the two tables. Pre-1995 data are reproduced from an excellent summary compiled by Cheong [26].

It is clear from the data presented in Table 1.1 that there are significant variations in the optical properties derived from measurements on excised brain tissue. This is particularly evident in studies using very thin samples, where the optical properties are sensitively dependent on the tissue preparation technique [17, 27]. The absorption coefficient is especially sensitive to tissue preparation artifacts such as dehydration and loss of blood. For example, a number of studies have shown that the optical penetration depth in tissue can vary by a factor of 2 or more in the visible wavelength region where blood is the main absorber [20, 27]. Freezing and thawing affect tissue water content and result in structural changes that impact the scattering properties [17]. In cases where measurements are made on bulk tissues, variability in the derived optical properties may be due to differences in the source–detector fiber orientation (in the case of interstitial measurements), and the type of fiber used (flat cut vs. spherical diffuser, which have markedly different numerical apertures).

Table 1.1 Optical properties of brain tissues in vitro

Species	λ (nm)	μ_a (cm^{-1})	μ_s (cm^{-1})	g	μ_s' (cm^{-1})	δ (cm)	Tissue preparation	Experimental method	Theory
Calf [31, 49]	633	0.19	–	–	6.6	0.51	Thin slabs, frozen and thawed	Integrating sphere; interstitial fiber detectors	Similarity transform + 2-parameter phase; diffusion theory
	1,064	0.36	–	–	6.7	0.36			
	1,320	0.84	–	–	5.4	0.25			
Cat [31]	488	–	–	–	–	0.09	*Post mortem* bulk tissue	Interstitial fiber detectors	Diffusion theory
	514	–	–	–	–	0.08			
	630	–	–	–	–	0.11–0.19			
Human adult [50]	488	–	–	–	–	0.04–0.07	*Post mortem* bulk tissue	Interstitial fiber detectors	Diffusion theory
	514	–	–	–	–	0.06–0.07			
	660	–	–	–	–	0.08–0.14			
	1,060	–	–	–	–	2.9–4.3			
Human adult [51]	630	0.3–1.0			30–40	0.12	*Post mortem* slab	Integrating sphere	Diffusion + Kubelka Munk
Human adult white matter [29]	633	2.2 ± 0.2	532 ± 41	0.82 ± 0.01	91 ± 5	0.042	Freshly resected, used within 12 h; slabs	Integrating sphere	Inverse adding-doubling
	1,064	3.2 ± 0.4	469 ± 34	0.87 ± .01	60.3 ± 2.5	0.041			
Gray matter [29]	633	2.7 ± 0.2	354 ± 37	0.94	20.6 ± 0.2	0.08	Same as above	Same as above	Same as above
	1,064	5.0 ± 0.5	134 ± 14	0.90	11.8 ± 0.9	0.06			
White matter [28]	630	0.8	409	0.84	65.44	0.079	Thin slabs, frozen and thawed	Integrating sphere and collimated transmittance	Monte Carlo
	670	0.7	401	0.85	60.15	0.083			
	850	1.0	342	0.88	41.0	0.09			
	1,064	1.6	513	0.89	32.56	0.1			
White matter coagulated [28]	630	1.8	460	0.91	41.4	0.065	Same as above	Same as above	Same as above
	670	1.5	430	0.92	34.4	0.079			
	850	1.7	380	0.95	19.0	0.097			
	1,064	2.2	360	0.96	14.4	0.096			

(continued)

Table 1.1 (continued)

Species	λ (nm)	μ_a (cm^{-1})	μ_s (cm^{-1})	g	μ_s' (cm^{-1})	δ (cm)	Tissue preparation	Experimental method	Theory
Gray matter [28]	630	0.2	90	0.89	9.9	0.41	Same as above	Same as above	Same as above
	670	0.2	84	0.90	8.4	0.44			
	850	0.4	75	0.90	7.5	0.32			
	1,064	0.5	57	0.90	5.7	0.33			
White matter [30]	630	0.81	–	–	53.4	0.087	Thin slabs, frozen and thawed	Integrating sphere	Inverse adding-doubling
	670	0.71	–	–	50.1	0.096			
	850	0.64	–	–	39.7	0.11			
Human adult gray matter [30]	630	0.93	–	–	10.4	0.18	Thin slabs, frozen and thawed	Integrating sphere	Inverse adding-doubling
	670	0.81	–	–	9.5	0.20			
	850	0.47	–	–	7.6	0.30			
Human adult cerebellum [28]	630	0.7	290	0.87	37.7	0.11	Thin slabs, frozen and thawed	Integrating sphere and collimated transmittance	Monte Carlo
	670	0.6	290	0.88	34.8	0.13			
	850	0.6	240	0.90	24	0.15			
	1,064	0.7	210	0.91	18.9	0.16			
Human adult pons [28]	630	0.5	100	0.92	8.0	0.28	Same as above	Same as above	Same as above
	670	0.4	100	0.92	8.0	0.31			
	850	0.5	80	0.92	6.4	0.31			
	1,064	1.0	65	0.93	4.6	0.24			
Human adult thalamus [28]	630	0.65	190	0.87	24.7	0.14	Same as above	Same as above	Same as above
	670	0.5	190	0.88	22.8	0.17			
	850	0.5	150	0.90	15.0	0.21			
	1,064	0.95	140	0.91	12.6	0.16			
Human brain tumor [52]	488	–	–	–	–	0.14–0.05	Freshly resected, in situ	Interstitial fiber detectors	Diffusion theory
	514	–	–	–	–	0.14–0.05			
	635	–	–	–	–	0.26–0.17			
	1,060	–	–	–	–	0.53–0.30			

Human brain tumor astrocytoma [28]	630	1.0	120	0.95	6.0	0.22	Thin slabs, frozen and thawed	Integrating sphere and collimated transmittance	Monte Carlo
	670	0.7	110	0.96	4.4	0.31			
	850	0.5	80	0.96	3.2	0.42			
	1,064	0.65	75	0.97	2.3	0.42			
Human brain tumor meningioma [28]	630	0.35	185	0.95	9.3	0.31	Same as above	Same as above	Same as above
	670	0.3	180	0.95	9.0	0.35			
	850	0.25	130	0.95	6.5	0.44			
	1,064	0.6	110	0.96	4.4	0.33			
Human brain tumor glioma [30]	630	0.81	–	–	22.0	0.13	Thin slabs, frozen and thawed	Integrating sphere	Inverse adding-doubling
	670	0.71	–	–	21.0	0.15			
	850	0.64	–	–	18.0	0.17			
Human infant [50]	488	–	–	–	–	0.13–0.17	*Post mortem* bulk tissue	Interstitial fiber detectors	Diffusion theory
	514	–	–	–	–	0.11–0.17			
	660	–	–	–	–	0.30–0.40			
	1,060	–	–	–	–	0.71–0.91			
Human cranial bone [36]	800	0.11	–	–	19.5	0.39	Thin slabs	Integrating sphere	Inverse adding-doubling
	900	0.15	–	–	18.0	0.35			
	1,000	0.22	–	–	17.1	0.30			
	1,100	0.15	–	–	16.2	0.37			
Pig [27, 53]	633	–	52–57	0.945 [20]	–	0.07–0.23	*Post mortem* bulk tissue	Interstitial fiber detectors	Diffusion theory; added absorber
Pig white matter [54]	633	2.0	–	–	100	0.04	Thin slabs, frozen and thawed	Integrating sphere	Inverse adding-doubling
Pig white matter coagu-lated [54]	633	3.0	–	–	65	0.04	Thin slabs, frozen and thawed	Reflectance + transmittance	Multiple polynomial regression

(continued)

Table 1.1 (continued)

Species	λ (nm)	μ_a (cm^{-1})	μ_s (cm^{-1})	g	μ_s' (cm^{-1})	δ (cm)	Tissue preparation	Experimental method	Theory
Rat white matter [55]	830	–	–	–	–	0.035	Bulk tissue, freshly resected	Transmission	Beer's Law
Rat grey matter [55]	830	–	–	–	–	0.041	Same as above	Same as above	Same as above
Rat [56]	532	–	–	–	62.5 ± 31.3		Thin slabs, frozen and thawed	Interferometry	Fourier transform light scattering

In Ref. [28], optical properties measured from 360 to 1,100 nm

In Ref. [30], optical properties measured from 400 to 1,300 nm

Table 1.2 Optical properties of brain tissues in vivo

Species	λ (nm)	μ_a (cm^{-1})	μ_s (cm^{-1})	g	μ_s' (cm^{-1})	δ (cm)	Tissue preparation	Experimental method	Theory
Cat [31, 32]	405	–	–	–		0.023	In situ	Interstitial fiber detectors	Diffusion theory
	545	–	–	–		0.029			
	577	–	–	–		0.039			
	631	–	–	–		0.10–0.20			
Human adult [33]	630	–	–	–	–	0.10–0.21	In situ	Interstitial detectors and balloon light source during PDT	Diffusion theory
Human adult [57]	800	0.16	–	–	9.4	0.47	Surface of head	Time-resolved reflectance	Diffusion theory
Human adult [38]	674	<0.2	–	–	10.0	0.40	In situ frontal lobe	Spatially resolved diffuse reflectance	Monte Carlo
	811	<0.1	–	–	9.1	0.60			
	849	<0.1	–	–	9.2	0.60			
	956	0.15	–	–	8.9	0.50			
	674	0.173	–	–	11.2	0.41	Same as above	Frequency-domain photon migration	Diffusion theory
	811	0.182	–	–	7.4	0.49	In situ cerebellar white matter	Spatially resolved diffuse reflectance	Monte Carlo
	849	0.185	–	–	7.4	0.49			
	956	0.206	–	–	8.0	0.44			
	674	2.5	–	–	13.5	0.09			
	849	0.95	–	–	8.5	0.19			
	956	0.90	–	–	7.8	0.21			
	674	0.165	–	–	13.4	0.39	Same as above	Frequency-domain photon migration	Diffusion theory
	849	0.132	–	–	9.8	0.50			
	956	0.299	–	–	8.4	0.36			
Human adult [40]	830	0.140	–	–	4.0	0.76	surface of head	Frequency-domain photon migration	Two-layer diffusion theory

(continued)

Table 1.2 (continued)

Species	λ (nm)	μ_a (cm^{-1})	μ_s (cm^{-1})	g	μ_s' (cm^{-1})	δ (cm)	Tissue preparation	Experimental method	Theory
Human adult [41]	700	0.08–0.23	–	–	5.8–8.8	0.40–0.84	Surface of head	Time-resolved reflectance	Diffusion theory and Monte Carlo
	800	0.08–0.22	–	–	4.3–7.9	0.43–0.98			
	900	0.11–0.30	–	–	4.0–7.5	0.38–0.86			
Human brain tumor glioma [33, 34]	630	–	–	–	–	0.15–0.45	In situ	Interstitial detectors and spherical source	Diffusion theory
Human brain tumor medulloblastoma [38]	674	2.6	–	–	14.0	0.09	In situ	Spatially resolved diffuse reflectance	Monte Carlo
	849	1.0	–	–	10.7	0.17			
	956	0.75	–	–	4.0	0.31			
	674	0.120	–	–	10.5	0.51	In situ	Frequency-domain photon migration	Diffusion theory
	849	0.079	–	–	6.6	2.84			
	956	0.239	–	–	5.4	0.50			
Human infant [58]	761	0.16 ± 0.04	–	–	6.46 ± 1.21	0.56	Surface of head	Time-resolved reflectance	Diffusion theory
	795	0.13 ± 0.03	–	–	5.90 ± 1.15	0.65			
	835	0.18 ± 0.04	–	–	6.40 ± 1.16	0.53			
Human infant [43]	788	0.078 ± 0.01	–	–	9.16 ± 1.22	0.68	Surface of head	Frequency-domain photon migration	Diffusion theory
	832	0.089 ± 0.02	–	–	8.42 ± 1.23	0.66			
Pig [27]	630	–	–	–	–	0.22–0.27	In situ	Interstitial detectors with surface irradiation	Diffusion theory
Pig [59]	758	0.135–0.168	–	–	8.9–9.7	0.46–0.50	Surface of head	Continuous wave and frequency-domain spectroscopy	Differential path length factor and diffusion theory
	830	0.110–0.150	–	–	7.7–8.7	0.50–0.60			
Pig [60]	759	0.12	–	–	24.0	0.34	Surface of head	Time-resolved reflectance	Diffusion theory
	794	0.075	–	–	27.0	0.41			
	824	0.13	–	–	27.0	0.31			

Rat [37]	630	–	–	–	–	0.13	In situ	Surface irradiation and interstitial detection with spherical diffuser	Diffusion theory
Rat white matter [35]	750	–	–	–	35–60		In situ	Interstitial source and detector probes	Monte Carlo
Rat grey matter [35]	750	–	–	–	12–25		Same as above	Same as above	Same as above
Rat [36]	632	0.57 ± 0.02	–	–	27.9 ± 2.4	0.14	In situ	Interstitial source and detector probes	Diffusion theory
Rat brain tumor glioma [36]	632	1.46 ± 0.09	–	–	5.45 ± 0.44	0.18	Same as above	Same as above	Same as above
	632	1.39	–	–	7.30	0.17	Same as above	Same as above	Monte Carlo

In Ref. [57], measurements made from 760 to 900 nm

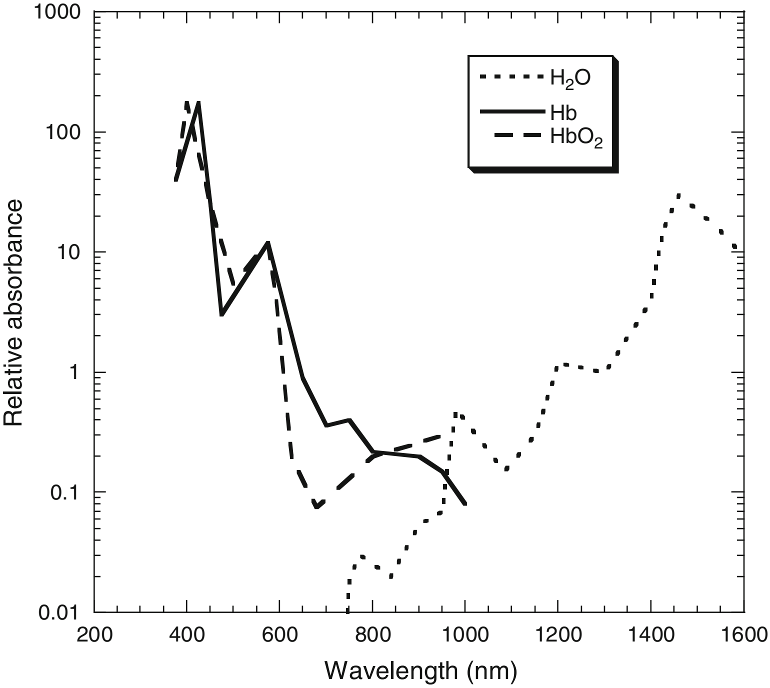

Fig. 1.2 Absorption spectra of hemoglobin and water in living tissues

Regardless of whether measurements are made on thin samples or bulk tissue, the derived optical properties depend on the type of theory used. In this regard, it is important to know the limitations of a given theory prior to using it for the intended application. A number of theories have been employed and, together with tissue preparation artifacts, account for the greatest variability in the derived optical properties determined in different studies.

As shown in Table 1.1, early studies were focused on measurements in the red wavelength region (630–670 nm), reflecting the interest in therapeutic applications such as photodynamic therapy. Later studies emphasized more the near-infrared, due to the emerging field of functional near-infrared spectroscopy (fNIRS). The optical properties of brain tissue at 1,064 nm have been the subject of numerous studies, reflecting the importance of the Nd:YAG laser as a tool for photocoagulation in (neuro)surgical applications.

The absorption coefficient provides information on the concentration of constituent tissue chromophores (e.g., hemoglobin, oxyhemoglobin, and melanin), while the scattering coefficient provides information on the form, size, and concentration of the scattering components. Brain tissue absorption spectra are dominated by hemoglobin absorption below 600 nm and water absorption above 1,000 nm (Fig. 1.2). Hence, due to the relatively low absorption by hemoglobin and water, an optical window exists in the red to near-infrared (approximately 600–1,400 nm) where light has optimal penetration in brain tissues. As illustrated in Table 1.1, scattering coefficients and anisotropy factors decrease and increase, respectively, with increasing wavelength. This is consistent with the diminishing effect of Rayleigh scattering and increased contribution of Mie scattering with increasing wavelength. The wavelength-dependent absorption of brain tissues is dominated by oxy- and deoxy-hemoglobin: however, since many reported measurements were made on excised tissues, there was likely a significant variability in the concentration of these chromophores, so that the specific values of the absorption coefficients presented in Table 1.1 are somewhat suspect. To some extent, this is also true for the scattering coefficient and anisotropy factor, since all optical properties are affected by sample preparation. As expected, due to decreased scattering, the penetration depth in brain tissues increases with increasing wavelength, although again the accuracy of the absolute values is unknown due in part to changes in chromophore concentrations and structural properties of excised tissues.

Not surprisingly, the results of Yaroslavky et al. [28] showed that tissue coagulation significantly alters the optical properties of brain tissues. This is obviously an important consideration in high-power therapeutic applications where changes in optical properties must be accounted for in order to achieve accurate dosimetry.

Again, not surprisingly, there are significant differences in the optical properties between white and grey matter [28, 29]. As shown in Table 1.1, human white matter was found to have significantly higher absorption and scattering compared to grey matter. The reasons for this are not entirely clear. The higher scattering of white matter may be due to the high density of myelinated axons—the predominant constituent of white matter [30]. The myelination itself may also contribute to the high scattering of this tissue.

Based on the data presented in Table 1.1, there do not appear to be significant absorption differences between tumor tissue and white matter [28, 30]. This is somewhat surprising, since brain tumors (especially meningiomas and high-grade gliomas) are highly vascularized, so that they should have increased absorption due to elevated hemoglobin content. These counterintuitive results are likely due to loss of blood from the excised specimens. Interestingly, excised brain tumor tissues appear to have significantly lower scattering compared to normal brain, reflecting structural differences between the two tissues, as expected.

In vivo optical property measurements (Table 1.2) can be divided into two categories: (1) noninvasive surface measurements, and (2) interstitial measurements. Due to their invasive nature, interstitial measurements are confined to experimental animal models and intraoperative procedures such as cytoreductive surgery. This technique is not appropriate for functional activation studies in healthy volunteers. A number of interstitial measurement approaches have been attempted including separate insertion of source and detector fibers [31–36], surface irradiation and detection via interstitial fiber detectors [27, 37], and insertion of small probes incorporating multiple source and detection fibers for light acquisition at multiple source–detector separations [38]. The last approach, using small probes, would appear to be the most appealing, since the source–detector separation is then known accurately. It should be noted, however, that uncertainties in the separation introduces significant errors in the derived optical properties. The choice of model to be used is especially critical in this approach, since diffusion theory is not applicable for small source–detector separations unless additional calibration procedures and/or spectral measurements are included [39]. In the absence of such measurements, more complex and/or time-consuming models are required (e.g., Monte Carlo).

The majority of studies using noninvasive surface measurements have employed either time-resolved diffuse reflectance spectroscopy or frequency-domain photon migration techniques. The primary drawback with surface measurements, where source and detector probes are placed on the surface of the head, is the limited interrogation volume—information is obtained only from the superficial structures of the brain. The interrogation depth can be controlled to some extent by varying the source–detector separation: the greater the separation, the deeper the interrogation. Unfortunately, the diffusely reflected near-infrared light signals diminish rapidly with increased source–detector separation due to attenuation by the brain and overlying structures. Thus, the maximum interrogation depth in the brain is approximately 0.5 cm. This is sufficient for most fNIRS studies but does not allow measurement of optical properties of deeper structures, which may be important for some applications.

In human brain mapping by fNIRS, the goal is to detect changes in the absorption properties of the brain due to the hemodynamic response following functional activation. In some instances, for example, response measurements in a single individual, knowledge of the relative changes in the optical properties are sufficient. However, determination of the absolute optical properties of the brain required in order to quantify physiological components, such as hemoglobin concentration and its oxygen saturation or cytochrome c oxidase concentration [40, 41]. Such absolute measurements are required for comparisons between individuals and in long time series studies in single subjects.

Accurate determination of the optical properties of the brain via noninvasive surface measurements is complicated by the multiple layered structures overlying the brain (scalp, skull, dura, and CSF). Furthermore, the scalp itself is layered, comprising skin, fat, and muscle that each contribute differently to the optical signals. Interpretation of noninvasive surface measurements is particularly challenging in human adults due to the thickness of the scalp (5–7 mm) and skull (7–8 mm) [42]. In contrast, noninvasive determination of the optical properties of the superficial neonate brain is more straightforward, since the combined thickness of the scalp and skull is <5 mm [43]. Two approaches have evolved for accurate noninvasive determination of the optical properties of the brain: (1) employing multilayer diffusion models to account for the multiple tissue layers and (2) combining a simple semi-infinite diffusion model with surface measurements made at large source–detector fiber separations, for which the effects of the scalp and skull are minimized. Obviously, solutions to the diffusion equation become more complex as the number of layers increase. In many studies, the scalp and skull have been modeled as one layer due to their similar absorption and scattering properties [22, 40, 42, 44]. Although the meninges overlying the brain contains cerebrospinal fluid, light-scattering membranes, and light-absorbing blood vessels, these structures do not significantly affect light penetration into the brain and this layer has been ignored in a number of studies [45]. Hence, 2-layer (scalp/skull + brain) [46] or 3-layer diffusion models (scalp/skull + CSF + brain) [47] are normally sufficient for accurate determination of the brain optical properties.

A simpler approach for determining the optical properties from noninvasive surface measurements has been proposed by Choi et al. [40], who found that a simple semi-infinite diffusion model could be used to determine the optical properties of the brain from reflectance data obtained at source–detector separations sufficiently large such that the photon sampling volume was confined primarily to the brain. In this technique, the influence of the overlying layers can be assessed simply by varying the source–detector separation.

Similar to the in vitro studies, the vast majority of in vivo experiments have been conducted using red and near-infrared wavelengths. As shown in Table 1.2, the variability in optical properties determined by different investigators is much less than that obtained from excised tissue specimens (Table 1.1), thus emphasizing the influence of tissue preparation artifacts and the importance of in vivo measurements for accurate assessment of tissue optical properties. Based on the data presented in Table 1.2, the red to NIR penetration depth in normal human brain ranges from approximately 0.4 to 0.9 cm. Due to the paucity of measurements, it is difficult to make comparisons to the optical properties of tumors. Such studies are also difficult in practical terms, since they involve intraoperative measurements. This is clearly an area requiring further investigation. An intraoperative fiberoptic probe system has recently been reported that can make such measurements [39, 48].

References

1. Ishimaru A (1978) Wave propagation and scattering in random media, Ch. 7 and 9. Academic, New York
2. Wilson BC, Patterson MS (1986) The physics of photodynamic therapy. Phys Med Biol 31:327–360
3. Wilson BC, Patterson MS (2008) The physics, biophysics and technology of photodynamic therapy. Phys Med Biol 53:R61–R109
4. Chandrasekhar S (1950) Radiative transfer. Oxford University Press, London
5. Rybicki GB (1971) The searchlight problem with isotropic scattering. J Quant Spectrosc Radiat Transfer 11:827–849
6. Duderstadt JJ, Hamilton LJ (1976) Nuclear reactor analysis. Wiley, New York, pp 103–144
7. van de Hulst HC (1980) Multiple light scattering tables, formulas and applications. Academic, New York
8. Wang LH, Jacques SL, Zheng LQ (1995) MCML—Monte Carlo modeling of light transport in multilayered tissues. Comput Methods Programs Biomed 47:131–146
9. Wilson BC, Adam G (1983) A Monte Carlo model for the absorption and flux distributions of light in tissue. Med Phys 10:824–830
10. Patterson MS, Wilson BC, Wyman DR (1991) The propagation of optical radiation in tissue. 1. Models of radiation transport and their application. Lasers Med Sci 6:155–168
11. Kubelka P, Munk F (1931) Ein beitrag zur optik der farbanstriche. Z Tech Phys 12:593–601

12. Kubelka P (1948) New contributions to the optics of intensely light scattering materials. J Opt Soc Am 38:448–457
13. Prahl SA, van Gemert MJC, Welch AJ (1993) Determining the optical properties of turbid media by using the adding-doubling method. Appl Opt 32:559–568
14. Pickering JW, Prahl SA, van Wieringen N, Beek JF, Sterenborg HJ, van Gemert MJC (1993) Double-integrating-sphere system for measuring the optical properties of tissue. Appl Opt 32:339–410
15. Pickering JW, Bosman S, Posthumus P, Blokland P, Beek JF, van Gemert MJC (1993) Changes in the optical properties (at 632.8 nm) of slowly heated myocardium. Appl Opt 32:367–371
16. Wilson BC (1995) Measurement of tissue optical properties: methods and theory. In: Welch AJ, van Gemert MJC (eds) Optical-thermal response of laser-irradiated tissue. Plenum, New York, pp 233–274
17. Cheong W, Prahl SA, Welch AJ (1990) A review of the optical properties of biological tissues. IEEE J Quantum Electron 26:2166–2185
18. Wilson BC, Patterson MS, Flock ST (1987) Indirect versus direct techniques for the measurement of the optical properties of tissues. Photochem Photobiol 46:929–935
19. Patterson MS, Wilson BC, Wyman DR (1991) The propagation of optical radiation in tissue. 2: optical properties of tissues and resulting fluence distributions. Lasers Med Sci 6:379–390
20. Flock ST, Wilson BC, Patterson MS (1987) Total attenuation coefficients and scattering phase functions of tissues and phantom materials at 633 nm. Med Phys 14:835–841
21. Key H, Davies ER, Jackson PC, Wells PNT (1991) Optical attenuation characteristics of breast tissues at visible and near-infrared wavelengths. Phys Med Biol 36:579–590
22. Firbank M, Hiraoka M, Essenpreis M, Delpy DT (1993) Measurement of the optical properties of the skull in the wavelength range 650–950 nm. Phys Med Biol 38:503–510
23. Ghosh N, Mohanty SK, Majumder SK, Gupta PK (2001) Measurement of optical transport properties of normal and malignant human breast tissue. Appl Opt 40:176–184
24. Popp AK, Valentine MT, Kaplan PD, Weitz DA (2003) Microscopic origin of light scattering in tissue. Appl Opt 42:2871–2880
25. van de Hulst HC (1980) Light scattering by small particles. Dover, New York
26. Cheong W (1995) Appendix to chapter 8: summary of optical properties. In: Welch AJ, van Gemert MJC (eds) Optical-thermal response of laser-irradiated tissue. Plenum, New York, pp 275–303
27. Wilson BC, Jeeves WP, Lowe DM (1985) *In vivo* and *post mortem* measurements of the attenuation spectra of light in mammalian tissues. Photochem Photobiol 42:153–162
28. Yaroslavsky AN, Schulze PC, Yaroslavsky IV, Schober R, Ulrich F, Schwarzmaier HJ (2002) Optical properties of selective native and coagulated human brain tissues in vitro in the visible and near infrared spectral range. Phys Med Biol 47:2059–2073
29. Beek JF, Blokland P, Posthumus P, Aalders M, Pickering JW, Sterenborg HJ, van Gemert MJ (1997) In vitro double-integrating-sphere optical properties of tissues between 630 and 1064 nm. Phys Med Biol, 42:2255–2261
30. Gebhart SC, Lin WC, Mahadevan-Jansen A (2006) *In vitro* determination of normal and neoplastic human brain tissue optical properties using inverse adding-doubling. Phys Med Biol 51:2011–2027
31. Doiron DR, Svaasand LO, Profio AE (1983) Light dosimetry in tissue applications to photoradiation therapy. In: Kessel D, Dougherty TJ (eds) Porphyrin photosensitization. Plenum Press, New York, pp 63–75
32. Doiron DR, Svaasand LO, Profio AE (1982) Wavelength and dosimetry considerations in photoradiation therapy (PRT). In: Berns M (ed) Proc. SPIE 357, lasers in surgery and medicine Bellingham, WA
33. Muller PJ, Wilson BC (1986) An update of the penetration depth of 630 nm light in normal and malignant human brain tissue *in vivo*. Phys Med Biol 31:1295–1297

34. Wilson BC, Muller PJ, Yanche JC (1986) Instrumentation and light dosimetry for intra-operative photodynamic therapy (PDT) of malignant brain tumors. Phys Med Biol 31:125–133
35. Johns M, Giller CA, German DC, Liu H (2005) Determination of reduced scattering coefficient of biological tissue from a needle-like probe. Opt Express 13:4828–4842
36. Bashkatov AN, Genina EA, Kochubey VI, Tuchin VV (2006) Optical properties of human cranial bone in the spectral range from 800 to 2000 nm. Proc SPIE 6163:616310
37. Chen Q, Chopp M, Madigan L, Dereski MO, Hetzel FW (1996) Damage threshold of normal rat brain in photodynamic therapy. Photochem Photobiol 64:163–167
38. Bevilacqua F, Piguet D, Marquet P, Gross JD, Tromberg BJ, Depeursinge C (1999) *In vivo* local determination of tissue optical properties: applications to human brain. Appl Opt 38:4939–4950
39. Kim A, Roy M, Dadani F, Wilson BC (2010) A fiberoptic reflectance probe with multiple source-collector separations to increase the dynamic range of derived tissue optical absorption and scattering coefficients. Opt Express 18:5580–5594
40. Choi J, Wolf M, Toronov V, Wolf U, Polzonetti C, Hueber D, Safonova LP, Gupta R, Michalos A, Mantulin W, Gratton E (2004) Nonivasive determination of the optical properties of adult brain: near-infrared spectroscopy approach. J Biomed Opt 9:221–229
41. Comelli D, Bassi A, Pifferi A, Taroni P, Torricelli A, Cubeddu R, Martelli F, Zaccanti G (2007) *In vivo* time-resolved spectroscopy of the human forehead. Appl Opt 46:1717–1725
42. Barnett AH, Culver JP, Sorensen AG, Dale A, Boas DA (2003) Robust inference of baseline optical properties of the human head with three-dimensional segmentation from magnetic resonance imaging. Appl Opt 42:3095–3108
43. Zhao J, Ding HS, Hou XL, Zhou CL, Chance B (2005) *In vivo* determination of the optical properties of infant brain using frequency-domain near-infrared spectroscopy. J Biomed Opt 10:024028-1
44. van der Zee P, Essenpreis M, Delpy DT (1993) Optical properties of brain tissue. In: Alfano RR, Chance B (eds) Photon migration and imaging in random media and tissues, Proc. SPIE, 1888. Bellingham, WA p 454–465
45. Deghani H, Delpy DT (2000) Near-infrared spectrometer of the adult head: effect of scattering and absorbing obstructions in the cerebrospinal fluid layer on light distribution in the tissue. Appl Opt 39:4721–4729
46. Kienle A, Patterson MS, Dognitz N, Bays R, Wagnieres G, van den Bergh H (1998) Nonivasive determination of the optical properties of two-layer media. Appl Opt 37:779–791
47. Martelli F, Sassaroli A, Del Bianco S, Zaccanti G (2007) Solution of the time-dependent diffusion equation for a three-layer medium: application to study photon migration through a simplified adult head model. Phys Med Biol 52:2827–2843
48. Kim A, Khurana M, Moriyama Y, Wilson BC (2010) Quantification of in vivo fluorescence decoupled from the effects of tissue optical properties using fiber-optic spectroscopy measurements. J Biomed Opt 15:0670061-12
49. Karagiannes JL, Zhang Z, Grossweiner B, Grossweiner LI (1989) Applications of the 1-D diffusion approximation to the optics of tissues and tissue phantoms. Appl Opt 28:2311–2317
50. Svaasand LO, Ellingsen R (1983) Optical properties of human brain. Photochem Photobiol 38:293–299
51. Sterenborg HJCM, van Gemert MJC, Kamphorst W, Wolbers JG, Hogervorst W (1989) The spectral dependence of the optical properties of the human brain. Lasers Med Sci 4:221–227
52. Svaasand LO, Ellingsen R (1985) Optical penetration in human intracranial tumors. Photochem Photobiol 41:73–76
53. Preuss LE, Bolin FP, Cain BW (1982) Tissue as a medium for laser light transport—implications for photoradiation therapy. In: Berns M (ed) Proc. SPIE 357, lasers in surgery and medicine. Bellingham, WA p 77–84
54. Yavari N, Dam JS, Antonsson J, Wårdell K, Andersson-Engels S (2005) *In vitro* measurements of optical properties of porcine brain using a novel compact device. Med Biol Eng Comput 43:658–666

55. Abdo A, Sahin M (2007) NIR light penetration in the rat peripheral nerve and brain cortex. Conf. Proc. IEEE Eng. Med. Biol. Soc. Washington, DC p 1723–1725
56. Ding H, Nguyen F, Boppart SA, Popescu G (2009) Optical properties of tissues quantified by Fourier-transform light scattering. Opt Lett 34:1372–1374
57. Matcher SJ, Cope M, Delpy DT (1997) *In vivo* measurements of the wavelength dependence of tissue-scattering coefficients between 760 and 900 nm measured with time-resolved spectroscopy. Appl Opt 36:386–396
58. Ijichi S, Kusaka T, Isobe K, Okubo K, Kawada K, Namba M, Okada H, Nishida T, Imai T, Itoh S (2005) Developmental changes of optical properties in neonates determined by near-infrared time-resolved spectroscopy. Pediatr Res 58:568–573
59. Fantini S, Hueber D, Franceschini MA, Gratton E, Rosenfeld W, Stubblefield PG, Maulik D, Stankovic MR (1999) Non-invasive optical monitoring of the newborn piglet brain using continuous-wave and frequency-domain spectroscopy. Phys Med Biol 44:1543–1563
60. Sassaroli A, Martelli F, Tanikawa Y, Tanaka K, Araki R, Onodera Y, Yamada Y (2000) Time-resolved measurements of *in vivo* optical properties of piglet brain. Opt Rev 7:420–425

Chapter 2
History of Diffuse Optical Spectroscopy of Human Tissue

Theodore J. Huppert

2.1 Introduction

Diffuse optical spectroscopy (DOS) is a method to noninvasively characterize tissue that uses low levels of light typically in the wavelength range of red to near-infrared (600–900 nm) [1–7]. Diffuse spectroscopy specifically relates to the measurement of the optical absorption and scattering properties of thick samples of tissue greater than several hundred micrometers. Because biological tissue is very turbid, thick tissue samples will scatter light multiple times causing photons to “bounce” through the sample. In contrast, conventional optical physics (often termed ray-optics) is based on the approximation that rays of light travel straight paths. Conventional microscopy tools such as optical lenses and prisms are all based on these principles of ray-optics. However, for samples thicker than approximately the scattering length of light (about 0.1 mm), scattering results in a stochastic propagation of photons through the sample and, hence, the term “diffuse” optical spectroscopy. In these turbid samples, photons of light will take a random path through the tissue before either being absorbed or exiting the surface of the tissue. Thus, it is impossible to know precisely where any single photon has actually traveled. Only the statistical probability of the ensemble of photons can be estimated. The uncertainty in the photon path results in a loss in spatial resolution, particularly deeper into the tissue where the light has become more dispersive. Thus, in DOS, spatial resolution is traded for penetration depth and by specifically measuring these diffuse photons. Diffuse measurements can reach several centimeters into biological tissue, which is deep enough to reach structures such as the cortex of the brain.

Although highly scattering, biological tissue has relatively low intrinsic absorption in the wavelength region of red to near-infrared from about 600 to 900 nm. In this

---

T.J. Huppert (✉)
Department of Radiology and Bioengineering, University of Pittsburgh, Pittsburgh,
PA 15219, USA
e-mail: hupertt@upmc.edu

S.J. Madsen (ed.), *Optical Methods and Instrumentation in Brain Imaging and Therapy*, Bioanalysis: Advanced Materials, Methods, and Devices 3,
DOI 10.1007/978-1-4614-4978-2_2,

wavelength region, which is commonly referred to as the “biological near-infrared window,” diffuse light can traverse several centimeters of tissue. Because of its use of near-infrared wavelengths, DOS is also sometimes referred to by the names near-infrared spectroscopy (NIRS), functional NIRS (fNIRS), diffuse optical imaging (DOI), or diffuse optical tomography (DOT). Although the acronym NIRS is the most widely used one in the field to date, the terms DOS (spectroscopy), DOI (imaging), or DOT (tomography) are currently preferred to distinguish in vivo DOI from the generic term NIRS commonly used in analytical spectroscopic characterizations. Generally speaking, the term NIRS applies to any method that uses near-infrared light and covers both diffuse and conventional ray-optics measurements, including many applications in analytic chemistry, food science, and industry processing. For this reason, several researchers in the field of diffuse optical brain imaging have advocated the “diffuse” terminology that will be followed in this chapter.

In the scientific literature, the terminology differences between DOS, imaging (DOI), and tomography (DOT) relates to the number and spatial arrangement of optical measurements and subsequent analysis as to whether or not images can be reconstructed from the data. DOS uses a small number of measurement pairs to record the optical properties from beneath a small patch of sensors, for example, to estimate the time-course of blood oxygenation changes in a muscle [8–10] or from the global perfusion of the brain [11–14]. Examples of DOS systems include the Casmed Foresight™ system (Casmed; Branford CT, USA), Somanetics INVOS™ system (Covidien; Dublin Ireland), or Hamamatsu NIRO™ generation systems (Hamamatsu Photonics; Hamamatsu City, Japan), which are all examples of cerebral pulse oximetry systems that have received FDA marketing approvals for clinical use (as reviewed in [15]). These systems use only a small number of diffuse optical measurements recorded with different optical source-detector spacing to provide separation of blood oxygenation of the skin and underlying brain [15–18]. These systems are examples of DOS. At the other extreme, DOT (tomography) requires a high-density grid of optical sensors (e.g., [19]) and uses spatially overlapping (i.e., tomographic) measurements to better localize optical properties. These systems are considerably more expensive to construct because of the requirement for low-noise lasers and detectors with high dynamic range. DOT systems provide full spatial coverage of the underlying tissue and have the potential to provide the highest spatial resolution images as will be discussed later. DOT studies are generally more difficult and time-consuming to set up and require some sort of encoding scheme to distinguish light emitted from multiple source positions. To date, very few brain imaging studies have actually been done with true optical tomography systems because of the added difficulty of both instrument construction and data acquisition. Most optical studies fall in the category of DOI. DOI systems do not use overlapping measurement geometries; however, they may still use a large number of optical source and detector pairs. Currently, several commercial companies manufacture DOS systems (see the later section on specific instrumentation). For DOS, source-detector pairs are generally arranged in a nearest-neighbor geometry, which means that only the nearest source to each detector is measured.

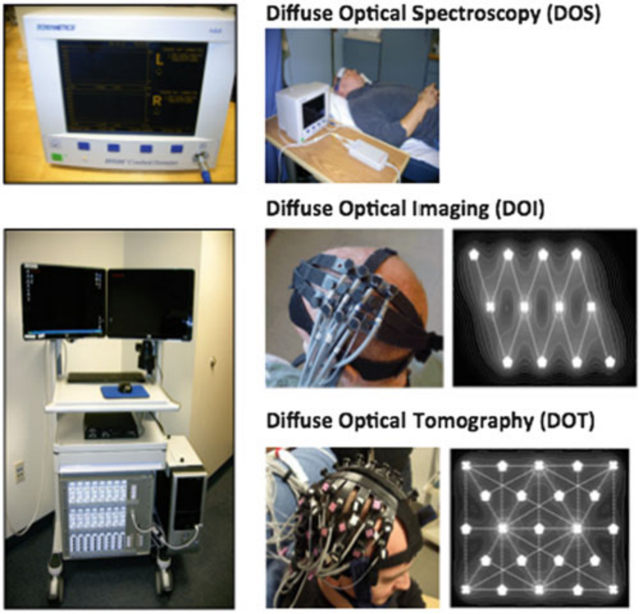

Fig. 2.1 Comparison of arrangements for diffuse optical spectroscopy (DOS), optical imaging (DOI), and optical tomography (DOT). In general, optical spectroscopy instruments (*top row*; showing a Somanetics INVOS™ system) use a limited number of measurement pairs usually based on spatially resolved spectroscopy measurements. These systems allow monitoring of regional blood oxygenation within a small patch of brain area. Optical imaging (DOI; *middle row*) and optical tomography (DOT; *bottom row*) systems use a greater number of spatially arranged optical measurement pairs to provide an ability to reconstruct images of the underlying spectroscopic changes. DOT uses high-density overlapping tomographic measurements to eliminate areas of low sensitivity on the imaging probe and provide better spatial resolution

In contrast, DOT systems will often measure second or third neighboring light sources, which provide overlap in measurements. Typical DOS, DOI, and DOT source-detector layouts are shown in Fig. 2.1.

2.1.1 History of Optical Spectroscopy

The history of using near-infrared light to measure the oxygen content of blood was started in the late 1860s when Felix Hoppe-Seyler from Germany demonstrated that optical absorption changed when blood was mixed with oxygen [20]. At that time the term “oxy-hemoglobin” was coined to describe hemoglobin-carrying oxygen. In 1864, Sir George Stokes confirmed that oxy-hemoglobin was the in vivo carrier of oxygen in a report to the Royal Society of London [21]. Almost a 100 years later, Max Perutz worked out the structure of hemoglobin using X-ray crystallography [22] for which he was awarded the 1962 Nobel prize in chemistry along with fellow

X-ray crystallography pioneer John Kendrew [23]. It is now known that hemoglobin is the iron center of four porphyrin rings bound at the center of the hemoglobin protein that allow each hemoglobin molecule to carry up to four oxygen (O_2) molecules. This binding allows hemoglobin to carry over 70-fold more oxygen compared to that dissolved in the blood.

Experiments into noninvasive pulse oximetry began in the late 1920s and 1930s when attempts were made to construct instruments to measure the oxygenation of blood (see review in [24]). In 1929, American physiologist Glen Allan Millikan used a photoelectric blood oxygen saturation meter to measure color changes over time when desaturated hemoglobin solutions were mixed with oxygen solutions in an experimental setting. In 1932, Ludwig Nicolai recorded changes in oxy-hemoglobin and deoxy-hemoglobin and noted linear changes over time in the logarithm of light [25], a principle, which forms the basis of quantitative assessment of hemoglobin levels (see section on the modified Beer-Lambert law [MBLL]).

In 1935, Kurt Kramer, a student of Ludwig Nicolai, demonstrated the first reproducible measurement of blood oxygen saturation using a red-filtered incandescent light, which showed that his device measured blood oxygen saturation to an accuracy of ±1% [26]. Two years later, Karl Matthes, a physiologist from Munich Germany, introduced the first two-wavelength earlobe-mounted blood oxygen saturation meter able to continuously monitor blood oxygen saturation in humans. Active research into oximetry instruments increased during World War II in response to the need for methods to monitor physiology, particularly for the detection of hypoxia in military pilots. Over the next 40 years, numerous groups worked to develop blood oxygen monitors based on the principles of transillumination and reflectance measurements [27]. These early oximeters were based on absolute measurements of optical absorption and thus were sensitive to differences in thickness, structure, and baseline optical properties of the tissue. As previously discussed, tissue is highly scattering and therefore the path of light through tissue could not be known at the time. These early oximeters required calibration to obtain absolute values (often based on inhalation of oxygen to set 100% saturation). However, differences between patients and the calibration media limited this accuracy. These early oximeters were conceptually similar to what we now call continuous wave (CW) DOS.

In the 1970s, the field of pulse oximetry diverged from what would become the study of diffuse optical brain imaging. In 1974, Takuo Aoyagi, an electrical engineer working in the research division of the Nihon Kohden Corporation (Tokyo, Japan), developed a new approach to oximetry based on detection of time-varying signals due to the cardiac pulse [28]. That same year, the Nihon Kohden Corporation introduced the OLV-5100, which was the first commercial pulse oximeter to noninvasively measure saturated blood oxygen without the need to sample blood. Takuo Aoyagi's pulse oximeter concept was unique in that it did not rely on absolute measurements of optical absorption, but rather on the pulsations of arterial blood. This method used the ratio of the absorption changes modulated by the cardiac pulse (AC) over the mean absorption (DC; nonpulsatile).

When signals were measured at two wavelengths, oxygen saturation could be estimated as a ratio of the ratios given by the following:

$$\mathrm{SpO_2} \propto \frac{\mathrm{AC_{red}}/\mathrm{DC_{red}}}{\mathrm{AC_{IR}}/\mathrm{DC_{IR}}} \tag{2.1}$$

By taking this ratio, the effect of background absorption was removed, providing a more robust estimate of the previous oximeter methods. Takuo Aoyagi's invention was similar to a system by Masaichiro Konishi and Akio Yamanishi of the Minolta camera company (Tokyo, Japan) who filed a similar patent with the Japanese patent office only 3 weeks after the patent filed by Takuo Aoyagi. In 1977, Minolta Camera Company introduced the Oximet MET-1471 fingertip pulse oximeter. Today, the pulse oximeter world market is worth about $400 million (USD) annually.

2.1.2 History of Optical Brain Imaging

In 1977, the same year the Minolta pulse oximeter came to market, Frans Jöbsis published his seminal paper, "Noninvasive, Infrared Monitoring of Cerebral and Myocardial Oxygen Sufficiency and Circulatory Parameters," in the peer-reviewed journal Science. This publication is cited universally as the study that introduced the use of near-IR light for brain imaging. In that study, Jobsis used transilluminated light between 760 and 865 nm to measure hemoglobin and cytochrome c oxidase in anesthetized cats. Fiber optic light sources from two monochromators were placed on one side of the temple of the immobilized cat and a detector fiber bundle was placed on the other side and sent to an IR-sensitive photomultiplier tube detector. Data were collected under normoxia, hypercapnia (15% carbon dioxide in 85% oxygen), and finally during death by asphyxiation. Dynamic measurements of hemoglobin and cytochrome C were measured. After validation in the cat model, Jobsis then applied the same transillumination measurements to the human head. Human measurements were made at 815 nm (close to the isobestic point where both oxy- and deoxy-hemoglobin equally absorb light) using a 13-cm source-detector spacing placed between the frontal/temporal region. Data were collected using a 10-s integration period during voluntary hyperventilation, which continued until the subject began to get too dizzy to continue. This was the first demonstration of in vivo diffuse optical measurements in the human brain.

In the years following, the field of diffuse optical brain imaging has greatly expanded as reviewed in several recent publications [29–31]. In 2010, the National Institutes of Health (NIH) had awarded over $16 million per year (USD) in grant awards for optical brain studies. To date, the NIH has awarded about $102 million in grant funds specifically toward optical brain research since the year 2000. The largest fraction, about a fourth of this funding, has come from the National Institute of Child Health and Human Development (NICHD) branch of the NIH and in a close second by the National Institute of Neurological Disorders and Stroke

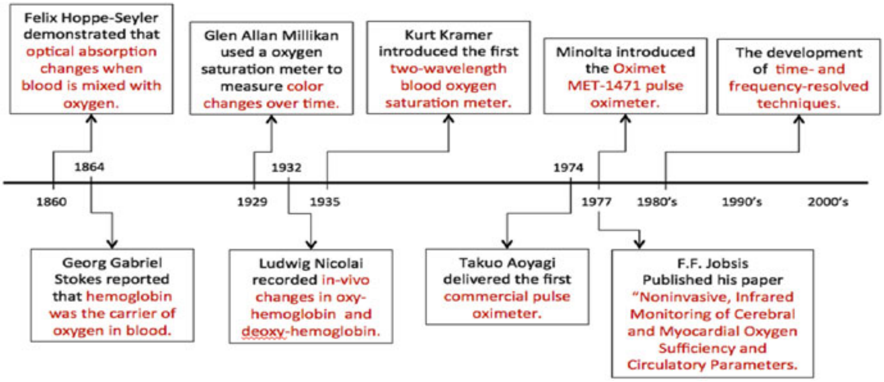

Felix Hoppe-Seyler demonstrated that optical absorption changes when blood is mixed with oxygen.

Glen Allan Millikan used a oxygen saturation meter to measure color changes over time.

Kurt Kramer introduced the first two-wavelength blood oxygen saturation meter.

Minolta introduced the Oximet MET-1471 pulse oximeter.

The development of time- and frequency-resolved techniques.

Georg Gabriel Stokes reported that hemoglobin was the carrier of oxygen in blood.

Ludwig Nicolai recorded in-vivo changes in oxy-hemoglobin and deoxy-hemoglobin.

Takuo Aoyagi delivered the first commercial pulse oximeter.

F.F. Jobsis Published his paper "Noninvasive, Infrared Monitoring of Cerebral and Myocardial Oxygen Sufficiency and Circulatory Parameters.

Fig. 2.2 History of diffuse optical technology

(NINDS). Child studies and clinical research remain the two most impacted fields by optical methods. Current applications and topics of optical brain imaging will be discussed later in this chapter after detailing the specific methods and options for the available tools and instruments in the field (Fig. 2.2).

2.2 Principles of Diffuse Optical Spectroscopy

DOS and imaging have origins common to the early principles of pulse oximetry based on trans-arterial illumination. In general, light in the visible-red to near-infrared range is shined upon tissue. As the light diffusely passes through the tissue, it is scattered multiple times and a fraction of the photons are absorbed before they can reach an optical detector. The amount of light that completes the trip from the source to detector position conveys information about the optical scattering and absorption within the diffuse volume between the measurement pair. Variations on this theme use different types of light sources (pulsed, amplitude modulated, or continuous wave) and detectors (e.g., time-gated, single-photon counting, or diode detector) to obtain optical measurements of tissue. These various optical systems differ in information content, utility, and cost. These systems will be detailed in the later instrumentation section of this chapter. All of these systems, however, are based on the same physical principles of light transport and physics in tissue, which will be detailed in this current section.

2.2.1 Optical Properties of Biological Tissue

The principles of light propagation are governed by the absorption and scattering properties of the underlying tissue, and, to a lesser extent, the dielectric properties and indices of refraction of the tissue. In the near-infrared "window," the primary

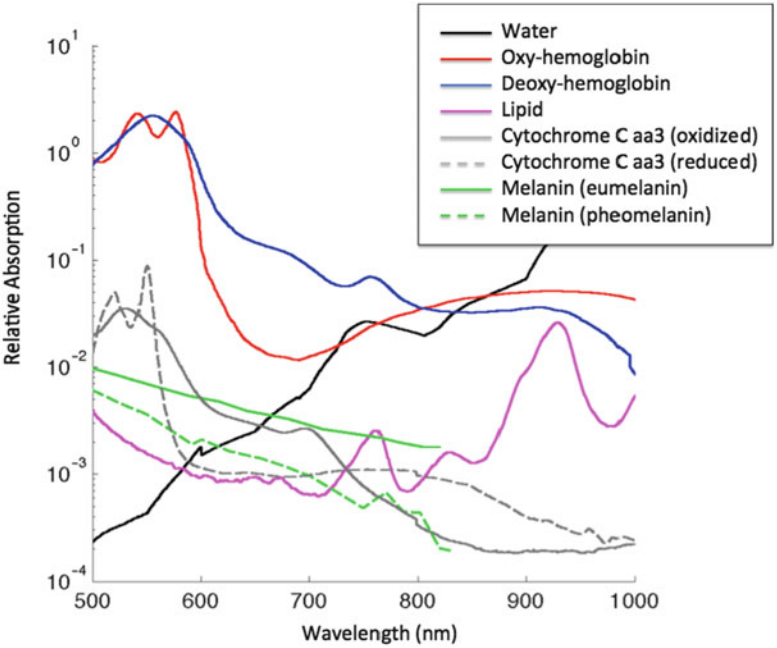

Fig. 2.3 The absorption spectra of biological components in the near-infrared window. Water absorption spectra from [39–41]. Lipid absorption spectra from [42] and shown assuming 20% fat-body mass ratio. Melanin spectra from [43] and assuming a biological concentration of 21 mg/mL and correcting for the partial volume of the epidermis. Hemoglobin spectra from [44–46] and assumes biological concentration of 60 μM and 70% saturation. Reduced and oxidized cyctochrome C aa3 spectra from [47, 48] and assuming a biological concentration of 3 μg/L. An attempt has been made to display the absorption values on a meaningful scale by assuming biologically relevant concentrations

static optical absorbers are water, lipid, and melanin. The optical absorption spectrum of these is shown in Fig. 2.3. Water is the dominant chromophore in the near-infrared to infrared (600–1,000 nm). At wavelengths above 900 nm, the absorption of water prevents penetration of light deep into tissue, thus setting the effective upper limit of the near-infrared window. At the wavelengths used in most diffuse optical systems, hemoglobin, water, and lipid are the dominant contributors to background optical absorption (see Fig. 2.3). Other absorbing compounds in tissue include the pigment melanin found in skin and hair. Melanin has particularly high absorption in the visible to ultra-violet region. Melanin is responsible for both hair color and skin pigmentation and varies between individuals in concentrations by over tenfold. Hair and skin colors are determined by the relative concentrations of two forms of melanin: eumelanin (dark brown) and pheomelanin (red). Both forms of melanin have relatively flat optical absorption spectra in the range of 600–900 nm. Although melanin has very high absorption within the near-infrared window, it is found primarily in the epidermis of the skin (around 60 μm), which limits its contribution to overall absorption. Lipid also absorbs light within the

Table 2.1 Absorption/scattering of tissues

Tissue type	Wavelength (nm)	Absorption coefficient (cm^{-1})	Reduced scattering coefficient (cm^{-1})	Anisotropy (g)	Reference
Skin	690	0.159	8.0	–	[49]
	760	0.178	7.3	–	[49]
	800	0.130	20.0	–	[50]
	830	0.191	6.0	–	[49]
Muscle	800	0.300	7.0	–	[50]
Skull	690	0.100	10.0	–	[49]
	760	0.125	9.3	–	[49]
	800	0.250	18.0	–	[51]
	830	0.191	6.6	–	[49]
CSF	690	0.004	0.1	–	[49]
	760	0.021	0.1	–	[49]
	800	0.022	0.0	–	[52]
	830	0.026	0.1	–	[49]
Gray matter brain (adult)	632	0.270	20.6	0.94	[53]
	690	0.178	12.5	–	[49]
	760	0.195	11.8	–	[49]
	830	0.186	11.1	–	
White matter brain (adult)	632	0.220	9.1	0.82	[53]
	690	0.178	12.5	–	[49]
	760	0.195	11.8	–	[49]
	830	0.186	11.1	–	[49]
Total brain (premature infant)	800	0.215	7.5	0.718	[54]
White matter brain (term infant)	800	0.373	6.6	0.919	[54]
Gray matter brain (term infant)	800	0.460	5.3	0.983	[54]
Arterial blood	800	3.980	10.0	–	[52]
Venous blood	800	3.960	10.0	–	[52]

near-infrared window (Fig. 2.3) and can be a major contributor to background absorption in tissue, particularly in DOI of tissues such as muscle [32] and breast [33–38]. In general, water, lipid, and melanin concentrations do not change appreciably on the time scale of most optical imaging measurements. These static optical absorbers determine the background properties of tissue. Typical absorption factors of these static absorbers are provided in Table 2.1.

Most DOS experiments of the brain are concerned with dynamic changes in chromophores. As with the use of pulsatile methods used in pulse oximetry since the 1970s, dynamic spectroscopy removes some of the need for calibration by marginalizing static background contributions. With regard to optical brain imaging, oxy- and deoxy-hemoglobin are the most important dynamic chromophores in the near-infrared range. Oxy- and deoxy-hemoglobin are often denoted as "HbO" and "HbR" (standing for oxidized and reduced) or otherwise "HbO_2" and "Hb" (standing for with and without the oxygen molecule, O_2). Hemoglobin provides functional contrast in the brain in the overwhelming majority of diffuse optical studies to date. Functional contrast based on blood oxygenation is often referred to as the BOLD (blood oxygen level dependent) effect, a term that is used for both optical and functional magnetic resonance imaging (fMRI) fields. The BOLD effect will be discussed in more detail later in this chapter.

Aside from hemoglobin, several other dynamic endogenous chromophores can be measured in the near-infrared range. These include myoglobin, the cytochromes (including the oxidized form of cytochrome C), nicotinamide dihydride ($NADH_2$), and other flavoenzymes. Other lesser forms of hemoglobin such as carboxyhemoglobin are also present in tissue. Although cytochromes and the flavoenzymes do change during metabolic brain activity, the expected concentration changes of these chromophores are much smaller then hemoglobin. Cytochrome C was originally measured in the cat brain in the 1977 seminal paper by Jobsis [7].

In addition to endogenous chromophores, several exogenous chromophores have also been used in human DOI. Indocyanine green (ICG) is a dye that is approved in the United States and many European countries for use as an intravenous diagnostic agent. ICG binds to plasma proteins in the blood and remains in the vasculature, which allows it to be used as a marker to measure blood flow and plasma volume in vivo. ICG has been used clinically to diagnose perfusion of tissues and organs and has been used in both noninvasive imaging studies [55] as well as during surgical procedures to directly visualize organ function [56–59]. Because ICG is removed solely by the liver at a nominal half-life of about 150–180 s, measurement of the rate of disappearance of ICG in the plasma has been used clinically to assess liver function [60–62]. More recently, the company Mivenion GmbH (Berlin, Germany) has introduced a technique called Rheumascan™ based on ICG imaging to quantify microcirculation in arthritis and rheumatoid arthritis.

2.2.2 *Optical Scattering of Tissue*

The diffuse nature of light propagation in tissue is the result of scattering. Like absorption, scattering is also dependent on the type and structure of the tissue. The two primary forms of scattering in biological tissue are Rayleigh scattering and Mie scattering. Both of these are elastic scattering events, meaning that the light does not change wavelength when scattered. Rayleigh scattering results from particles that are much smaller than the wavelength of light. Rayleigh scattering intensity has a strong inverse (fourth power) relationship with the wavelength of light. As a result, Rayleigh scattering is more dominant at lower wavelengths. Mie scattering is associated with particles whose size is similar to the wavelength of light.

In tissue, there are both static and dynamic compounds that contribute to scattering. Static biological scatterers include connective tissue, collagen, and skin. Light scattering also results from interaction with interfaces between fluids with different indices of refraction such as the interface of the extracellular fluid and the cell membrane and again at the cell membrane/cytosol interface. Mitochondria comprise about 20% (by mass) of the solid content of cells. Other cellular organelles (endoplasmic reticulum, the Golgi, tubules, filaments, etc.) are also sources of static scattering in tissue. Table 2.1 provides approximate values of typical scattering coefficients in various tissue types.

Although dynamic scattering changes are much smaller and often neglected in diffuse optical brain studies, there are several endogenous sources of scattering contrast. Erythrocytes (red blood cells) comprise about 5% of tissue volume and alter their concentration and velocity with blood flow changes and vasoreactivity. Dynamic scattering contrast from red blood cells is particularly relevant to a method called diffuse correlation spectroscopy (DCS) [63–66]. DCS, which is based on scattering from moving red blood cells, will be discussed later in this chapter. In excised neural tissue, scattering changes due to membrane depolarization, cellular swelling, and changes in ion concentrations at synapses have been demonstrated. Research into the "fast-optical" signal has been proposed based on the same contrast mechanism [67–69]. Debate exists over the nature of these measurements [70].

2.2.3 The Beer-Lambert Law

In 1932, Ludwig Nicolai noted that changes in the concentration of oxy-hemoglobin and deoxy-hemoglobin were linearly related to changes in the logarithm of the light detected in transillumination [25]. This relationship is known from analytical chemistry as the Beer-Lambert law named after German physicist/mathematician August Beer and Swiss mathematician Johann Lambert and introduced in their book *Einleitung in die höhere Optik* (Introduction to the Higher Optical) in 1854 [71]. The equation, however, was actually first discovered by Pierre Bouguer 100 years earlier [72]

$$\mathrm{OD} = -\log\frac{I}{I_{\mathrm{o}}} \tag{2.2}$$

Conventionally, optical density is expressed in log base e. Optical density (or absorption) is proportional to the concentrations of chromophores (molecules that absorb light). For example, if light is passed through a container of length L containing a solution of known identity (see Fig. 2.4), then the optical density of the sample can be used to calculate the concentration of the solution ($[X]$) from the expression

$$\mathrm{OD} = \varepsilon \cdot [X] \cdot L \tag{2.3}$$

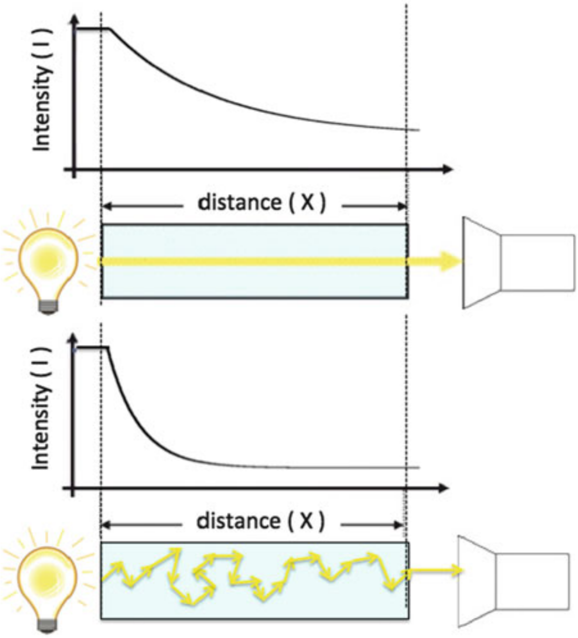

Fig. 2.4 Beer-Lambert. This schematic illustrates the effect of scattering on the Beer-Lambert relationship. Compared to a clear medium (*top*) light will take a diffuse path through a turbid sample. Light traveling through the turbid sample will travel a longer distance to reach the detector and the intensity of light reaching the detector will be lower due to this additional distance as described by the modified Beer-Lambert law. Figure adapted from [52]

where ε is the molar extinction coefficient for the compound. The extinction coefficient is a physical constant that describes the amount of light a compound will absorb. This is specific to the wavelength of light and the chemical state of the compound. For example, the extinction coefficient of hemoglobin (blood) differs depending on if it is bound or unbound to oxygen. The extinction coefficient is proportional to the molecular cross section of a compound by Avogadro's constant ($N_A = 6.02 \times 10^{23}\ \text{mol}^{-1}$). The extinction coefficient is also dependent on physical parameters such as extremes of temperature, pH, or osmolality. These factors can be neglected in the case of in vivo spectroscopy because they usually fall within a very narrow biological range. However, since the extinction coefficient is usually measured ex vivo, these factors should be considered when measuring or using literature values for extinction coefficients for use in in vivo DOS experiments.

As can be seen in Fig. 2.4, light intensity drops exponentially with penetration depth into the sample. The coefficient of this exponential decay is termed the absorption coefficient (μ_A) and is the product of the concentration and molar extinction coefficient. For samples with multiple absorbing compounds, the absorption coefficient is a linear combination of the contributions from each compound and is given by

$$\mu_A = \sum_i \varepsilon_i \cdot [X_i] \tag{2.4}$$

where ε_i and $[X_i]$ are the extinction coefficient and concentration for the *i*th compound, respectively. The absorption coefficient has units of inverse distance. For example, a typical absorption coefficient for the brain is around 0.4 cm^{-1} at 800 nm.

The Beer-Lambert law requires several conditions. First, the absorbing compounds must be independent of each other. Coupling effects such as Forster transfer or quenching violate this assumption. Secondly, the Beer-Lambert law assumes that the concentration of the absorbing compound is homogeneous along the light path. In the case of complex structures such as tissue, this is not true. Third, there can be no atomic effects such as multi-photon absorption, optical saturation, or stimulated emission. This is generally true provided the power of the incident light is low, which should be the case in in vivo studies due to safety concerns. Finally, the Beer-Lambert law assumes that the incident light consists of parallel rays that traverse the medium without scattering.

2.2.4 The Modified Beer-Lambert Law

The MBLL accounts for scattering in a turbid medium. In samples where optical scattering is a factor, the path length (L in (2.3)) is no longer simply the linear distance between the light source and detector, but rather represents the total distance traveled by a photon as it moves through the sample. The Beer-Lambert law adjusted for scattering is termed the MBLL and is an empirical description of optical attenuation in a highly scattering medium [5, 48]. The MBLL is given by the expression [1, 73]

$$\mathrm{OD} = \mu_{\mathrm{A}} \cdot L \cdot \mathrm{DPF} + G \tag{2.5}$$

where the linear distance between a light source and detector (L) has been corrected by a factor DPF (differential path-length factor) which is a number greater than 1 and accounts for the increase in the path length as the result of taking an indirect path through the sample. The last term (G) in (2.5) is the geometry factor. Because the light changes direction in the sample, some of the light will escape at the boundaries away from the detector, thus increasing the apparent absorption of the sample.

The MBLL equation (2.5) describes the absolute absorption and concentration of chromophores in the sample. However, this quantification of absolute concentrations in tissue is very difficult because of uncertainty in the values of DPF and G and the multitude of unknown nuisance chromophores in the tissue (e.g., water, lipid, melanin, etc.). Errors in the value of these background chromophores contribute to errors in the chromophores of interest (e.g., hemoglobin) and make direct quantification very difficult. If analysis of diffuse optical signals is restricted to changes in dynamic chromophore concentrations, then the contributions of background absorption can be marginalized. Changes in optical density (ΔOD) are given by the expression

$$\Delta \mathrm{OD} = \sum_{i} \varepsilon_i \cdot \Delta[C]_i \cdot L \cdot \mathrm{DPF} \tag{2.6}$$

where both background (static) contributions and the geometry factor are subtracted. As noted, optical density, DPF, and the extinction coefficient are specific for each wavelength of light. Thus, if measurements are made at multiple wavelengths, (2.6) represents a set of linear equations for each measurement. In general, at least one wavelength must be recorded for each unknown chromophore in the model in order to uniquely solve for all the concentrations. As an example, oxy- and deoxy-hemoglobin are the primary dynamic chromophores of interest in most brain imaging studies and thus at least two unique wavelengths are required to be measured to independently estimate these two chromophores. In the specific case of the estimation of oxy- and deoxy-hemoglobin, the MBLL is given by

$$\Delta \mathrm{OD}^{\lambda} = (\varepsilon^{\lambda}_{\mathrm{HbO}} \Delta[\mathrm{HbO_2}] + \varepsilon^{\lambda}_{\mathrm{Hb}} \Delta[\mathrm{Hb}])\mathrm{DPF}^{\lambda} L \tag{2.7}$$

where λ indicates a particular wavelength. Equation (2.7) explicitly accounts for independent concentration changes in oxy-hemoglobin ($\Delta[\mathrm{HbO_2}]$) and deoxy-hemoglobin ($\Delta[\mathrm{Hb}]$). By measuring ΔOD at two wavelengths (λ_1 and λ_2) and using the known extinction coefficients of oxy-hemoglobin ($\varepsilon_{\mathrm{HbO_2}}$) and deoxy-hemoglobin ($\varepsilon_{\mathrm{Hb}}$) at these wavelengths, we can then determine the concentration changes of oxy-hemoglobin and deoxy-hemoglobin by solving the system of linear equations defined in (2.7),

$$\begin{aligned}
\Delta[\mathrm{Hb}] &= \frac{\varepsilon^{\lambda_2}_{\mathrm{HbO}} \frac{\Delta \mathrm{OD}^{\lambda_1}}{B^{\lambda_1}} - \varepsilon^{\lambda_1}_{\mathrm{HbO}} \frac{\Delta \mathrm{OD}^{\lambda_2}}{B^{\lambda_2}}}{\left(\varepsilon^{\lambda_1}_{\mathrm{Hb}} \varepsilon^{\lambda_2}_{\mathrm{HbO_2}} - \varepsilon^{\lambda_2}_{\mathrm{Hb}} \varepsilon^{\lambda_1}_{\mathrm{HbO_2}}\right) L} \\
\Delta[\mathrm{HbO_2}] &= \frac{\varepsilon^{\lambda_1}_{\mathrm{Hb}} \frac{\Delta \mathrm{OD}^{\lambda_2}}{B^{\lambda_2}} - \varepsilon^{\lambda_2}_{\mathrm{Hb}} \frac{\Delta \mathrm{OD}^{\lambda_1}}{B^{\lambda_1}}}{\left(\varepsilon^{\lambda_1}_{\mathrm{Hb}} \varepsilon^{\lambda_2}_{\mathrm{HbO_2}} - \varepsilon^{\lambda_2}_{\mathrm{Hb}} \varepsilon^{\lambda_1}_{\mathrm{HbO_2}}\right) L}
\end{aligned} \tag{2.8}$$

The generalization of this inverse formula for more than two wavelengths can be found in [48]. Figure 2.3 plots the extinction coefficients for oxy- and deoxy-hemoglobin vs. wavelength as measured by Cope et al. [6, 48, 50].

2.2.5 Scattering

Similar to the absorption coefficient, the scattering coefficient (μ_s) is an exponential coefficient that describes the probability of a photon of light being scattered per unit length. Like absorption, the scattering coefficient also has units of inverse length, but is generally several orders of magnitude larger than the absorption coefficient. This means that light scatters many times for each absorption event. As an example, the scattering coefficient of the brain is around 5.3 cm^{-1} at 800 nm. This means that, on average, a photon has a 63% chance of changing direction every 1.7 mm.

When light scatters in tissue, the photon changes direction. The anisotropy factor (denoted g) is defined as the average of the cosine of the difference between the incident angle and the direction after the scattering event ($g = <\cos(\theta)>$). The anisotropy g is listed for various tissue types in Table 2.1. Anisotropy increases the effective scattering length. The reduced scattering coefficient (denoted $\mu_s{}'$) incorporates the scattering coefficient and the anisotropy term and is defined as

$$\mu_s^{'} = \mu_s \cdot (1 - g) \tag{2.9}$$

2.3 Transport of Light in Tissue

To more precisely describe the quantification of optical absorption and scattering via diffuse optical methods, we have to first understand how light is transported through a turbid sample such as tissue. Formally, light transport is described by the radiative transport equation or Boltzmann equation. The Boltzmann equation is in essence a mass-balance equation describing how the radiance (R) of light is spatially and temporally distributed in a sample. Radiance is defined as the energy flow per unit normal area per unit solid angle per unit time and has units of $\mathrm{W{\cdot}sr^{-1}{\cdot}cm^{-2}}$. In other words, radiance is the flow of energy that is passing through a particular point in space and traveling in a particular direction. Fluence rate (Φ) is the flow of energy passing through a particular point but traveling in any direction. Fluence rate is defined as energy flow per unit normal area per unit time ($\mathrm{W{\cdot}cm^{-2}}$). Fluence rate is equal to the integral of radiance over all possible directions (solid angles; Ω). The Boltzmann equation is a differential equation that describes the change in radiance over time and is given by

$$\begin{aligned}\frac{\partial R(\vec{r},\hat{s},t)/c}{\partial t} = &- \hat{s} \cdot \nabla R(\vec{r},\hat{s},t) - (\mu_A + \mu_S) \cdot R(\vec{r},\hat{s},t) \\ &+ \mu_S \cdot \int R(\vec{r},\hat{s}',t) \cdot P(\hat{s},\hat{s}') \cdot \mathrm{d}\Omega + S(\vec{r},\hat{s},t)\end{aligned} \tag{2.10}$$

As a note, radiance is usually denoted by "L" in other literature, but to avoid confusion with the source-detector distance in the Beer-Lambert expression, we have used "*R*" for radiance here. Equation (2.10) can be thought of as a mass-balance expression, that is, the rate of change in radiance is equal to all the terms that increase radiance minus all the terms that decrease radiance. The first term on the right-hand side $\left(-\hat{s}\cdot\nabla R(\vec{r},\hat{s},t)\right)$ describes radiance changes at the position due to the spatial gradient in radiance. This is akin to the diffusion of a compound from an area of high to low concentration. The radiance will decrease (or increase) as light spreads through the sample until the light is uniformly distributed (e.g., the spatial gradient is zero). The second term on the right-hand side $\left((\mu_{\mathrm{A}}+\mu_{\mathrm{S}})\cdot R(\vec{r},\hat{s},t)\right)$ describes loss to absorption and scattering at that particular position. At that position in space, light can be absorbed (determined by the absorption coefficient) or it can change direction due to scattering. Because radiance is light propagating in a particular direction, a change in direction away from $\hat{s}$ will decrease radiance. The third term on the right-hand side $(\mu_{\mathrm{S}}\cdot\int R(\vec{r},\hat{s}',t)\cdot P(\hat{s},\hat{s}')\cdot \mathrm{d}\Omega)$ describes the gain of radiance that results from energy (light) changing direction from $\hat{s}'$ to $\hat{s}$. $R(\vec{r},\hat{s}',t)$ is the radiance at that position with angle $\hat{s}'$ and $P(\hat{s},\hat{s}')$ describing the probability of a direction change from $\hat{s}'$ to $\hat{s}$. This term is integrated over all angles to represent the total amount of radiance that changed directions from $\hat{s}'$ to $\hat{s}$. This term represents light at that position in space that was previously traveling in one direction ($\hat{s}'$) and due to a scattering event has now changed direction to now point in the direction of $\hat{s}$. The final term $\left(S(\vec{r},\hat{s},t)\right)$ is the addition of any sources of light, for example, at the position of an optical fiber.

Equation (2.10) can be approximated by expansion of the angular dependence of the radiance term in spherical harmonics, namely,

$$R(\vec{r},\hat{s},t)\approx R_{0,0}(\vec{r},t)\cdot Y_{0,0}(\hat{s})+\sum_{m=-1}^{1}R_{1,m}(\vec{r},t)\cdot Y_{1,m}(\hat{s}) \tag{2.11}$$

In this expression, only the isotropic ($Y_{0,0}$) and first-order anisotropic terms ($Y_{1,m}$) are retained. Under this first-order approximation to the Boltzmann equation, the expression can be reduced to the diffusion approximation. The diffusion approximation holds for samples in which the scattering length is much shorter than the absorption length (e.g., there are many scattering events for each absorption event). The diffusion approximation to the Boltzmann equation is given by the equation [51–53]

$$\frac{\partial\phi(\vec{r},t)}{c\cdot\partial t}=-D\cdot\nabla^2\phi(\vec{r},t)=S(\vec{r},t)-\mu_{\mathrm{A}}\cdot\phi(\vec{r},t) \tag{2.12}$$

where a substitution has been made based on the definition of fluence rate and radiance to generate this expression. In (2.12), $\Phi(\mathrm{r},t)$ is the photon fluence rate at position r and time t as previously defined. The term D is the effective diffusion constant and is defined as $D=1/(3\mu_{\mathrm{A}}+3\mu_{\mathrm{S}}')$.

2.3.1 Solutions to the Transport Equation

An analytical solution to the diffusion equation only exists for simple media and can be found in [74]. For many experiments, the tissue can be approximated as a homogeneous, semi-infinite medium (e.g., a flat surface that is infinitely deep) (Fig. 2.5). The solution to the diffusion equation for a semi-infinite medium is given by [74].

$$\mathrm{OD} = \frac{1}{2} \cdot \left(\frac{3 \cdot \mu_{\mathrm{S}}'}{\mu_{\mathrm{A}}}\right)^{1/2} \cdot \left(1 - \frac{1}{\sqrt{1 + L \cdot (3 \cdot \mu_{\mathrm{S}}' \cdot \mu_{\mathrm{A}})}}\right) \cdot \mu_{\mathrm{A}} \cdot L \tag{2.13}$$

Equation (2.13) also explicitly defines the DPF by comparison to the modified Beer-Lambert equation (2.5) for a semi-infinite medium, which was introduced in (2.3), as

$$DPF \approx \frac{1}{2} \cdot \left(\frac{3 \cdot \mu_S'}{\mu_A}\right)^{1/2} \cdot \left(1 - \frac{1}{\sqrt{1 + L \cdot \left(3 \cdot \mu_S' \cdot \mu_A\right)}}\right) \tag{2.14}$$

This shows that *DPF* depends on tissue scattering, initial chromophore concentration, extinction coefficient, and optode separation. In practice, the validity of the assumption that *DPF* is independent of μ_{a} and L has often been ignored since *DPF* is in general empirically determined and the changes in μ_{a} are typically small. There are, however, experimental situations in which this is not true, such as large changes in blood flow induced by pharmacological challenges or stroke. Note also that because of the dependence on the scattering coefficient, if tissue scattering changes over time, then the path-length factor will also change. For more complex media (such as the human brain), numerical methods can also be used to approximate the solution to the diffusion equation. Several Monte Carlo [75–79] or finite element [80]-based methods have been proposed and are reviewed in [34].

2.4 Instrumentation for Optical Brain Imaging

There are three basic variations in optical instruments, which are summarized in Fig. 2.6. These are continuous wave (CW), frequency modulated (FM), and time-resolved (TR). Several commercial systems exist and are provided in Table 2.2.

Continuous wave (CW) optical systems are both the simplest and cheapest of the system arrangements. In this system, the tissue is illuminated using a continuous beam light source (see Fig. 2.6). A light detector, either in a transmission or back-reflectance geometry, records the intensity of light passing through the tissue. The intensity of light output is related to the optical absorption of the sample.

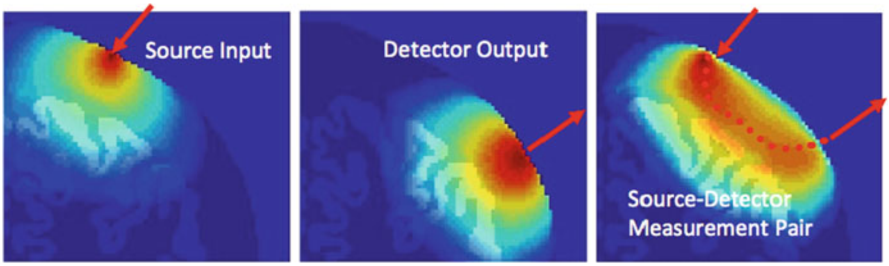

Fig. 2.5 Light diffusion model. Light entering the tissue at a source position (*left*) will spread radially as it diffuses through the tissue. Likewise, the light detected at a position converges on that position with a similar radial distribution (*middle* image). Due to reciprocity, the spread of light leaving a detector has the same distribution as the light traveling through the tissue to reach a detector. An optical measurement taken between a source and detector position is the product of these two profiles (*right* image) and describes the probability of light propagation at a particular location in the tissue

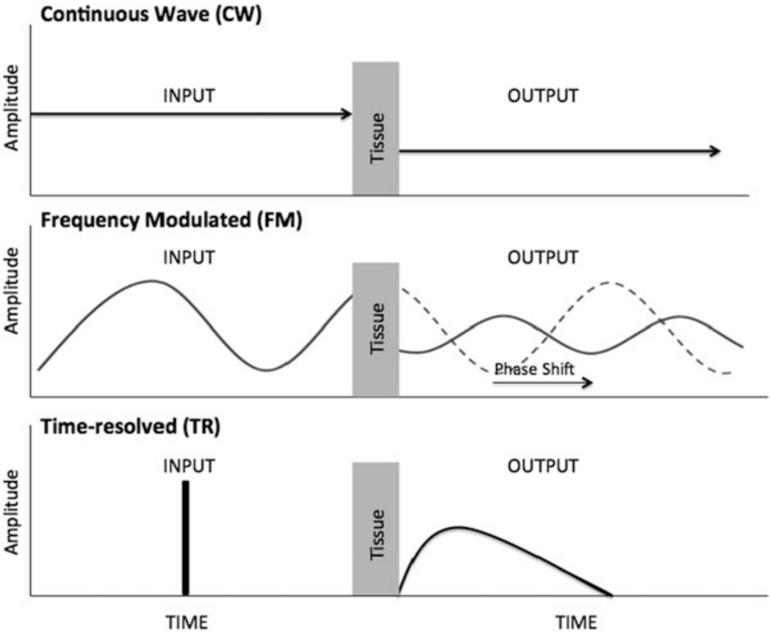

Fig. 2.6 Types of diffuse optical systems. There are three basic types of optical systems. Continuous wave (CW; *top row*) systems use a continuous beam of light and measure the amplitude of the light transmitted through the tissue. CW measurements are used to report the optical absorption of the tissue and assume no scattering changes have occurred. Frequency-modulated (FM; *middle row*) systems use sinusoidal-modulated light and measure the phase and amplitude of the transmitted light. These two parameters are used to report both the absorption and scattering of the sample. Time-resolved (TR) systems use a brief pulse of light and measure the amplitude and time of flight of the transmitted light. Time-resolved measurements are used to determine the pathlength, scattering, and absorption of the sample

Table 2.2 Commercial diffuse optical systems

Company	Instrument	Technique	Website
Artinis (The Netherlands)	Oxymon	CW	http://www.artinis.com
	PortaMon	CW	
	PortaLite	CW	
Casmed (USA)	FORE-SIGHT	CW	http://www.casmed.com
Hamamatsu (Japan)	NIRO-100	CW	http://www.hamamatsu.com
	NIRO-200	CW	
	TRS-20	TR	
Hitachi (Japan)	ETG-4000	CW	http://www.hitachimed.com
Hutchison Technology (USA)	InSpectra StO2	CW	http://www.htibiomeasurement.com
ISS (USA)	Oxiplex TS	FM	http://www.iss.com
	Imagent	FM	
LEA (Germany)	O2C	CW	http://www.lea.de
NIROX (Italy)	NIMO	CW	http://www.nirox.it
NIRx (USA)	Dynot	CW	http://www.nirx.net
	NIRScout	CW	
	NIRScout Xtended	CW	
Omegawave (Japan)	BOM-L1	CW	http://www.omegawave.co.jp
	BOM-L1 TR	CW	
Shimadzu (Japan)	FIORE 3000	CW	http://www.med.shimadzu.co.jp
Somanetics (USA)	INVOS 5100C	CW	http://www.somanetics.com
Techen (USA)	NIRS 2CE	CW	http://www.nirsoptix.com
	CW6	CW	

List of commercial optical systems available as of the year 2012. CW indicates a continuous wave system. FM indicates a frequency-modulated system. TR indicates a time-resolved system

CW systems are similar to the oximeter systems of the 1930–1970s. Like the oximeters, these systems are sensitive to background absorption and scattering. Most CW optical studies of brain activity are restricted to changes in optical absorption, thereby minimizing differences in this background absorption.

Time-resolved or time-domain DOS systems use pulsed laser light and time-of-flight measurements to estimate optical absorption, scattering, and path-length information about the sample. A typical time-resolved DOS system consists of a fast-pulsed laser with a pulse width of no more than a few tens of picoseconds. This pulsed light is sent into the tissue. As the light diffuses through the tissue, the temporal dispersion of the light is a function of the reduced scattering coefficient. As the light exits, a time-resolved DOS system records the time of flight of the light using a fast-gated photon detector. The delay time between the firing of the laser and the opening of the detector is changed to sample over a few nanoseconds in order to recover the temporal point spread function of the exiting light. Because of the requirement for specialized lasers, gating circuits, and fast detectors, time-resolved DOS systems are typically expensive and more difficult to construct. In a time-resolved DOS setup, the arrival time of photons can be used to determine the differential path length of light in the sample. This can also be used to provide depth sensitivity since photons that arrive earlier have traveled a shorter distance and thus probed superficial structures compared to late-arriving photons.

Frequency-modulated (FM) DOS systems [81, 82] are in between CW and time-resolved methods in terms of cost, complexity, and information content. An FM-DOS system uses an amplitude-modulated laser (typically 100–200 MHz). As the light diffuses through tissue its amplitude decreases and a phase shift, proportional to the propagation distance, is introduced. Fast detectors are used to record the amplitude and phase of the exiting light with reference to the input modulation. The amplitude and phase of the detected signal can then be related to absorption and scattering changes as discussed in the following section. FM-DOS systems are generally more expensive compared to CW-DOS due to the more complicated electronics required to modulate the laser light. Currently, there is only one commercial company with a marketed FM-DOS system (ISS Inc., Urbana, IL USA).

2.4.1 Diffuse Correlation Spectroscopy

DCS is a new technique developed at the University of Pennsylvania [63, 83, 84], which is closely related to DOS. Unlike DOS, which is based on spectroscopic measurements of light intensity for the determination of absorption and scattering parameters, DCS is based on the scattering interaction between light and moving objects. In particular, DCS contrast originates from moving red blood cells (or similar objects) and provides information about blood flow in the tissue. DCS is a variation of a similar method called laser speckle imaging [85] to account for multiple-scattering events [84, 86]. The DCS instrument uses a long coherence length laser and a single-photon counting detector module feeding into a temporal autocorrelator. The coherence length of a laser is the distance that the laser light will maintain its wave nature. A DCS system also requires the use of single-mode fiber optics, which maintain coherence as they transmit light. In brief, when coherent light scatters from a surface, it will create an interference pattern due to the wave nature of light. If the surface is moving, the interference pattern will change over time as a function of speed of the surface. Random (Brownian) and ballistic movement result in different characteristic effects. By measuring the first-order temporal autocorrelation ($g_1(\tau)$) between the arrival time of photons (e.g., the distribution of time waited before the next photon arrives), the motion of the object can be estimated. The expression for the autocorrelation function is given by [83]

$$g_1(\tau) = \frac{\langle E(t) \cdot E(t+\tau) \rangle}{\langle E(t) \cdot E(t) \rangle} \propto \mathrm{e}^{-\frac{1}{3}\mu_\mathrm{A} \cdot \mu_\mathrm{s}'} \cdot \mathrm{e}^{\mu_\mathrm{s}' \cdot {k_0}^2 \cdot \alpha \langle \Delta r^2(\tau) \rangle} \tag{2.15}$$

where

$$\langle \Delta r^2(\tau) \rangle = 6 D_\mathrm{B} \tau \text{ Brownian motion}$$

$$\langle \Delta r^2(\tau) \rangle = V^2 \tau^2 \text{ Random balistic motion}$$

where τ is the autocorrelation delay time. The term k_0 is the wavevector magnitude of the incident light vector ($k_0 = 2 \cdot \pi \cdot n/\lambda$, where n is the index of refraction of the medium and λ is the wavelength of light). Finally, the term α is a unit-less scalar factor equal to the fraction of the light-scattering events from moving scatterers. This is an unknown term which is usually grouped with absorption to create an effective absorption term. The DCS expression depends on the absorption and scattering coefficients and is specific for Brownian vs. ballistic motion of the scatters. Over the last few years, there has been debate as to which of these two models is more accurate for describing the effects of flow in tissue. For this reason, the interpretation of DCS results is still somewhat uncertain since blood flow is neither ballistic nor Brownian. DCS systems have now been used by several research groups and have been applied to study blood flow changes in the brain and muscle [87–89].

2.4.2 Spatially Resolved Spectroscopic Measurements

Quantitative recovery of hemoglobin (or other chromophores) via the MBLL (2.5) is limited by knowledge of the DPF. Using time-resolved DOS methods, the DPF factor can be directly estimated by time-of-flight measurements. The DPF factor measured by time-resolved DOS has been tabulated for various tissues [49, 94–97]. The majority of DOS brain studies use CW-DOS methods. In this case, the DPF cannot be directly measured and in most cases must be estimated either from numerical models of the diffusion solution or obtained from tabulated DPF values [98–100]. This approach suffers from uncertainties in the DPF, which varies between people, tissue types [98], and with age [99]. Alternatively, one can calibrate the DPF against the cardiac-induced arterial pulsation [92], but this requires an accurate measurement of the cardiac pulsation within the optical signal, which is not always achievable.

Spatially resolved spectroscopy (SRS) can be used to estimate the differential path-length factor based on a model of how light intensity (and/or phase) varies as a function of the source-detector distance. For homogeneous, semi-infinite media, (2.13) predicts the intensity of light as a function of source-detector spacing and the underlying absorption and scattering coefficients of the sample. From algebraic manipulation of this expression (see [90]), it can be shown that the log of the expected intensity of light (U_{dc}) between a source and detector spaced at a distance L has the following relationship:

$$log(U_{\mathrm{dc}}(L) \cdot L) = -\left[\left(\frac{\mu_{\mathrm{a}}}{D}\right)^{1/2}\right] \cdot L + \mathrm{Int}_{\mathrm{dc}} \tag{2.16}$$

where D is the diffusion constant as previously defined. By plotting the log ($U_{\mathrm{dc}}(L)^{\cdot}L$) versus L, the slope of this line is directly related to the absorption and scattering coefficients. The intercept of this curve ($\mathrm{Int}_{\mathrm{dc}}$) has a rather complex form and is detailed in [90]. Because this term is more difficult to estimate, it is often ignored. The slope, which can be estimated by measurements of the light intensity at differing source-detector spacing, contains two unknowns (μ_{A} and $\mu_{\mathrm{S}}{}'$). For CW-DOS systems, which only measure the intensity of light, the absorption coefficient can be estimated under the assumption of a fixed scattering coefficient.

Frequency-modulated and time-resolved DOS systems record additional time-of-flight information, which can be used to further separate absorption and scattering. In the case of frequency-modulated DOS, additional information about the phase (Φ) and modulated (U_{AC}) components of the signal can be used to estimate both absorption and scattering (see Fig. 2.6 for definitions). As derived in [90],

$$log(U_{\mathrm{ac}}(L)\cdot L) = -\left(\left(\frac{\mu_{\mathrm{a}}}{D}\right)^{1/2}\left(\left[1+\left(\frac{\omega}{v\cdot\mu_{\mathrm{a}}}\right)^{2}\right]^{1/2}+1\right)^{1/2}\right)\cdot L + \mathrm{Int}_{\mathrm{AC}} \quad (2.17)$$

$$\Phi(L) = \left(\left(\frac{\mu_{\mathrm{a}}}{2D}\right)^{1/2}\left(\left[1+\left(\frac{\omega}{v\mu_{\mathrm{a}}}\right)^{2}\right]^{1/2}-1\right)^{1/2}\right)\cdot L + \mathrm{Int}_{\Phi} \quad (2.18)$$

where ω is the modulation frequency of the light (usually 100–200 MHz) and v is the speed of light in the medium. Similar to the DC component, the log ($U_{\mathrm{AC}}\cdot L$) and phase have a linear relationship with the source-detector spacing (L) for which the slope can be estimated from spatially resolved measurements. The slope of all three expressions contains two unknowns (μ_{A} and $\mu_{\mathrm{S}}{}'$). By combining any two of the three measurements, absorption and scattering can be estimated. For the case of AC and phase, the absorption and scattering coefficients are given by [90]

$$\mu'_{\mathrm{s}} = \left(\frac{\mathrm{Slope}_{\mathrm{ac}}{}^{2} - \mathrm{Slope}_{\Phi}{}^{2}}{3\mu_{\mathrm{a}}}\right) - \mu_{\mathrm{a}} \quad (2.19)$$

$$\mu_{\mathrm{a}} = \frac{\omega}{2v}\left(\frac{\mathrm{Slope}_{\Phi}}{\mathrm{Slope}_{\mathrm{ac}}} - \frac{\mathrm{Slope}_{\mathrm{ac}}}{\mathrm{Slope}_{\Phi}}\right) \quad (2.20)$$

where $\mathrm{Slope}_{\mathrm{X}}$ denotes the estimated slope obtained from (2.17) and (2.18).

2.5 Design of Functional Brain Imaging Studies

In a typical DOI study of brain function, a grid of light sources and light detectors is positioned on the head of a subject as is pictured in Fig. 2.1. Often this is done using fiber optics. One end of these fibers is secured into a headgear device, while the other end of the fiber is connected to the imaging instrument. The arrangement of these optodes on the head determines the depth sensitivity of the measurements to underlying cerebral changes. This arrangement will also, in part, dictate the spatial resolution and the magnitude of partial volume errors in the resulting image. In practice, the design of the optical head cap is dictated by availability of instrumentation, the area of the brain expected to be involved in the task, and by the amount of time and effort needed to set up the cap. In many experiments, for example in children or clinical populations, a sparse optical probe with a limited number of sensors positioned over a particular region of interest is appropriate in order to reduce subject burden and experiment setup time. The success of setting up the optical cap is also determined by the location on the head. In regions of the head with a high degree of curvature (e.g., the occipital or parietal regions), it may be more difficult to achieve uniform contact of the fiber optics with the scalp. These areas may also have more hair which is a consideration when positioning the optode sensors. In general, one can expect the detected light intensity to be several orders of magnitude lower than the input intensity due to absorption and scattering in the tissue. If the sensor is not fully in contact with the scalp, light may scatter across the surface and directly into the detector, producing a signal that may be orders of magnitude higher than the signal due to the remitted light from the brain. To prevent this effect, padding, foam, or other dark materials on the underside of the optical probe are often used to absorb some of this surface light. Subject comfort is another factor that can impact the experimental outcome. If the optical cap is too heavy because it contains a large number of fiber optics or is placed too tightly on the head, the subject may become restless and create motion artifacts (this is particularly a problem in child and infant studies). Placing the cap too loosely may in turn also increase motion artifacts due to the possibility of probe movement. Motion artifacts in optical imaging may arise due to movement of the probe relative to the head. However, if the probe is fixed properly to the head, the subject may still be able to move during imaging. For example, optical studies have been done during walking and balance tasks (see Fig. 2.7). Motion artifacts for DOI can sometimes arise from movement of the muscles beneath the probe, such as those controlling the eyebrows in the frontal pole or the jaw muscles which run along the side of the head and over Wernicke's and Broca's areas. The design of the optical probe must consider such artifacts, and, with care, these can be avoided in many cases.

2.5.1 Applications of Functional Optical Imaging

In comparison to other vascular imaging modalities such as MRI or positron emission tomography (PET), DOI is inexpensive and portable. As previously detailed, one drawback of diffuse methods is the inherent stochastic nature of light diffusion in a turbid media, which greatly limits the penetration depth and spatial resolution. Therefore, DOI is not a replacement for high-resolution imaging

Fig. 2.7 Examples of diffuse optical experiments. Examples of diffuse optical imaging studies conducted at the University of Pittsburgh. (**a**) DOI being used during a clinical balance test. (**b**) A wireless DOI system being used during rotational vestibular testing. (**c**) Optical measurements during a tilt-test study of auto-regulation, (**d**) DOI measurements during caloric vestibular stimulation of the inner ear, (**e**) a close-up of a small four-channel optical probe used during rotational testing, (**f**) optical measurements during a computer test, (**g**, **h**) optical measurements of a child and adult. (**i**) Example of DOI recordings concurrently with MRI and (**j**) with magnetoencephalography (MEG)

methods like MRI and PET, but rather is often used to fill a unique niche with the ability to scan populations or address scientific questions that would otherwise be difficult to address. In particular, DOI has been used successfully in a number of clinical and psychological studies of the brain as reviewed in several recent publications [29, 91–97].

2.5.2 *Clinical Applications of DOS*

Since DOS systems are portable they can be brought to the bedside. Several clinical DOS systems based on spatially resolved spectroscopy have already received approval in the US and Europe. DOS provides the ability to measure cerebral blood oxygenation, volume, or flow using portable instrumentation available for bedside monitoring. To date, most of the clinical studies investigating DOS have used spatially resolved spectroscopy (SRS) methods [15, 97–99]. DOS has been used to investigate several clinical areas of research over the last three decades (reviewed in [31]). DOS has been applied in various situations including monitoring of the brain during cardiac surgery [100–102], hypothermic cooling [103, 104], carotid endarterectomy [105, 106], and during anesthesia [107]. The outcomes of many of these studies have shown mixed success (reviewed in [108]).

In addition to the use of DOS as a monitoring device during clinical interventions, it has also been proposed as a diagnostic/assessment tool. DOS has been used to investigate the efficacy of the technique in various cerebral injuries including hypoxia and ischemia [109], brain trauma [110, 111], metabolic failure [112], and cerebral autoregulation impairments [113].

In recent years, the accuracy of estimates of cerebral blood oxygenation by DOS has been questioned in a number of reviews [15, 98, 99]. This pertains in particular to many of the CW-DOS-based commercial optical systems. However, it is important to recall (refer to (2.16)) that SRS contains two unknown terms (absorption and scattering); however, since CW-DOS systems measure only the amplitude of the light intensity, only one of these terms can be estimated and the other (usually scattering) must be assumed. The absolute value for blood oxygenation reported by many of these systems uses calibration tables rather than empirical measurements of the scattering term. In addition, the SRS is based on the solution to the diffusion equation for homogeneous semi-infinite slab geometry. New DOS approaches based on frequency-modulated or time-resolved methods may offer improvements over the CW-based SRS technique. For example, FM-DOS has been applied to measurements of cerebral blood volume and oxygen saturation in neonates [114, 115] and has also been used in combination with DCS blood flow measurements to estimate oxygen metabolism in the brain [116].

2.5.3 Adult and Child Psychology Studies

With the development of multi-channel DOS and DOI systems in the 1990s, optical brain imaging was applied to various psychology functional tests in adults (reviewed in [30, 92, 117, 118]), children [29, 119], and more recently infants [120, 121]. In adults, optical brain imaging has been applied to many tasks ranging from classic psychological tests such as N-back [122, 123], Stroop [124–126], emotion [127], speech [120, 128, 129], and other attention or memory tasks [130] to very novel tasks such as fine motor skills [131], attention while driving a car [132], or social engagement [133, 134] (reviewed in [30]). Many of these classic experiments have been used to show correspondence between optical methods and other modalities such as functional MRI or PET. To date, numerous multi-modal studies (reviewed in [92]) have been done to compare DOI with fMRI [92, 135–140] or PET [141, 142], which have further confirmed optical methods. Optical studies are less expensive and can accommodate more flexible experimental designs compared to fMRI or PET methods.

Optical brain imaging has also been widely used in the field of child and infant psychology (reviewed in [143]). It is possible to build a lightweight, nonintrusive optical head cap, which can be comfortably worn by children. In some cases, this head cap can be created to resemble a costume hat or helmet that encourages the child to wear the DOI sensors throughout the experiment.

2.5.4 Studies of Movement and Balance

As long as the optical head cap remains fixed to the head, optical study participants can actually move during experiments. In recent years, DOI has been applied to various studies including balance [144], walking and gait [145, 146], and vestibular testing [147, 148]. Several groups have created wireless and wearable instruments that allow full subject motion during experiments [149]. This technology has opened the door to a new range of experiments based on real-world activities. Portable DOI has also been used in studies of brain activity during mobility tasks such as driving a car [132] or in airplane pilots [150–155] and astronauts [156].

2.5.5 Multimodal Optical Imaging

Many of the commercial and custom DOI systems utilize fiber optics to couple the instrument's optical detectors and sources to a head cap worn by the subject. Fiber optics allows for an extended distance between the subject and instrumentation and thus makes it possible to record optical signals concurrently with other modalities. Typical commercial fiber optics have attenuation factors of only about 20 db/km, which means that very long fibers can be used with virtually no loss of light. Glass fiber optics and plastic head cap materials can be made to be compatible with other modalities such as fMRI [92, 131, 138–140, 157], PET [141, 142, 158], transcranial magnetic stimulation (TMS) [159, 160] or magnetoencephalography (MEG) [161, 162]. Several research groups have developed integrated electroencephalography (EEG) and optical sensors [163, 164], which allow concurrent recordings of neural and vascular signals. These instruments have been applied to detect and classify seizures in adults [165–167] and infants [168–172].

References

1. Cope M, Delpy DT, Reynolds EO, Wray S, Wyatt J, van der Zee P (1988) Methods of quantitating cerebral near infrared spectroscopy data. Adv Exp Med Biol 222:183–189
2. Delpy DT, Cope MC, Cady EB, Wyatt JS, Hamilton PA, Hope PL, Wray S, Reynolds EO (1987) Cerebral monitoring in newborn infants by magnetic resonance and near infrared spectroscopy. Scand J Clin Lab Invest Suppl 188:9–17

3. Chance B, Leigh JS, Miyake H, Smith DS, Nioka S, Greenfeld R, Finander M, Kaufmann K, Levy W, Young M et al (1988) Comparison of time-resolved and -unresolved measurements of deoxyhemoglobin in brain. Proc Natl Acad Sci U S A 85(14):4971–4975
4. Hoshi Y (2003) Functional near-infrared optical imaging: utility and limitations in human brain mapping. Psychophysiology 40(4):511–520
5. Hoshi Y, Tamura M (1993) Dynamic multichannel near-infrared optical imaging of human brain activity. J Appl Physiol 75(4):1842–1846
6. Villringer A, Chance B (1997) Non-invasive optical spectroscopy and imaging of human brain function. Trends Neurosci 20(10):435–442
7. Jobsis FF (1977) Noninvasive, infrared monitoring of cerebral and myocardial oxygen sufficiency and circulatory parameters. Science 198(4323):1264–1267
8. De Blasi RA, Quaglia E, Gasparetto A, Ferrari M (1992) Muscle oxygenation by fast near infrared spectrophotometry (NIRS) in ischemic forearm. Adv Exp Med Biol 316:163–172
9. Chance B, Bank W (1995) Genetic disease of mitochondrial function evaluated by NMR and NIR spectroscopy of skeletal tissue. Biochim Biophys Acta 1271(1):7–14
10. Boushel R, Piantadosi CA (2000) Near-infrared spectroscopy for monitoring muscle oxygenation. Acta Physiol Scand 168(4):615–622
11. Colier WN, van Haaren NJ, Oeseburg B (1995) A comparative study of two near infrared spectrophotometers for the assessment of cerebral haemodynamics. Acta Anaesthesiol Scand Suppl 107:101–105
12. Torella F, Cowley R, Thorniley MS, McCollum CN (2002) Monitoring blood loss with near infrared spectroscopy. Comp Biochem Physiol A Mol Integr Physiol 132(1):199–203
13. Hyttel-Sorensen S, Sorensen LC, Riera J, Greisen G (2011) Tissue oximetry: a comparison of mean values of regional tissue saturation, reproducibility and dynamic range of four NIRS-instruments on the human forearm. Biomed Opt Express 2(11):3047–3057, PMCID:3207374
14. Reed CA, Baker RS, Lam CT, Hilshorst JL, Ferguson R, Lombardi J, Eghtesady P (2011) Application of near-infrared spectroscopy during fetal cardiac surgery. J Surg Res 171 (1):159–163
15. van Bel F, Lemmers P, Naulaers G (2008) Monitoring neonatal regional cerebral oxygen saturation in clinical practice: value and pitfalls. Neonatology 94(4):237–244
16. Adcock LM, Wafelman LS, Hegemier S, Moise AA, Speer ME, Contant CF, Goddard-Finegold J (1999) Neonatal intensive care applications of near-infrared spectroscopy. Clin Perinatol 26(4):893–903, ix
17. Nicklin SE, Hassan IA, Wickramasinghe YA, Spencer SA (2003) The light still shines, but not that brightly? The current status of perinatal near infrared spectroscopy. Arch Dis Child Fetal Neonatal Ed 88(4):F263–F268, PMCID:1721587
18. Greisen G (2006) Is near-infrared spectroscopy living up to its promises? Semin Fetal Neonatal Med 11(6):498–502
19. Zeff BW, White BR, Dehghani H, Schlaggar BL, Culver JP (2007) Retinotopic mapping of adult human visual cortex with high-density diffuse optical tomography. Proc Natl Acad Sci U S A 104(29):12169–12174
20. Hoppe-Seyler F (1866) Über die Oxydation in lebenden Blute. Med Chem Untersuch Lab 1:133–140
21. Stokes GG (1864) On the reduction and oxidation of the colouring matter of the blood. Proc R Soc Lond 13:355–364
22. Perutz MF, Rossmann MG, Cullis AF, Muirhead H, Will G, North AC (1960) Structure of haemoglobin: a three-dimensional Fourier synthesis at 5.5-A. resolution, obtained by X-ray analysis. Nature 185(4711):416–422
23. Nobelprize.org (1962) The Nobel Prize in Chemistry 1962. [cited 2012 March 22]
24. Severinghaus JW, Astrup PB (1986) History of blood gas analysis. V. Oxygen measurement. J Clin Monit 2(3):174–189
25. Nicolai L (1932) Uber Sichtbarmachung, Verlauf und chemische Kinetik der Oxyhemoglobinreduktion im lebenden Gewebe, besonders in der menschlichen Haut. Arch Ges Physiol 229:372–389

26. Kramer K (1935) Ein Verfahren zur fortlaufenden Messung des Sauerstoffgehaltes im stromenden Blute an uner6ffneten Gefassen. Z Biol 96:61–75
27. Severinghaus JW, Astrup PB (1986) History of blood gas analysis. VI. Oximetry. J Clin Monit 2(4):270–288
28. Severinghaus JW (2007) Takuo Aoyagi: discovery of pulse oximetry. Anesth Analg 105(6 suppl):S1–S4, tables of contents
29. Nagamitsu S, Yamashita Y, Tanaka H, Matsuishi T (2012) Functional near-infrared spectroscopy studies in children. Biopsychosoc Med 6(1):7
30. Ferrari M, Quaresima V (2012) A brief review on the history of human functional near-infrared spectroscopy (fNIRS) development and fields of application. Neuroimage 63(2): 921-–35
31. Smith M (2011) Shedding light on the adult brain: a review of the clinical applications of near-infrared spectroscopy. Philos Trans A Math Phys Eng Sci 369(1955):4452–4469
32. Bourdillon N, Mollard P, Letournel M, Beaudry M, Richalet JP (2009) Interaction between hypoxia and training on NIRS signal during exercise: contribution of a mathematical model. Respir Physiol Neurobiol 169(1):50–61
33. Durduran T, Choe R, Culver JP, Zubkov L, Holboke MJ, Giammarco J, Chance B, Yodh AG (2002) Bulk optical properties of healthy female breast tissue. Phys Med Biol 47(16):2847–2861
34. Gibson AP, Hebden JC, Arridge SR (2005) Recent advances in diffuse optical imaging. Phys Med Biol 50(4):R1–R43
35. Boverman G, Miller EL, Li A, Zhang Q, Chaves T, Brooks DH, Boas DA (2005) Quantitative spectroscopic diffuse optical tomography of the breast guided by imperfect a priori structural information. Phys Med Biol 50(17):3941–3956
36. Srinivasan S, Pogue BW, Jiang S, Dehghani H, Kogel C, Soho S, Gibson JJ, Tosteson TD, Poplack SP, Paulsen KD (2006) In vivo hemoglobin and water concentrations, oxygen saturation, and scattering estimates from near-infrared breast tomography using spectral reconstruction. Acad Radiol 13(2):195–202
37. Enfield LC, Gibson AP, Hebden JC, Douek M (2009) Optical tomography of breast cancer-monitoring response to primary medical therapy. Target Oncol 4(3):219–233
38. Choe R (2009) Diffuse optical tomography & spectroscopy in breast cancer characterization & therapy monitoring at UPENN. Conf Proc IEEE Eng Med Biol Soc 2009:6335–6337
39. Irvine WM, Pollack JB (1968) Infrared optical properties of water and ice spheres. Icarus 8:324–360
40. Kopelevich OV (1976) Optical properties of pure water in the 250-600nm range. Opt Spectrosc 41:391–392
41. Palmer KF, Williams D (1974) Optical properties of water in the near infrared. J Opt Soc Am 64:1107–1110
42. van Veen RLP, Sterenborg HJCM, Pifferi A, Torricelli A, Cubeddu R (2004) Determination of VIS- NIR absorption coefficients of mammalian fat, with time- and spatially resolved diffuse reflectance and transmission spectroscopy. in OSA Annual BIOMED Topical Meeting
43. Sarna T, Sealy R (1984) Photoinduced oxygen consumption in melanin systems. Action spectra and quantum yields for eumelanin and synthetic melanin. Photochem Photobiol 39:69–74
44. Takatani S, Graham MD (1987) Theoretical analysis of diffuse reflectance from a two-layer tissue model. IEEE Trans Biomed Eng 26:656–664
45. Moaveni MK (1970) A multiple scattering field theory applied to whole blood, in Dept. of Electrical Engineering. University of Washington
46. Prahl S. http://omlc.ogi.edu/spectra
47. Heinrich U (1981) Untersuchungen zur qualitativen photometrischen analyse der redox-zustande der atmungskette in vitro und in vivo am beispiel des gehirns., in Abteilung fur Biologie. Ruhr-Universitat Bochum

48. http://www.medphys.ucl.ac.uk
49. Strangman G, Franceschini MA, Boas DA (2003) Factors affecting the accuracy of near-infrared spectroscopy concentration calculations for focal changes in oxygenation parameters. Neuroimage 18(4):865–879
50. Simpson CR, Kohl M, Essenpreis M, Cope M (1998) Near-infrared optical properties of ex vivo human skin and subcutaneous tissues measured using the Monte Carlo inversion technique. Phys Med Biol 43(9):2465–2478
51. Firbank M, Hiraoka M, Essenpreis M, Delpy DT (1993) Measurement of the optical properties of the skull in the wavelength range 650–950 nm. Phys Med Biol 38(4):503–510
52. Hillman EM (2002) Experimental and theoretical investigations of near infrared tomographic imaging methods and clinical applications. In: Department of medical physics and bioengineering. University College London, London
53. Cheong WF, Prahl SA, Welch AJ (1990) A review of the optical properties of biological tissues. IEEE J Quantum Electron 26:2166–2185
54. van-der-Zee P (1992) Measurement and modelling of the optical properties of human tissue in the near infrared. In: Department of medical physics and bioengineering. University College London, London
55. Patel J, Marks K, Roberts I, Azzopardi D, Edwards AD (1998) Measurement of cerebral blood flow in newborn infants using near infrared spectroscopy with indocyanine green. Pediatr Res 43(1):34–39
56. Te Velde EA, Veerman T, Subramaniam V, Ruers T (2010) The use of fluorescent dyes and probes in surgical oncology. Eur J Surg Oncol 36(1):6–15
57. Luo S, Zhang E, Su Y, Cheng T, Shi C (2011) A review of NIR dyes in cancer targeting and imaging. Biomaterials 32(29):7127–7138
58. van den Berg NS, van Leeuwen FW, van der Poel HG (2012) Fluorescence guidance in urologic surgery. Curr Opin Urol 22(2):109–120
59. Mizuno S, Isaji S (2010) Indocyanine green (ICG) fluorescence imaging-guided cholangiography for donor hepatectomy in living donor liver transplantation. Am J Transplant 10 (12):2725–2726
60. Kleine M, Joahnning K, Kousoulas L, Schrem H, Lehner F, Bektas H, Klempnauer J, Kaaden S (2011) Observations with impact on the indication for kinetic therapy in critically ill liver transplant patients. Ann Transplant 16(4):25–31
61. Ren Z, Xu Y, Zhu S (2011) Indocyanine green retention test avoiding liver failure after hepatectomy for hepatolithiasis. Hepatogastroenterology 59:115–116
62. Mohnle P, Kilger E, Adnan L, Beiras-Fernandez A, Vicol C, Weis F (2012) Indocyanine green clearance after cardiac surgery: the impact of cardiopulmonary bypass. Perfusion 27:292–299
63. Yu G, Floyd TF, Durduran T, Zhou C, Wang J, Detre JA, Yodh AG (2007) Validation of diffuse correlation spectroscopy for muscle blood flow with concurrent arterial spin labeled perfusion MRI. Opt Express 15(3):1064–1075
64. Yodh AG (2009) Diffuse optics for monitoring brain hemodynamics. Conf Proc IEEE Eng Med Biol Soc 2009:1991–1993
65. Durduran T, Zhou C, Buckley EM, Kim MN, Yu G, Choe R, Gaynor JW, Spray TL, Durning SM, Mason SE, Montenegro LM, Nicolson SC, Zimmerman RA, Putt ME, Wang J, Greenberg JH, Detre JA, Yodh AG, Licht DJ (2010) Optical measurement of cerebral hemodynamics and oxygen metabolism in neonates with congenital heart defects. J Biomed Opt 15(3):037004, PMCID:2887915
66. Kim MN, Durduran T, Frangos S, Edlow BL, Buckley EM, Moss HE, Zhou C, Yu G, Choe R, Maloney-Wilensky E, Wolf RL, Grady MS, Greenberg JH, Levine JM, Yodh AG, Detre JA, Kofke WA (2010) Noninvasive measurement of cerebral blood flow and blood oxygenation using near-infrared and diffuse correlation spectroscopies in critically brain-injured adults. Neurocrit Care 12(2):173–180, PMCID:2844468

67. Gratton G, Fabiani M, Corballis PM, Hood DC, Goodman-Wood MR, Hirsch J, Kim K, Friedman D, Gratton E (1997) Fast and localized event-related optical signals (EROS) in the human occipital cortex: comparisons with the visual evoked potential and fMRI. Neuroimage 6(3):168–180
68. Gratton G, Fabiani M, Goodman-Wood MR, Desoto MC (1998) Memory-driven processing in human medial occipital cortex: an event-related optical signal (EROS) study. Psychophysiology 35(3):348–351
69. Gratton G, Fabiani M (2003) The event-related optical signal (EROS) in visual cortex: replicability, consistency, localization, and resolution. Psychophysiology 40(4):561–571
70. Radhakrishnan H, Vanduffel W, Deng HP, Ekstrom L, Boas DA, Franceschini MA (2009) Fast optical signal not detected in awake behaving monkeys. Neuroimage 45(2):410–419, PMCID:2648855
71. Beer A, Lambert J (1854) Einleitung in die höhere Optik (Introduction to the Higher Optical)
72. Bouguer P (1729) Essai d'Optique, sur la gradation de la lumiere. Paris, France
73. Delpy DT, Cope M, van der Zee P, Arridge S, Wray S, Wyatt J (1988) Estimation of optical pathlength through tissue from direct time of flight measurement. Phys Med Biol 33 (12):1433–1442
74. Haskell RC, Svaasand LO, Tsay TT, Feng TC, McAdams MS, Tromberg BJ (1994) Boundary conditions for the diffusion equation in radiative transfer. J Opt Soc Am A Opt Image Sci Vis 11(10):2727–2741
75. Flock ST, Wilson BC, Patterson MS (1989) Monte Carlo modeling of light propagation in highly scattering tissues–II: comparison with measurements in phantoms. IEEE Trans Biomed Eng 36(12):1169–1173
76. Flock ST, Patterson MS, Wilson BC, Wyman DR (1989) Monte Carlo modeling of light propagation in highly scattering tissue–I: model predictions and comparison with diffusion theory. IEEE Trans Biomed Eng 36(12):1162–1168
77. Hiraoka M, Firbank M, Essenpreis M, Cope M, Arridge SR, van der Zee P, Delpy DT (1993) A Monte Carlo investigation of optical pathlength in inhomogeneous tissue and its application to near-infrared spectroscopy. Phys Med Biol 38(12):1859–1876
78. Wang L, Jacques SL, Zheng L (1995) MCML–Monte Carlo modeling of light transport in multi-layered tissues. Comput Methods Programs Biomed 47(2):131–146
79. Quan G, Gong H, Deng Y, Fu J, Luo Q (2011) Monte Carlo-based fluorescence molecular tomography reconstruction method accelerated by a cluster of graphic processing units. J Biomed Opt 16(2):026018
80. Dehghani H, Eames ME, Yalavarthy PK, Davis SC, Srinivasan S, Carpenter CM, Pogue BW, Paulsen KD (2008) Near infrared optical tomography using NIRFAST: algorithm for numerical model and image reconstruction. Commun Numer Methods Eng 25(6):711–732, PMCID:2826796
81. Fantini S, Hueber D, Franceschini MA, Gratton E, Rosenfeld W, Stubblefield PG, Maulik D, Stankovic MR (1999) Non-invasive optical monitoring of the newborn piglet brain using continuous-wave and frequency-domain spectroscopy. Phys Med Biol 44(6):1543–1563
82. Hueber DM, Franceschini MA, Ma HY, Zhang Q, Ballesteros JR, Fantini S, Wallace D, Ntziachristos V, Chance B (2001) Non-invasive and quantitative near-infrared haemoglobin spectrometry in the piglet brain during hypoxic stress, using a frequency-domain multidistance instrument. Phys Med Biol 46(1):41–62
83. Boas D (1996) Diffuse photon probes of structural and dynamical properties of turbid media: theory and biomedical applications. In: Physics. University of Pennsylvania
84. Durduran T, Yu G, Burnett MG, Detre JA, Greenberg JH, Wang J, Zhou C, Yodh AG (2004) Diffuse optical measurement of blood flow, blood oxygenation, and metabolism in a human brain during sensorimotor cortex activation. Opt Lett 29(15):1766–1768
85. Dunn AK, Bolay H, Moskowitz MA, Boas DA (2001) Dynamic imaging of cerebral blood flow using laser speckle. J Cereb Blood Flow Metab 21(3):195–201

86. Durduran T, Choe R, Yu G, Zhou C, Tchou JC, Czerniecki BJ, Yodh AG (2005) Diffuse optical measurement of blood flow in breast tumors. Opt Lett 30(21):2915–2917
87. Sunar U, Quon H, Durduran T, Zhang J, Du J, Zhou C, Yu G, Choe R, Kilger A, Lustig R, Loevner L, Nioka S, Chance B, Yodh AG (2006) Noninvasive diffuse optical measurement of blood flow and blood oxygenation for monitoring radiation therapy in patients with head and neck tumors: a pilot study. J Biomed Opt 11(6):064021
88. Zhou C, Choe R, Shah N, Durduran T, Yu G, Durkin A, Hsiang D, Mehta R, Butler J, Cerussi A, Tromberg BJ, Yodh AG (2007) Diffuse optical monitoring of blood flow and oxygenation in human breast cancer during early stages of neoadjuvant chemotherapy. J Biomed Opt 12 (5):051903
89. Edlow BL, Kim MN, Durduran T, Zhou C, Putt ME, Yodh AG, Greenberg JH, Detre JA (2010) The effects of healthy aging on cerebral hemodynamic responses to posture change. Physiol Meas 31(4):477–495
90. Fantini S, Franceschini MA, Fishkin JB, Barbieri B, Gratton E (1994) Quantitative determination of the absorption spectra of chromophores in strongly scattering media: a light-emitting-diode based technique. Appl Opt 33(22):5204–5213
91. Obrig H, Villringer A (2003) Beyond the visible—imaging the human brain with light. J Cereb Blood Flow Metab 23(1):1–18
92. Steinbrink J, Villringer A, Kempf F, Haux D, Boden S, Obrig H (2006) Illuminating the BOLD signal: combined fMRI-fNIRS studies. Magn Reson Imaging 24(4):495–505
93. Toet MC, Lemmers PM (2009) Brain monitoring in neonates. Early Hum Dev 85(2):77–84
94. Moerman A, Wouters P (2010) Near-infrared spectroscopy (NIRS) monitoring in contemporary anesthesia and critical care. Acta Anaesthesiol Belg 61(4):185–194
95. Lloyd-Fox S, Blasi A, Elwell CE (2010) Illuminating the developing brain: the past, present and future of functional near infrared spectroscopy. Neurosci Biobehav Rev 34(3):269–284
96. Hoshi Y (2011) Towards the next generation of near-infrared spectroscopy. Philos Trans A Math Phys Eng Sci 369(1955):4425–4439
97. Pellicer A, Bravo Mdel C (2011) Near-infrared spectroscopy: a methodology-focused review. Semin Fetal Neonatal Med 16(1):42–49
98. Highton D, Elwell C, Smith M (2010) Noninvasive cerebral oximetry: is there light at the end of the tunnel? Curr Opin Anaesthesiol 23(5):576–581
99. Kasman N, Brady K (2011) Cerebral oximetry for pediatric anesthesia: why do intelligent clinicians disagree? Paediatr Anaesth 21(5):473–478
100. Chen CS, Leu BK, Liu K (1996) Detection of cerebral desaturation during cardiopulmonary bypass by cerebral oximetry. Acta Anaesthesiol Sin 34(4):173–178
101. Nemoto EM, Yonas H, Kassam A (2000) Clinical experience with cerebral oximetry in stroke and cardiac arrest. Crit Care Med 28(4):1052–1054
102. Tortoriello TA, Stayer SA, Mott AR, McKenzie ED, Fraser CD, Andropoulos DB, Chang AC (2005) A noninvasive estimation of mixed venous oxygen saturation using near-infrared spectroscopy by cerebral oximetry in pediatric cardiac surgery patients. Paediatr Anaesth 15(6):495–503
103. Hassan IA, Wickramasinghe YA, Spencer SA (2003) Effect of limb cooling on peripheral and global oxygen consumption in neonates. Arch Dis Child Fetal Neonatal Ed 88(2):F139–F142, PMCID:1721525
104. Ancora G, Maranella E, Locatelli C, Pierantoni L, Faldella G (2009) Changes in cerebral hemodynamics and amplitude integrated EEG in an asphyxiated newborn during and after cool cap treatment. Brain Dev 31(6):442–444
105. Pennekamp CW, Bots ML, Kappelle LJ, Moll FL, de Borst GJ (2009) The value of near-infrared spectroscopy measured cerebral oximetry during carotid endarterectomy in perioperative stroke prevention. A review. Eur J Vasc Endovasc Surg 38(5):539–545
106. Pennekamp CW, Moll FL, de Borst GJ (2011) The potential benefits and the role of cerebral monitoring in carotid endarterectomy. Curr Opin Anaesthesiol 24(6):693–697

107. Casati A, Spreafico E, Putzu M, Fanelli G (2006) New technology for noninvasive brain monitoring: continuous cerebral oximetry. Minerva Anestesiol 72(7–8):605–625
108. Garreffa G, Carni M, Gualniera G, Ricci GB, Bozzao L, De Carli D, Morasso P, Pantano P, Colonnese C, Roma V, Maraviglia B (2003) Real-time MR artifacts filtering during continuous EEG/fMRI acquisition. Magn Reson Imaging 21(10):1175–1189
109. Skjoth-Rasmussen J, Schulz M, Kristensen SR, Bjerre P (2004) Delayed neurological deficits detected by an ischemic pattern in the extracellular cerebral metabolites in patients with aneurysmal subarachnoid hemorrhage. J Neurosurg 100(1):8–15
110. Ghalenoui H, Saidi H, Azar M, Yahyavi ST, Borghei Razavi H, Khalatbari M (2008) Near-infrared laser spectroscopy as a screening tool for detecting hematoma in patients with head trauma. Prehosp Disaster Med 23(6):558–561
111. Kirkpatrick PJ, Smielewski P, Czosnyka M, Menon DK, Pickard JD (1995) Near-infrared spectroscopy use in patients with head injury. J Neurosurg 83(6):963–970
112. Hou X, Ding H, Teng Y, Zhou C, Tang X, Li S (2007) Research on the relationship between brain anoxia at different regional oxygen saturations and brain damage using near-infrared spectroscopy. Physiol Meas 28(10):1251–1265
113. Moroz T, Banaji M, Robertson NJ, Cooper CE, Tachtsidis I (2012) Computational modelling of the piglet brain to simulate near-infrared spectroscopy and magnetic resonance spectroscopy data collected during oxygen deprivation. J R Soc Interface 9:1499–1509
114. Franceschini MA, Thaker S, Themelis G, Krishnamoorthy KK, Bortfeld H, Diamond SG, Boas DA, Arvin K, Grant PE (2007) Assessment of infant brain development with frequency-domain near-infrared spectroscopy. Pediatr Res 61(5 Pt 1):546–551, PMCID:2637818
115. Grant PE, Roche-Labarbe N, Surova A, Themelis G, Selb J, Warren EK, Krishnamoorthy KS, Boas DA, Franceschini MA (2009) Increased cerebral blood volume and oxygen consumption in neonatal brain injury. J Cereb Blood Flow Metab 29(10):1704–1713, PMCID:2762197
116. Roche-Labarbe N, Carp SA, Surova A, Patel M, Boas DA, Grant PE, Franceschini MA (2010) Noninvasive optical measures of CBV, StO(2), CBF index, and rCMRO(2) in human premature neonates' brains in the first six weeks of life. Hum Brain Mapp 31(3):341–352, PMCID:2826558
117. Boas DA, Dale AM, Franceschini MA (2004) Diffuse optical imaging of brain activation: approaches to optimizing image sensitivity, resolution, and accuracy. Neuroimage 23(suppl 1):S275–S288
118. Huppert TJ, Diamond SG, Franceschini MA, Boas DA (2009) HomER: a review of time-series analysis methods for near-infrared spectroscopy of the brain. Appl Opt 48(10): D280–D298, PMCID:2761652
119. Aslin RN (2012) Questioning the questions that have been asked about the infant brain using near-infrared spectroscopy. Cogn Neuropsychol, http://dx.doi.org/10.1080/02643294.2012.654773
120. Minagawa-Kawai Y, Cristia A, Dupoux E (2011) Cerebral lateralization and early speech acquisition: a developmental scenario. Dev Cogn Neurosci 1(3):217–232
121. Minagawa-Kawai Y, Mori K, Hebden JC, Dupoux E (2008) Optical imaging of infants' neurocognitive development: recent advances and perspectives. Dev Neurobiol 68 (6):712–728
122. Herrmann MJ, Walter A, Schreppel T, Ehlis AC, Pauli P, Lesch KP, Fallgatter AJ (2007) D4 receptor gene variation modulates activation of prefrontal cortex during working memory. Eur J Neurosci 26(10):2713–2718
123. Ehlis AC, Bahne CG, Jacob CP, Herrmann MJ, Fallgatter AJ (2008) Reduced lateral prefrontal activation in adult patients with attention-deficit/hyperactivity disorder (ADHD) during a working memory task: a functional near-infrared spectroscopy (fNIRS) study. J Psychiatr Res 42(13):1060–1067
124. Azechi M, Iwase M, Ikezawa K, Takahashi H, Canuet L, Kurimoto R, Nakahachi T, Ishii R, Fukumoto M, Ohi K, Yasuda Y, Kazui H, Hashimoto R, Takeda M (2010) Discriminant

analysis in schizophrenia and healthy subjects using prefrontal activation during frontal lobe tasks: a near-infrared spectroscopy. Schizophr Res 117(1):52–60

125. Schroeter ML, Zysset S, Kupka T, Kruggel F, Yves von Cramon D (2002) Near-infrared spectroscopy can detect brain activity during a color-word matching Stroop task in an event-related design. Hum Brain Mapp 17(1):61–71
126. Ehlis AC, Herrmann MJ, Wagener A, Fallgatter AJ (2005) Multi-channel near-infrared spectroscopy detects specific inferior-frontal activation during incongruent Stroop trials. Biol Psychol 69(3):315–331
127. Moghimi S, Kushki A, Power S, Guerguerian AM, Chau T (2012) Automatic detection of a prefrontal cortical response to emotionally rated music using multi-channel near-infrared spectroscopy. J Neural Eng 9(2):026022
128. Sato Y, Uzuka T, Aoki H, Natsumeda M, Oishi M, Fukuda M, Fujii Y (2012) Near-infrared spectroscopic study and the Wada test for presurgical evaluation of expressive and receptive language functions in glioma patients: with a case report of dissociated language functions. Neurosci Lett 510(2):104–109
129. Kahlaoui K, Sante GD, Barbeau J, Maheux M, Lesage F, Ska B, Joanette Y (2012) Contribution of NIRS to the study of prefrontal cortex for verbal fluency in aging. Brain Lang 121(2):164–173
130. Jausovec N, Jausovec K (2012) Working memory training: improving intelligence—changing brain activity. Brain Cogn 79(2):96–106
131. Okamoto M, Dan H, Shimizu K, Takeo K, Amita T, Oda I, Konishi I, Sakamoto K, Isobe S, Suzuki T, Kohyama K, Dan I (2004) Multimodal assessment of cortical activation during apple peeling by NIRS and fMRI. Neuroimage 21(4):1275–1288
132. Li ZY, Dai SX, Zhang XY, Li Y, Yu XX (2010) Assessment of cerebral oxygen saturation using near infrared spectroscopy under driver fatigue state. Guang Pu Xue Yu Guang Pu Fen Xi 30(1):58–61
133. Naoi N, Minagawa-Kawai Y, Kobayashi A, Takeuchi K, Nakamura K, Yamamoto J, Kojima S (2012) Cerebral responses to infant-directed speech and the effect of talker familiarity. Neuroimage 59(2):1735–1744
134. Nomura Y, Ogawa T, Nomura M (2010) Perspective taking associated with social relationships: a NIRS study. Neuroreport 21(17):1100–1105
135. Kleinschmidt A, Obrig H, Requardt M, Merboldt KD, Dirnagl U, Villringer A, Frahm J (1996) Simultaneous recording of cerebral blood oxygenation changes during human brain activation by magnetic resonance imaging and near-infrared spectroscopy. J Cereb Blood Flow Metab 16(5):817–826
136. Dunn JF, Zaim-Wadghiri Y, Pogue BW, Kida I (1998) BOLD MRI vs. NIR spectrophotometry. Will the best technique come forward? Adv Exp Med Biol 454:103–113
137. D’Arceuil HE, Hotakainen MP, Liu C, Themelis G, de Crespigny AJ, Franceschini MA (2005) Near-infrared frequency-domain optical spectroscopy and magnetic resonance imaging: a combined approach to studying cerebral maturation in neonatal rabbits. J Biomed Opt 10(1):11011, PMCID:2637814
138. Sassaroli A, de BFB, Tong Y, Renshaw PF, Fantini S (2006) Spatially weighted BOLD signal for comparison of functional magnetic resonance imaging and near-infrared imaging of the brain. Neuroimage 33(2):505–514
139. Toronov VY, Zhang X, Webb AG (2007) A spatial and temporal comparison of hemodynamic signals measured using optical and functional magnetic resonance imaging during activation in the human primary visual cortex. Neuroimage 34:1136–1148
140. Huppert TJ, Hoge RD, Diamond SG, Franceschini MA, Boas DA (2006) A temporal comparison of BOLD, ASL, and NIRS hemodynamic responses to motor stimuli in adult humans. Neuroimage 29(2):368–382, PMCID:2692693
141. Hock C, Villringer K, Muller-Spahn F, Hofmann M, Schuh-Hofer S, Heekeren H, Wenzel R, Dirnagl U, Villringer A (1996) Near infrared spectroscopy in the diagnosis of Alzheimer’s disease. Ann N Y Acad Sci 777:22–29

142. Rostrup E, Law I, Pott F, Ide K, Knudsen GM (2002) Cerebral hemodynamics measured with simultaneous PET and near-infrared spectroscopy in humans. Brain Res 954(2):183–193
143. Gervain J, Mehler J, Werker JF, Nelson CA, Csibra G, Lloyd-Fox S, Shukla M, Aslin RN (2011) Near-infrared spectroscopy: a report from the McDonnell infant methodology consortium. Dev Cogn Neurosci 1(1):22–46
144. Karim H, Schmidt B, Dart D, Beluk N, Huppert T (2012) Functional near-infrared spectroscopy (fNIRS) of brain function during active balancing using a video game system. Gait Posture 35:367–372
145. Miyai I, Tanabe HC, Sase I, Eda H, Oda I, Konishi I, Tsunazawa Y, Suzuki T, Yanagida T, Kubota K (2001) Cortical mapping of gait in humans: a near-infrared spectroscopic topography study. Neuroimage 14(5):1186–1192
146. Suzuki M, Miyai I, Ono T, Kubota K (2008) Activities in the frontal cortex and gait performance are modulated by preparation. An fNIRS study. Neuroimage 39(2):600–607
147. Iida M, Haida M, Igarashi M (2009) Vertigo and cerebral hemoglobin changes during unilateral caloric stimulation: a near-infrared spectroscopy study. Ann N Y Acad Sci 1164:386–389
148. Kobayashi A, Cheung B (2006) Detection of cerebral oxyhaemoglobin changes during vestibular Coriolis cross-coupling stimulation using near infrared spectroscopy. Neurosci Lett 394(2):83–87
149. Hamaoka T, McCully KK, Niwayama M, Chance B (2011) The use of muscle near-infrared spectroscopy in sport, health and medical sciences: recent developments. Philos Trans A Math Phys Eng Sci 369(1955):4591–4604
150. Ryoo HC, Sun HH, Shender BS, Hrebien L (2004) Consciousness monitoring using near-infrared spectroscopy (NIRS) during high +Gz exposures. Med Eng Phys 26(9):745–753
151. Benni PB, Li JK, Chen B, Cammarota J, Amory DW (2003) Correlation of NIRS determined cerebral oxygenation with severity of pilot +Gz acceleration symptoms. Adv Exp Med Biol 530:381–389
152. Benni PB, Li JK, Chen B, Cammarota J, Amory DW (2003) NIRS monitoring of pilots subjected to +Gz acceleration and G-induced loss of consciousness (G-LOC). Adv Exp Med Biol 530:371–379
153. Shender BS, Forster EM, Hrebien L, Ryoo HC, Cammarota JP Jr (2003) Acceleration-induced near-loss of consciousness: the “A-LOC” syndrome. Aviat Space Environ Med 74(10):1021–1028
154. Kobayashi A, Tong A, Kikukawa A (2002) Pilot cerebral oxygen status during air-to-air combat maneuvering. Aviat Space Environ Med 73(9):919–924
155. Ryoo HC, Hrebien L, Shender BS (2002) Noninvasive monitoring of human consciousness by near-infrared spectroscopy (NIRS) during high +Gz stress. Biomed Sci Instrum 38:1–7
156. Genik RJ II, Green CC, Graydon FX, Armstrong RE (2005) Cognitive avionics and watching spaceflight crews think: generation-after-next research tools in functional neuroimaging. Aviat Space Environ Med 76(6 suppl):B208–B212
157. Gagnon L, Yucel MA, Dehaes M, Cooper RJ, Perdue KL, Selb J, Huppert TJ, Hoge RD, Boas DA (2012) Quantification of the cortical contribution to the NIRS signal over the motor cortex using concurrent NIRS-fMRI measurements. Neuroimage 59:3933–3940
158. Villringer K, Minoshima S, Hock C, Obrig H, Ziegler S, Dirnagl U, Schwaiger M, Villringer A (1997) Assessment of local brain activation. A simultaneous PET and near-infrared spectroscopy study. Adv Exp Med Biol 413:149–153
159. Eschweiler GW, Wegerer C, Schlotter W, Spandl C, Stevens A, Bartels M, Buchkremer G (2000) Left prefrontal activation predicts therapeutic effects of repetitive transcranial magnetic stimulation (rTMS) in major depression. Psychiatry Res 99(3):161–172
160. Ziemann U (2011) Transcranial magnetic stimulation at the interface with other techniques: a powerful tool for studying the human cortex. Neuroscientist 17(4):368–381

161. Sander TH, Liebert A, Burghoff M, Wabnitz H, Macdonald R, Trahms L (2007) Cross-correlation analysis of the correspondence between magnetoencephalographic and near-infrared cortical signals. Methods Inf Med 46(2):164–168
162. Mackert BM, Wubbeler G, Leistner S, Uludag K, Obrig H, Villringer A, Trahms L, Curio G (2004) Neurovascular coupling analyzed non-invasively in the human brain. Neuroreport 15(1):63–66
163. Lareau E, Lesage F, Pouliot P, Nguyen D, Le Lan J, Sawan M (2011) Multichannel wearable system dedicated for simultaneous electroencephalographynear-infrared spectroscopy real-time data acquisitions. J Biomed Opt 16(9):096014
164. Fazli S, Mehnert J, Steinbrink J, Curio G, Villringer A, Muller KR, Blankertz B (2012) Enhanced performance by a hybrid NIRS-EEG brain computer interface. Neuroimage 59 (1):519–529
165. Machado A, Lina JM, Tremblay J, Lassonde M, Nguyen DK, Lesage F, Grova C (2011) Detection of hemodynamic responses to epileptic activity using simultaneous Electro-EncephaloGraphy (EEG)/Near Infra Red Spectroscopy (NIRS) acquisitions. Neuroimage 56(1):114–125
166. Lee S, Lee M, Koh D, Kim BM, Choi JH (2010) Cerebral hemodynamic responses to seizure in the mouse brain: simultaneous near-infrared spectroscopy-electroencephalography study. J Biomed Opt 15(3):037010
167. Roche-Labarbe N, Zaaimi B, Mahmoudzadeh M, Osharina V, Wallois A, Nehlig A, Grebe R, Wallois F (2010) NIRS-measured oxy- and deoxyhemoglobin changes associated with EEG spike-and-wave discharges in a genetic model of absence epilepsy: the GAERS. Epilepsia 51 (8):1374–1384
168. Ancora G, Maranella E, Grandi S, Sbravati F, Coccolini E, Savini S, Faldella G (2011) Early predictors of short term neurodevelopmental outcome in asphyxiated cooled infants. A combined brain amplitude integrated electroencephalography and near infrared spectroscopy study. Brain Dev (in press)
169. Gucuyener K, Beken S, Ergenekon E, Soysal S, Hirfanoglu I, Turan O, Unal S, Altuntas N, Kazanci E, Kulali F, Koc E, Turkyilmaz C, Onal E, Atalay Y (2012) Use of amplitude-integrated electroencephalography (aEEG) and near infrared spectroscopy findings in neonates with asphyxia during selective head cooling. Brain Dev 34:280–286
170. ter Horst HJ, Verhagen EA, Keating P, Bos AF (2011) The relationship between electrocerebral activity and cerebral fractional tissue oxygen extraction in preterm infants. Pediatr Res 70(4):384–388
171. Wallois F, Patil A, Heberle C, Grebe R (2010) EEG-NIRS in epilepsy in children and neonates. Neurophysiol Clin 40(5–6):281–292
172. Aarabi A, Grebe R, Wallois F (2007) A multistage knowledge-based system for EEG seizure detection in newborn infants. Clin Neurophysiol 118(12):2781–2797

Chapter 3
Diffuse Optical Tomography for Brain Imaging: Continuous Wave Instrumentation and Linear Analysis Methods

Paolo Giacometti and Solomon G. Diamond

3.1 Introduction

Near-infrared spectroscopy (NIRS) allows for noninvasive measurements of blood volume and blood oxygenation changes in tissue with high temporal resolution. Light sources illuminate near-infrared (NIR) laser light into tissue and light detectors collect remitted light. The detected light is spectroscopically analyzed to calculate blood volume and oxygenation changes. The results from these calculations are obtained in the form of variations of oxygenated and deoxygenated hemoglobin concentration. NIRS is specifically useful in functional neuroimaging because of the relationship between neural and hemodynamic activity [12, 20, 35]. During functional activation in the brain, there is an increase of oxygen demand in the area of activation and complex signaling to the vasculature that is mediated by astrocytes and neurotransmitters. This signaling results in a local increase in blood flow, blood volume, and also an increase in blood oxygenation in a stereotyped hemodynamic response [38]. Obtaining measurements of the hemodynamic response of localized regions of the brain allows for inferences to be made regarding local neural activity. When light sources and detectors are placed over the scalp, measurements across several regions of the brain can be performed simultaneously. These measurements allow for tomographic images to be reconstructed into images of brain activation with a technique called diffuse optical tomography (DOT). The images generated show variations of local oxygenation changes and blood volume dynamics prompted by functional brain activation.

NIRS systems are a combination of laser sources and light detectors. There are three main types of NIRS systems: continuous wave (CW), time resolved (TR), and frequency domain (FD) [7]. These are systems that require different hardware and signal processing. Selecting the right instrument depends on the desired

---

P. Giacometti (✉) • S.G. Diamond
Thayer School of Engineering at Dartmouth, Hanover, NH, USA
e-mail: Paolo.Giacometti@Dartmouth.edu; Solomon.G.Diamond@Dartmouth.edu

S.J. Madsen (ed.), *Optical Methods and Instrumentation in Brain Imaging and Therapy*, Bioanalysis: Advanced Materials, Methods, and Devices 3,
DOI 10.1007/978-1-4614-4978-2_3,

information, application, and allowable cost of the system. There are several types of lasers and detectors used in NIRS systems. These vary depending on the type of NIRS system, the application, the choice of wavelength, the signal to noise ratio (SNR) needed, and the cost.

This review focuses on the description and mathematical analysis behind CW-NIRS and the construction of a linear forward model for DOT. In the CW case, laser diodes and photodiode detectors are often used to illuminate and detect the remitted light respectively via fiber optics in order to obtain signals with high sensitivity and low noise. There are several ways of analyzing the signals measured with NIRS to obtain meaningful information. For CW-NIRS systems, changes in blood oxygenation can be measured by analyzing the attenuation in the remitted light using a combination of the modified Beer–Lambert law (MBLL) and the diffusion approximation to the radiative transport equation (RTE). This method provides a linear method for NIRS data and is the focus of this review. There are other methods that can be used to model CW-NIRS, such as Monte Carlo simulation [3] and higher order approximations of the RTE [23]. In order to understand the mathematical analysis and models behind NIRS, several background concepts must first be established.

3.2 Fundamental Concepts Related to NIRS

3.2.1 Light Interaction with Tissue

Spectroscopy is the study of light and its interaction with matter. For the case of CW-NIRS, it is the analysis of light absorbance measurements to obtain chromophore concentration changes. NIRS is based on the light absorption characteristics that tissue has in the NIR range. Light absorption by different hemoglobin species varies with wavelength. Generally, when light is illuminated into tissue, water dominates photon absorption and attenuation. However, there is an optical window in the near-infrared (NIR) range where water absorption is low enough so that absorbance measurements at a few centimeters deep into biological tissue can be acquired with diffuse photon propagation [5, 8]. Light absorption by hemoglobin is dependent on whether it is in the oxygenated (HbO_2) state, or the deoxygenated or reduced (HbR) state [27]. Figure 3.1 shows the absorption spectra for hemoglobin in its oxygenated and deoxygenated state as well as water as a function of wavelength.

The 690 to 930 nm range is optimal for NIRS because hemoglobin dominates light absorption and also because there is low enough absorption by water that light can get through tissue to adequate depth for studies of human brain function. Light absorption is first dominated by deoxygenated hemoglobin at the lower wavelengths and then, above the isobestic point at 808 nm, by oxygenated hemoglobin.

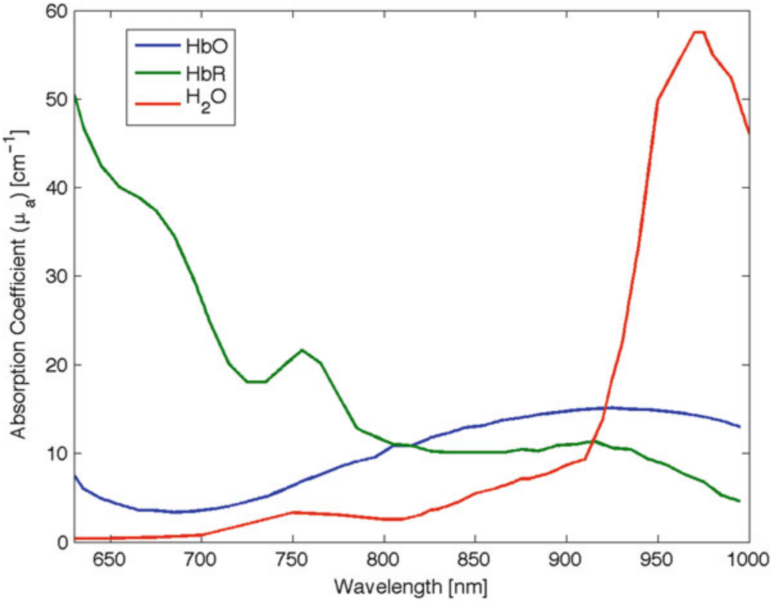

Fig. 3.1 Absorption spectra for hemoglobin, assuming 150 g of Hb per liter of whole blood and a molecular weight of 64,500 g/mol, and water, assuming 1,000 g/l and a molecular weight of 18.015 g/mol [34]

3.2.2 Wavelength Choice

In order to solve for changes in blood oxygenation using the MBLL, at least two wavelengths of light must be used. These wavelengths are chosen to minimize cross-talk between chromophores [4, 33, 36]. If three or more wavelengths are chosen, then it is useful to choose one wavelength before the isobestic point of 808 nm where HbO_2 and HbR have the same level of absorption to provide a measure of changes in blood volume. Assuming that other elements in the blood remain relatively constant during changes in blood oxygenation (constant hematocrit), the total change in hemoglobin (ΔHbT) can be set equal to the total change in blood volume (ΔBV) [40]

$$\Delta BV = \Delta HbT = \Delta HbO_2 + \Delta HbR.$$

Furthermore, some research groups use more than two wavelengths in order to have an over-defined system or for estimation of additional chromophores, such as cytochrome oxidase [5, 7]. Having an over-defined system can provide a measure of uncertainty in the spectroscopic calculations due to inaccuracies in the model assumptions discussed in Sect. 3.4. Using more than two wavelengths allows for correction of the differential pathlength factor discussed in Sect. 3.4 [33, 37].

Fig. 3.2 Photon interaction with matter

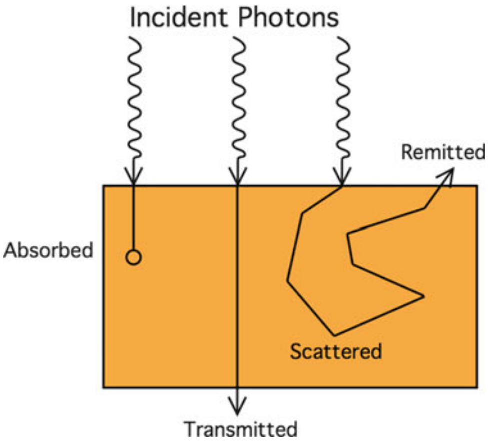

3.2.3 Absorption and Scattering

There are three main types of photon scattering, Rayleigh, Debye, and Mie [25, 27]. Rayleigh scattering is produced by the interaction of photons of wavelength λ and particles with radii much smaller than the wavelength $r \ll \lambda$ [27]. Debye scattering is produced by the interaction of photons with particles with radii smaller than λ but much bigger than those producing Rayleigh scattering [27]. Mie scattering is produced in the interaction of particles with radii bigger than the wavelength $r > \lambda$ [25, 27]. Mie scattering is what predominates in NIRS as cells and other particles within the tissue have radii bigger than the wavelengths of light illuminated [25].

When photons enter a medium, they have three possible outcomes: they are absorbed, they are transmitted through, or they are scattered to a different direction of propagation. Scattered photons can again have any of those three outcomes, making it possible for photons to be scattered enough to be remitted back toward the surface and out of the head (Fig. 3.2).

Depending on the properties of the medium the probabilities of each outcome change. In human tissue, scattering dominates and the highest percentage of photons are scattered to a different direction of propagation [2, 7].

Brain NIRS is particularly well suited to studies of neonates because their head sizes are small, and neonate skulls are thin. This allows for diffuse light transmission through the head where it is detected at the opposite side from the source position. Enough light scatters through the head without being absorbed so that the detected light is above the noise floor. For adults, the only way of using NIRS to study brain function is by detecting remitted light from a detector located a few centimeters away from the source position. This reflectance geometry remitted light is of sufficiently high intensity because of the high scattering properties of tissues in the head.

3.3 Instrumentation

NIRS system hardware is composed of three main components that provide illumination with NIR light, optical coupling of light with the subject, and detection of remitted light. These components are (1) a laser source coupled to optical fibers, (2) optical fibers connected to optical terminals that are positioned in contact with the tissue illuminating and collecting remitted light, (3) optical fibers connected to those terminals coupled to light detectors which measure incoming light. The source and detector optical terminals at the scalp surface are referred to as "optodes." Optodes vary depending on the use and are designed to maximize optical coupling with the head. Grid arrangements of sources and detectors are often used to measure larger areas and to produce tomographic images of the measurements. DOT uses optode grid arrangements to image the hemodynamic activity over areas of the brain. Head probes are sometimes used to fasten the optodes onto the surface of the head in order to increase positional accuracy across studies, and to improve stability and optical coupling. Different laser systems are used for brain imaging with NIRS but the most common is the semiconductor laser diode [5, 6]. Several light detectors have been used in NIRS systems, typically photomultiplier tubes (PMT) and photodiodes or avalanche photodiodes (APD) [5, 7].

3.3.1 Types of NIRS Systems

The different types of NIRS systems, continuous wave (CW), time resolved (TR), and frequency domain (FD) provide different information [7]. They also vary in cost, hardware setup, and application. CW-NIRS systems illuminate light at one constant intensity and detect it at another attenuated constant intensity. They commonly use laser diodes or light emitting diodes (LED) at discreet wavelengths as source, and photodiodes or APD for detectors [7]. In TR-NIRS, a very short duration pulse of light (on the order of picoseconds) is illuminated into the tissue. This pulse is detected as a broadened temporal point spread function (TPSF) with attenuated amplitude and longer decay. The tissue properties scattering coefficient and absorption coefficient can be computed from the shape of the TPSF [23]. These tissue properties are discussed in more detail in Sect. 3.5. TR-NIRS systems use semiconductor, dye, or solid state lasers for sources, and streak cameras, PMT, or APD for detectors [7]. Frequency domain NIRS illuminates the tissue with sinusoidally modulated intensity with an initial amplitude and phase. The detected signal is another sinusoid with attenuated intensity and a phase shift. Tissue scattering and absorption properties can be computed from the frequency and phase shift [2, 19, 31]. FD-NIRS systems commonly use laser diodes or LED for sources and PMT detectors [7]. CW systems tend to be less expensive and have faster sampling rates for calculated hemodynamics than TR and FD-NIRS.

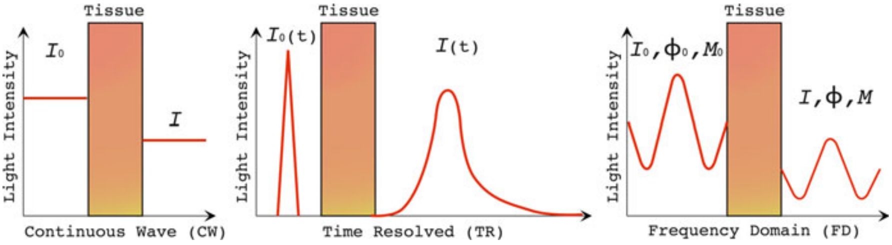

Fig. 3.3 Types of NIRS systems

CW-NIRS systems commonly use laser diodes for light illumination and photodiodes or APD for light detection (Fig. 3.3).

The mathematical models and analysis of the data obtained with these systems also vary. In TR spectroscopy optical properties can be obtained from the TPSF. This review focuses on the instrumentation and mathematical analysis behind CW-NIRS.

3.3.2 Laser Diodes

Laser diodes are semiconductor lasers that convert an applied electrical voltage into emitted light. A laser requires light production, amplification, and feedback. A forward bias voltage across a semiconductor produces carriers (electron-positive ion pairs) in an active region that recombine emitting photons. Feedback is provided by cleaved edges of the semiconductor material that act as mirrors because of the high index of refraction difference between the semiconductor and the air. The emitted photons are thus reflected back into an active region and amplified within the active region by stimulated emission, where an incoming photon excites a carrier which then recombines into another emitted photon, resulting in laser gain. The combination of these processes generates, amplifies, and emits light with high coherence, power, and efficiency. Laser diodes are very small and thus easy to use in systems that have size restrictions. Also, they can emit light at a wide range of wavelengths ($\sim$ 400 nm $\rightarrow \sim$ 2,500 nm) depending on the material and size [28].

3.3.3 Photodiodes

Photodiodes are semiconductor light detectors that convert incoming photons into an electrical current. When light enters the photodiode, a carrier is excited. A reverse bias voltage applied across the semiconductor drives the electron to an anode and the positive ion to a cathode, creating a photocurrent. The photocurrent is the electrical signal measured. Since there is a direct relationship between the incoming light and the measured photocurrent, quantitative measurements can be made with this device. Photodiodes can detect light with a large wavelength range of 180 to 2,600 nm [28]. Technological advances allows for the manufacturing of photodiodes to be cheap and mass-produced. They are very small light sensors that can be easily paired to fiber optics for light detection; their size makes them a desirable light detector for any device. Photodiodes have low sensitivity because they have no gain, so an external amplifier is generally needed to amplify the signal and this adds noise to the system reducing the SNR. However, they are very fast, so temporal resolution of the signal obtained is very high.

3.3.4 Avalanche Photodiodes

APD are a type of photodiode that has a large reverse bias voltage applied to it. The large electric field allows for signal amplification to be generated within the photodiode and have much higher quantum efficiency. Since signal is amplified within the device, they can be used in applications that require high sensitivity and can measure lower level light. APD can detect light of wavelengths of 300 to 1,600 nm, depending on the material used [14]; some have been manufactured to detect wavelengths of up to 4 μm [28].

3.3.5 Optode and Head Probe Design

Important design criteria for optode design are based on maximizing optical coupling between the optodes and the scalp, or minimizing the losses of light. Light is lost at the interface between the source optodes and the scalp for light delivery and again between the scalp and the detector optodes during collection of remitted light. Also, there might be interfaces within the optode, depending on its design. Optodes are often just the polished ends of the optical fibers, usually in a plastic encasing. Optical components such as lenses and prisms are used to improve the numerical aperture or to change the direction of light propagation from the optodes. Instead of prisms, fibers are bent to a 90° angle in some designs to obtain the same effect without adding another interface. In this case, the optode tends to be bigger as fibers have a limit on the radius of curvature. Some causes of reduced optical coupling include hair and natural oils that infiltrate between the optode and the scalp, reducing the effective detection area of the optode. Some designs address these issues by adding convex tips to the optodes or by shifting them down through the hair upon placement. For single NIRS measurements, or when only a few optodes are used, optodes can just be fastened to the head with headbands or caps. Stability during head movements is essential to acquire useful data. For larger coverage, multiple optodes are used. There are different solutions used by different groups, often using probes to hold the optodes in place [35, 41].

More complex head probes are sometimes used to fasten optodes onto the surface of the head. These can provide a repeatable way of positioning optodes in the head in a stable way, increasing positional accuracy and ease of use. Probes are often designed around the inter-optode distance desired and the dimensions of the optodes. Design considerations include getting through hair and in contact with the scalp effectively, holding optodes normal to the surface of the scalp in a stable way, applying pressure on optodes for effective coupling without injuring the subject, positioning the optodes accurately for clinical translation, among others. All of these considerations must be repeatable across subjects and done in an efficient way to minimize set up time. Probe design evaluation criteria include stability during head movement, head size and shape variability, ease of use, durability, and sometimes standardized positioning or low profile. In case of multimodal brain imaging, head probes must consider materials compatibility, particularly for the case of MRI or MEG.

3.4 Linear Analysis Methods for NIRS

NIRS measures light intensity at different locations in the scalp at different wavelengths. For the CW-NIRS case, a linear forward model may be used to analyze the data. This linear relationship is derived from the Beer–Lambert Law, which relates the input and output intensities with the length between source and detector, sample concentration, and extinction coefficient of the sample measured. Certain modifications need to be performed to this law in order to apply it to measurements in tissue to account for light scattering and geometric uncertainty. The MBLL accounts for scattering and geometric factors [18]. Chromophore concentration changes can be obtained from NIRS intensity measurements using MBLL.

3.4.1 Transmission Model

The Beer–Lambert Law is a mathematical model that approximates light absorption for the transmission model shown in Fig. 3.4. This model assumes dilute samples where light scattering effects can be ignored, regular geometry where the length of the sample is readily obtained, and simple sample geometry such that light travels coherently in a straight path. If the sample is a tissue rather than a dilute chemical, the optical properties produce a high degree of scattering and the transmission model and the mentioned assumptions no longer apply.

For a model of light transmitted through a sample without scattering, the Beer–Lambert Law is

$$I = I_o e^{-\mu_a L}, \tag{3.1}$$

Fig. 3.4 Light propagation through sample

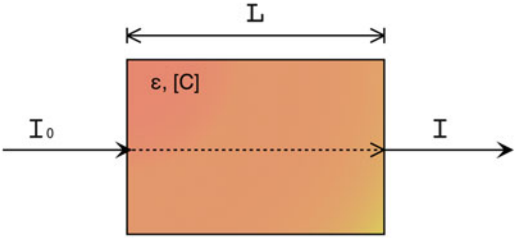

where I is the measured intensity, I_o is the input intensity, μ_a is the absorption coefficient, and L is the length of the sample as seen in Fig. 3.4, or the distance between input source and output detector. Using the definition of the absorption coefficient

$$\mu_a = ln(10)\varepsilon_\lambda[C], \tag{3.2}$$

the Beer–Lambert law can be rewritten as

$$\begin{aligned} I &= I_o e^{-ln(10)\varepsilon_\lambda[C]L} \\ I &= I_o 10^{-\varepsilon_\lambda[C]L}, \end{aligned} \tag{3.3}$$

where ε_λ is the molar extinction coefficient of the sample at wavelength λ, $[C]$ is the sample concentration. The base e in Eq. (3.1) is changed to base 10 in Eq. (3.3) because the values for ε_λ are usually tabulated in logarithms of base 10 [17, 39, 43].

3.4.2 Light Absorption

Light transmittance T and absorption A, also called optical density OD, are defined from the Beer–Lambert Law as

$$T = \frac{I}{I_o} \tag{3.4}$$

$$\begin{aligned} A = OD &= -\log_{10}(T) \\ &= \log_{10}\left(\frac{I_o}{I}\right) \\ OD &= \varepsilon_\lambda[C]L \end{aligned} \tag{3.5}$$

With Eq. (3.5), values for concentration can be calculated from measured input and output intensities, provided a value for extinction coefficient and length L of the given sample. For several chromophores and wavelengths, given known extinction coefficients, the absorption can be extended to

Fig. 3.5 Scattering light propagation through sample

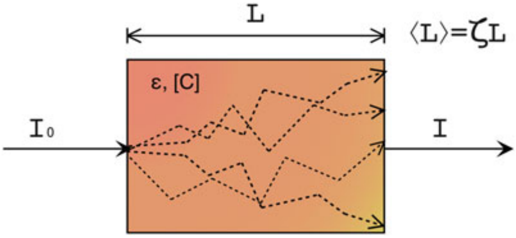

$$OD_\lambda = \sum_i \varepsilon_{i,\lambda}[C]_i L. \tag{3.6}$$

Calculating values of $[C]_i$ in this case requires solving a system of equations. For example, for three chromophore concentrations measured with three wavelengths, the equations are

$$\begin{aligned} OD_{\lambda_1} &= (\varepsilon_{1,\lambda_1}[C]_1 + \varepsilon_{2,\lambda_1}[C]_2 + \varepsilon_{3,\lambda_1}[C]_3)L \\ OD_{\lambda_2} &= (\varepsilon_{1,\lambda_2}[C]_1 + \varepsilon_{2,\lambda_2}[C]_2 + \varepsilon_{3,\lambda_2}[C]_3)L \\ OD_{\lambda_3} &= (\varepsilon_{1,\lambda_3}[C]_1 + \varepsilon_{2,\lambda_3}[C]_2 + \varepsilon_{3,\lambda_3}[C]_3)L\,. \end{aligned} \tag{3.7}$$

3.4.3 Modified Beer–Lambert Law

The Beer–Lambert Law must be modified to account for changes in light propagation through samples that have scattering. The changes take into consideration the extra length the light travels before being detected. As opposed to using the source-detector separation distance, it uses a mean optical path length. The Beer–Lambert law is thus changed to

$$OD_{\lambda_i} = \varepsilon_{\lambda_i}[C]\langle L\rangle + G, \tag{3.8}$$

where the mean optical path length is

$$\langle L\rangle = \zeta L, \tag{3.9}$$

L is the sample length and ζ is the differential pathlength factor. This length correction by ζ accounts for the increased travel distance of photons due to scattering as shown in Fig. 3.5.

This modification allows for the calculation of tissue concentration given measured input and output intensities, extinction coefficients, length of the sample, and the differential pathlength factor. However, this is an empirical model that requires an extra geometry-dependent scattering term G to account for losses due to scattering and more complex geometries encountered with in vivo measurments [8]. The resulting equation is known as the modified Beer-Lambert Law (MBLL).

3.4.4 Concentration Changes

Absolute estimates of concentration cannot be obtained without knowing the geometry-dependent term G. However, changes in concentration from a baseline condition are of primary interest in functional brain imaging and do not depend on G. For measurements at times t_1 and t_2, the extinction coefficient ε_λ, differential pathlength factor ζ, length L, and scattering term G remain approximately constant. Computing change in absorption removes the scattering term and yields change in concentration

$$\begin{aligned}\Delta OD_\lambda &= OD_{2,\lambda} - OD_{1,\lambda}\\ \Delta OD_\lambda &= \varepsilon_\lambda[C]_2\zeta L + G - \varepsilon_\lambda[C]_1\zeta L - G\\ \Delta OD_\lambda &= \varepsilon_\lambda([C]_2 - [C]_1)\zeta L\\ \Delta OD_\lambda &= \varepsilon_\lambda\Delta[C]\zeta L,\end{aligned} \tag{3.10}$$

where $\Delta\mathrm{OD}_\lambda$ is the change of absorption at wavelength λ and $\Delta[C]$ is the change in concentration from t_1 to t_2. This difference calculation yields concentration changes from a change in absorption and the remaining terms that were previously known. The change in absorption can be calculated with simple logarithm identities as

$$\begin{aligned}\Delta OD_\lambda &= OD_{2,\lambda} - OD_{1,\lambda}\\ \Delta OD_\lambda &= \log_{10}\left(\frac{I_o}{I_2}\right) - \log_{10}\left(\frac{I_o}{I_1}\right)\\ \Delta OD_\lambda &= \log_{10}\left(\frac{I_o}{I_2}\cdot\frac{I_1}{I_o}\right)\\ \Delta OD_\lambda &= -\log_{10}\left(\frac{I_2}{I_1}\right)\end{aligned} \tag{3.11}$$

where there is no need for an initial intensity value, and a change in concentration can readily be obtained from available measurements. A concentration change between any two times of measurement can be obtained by providing the measurements of the intensities at those times. This calculation also allows for continuous measurement of concentration change starting at any time point yielding the desired graphs of concentration change over time.

3.4.5 Brain Measurements with NIRS

For the case of cerebral NIRS, the MBLL accounts for scattering of light through the tissue. For this case, the measurements of interest are generally oxygenated hemoglobin (HbO_2), deoxygenated or reduced hemoglobin (HbR), and sometimes additionally cytochrome oxidase aa_3. Concentration changes for these chromophores obtained from, for example, a four-wavelength NIRS system use the model

$$\begin{aligned}\Delta OD_{\lambda_1} &= L\zeta_{\lambda_1}\left(\varepsilon_{HbO_2,\lambda_1}[C]_{HbO_2} + \varepsilon_{HbR,\lambda_1}[C]_{HbR} + \varepsilon_{aa_3,\lambda_1}[C]_{aa_3}\right)\\ \Delta OD_{\lambda_2} &= L\zeta_{\lambda_2}\left(\varepsilon_{HbO_2,\lambda_2}[C]_{HbO_2} + \varepsilon_{HbR,\lambda_2}[C]_{HbR} + \varepsilon_{aa_3,\lambda_2}[C]_{aa_3}\right)\\ \Delta OD_{\lambda_3} &= L\zeta_{\lambda_3}\left(\varepsilon_{HbO_2,\lambda_3}[C]_{HbO_2} + \varepsilon_{HbR,\lambda_3}[C]_{HbR} + \varepsilon_{aa_3,\lambda_3}[C]_{aa_3}\right)\\ \Delta OD_{\lambda_4} &= L\zeta_{\lambda_4}\left(\varepsilon_{HbO_2,\lambda_4}[C]_{HbO_2} + \varepsilon_{HbR,\lambda_4}[C]_{HbR} + \varepsilon_{aa_3,\lambda_4}[C]_{aa_3}\right)\end{aligned} \tag{3.12}$$

This can be written in matrix form as

$$\mathbf{\Delta OD} = \langle \mathbf{L} \rangle \mathbf{E} \Delta[\mathbf{C}], \tag{3.13}$$

where

$$\begin{aligned}\mathbf{\Delta OD} &= \begin{bmatrix}\Delta OD_{\lambda_1}\\ \Delta OD_{\lambda_2}\\ \Delta OD_{\lambda_3}\\ \Delta OD_{\lambda_4}\end{bmatrix}, \mathbf{E} = \begin{bmatrix}\varepsilon_{HbO_2,\lambda_1} & \varepsilon_{HbR,\lambda_1} & \varepsilon_{aa_3,\lambda_1}\\ \varepsilon_{HbO_2,\lambda_2} & \varepsilon_{HbR,\lambda_2} & \varepsilon_{aa_3,\lambda_2}\\ \varepsilon_{HbO_2,\lambda_3} & \varepsilon_{HbR,\lambda_3} & \varepsilon_{aa_3,\lambda_3}\\ \varepsilon_{HbO_2,\lambda_4} & \varepsilon_{HbR,\lambda_4} & \varepsilon_{aa_3,\lambda_4}\end{bmatrix},\\ \Delta[\mathbf{C}] &= \begin{bmatrix}\Delta[C]_{HbO_2}\\ \Delta[C]_{HbR}\\ \Delta[C]_{aa_3}\end{bmatrix}, \langle \mathbf{L} \rangle = \begin{bmatrix}L_{\lambda_1}\zeta_{\lambda_1} & 0 & 0 & 0\\ 0 & L_{\lambda_2}\zeta_{\lambda_2} & 0 & 0\\ 0 & 0 & L_{\lambda_3}\zeta_{\lambda_3} & 0\\ 0 & 0 & 0 & L_{\lambda_4}\zeta_{\lambda_4}\end{bmatrix}.\end{aligned} \tag{3.14}$$

This MBLL equation allows for mathematical calculations that can be performed in real-time during experimentation that give chromophore concentration changes relative to an initial reference measurement. Using the Moore–Penrose pseudoinverse, a least squares result of the chromophore concentration change can be obtained as

$$\Delta[\hat{\mathbf{C}}] = \left(\mathbf{F}\mathbf{F}^T\right)^{-1}\mathbf{F}^T\mathbf{\Delta OD}, \tag{3.15}$$

where

$$\mathbf{F} = \langle \mathbf{L} \rangle \mathbf{E}. \tag{3.16}$$

In the case of NIRS for brain function, L is no longer the thickness of the sample but the separation between source and detector, which is typically on the same side of the head in a reflectance geometry, as seen in Fig. 3.6.

Various methods are used to obtain numerical values for ζ depending on the experimental objectives and the level of accuracy desired. Experimentally

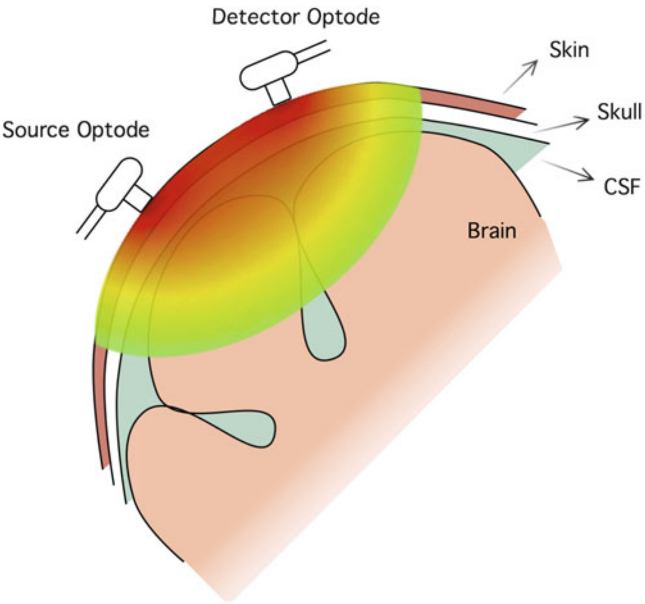

Fig. 3.6 Functional near-infrared spectroscopy

measured values for ζ have been made using TR and FD-NIRS, and those values are often used in CW-NIRS studies [10]. In many cases, ζ is assumed to be constant for all NIR wavelengths. Also, even though ζ varies over different regions of the head [42], some experimenters use a single value for measurements regardless of where on the head the source and detectors are placed, assuming that the underlying structure and tissue thicknesses are similar enough that the discrepancy does not affect the result significantly.

3.5 Diffusion Approximation to the RTE

There are also ways for obtaining the differential pathlength factor ζ that use simulation of the propagation of light in the tissue to determine ζ. A common method used is Monte Carlo (MC) simulation, where the paths taken by millions of photons are simulated in a three-dimensional head model to generate a model of the measurements [3]. MC simulations provide estimates of the differential pathlength factor that can be used in data analysis. This method is computationally intensive and is only as accurate as the anatomical model and tissue properties used. The anatomical models for MC are typically obtained from high-resolution magnetic resonance imaging (MRI) scans. Another method to obtain the differential pathlength factor is solving the RTE using approximations of the physics to simulate the propagation of light in the tissue. This approximate method can be more time-efficient than using MC simulation. This result yields a value for ζ that can be used in combination with the MBLL to obtain chromophore concentration changes from light intensity measurements.

The diffusion approximation to the RTE presented herein only applies to media that is highly scattering, such as most biological tissues in the head, and where scattering dominates over absorption. Also, it is assumed that scattering is only linearly anisotropic and that the rate of change of the radiance is much lower than the collision frequency [24]. The diffusion equation is the P_N approximation to the RTE with $N = 1$ [2]. For the case of CW-NIRS, a steady-state solution is assumed.

3.5.1 The Radiative Transport Equation

The RTE is an expression for conservation of radiance over a control volume,

$$\begin{aligned}\frac{1}{c_m}\cdot\frac{\partial L(r,t,\hat{s})}{\partial t}+\nabla\cdot\hat{s}L(r,t,\hat{s}) &= -\mu_t L(r,t,\hat{s})+\mu_s\int_{4\pi}L(r,t,\hat{s})f(\hat{s},\hat{s}')d\omega' \\ &\quad + S(r,t,\hat{s}),\end{aligned} \tag{3.17}$$

where $c_m\left[\frac{m}{s^2}\right]$ is the speed of light in the medium, and $L(r,t,\hat{s})[Wm^{-2}sr^{-1}]$ is the radiance in position r, at time t, and direction $\hat{s}$. The total attenuation coefficient $\mu_t[cm^{-1}]$ is

$$\mu_t = \mu_a + \mu_s, \tag{3.18}$$

where $\mu_a[cm^{-1}]$ is the absorption coefficient, and $\mu_s[cm^{-1}]$ is the scattering coefficient. The term $\frac{1}{cm}\cdot\frac{\partial L(r,t,\hat{s})}{\partial t}$ in the RTE is the rate of change of the radiance, or the difference of photons entering and leaving the volume; $\nabla\cdot\hat{s}L(r,t,\hat{s})$ is the flux of radiance out of a controlled volume; $-\mu_t L(r,t,\hat{s})$ accounts for the losses of radiance due to absorption and scattering; $\mu_s\int_{4\pi}L(r,t,\hat{s})f(\hat{s},\hat{s}')d\omega'$ accounts for corresponding radiance gains where $f(\hat{s},\hat{s}')$ is the normalized differential scattering phase function, or the probability that a photon traveling in direction $\hat{s}'$ will be scattered into direction $\hat{s}$; and $S(r,t,\hat{s})[Wm^{-3}sr^{-1}]$ is a source term that accounts for irradiance on the tissue or fluorescence within the tissue.

3.5.2 The Diffusion Equation Approximation

Using the definition of fluence rate $\Phi(r,t)[Wm^{-2}]$ and flux density $J(r,t)[Wm^{-2}]$, and assuming scattering is only linearly anisotropic, one can derive the diffusion equation as an approximation to the RTE. Fluence rate is defined as

$$\Phi(r,t) = \int_{4\pi} L(r,t,\hat{s})d\omega, \tag{3.19}$$

and flux density is defined as

$$J(r,t) = \int_{4\pi} L(r,t,\hat{s}) \cdot \hat{s}d\omega. \tag{3.20}$$

Conservation of energy is applied and the transport equation is first integrated for all solid angles $(\hat{s})$. Doing this for the first term yields

$$\begin{aligned}\int_{4\pi} \frac{1}{c_m} \cdot \frac{\partial L(r,t,\hat{s})}{\partial t} d\omega &= \frac{1}{c_m} \int_{4\pi} \frac{\partial L(r,t,\hat{s})}{\partial t} d\omega = \frac{1}{c_m} \frac{\partial}{\partial t} \left(\int_{4\pi} L(r,t,\hat{s})d\omega \right) \\ &= \frac{1}{c_m} \frac{\partial \Phi(r,t)}{\partial t}.\end{aligned} \tag{3.21}$$

For the second term this yields

$$\int_{4\pi} \nabla \cdot \hat{s}L(r,t,\hat{s})d\omega = \nabla \cdot \int_{4\pi} \hat{s}L(r,t,\hat{s})d\omega = \nabla \cdot J(r,t). \tag{3.22}$$

For the third term this yields

$$\int_{4\pi} -\mu_t L(r,t,\hat{s})d\omega = -\mu_t \int_{4\pi} L(r,t,\hat{s})d\omega = -\mu_t \Phi(r,t). \tag{3.23}$$

The integral term becomes

$$\begin{aligned}\int_{4\pi} \mu_s \int_{4\pi} L(r,t,\hat{s}) f(\hat{s},\hat{s}')d\omega' d\omega &= \mu_s \iint_{4\pi} L(r,t,\hat{s}) f(\hat{s},\hat{s}')d\omega' d\omega \\ &= \mu_s \int_{4\pi} L(r,t,\hat{s}) \left[\int_{4\pi} f(\hat{s},\hat{s}')d\omega' \right] d\omega \\ &= \mu_s \int_{4\pi} L(r,t,\hat{s})d\omega \\ &= \mu_s \Phi(r,t),\end{aligned} \tag{3.24}$$

where

$$\int_{4\pi} f(\hat{s},\hat{s}')d\omega' = 1, \tag{3.25}$$

given that the definition of the differential scattering function is normalized. Finally, the last term becomes

$$\int_{4\pi} S(r,t,\hat{s})d\omega = S_o(r,t). \tag{3.26}$$

Combining all these results yields

$$\frac{1}{c_m}\frac{\partial \Phi(r,t)}{\partial t} + \nabla \cdot J(r,t) = -\mu_t \Phi(r,t) + \mu_s \Phi(r,t) + S_o(r,t). \tag{3.27}$$

Fick's law states that the flux of a quantity is proportional to its concentration gradient [16, 23]. Applying this to fluence rate, Fick's law states that photon power results from the gradient of fluence rate

$$J(r,t) = -D'\nabla\Phi(r,t), \tag{3.28}$$

where D' is the photon diffusion coefficient or diffusion factor. Using Fick's law in the result obtained above at steady state produces

$$\begin{gathered}\frac{1}{c_m}\frac{\partial \Phi(r,t)}{\partial t} + \nabla \cdot J(r,t) = -\mu_t \Phi(r,t) + \mu_s \Phi(r,t) + S_o(r,t),\\ \frac{\partial \Phi(r,t)}{\partial t} = 0,\\ -D'\nabla^2\Phi(r,t) = -\mu_t \Phi(r,t) + \mu_s \Phi(r,t) + S_o(r,t)\end{gathered} \tag{3.29}$$

Combining the fluence rate using the definition of total attenuation coefficient $\mu_t = \mu_a + \mu_s$ yields the steady-state diffusion equation for fluence rate.

$$-D'\nabla^2\Phi(r,t) = -\mu_a \Phi(r,t) + S_o(r,t). \tag{3.30}$$

This derivation shows that the transport equation can be approximated by the steady-state diffusion equation subject to assumptions that the process is dominated by linearly anisotropic scattering. The diffusion equation can be solved analytically for simple geometries or using finite element or finite difference analysis for more complex tissue geometries. Experimentally obtained values for the absorption coefficient and diffusion coefficient can be used for the calculations. Using this model has been found to reasonably approximate light-tissue interaction everywhere in the head except for in the cerebrospinal fluid (CSF), where scattering is less dominant [21].

3.5.3 The Diffusion Coefficient

Fick's Law in Eq. (3.28) uses the diffusion coefficient D' as a proportionality constant. To determine the diffusion coefficient, a derivation from the RTE must be performed once again. In this case, the RTE is first multiplied by the direction vector $\hat{s}$ and then integrated over all solid angles. As done for the previous derivation, the definitions for fluence rate and flux density are used and the term by term solution is provided. Again, the RTE is

$$\begin{aligned}\frac{1}{c_m}\cdot\frac{\partial L(r,t,\hat{s})}{\partial t}+\nabla\cdot\hat{s}L(r,t,\hat{s})=-\mu_t L(r,t,\hat{s})+\mu_s\int_{4\pi}L(r,t,\hat{s})f(\hat{s},\hat{s}')d\omega'\\+S(r,t,\hat{s}).\end{aligned}\tag{3.31}$$

For the first term, the multiplication and integration produce

$$\begin{aligned}\int_{4\pi}\frac{\hat{s}}{c_m}\cdot\frac{\partial L(r,t,\hat{s})}{\partial t}d\omega&=\frac{1}{c_m}\int_{4\pi}\hat{s}\frac{\partial L(r,t,\hat{s})}{\partial t}d\omega\\&=\frac{1}{c_m}\frac{\partial}{\partial t}\left(\int_{4\pi}\hat{s}L(r,t,\hat{s})d\omega\right)=\frac{1}{c_m}\frac{\partial J(r,t)}{\partial t}.\end{aligned}\tag{3.32}$$

For the second term the identities

$$\left.\begin{aligned}\int_{4\pi}\hat{s}(\hat{s}\cdot A)d\omega=\frac{4\pi}{3}A\\\int_{4\pi}\hat{s}[\hat{s}\cdot\nabla(A\cdot\hat{s})]d\omega=0\end{aligned}\right\}\text{ for any vector }A,\tag{3.33}$$

are needed. Also, the Legendre polynomial expansion

$$\begin{aligned}L(r,t,\hat{s})&=\frac{1}{4\pi}\int_{4\pi}L(r,t,\hat{s})d\omega+\frac{3}{4\pi}\int_{4\pi}L(r,t,\hat{s}')\hat{s}'\hat{s}d\omega'\\L(r,t,\hat{s})&=\frac{1}{4\pi}\Phi(r,t)+\frac{3}{4\pi}J(r,t)\hat{s}\end{aligned}\tag{3.34}$$

can be used assuming that scattering is only linearly anisotropic. Applying the identities and polynomial expansion to solve the multiplication and integration of the second term yields

$$\begin{aligned}\int_{4\pi}\hat{s}\nabla\cdot\hat{s}L(r,t,\hat{s})d\omega&=\int_{4\pi}\hat{s}[\hat{s}\cdot\nabla L(r,t,\hat{s})]d\omega\\&=\frac{1}{4\pi}\int_{4\pi}\hat{s}[\hat{s}\cdot\nabla\Phi(r,t)]d\omega+\frac{3}{4\pi}\int_{4\pi}\hat{s}[\hat{s}\cdot\nabla J(r,t)\hat{s}]d\omega\\&=\frac{1}{4\pi}\left[\frac{4\pi}{3}\nabla\Phi(r,t)\right]\\&=\frac{1}{3}\nabla\Phi(r,t).\end{aligned}\tag{3.35}$$

For the third term this yields

$$\int_{4\pi} -\mu_t \hat{s} L(r,t,\hat{s}) d\omega = -\mu_t \int_{4\pi} \hat{s} L(r,t,\hat{s}) d\omega = -\mu_t J(r,t). \tag{3.36}$$

The integral term becomes

$$\begin{aligned}\int_{4\pi} \mu_s \hat{s} \int_{4\pi} L(r,t,\hat{s}) f(\hat{s},\hat{s}') d\omega' d\omega &= \mu_s \iint_{4\pi} \hat{s} L(r,t,\hat{s}) f(\hat{s},\hat{s}') d\omega' d\omega \\ &= \mu_s \int_{4\pi} \hat{s} L(r,t,\hat{s}) \left[\int_{4\pi} f(\hat{s},\hat{s}') d\omega' \right] d\omega \\ &= \mu_s g \int_{4\pi} \hat{s} L(r,t,\hat{s}) d\omega \\ &= \mu_s g J(r,t),\end{aligned} \tag{3.37}$$

given that

$$\int_{4\pi} f(\hat{s},\hat{s}') d\omega' = g, \tag{3.38}$$

where g is the average cosine of the scattering angle or the anisotropic factor, which will be discussed in Sect. 3.5.4. Finally, the source term integrates to a flux source term that can be neglected away from the source location. Combining all these results yields

$$\frac{1}{c_m} \frac{\partial J(r,t)}{\partial t} + \frac{1}{3} \nabla \Phi(r,t) = -\mu_t J(r,t) + \mu_s g J(r,t). \tag{3.39}$$

The reduced scattering coefficient is defined as

$$\mu_s' \equiv (1-g)\mu_s, \tag{3.40}$$

where the scattering coefficient is reduced by the amount that light traveling in other directions is scattered back toward direction $\hat{s}$, described by the anisotropic factor g. Similarly, the reduced total attenuation coefficient is defined as

$$\mu_{tr} \equiv \mu_a + \mu_s'. \tag{3.41}$$

Using these definitions and the definition of total attenuation coefficient μ_t, Eq. (3.39) simplifies to

$$\begin{aligned}\frac{1}{c_m}\frac{\partial J(r,t)}{\partial t}+\frac{1}{3}\nabla\Phi(r,t) &= -(\mu_t-\mu_s g)J(r,t)\\ &= -(\mu_a+\mu_s-\mu_s g)J(r,t)\\ &= -(\mu_a+(1-g)\mu_s)J(r,t)\\ &= -(\mu_a+\mu_s')J(r,t)\\ &= -\mu_{tr}J(r,t)\end{aligned} \tag{3.42}$$

Due to the highly scattering nature of light transport in biological tissue, it can be assumed that the rate of change of the radiance is much lower than the collision frequency [24]:

$$\frac{dL(r,t,\hat{s})}{dt}=0. \tag{3.43}$$

This assumption implies that the diffusion coefficient remains constant in time and can be calculated in steady state. In steady state the solution becomes

$$\begin{aligned}\frac{1}{c_m}\frac{\partial J(r,t)}{\partial t}+\frac{1}{3}\nabla\Phi(r,t) &= -\mu_{tr}J(r,t)\\ \frac{1}{3}\nabla\Phi(r,t) &= -\mu_{tr}J(r,t), \frac{\partial J(r,t)}{\partial t}=0.\end{aligned} \tag{3.44}$$

Solving for the flux density yields

$$J(r,t)=-\frac{1}{3\mu_{tr}}\nabla\Phi(r,t) \tag{3.45}$$

which has the form of Fick's law for fluence rate as defined in Eq. (3.28). The diffusion coefficient can be obtained by comparison as

$$D'=\frac{1}{3\mu_{tr}}. \tag{3.46}$$

3.5.4 Scattering Phase Function

The scattering phase function $f(\hat{s},\hat{s}')$ is the probability that a photon traveling in direction $\hat{s}'$ will be scattered into direction $\hat{s}$. The anisotropic factor g is the average cosine of the scattering angle. This factor is useful to describe the distribution of scattering in a medium because it provides a way to quantify the amount of scattering in each direction with one term. For instance, $g = 1$ refers to forward scatter, $g = 0$ refers to isotropic scatter, and $g = -1$ refers to backscatter [27]. The Henyey–Greenstein phase function

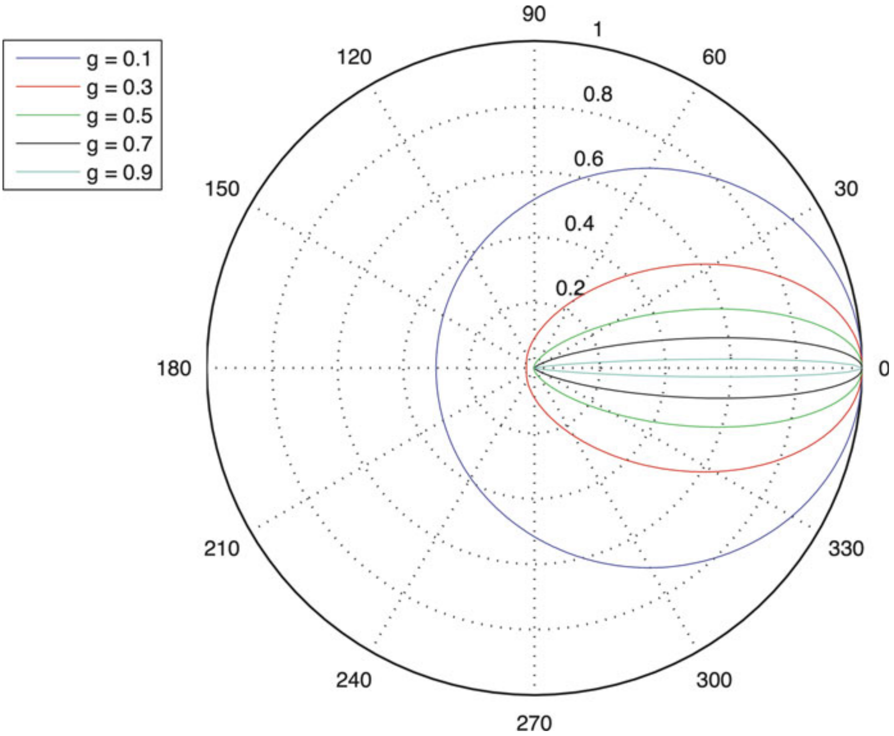

Fig. 3.7 Henyey–Greenstein phase function

$$p_{HG} = \frac{1 - g^2}{(1 + g^2 - 2g\cos\theta)^{\frac{3}{2}}} \tag{3.47}$$

is related to the anisotropy coefficient g and is often used as it depends only on the value of the angle and closely describes the linearly anisotropic diffusion of light in tissue. Figure 3.7 shows the normalized probability distribution p_{HG} for several values of g.

The attenuation seen in the intensity of light in the medium as it propagates through depends not only on absorption but also on scattering. The contribution to attenuation due to scattering is quantified in the ratio of attenuation due to scattering and the total attenuation

$$\Lambda = \frac{\mu_s}{\mu_s + \mu_a} \tag{3.48}$$

and is called the albedo [27].

3.5.5 Boundary Conditions and Source Term Modeling

The diffusion approximation to the RTE is valid provided that light scattering is isotropic or linearly anisotropic. This is not the case at the boundaries, where light changes suddenly from linearly anisotropic scattering inside the tissue to non-scattering outside. Since the measurements are made in the tissue boundaries, appropriate boundary conditions must be added to the model so that calculations are accurate. First, the flux into tissue is given by input intensity. Also, given that measurements are made at the surface of the head and that as photons move deeper into the head the likelihood of them being absorbed rather than scattered increases, it can be assumed that the fluence rate approaches zero at large depths. Since air is a non-scattering medium, light does not reflect back into tissue once it exits. So, fluence can be assumed to be zero anywhere outside the model. Finally, there is some Fresnel reflection of light back into tissue at the boundary. This light is effectively the same as if there was light incident from the outside and can be considered as an additional source term [15].

Light exiting a laser source and entering the tissue is coherent and collimated. This means that the illuminated light is mainly composed of ballistic photons, or photons traveling in a straight path. The highly scattering medium they encounter as they enter the tissue changes this property and, approximately one scattering event in length deep, photons start diffusing through tissue. At this point, light scattering is approximately linearly anisotropic and the model assumptions hold. So, photons can be modeled as traveling in a ballistic manner for a small depth until the diffusion model applies. To compute this, the input sources and detectors are placed $\frac{1}{\mu_s'}$ deep into the tissue in the model [30].

3.6 Modeling the Optical Pathlength

With the diffusion coefficient calculated it is then possible to compute solutions to the diffusion equation to obtain a map of steady-state fluence rate in tissue. The final steady-state diffusion equation is

$$-\frac{1}{3\mu_{tr}}\nabla^2\Phi(r,t) = -\mu_a\Phi(r,t) + S_o(r,t). \tag{3.49}$$

It must be noted that time-variation in the diffusion coefficient, meaning changes in the absorption coefficient or the reduced scattering coefficient, will violate the assumptions made in order to approximate the RTE with the diffusion equation. Computation of the diffusion equation can be performed using the solution above using experimentally obtained coefficients and approximating the source term to be the value of illuminated irradiance onto the tissue in the source locations and zero everywhere else. In this way a distribution of fluence rate in tissue can be calculated as shown in Fig. 3.8.

A similar calculation is performed with Eq. (3.49) to obtain a fluence rate distribution for a source if it was located at the detector position. This detector-as-source calculation is used to represent the path distribution of photons that are remitted from the tissue at the detector. The fluence rate distributions from the source and detector are then multiplied to obtain a spatial sensitivity function (Fig. 3.9) for NIRS/DOT following the Rytov approximation as discussed in Sect. 3.6.3.

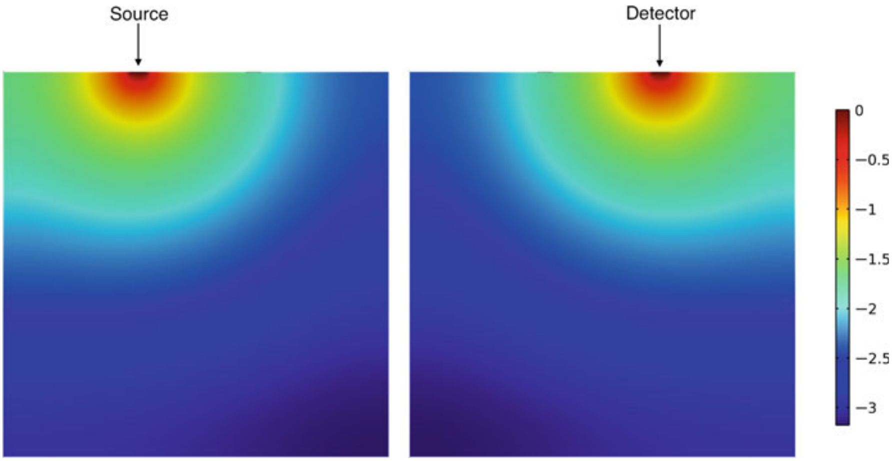

Fig. 3.8 Cross-sectional views of the normalized photon fluence rate distribution on a $\log_{10}$ scale from a single continuous-wave laser source illuminating a slab of homogeneous tissue (*left*) and a source located at the detector position (*right*). These solutions were simulated using the diffusion approximation to the radiative transport equation

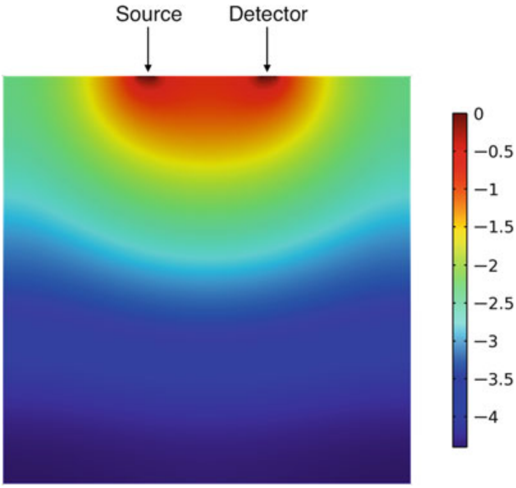

Fig. 3.9 Sensitivity function for NIRS/DOT on a $\log_{10}$ scale showing the spatial distribution of photon paths that originate at the source position and are remitted from the tissue to the detector position. Normalized using the Rytov approximation

3.6.1 Mean Optical Pathlength for NIRS

Connecting MBLL with the diffusion equation requires the establishment of a relationship between the mean optical pathlength $\langle L \rangle$ and fluence rate Φ. The mean optical path length $\langle L \rangle = \zeta L$ from equations (3.9)–(3.11) is defined as

$$\langle L\rangle = \frac{\Delta OD_\lambda}{\varepsilon_\lambda \Delta[C]} = -\frac{\log_{10}\left(\frac{I_2(r_d)}{I_1(r_d)}\right)}{\varepsilon_\lambda \Delta[C]} \tag{3.50}$$

or

$$\langle L\rangle = \frac{\Delta OD_\lambda}{ln(10)\Delta\mu_a} = -\frac{ln\left(\frac{I_2(r_d)}{I_1(r_d)}\right)}{\Delta\mu_a}, \tag{3.51}$$

where r_d is the detector position. When expressed in this way, $\langle L\rangle$ can be viewed as the sensitivity of the ΔOD measurements to absorption or concentration changes in the tissue. This can be calculated by solving equation (3.49) for two slightly different values of μ_a and then evaluating the ratio of the fluence rate at the detector, which will equal the intensity ratio

$$\frac{\Phi_{s,2}(r_d)}{\Phi_{s,1}(r_d)} = \frac{I_2(r_d)}{I_1(r_d)}. \tag{3.52}$$

This requires assuming the baseline values of μ_a, μ_s, and g and provides the final term required to be able to solve the MBLL in Eq. (3.9) or (3.15) from given measurement data. Given ζ, the solution to the diffusion equation presented above, the necessary components for solving the MBLL are the source-detector separation and the measured intensities at different times. This is a straightforward way of obtaining chromophore concentration changes from intensity measurements.

3.6.2 Modeling the Partial Optical Pathlength for DOT

Brain imaging with DOT requires that the mean optical pathlength can be extended to the concept of a partial optical pathlength $\langle L_V\rangle$ that indicates the sensitivity of ΔOD_λ to changes in chromophore concentration in a volume V in the tissue

$$\langle L_V\rangle = \frac{\partial OD_\lambda}{\varepsilon_\lambda \partial[C]_V}, \tag{3.53}$$

or

$$\langle L_V\rangle = \frac{\partial OD_\lambda}{ln(10)\partial\mu_{a,V}}. \tag{3.54}$$

The spatial distribution of $\langle L_V(r)\rangle$ at position r is proportional to the fluence rate distribution from the diffusion approximation subject to the Rytov approximation [11]

$$\langle L_V(r)\rangle = \alpha \frac{\Phi_s(r)\Phi_d(r)}{\Phi_s(r_d)} dV, \tag{3.55}$$

where α is the constant of proportionality, *r* is the location of the volume region *V*, the subscript s is for the source fluence function, and d is for the detector fluence function. The proportionality is resolved by equating the integral of the Rytov approximation with the mean optical pathlength

$$\langle L\rangle = \alpha \int_V \frac{\Phi_s(r)\Phi_d(r)}{\Phi_s(r_d)} dV(r). \tag{3.56}$$

The relation between $\langle L\rangle$, $\Delta\mu_a$, and ΔOD_λ in Eq. (3.51) used to replace $\langle L\rangle$ resolves the constant of proportionality

$$\alpha \int_V \frac{\Phi_s(r)\Phi_d(r)}{\Phi_s(r_d)} dV(r) = -\frac{ln\left(\frac{I_2(r_d)}{I_1(r_d)}\right)}{\Delta\mu_a},$$

$$\alpha = -\frac{ln\left(\frac{I_2(r_d)}{I_1(r_d)}\right)}{\Delta\mu_a \int_V \frac{\Phi_s(r)\Phi_d(r)}{\Phi_s(r_d)} dV(r)}. \tag{3.57}$$

The partial optical pathlength is obtained by substituting equation (3.57) into Eq. (3.55).

3.6.3 Linear Forward Model for DOT

The partial pathlength form of the matrix MBLL in Eq. (3.13) is the volume integral over the tissue sample

$$\Delta OD = \int_V \langle L_V\rangle\, E\Delta[C]_V. \tag{3.58}$$

For a sample that is discretized into *N* voxels of volume V_n, the integral becomes the sum

$$\Delta OD = \sum\nolimits_{n=1}^{N} \langle L_n\rangle\, E\Delta[C_n], \tag{3.59}$$

where $\langle L_n\rangle$ is the partial optical pathlength in the *n*th voxel

$$\langle L_n\rangle = \int_{V_n} \langle L_V\rangle. \tag{3.60}$$

A matrix form linear forward model for DOT can now be formulated. Suppose there are N_i chromophores indexed by i, and N_j source-detector optode measurement pairs, indexed by j, that contain the N_k wavelengths, indexed by k. The ΔOD measurement for the jth source-detector pair of the kth wavelength is modeled as

$$\Delta OD_{j,k} = \sum\nolimits_{n=1}^{N} \sum\nolimits_{i=1}^{N_i} \langle L_{n,j,k} \rangle E_{k,i} \Delta[C_{n,i}]. \tag{3.61}$$

Equation (3.61) can be expressed in matrix form as a linear system of equations similar to Eq. (3.13) where **F** is the DOT forward model

$$\mathbf{\Delta OD} = \mathbf{F} \Delta [\mathbf{C}], \tag{3.62}$$

where, for example with $N_j = 4$ source-detector pairs, $N_k = 2$ wavelengths, $N_i = 2$ chromophores, and $N = 4$ voxels

$$\mathbf{\Delta OD}_{(j,k)} = \begin{bmatrix} \Delta OD_{1,1} \\ \Delta OD_{1,2} \\ \Delta OD_{2,1} \\ \Delta OD_{2,2} \\ \Delta OD_{3,1} \\ \Delta OD_{3,2} \\ \Delta OD_{4,1} \\ \Delta OD_{4,2} \end{bmatrix}, \Delta[\mathbf{C}_{(n,i)}] = \begin{bmatrix} \Delta[C_{1,1}] \\ \Delta[C_{2,1}] \\ \Delta[C_{3,1}] \\ \Delta[C_{4,1}] \\ \Delta[C_{1,2}] \\ \Delta[C_{2,2}] \\ \Delta[C_{3,2}] \\ \Delta[C_{4,2}] \end{bmatrix}, \tag{3.63}$$

$$\mathbf{F}_{(n,j,k)(k,i)} = \begin{bmatrix} \langle L_{1,1,1} \rangle E_{1,1} & \langle L_{2,1,1} \rangle E_{1,1} & \langle L_{3,1,1} \rangle E_{1,1} & \langle L_{4,1,1} \rangle E_{1,1} & \langle L_{1,1,1} \rangle E_{1,2} & \langle L_{2,1,1} \rangle E_{1,2} & \langle L_{3,1,1} \rangle E_{1,2} & \langle L_{4,1,1} \rangle E_{1,2} \\ \langle L_{1,1,2} \rangle E_{2,1} & \langle L_{2,1,2} \rangle E_{2,1} & \langle L_{3,1,2} \rangle E_{2,1} & \langle L_{4,1,2} \rangle E_{2,1} & \langle L_{1,1,2} \rangle E_{2,2} & \langle L_{2,1,2} \rangle E_{2,2} & \langle L_{3,1,2} \rangle E_{2,2} & \langle L_{4,1,2} \rangle E_{2,2} \\ \langle L_{1,2,1} \rangle E_{1,1} & \langle L_{2,2,1} \rangle E_{1,1} & \langle L_{3,2,1} \rangle E_{1,1} & \langle L_{4,2,1} \rangle E_{1,1} & \langle L_{1,2,1} \rangle E_{1,2} & \langle L_{2,2,1} \rangle E_{1,2} & \langle L_{3,2,1} \rangle E_{1,2} & \langle L_{4,2,1} \rangle E_{1,2} \\ \langle L_{1,2,2} \rangle E_{2,1} & \langle L_{2,2,2} \rangle E_{2,1} & \langle L_{3,2,2} \rangle E_{2,1} & \langle L_{4,2,2} \rangle E_{2,1} & \langle L_{1,2,2} \rangle E_{2,2} & \langle L_{2,2,2} \rangle E_{2,2} & \langle L_{3,2,2} \rangle E_{2,2} & \langle L_{4,2,2} \rangle E_{2,2} \\ \langle L_{1,3,1} \rangle E_{1,1} & \langle L_{2,3,1} \rangle E_{1,1} & \langle L_{3,3,1} \rangle E_{1,1} & \langle L_{4,3,1} \rangle E_{1,1} & \langle L_{1,3,1} \rangle E_{1,2} & \langle L_{2,3,1} \rangle E_{1,2} & \langle L_{3,3,1} \rangle E_{1,2} & \langle L_{4,3,1} \rangle E_{1,2} \\ \langle L_{1,3,2} \rangle E_{2,1} & \langle L_{2,3,2} \rangle E_{2,1} & \langle L_{3,3,2} \rangle E_{2,1} & \langle L_{4,3,2} \rangle E_{2,1} & \langle L_{1,3,2} \rangle E_{2,2} & \langle L_{2,3,2} \rangle E_{2,2} & \langle L_{3,3,2} \rangle E_{2,2} & \langle L_{4,3,2} \rangle E_{2,2} \\ \langle L_{1,4,1} \rangle E_{1,1} & \langle L_{2,4,1} \rangle E_{1,1} & \langle L_{3,4,1} \rangle E_{1,1} & \langle L_{4,4,1} \rangle E_{1,1} & \langle L_{1,4,1} \rangle E_{1,2} & \langle L_{2,4,1} \rangle E_{1,2} & \langle L_{3,4,1} \rangle E_{1,2} & \langle L_{4,4,1} \rangle E_{1,2} \\ \langle L_{1,4,2} \rangle E_{2,1} & \langle L_{2,4,2} \rangle E_{2,1} & \langle L_{3,4,2} \rangle E_{2,1} & \langle L_{4,4,2} \rangle E_{2,1} & \langle L_{1,4,2} \rangle E_{2,2} & \langle L_{2,4,2} \rangle E_{2,2} & \langle L_{3,4,2} \rangle E_{2,2} & \langle L_{4,4,2} \rangle E_{2,2} \end{bmatrix}.$$

In this example **F** is a full rank square matrix, so Eq. (3.62) will be well posed with an explicit inverse solution

$$\Delta[\hat{\mathbf{C}}] = \mathbf{F}^{-1} \mathbf{\Delta OD}. \tag{3.64}$$

Often with DOT, the number of unknown chromophore concentrations in voxels Δ[**C**] exceeds the number of observed source-detector pairs and wavelengths **ΔOD**, making the DOT forward model ill-posed. In this case, regularization of the system of equations is required, such as with the Moore–Penrose pseudoinverse, Tikhonov regularization, truncated singular valued decomposition, or another method from the rich field of inverse problems [1]. In DOT sometimes a cortical constraint is applied in the reconstruction, or prior information about the activated region may be combined as a statistical prior such as with Bayesian methods [13].

3.7 Sources of Uncertainty in NIRS and DOT

Besides taking into account assumptions in the model, there are other aspects that could be potential sources of error in the calculations, model, or results, and must be taken into consideration [22]. This is particularly necessary on systems and devices that measure physiological information, such as NIRS, because of the degree of accuracy they require if used medically and because of the amount of variability that human subjects introduce. These sources of uncertainty can be arranged in three main groups: errors due to model error, due to instrumentation, and due to background physiology.

In NIRS, sources of error arising from the model include inaccuracies in tissue size and structure, the method of determination of the differential pathlength, and the assumptions made on the propagation of light through the medium. As mentioned in Sects. 3.4 and 3.5, there are several assumptions made to obtain a value for the differential pathlength factor and different methods to obtain it, depending on the level of accuracy desired. For each method of differential pathlength factor calculation there is a different error introduced, which must be considered during analysis and conclusions drawn from the measurements. Also, the differential pathlength factor has a wavelength dependance and varies with tissue type and structure [29]. So, the accuracy of the results will depend on whether all these variables are taken into account. As mentioned before, scattering is assumed to be linearly anisotropic and the diffusion coefficient is assumed constant. These are approximations, so the results obtained will not be exact.

For NIRS systems in general, a significant source of error can be the choice of wavelength. If the wavelengths are chosen at values where chromophore absorption is high for one wavelength and low for another, then the concentration estimates will be subject to partial volume and cross-talk [36]. Furthermore, the MBLL can be used to calculate concentration for several tissues given the extinction coefficients. In NIRS calculations, it is used for homogeneous changes in oxygenated, deoxygenated hemoglobin, and sometimes for cytochrome aa_3. Even though these are the dominant absorbers, there are other chromophores such as water and lipids present in tissue that contribute to attenuation. The attenuation that other absorbers introduce and the amount of absorbers present is assumed constant relative to changes in hemoglobin, and so the error is less prominent when analyzing changes in concentrations rather than absolute quantities. Other issues are that absorption changes are usually not homogeneous, leading to partial volume errors, and scattering losses are not constant, leading to cross-talk errors [18]. Also, since DOT involves simultaneous multichannel testing with often more than 100 channels, there is a risk of Type I false discovery error [32].

The experimental set up must also be accounted for during analysis. The source-detector separation is integral in the calculations and must be measured accurately. Also, the optical coupling between optodes and scalp needs to be maximized in order for all the light to be illuminated into tissue without any losses to air. Sources of error or causes for attenuation in the light illuminated or detected can be produced by issues with optical coupling. Optodes are designed in order to maximize optical coupling, as discussed in Sect. 3.3. Issues with getting through hair and in contact with the scalp, holding optodes normal to the head, positioning the optodes accurately, optode instability during head movement [26], and repeatability across head size and shape variability, can introduce errors in the results.

Physiological signals and processes are confounding factors in the measurements obtained and have to be considered. Particularly in NIRS, physiological processes that change the hemodynamic activity in the body will influence the measurements. Physiological noise is any signal measured that is not part of the desired results. Physiological processes that could be sources of noise include blood pressure oscillations, pulse, respiration, superficial tissue layer hemodynamics, and spontaneous neural activity [9].

3.8 Conclusion

In summary, the MBLL provides a measure of cerebral chromophore concentration, oxygenation, and volume changes, given CW-NIRS measurements of light intensity from the surface of the head. Simulations using the diffusion approximation to the RTE allow for the calculations of optical properties required by the MBLL. DOT images can be created by expanding the individual NIRS measurements to multiple measurements throughout the head in combination with appropriate inverse problem solutions.

References

1. Arridge SR (1999) Optical tomography in medical imaging. Inverse Probl 15(2):R41–R93
2. Arridge SR, Cope M, Delpy DT (1992) The theoretical basis for the determination of optical pathlengths in tissue: temporal and frequency analysis. Phys Med Biol 37(7):1531–1560
3. Boas DA, Culver JP, Stott J, Dunn A (2002) Three dimensional Monte Carlo code for photon migration through complex heterogeneous media including the adult human head. Opt Express 10(3):159–170
4. Boas DA, Gaudette T, Strangman G, Cheng X, Marota JJ, Mandeville JB (2001) The accuracy of near infrared spectroscopy and imaging during focal changes in cerebral hemodynamics. NeuroImage 13(1):76–90
5. Cope M, Delpy DT (1988) System for long-term measurement of cerebral blood and tissue oxygenation on newborn infants by near infra-red transillumination. Med Biol Eng 26:289–294
6. Cope M, Delpy DT, Reynolds EOR, Wray S, Wyatt JS, van der Zee P, Methods of quantitating cerebral near infrared spectroscopy data. Adv Exp Med Biol 222:183–189
7. Delpy DT (1997) Quantification in tissue near-infrared spectroscopy. itPhilos Trans R Soc B Biol Sci 352(1354):649–659
8. Delpy DT, Cope M, van der Zee P, Arridge SR, Wray S, Wyatt JS (1988) Estimation of optical pathlength through tissue from direct time of flight measurement. Phys Med Biol 33(12):1433–1442

9. Diamond SG, Huppert TJ, Kolehmainen V, Franceschini MA, Kaipio JP, Arridge SR, Boas DA (2006) Dynamic physiological modeling for functional diffuse optical tomography. NeuroImage 30(1):88–101
10. Duncan A, Meek JH, Clemence M, Elwell CE, Tyszczuk L, Cope M, Delpy DT (1995) Optical pathlength measurements on adult head, calf and forearm and the head of the newborn infant using phase resolved optical spectroscopy. Phys Med Biol 40(2):295–304
11. Gibson AP, Hebden JC, Arridge SR (2005) Recent advances in diffuse optical imaging. Phys Med Biol 50(4):R1–R43
12. Girouard H, Iadecola C (2006) Neurovascular coupling in the normal brain and in hypertension, stroke, and Alzheimer disease. J Appl Phys (Bethesda, MD: 1985) 100(1):328–335
13. Guven M, Yazici B, Intes X, Chance B (2005) Diffuse optical tomography with a priori anatomical information. Phys Med Biol 50(12):2837–2858
14. Renker D, Lorenz E (2009) Advances in solid state photon detectors. J Inst 4(4):P04004
15. Haskell RC, Svaasand LO, Tsay TT, Feng TC, McAdams MS, Tromberg BJ (1994) Boundary conditions for the diffusion equation in radiative transfer. J Opt Soc Am A Opt Image Sci Vis 11(10):2727–2741
16. Kety SS, Schmidt CF (1947) The nitrous oxide method for the quantitative determination of cerebral blood flow in man: theory, procedure and normal values. J Clin Investig 27(4):476–483
17. Kim JG, Xia M, Liu H (2005) Engineering in genomics. IEEE Eng Med Biol 2–5
18. Kocsis L, Herman P, Eke A (2006) The modified Beer-Lambert law revisited. Phys Med Biol 51(5):N91–N98
19. Lakowicz JR, Berndt K (1990) Frequency-domain measurements of photon migration in tissues. Chem Phys Lett 166(3):246–252
20. Leff DR, Orihuela-Espina F, Elwell CE, Athanasiou T, Delpy DT, Darzi AW, Yang G-Z (2011) Assessment of the cerebral cortex during motor task behaviours in adults: a systematic review of functional near infrared spectroscopy (fNIRS) studies. NeuroImage 54(4):2922–2936
21. Okada E, Delpy DT (2003) Near-infrared light propagation in an adult head model. I. Modeling of low-level scattering in the cerebrospinal fluid layer. Appl Opt 42(16):2906–2914
22. Orihuela-Espina F, Leff DR, James DRC, Darzi AW, Yang G-Z (2010) Quality control and assurance in functional near infrared spectroscopy (fNIRS) experimentation. Phys Med Biol 55(13):3701–3724
23. Patterson MS, Chance B, Wilson BC (1989) Time resolved reflectance and transmittance for the non-invasive measurement of tissue optical properties. Appl Opt 28(12):2331–2336
24. Pogue BW, Geimer S, McBride TO, Jiang S, Osterberg UL, Paulsen KD (2001) Three-dimensional simulation of near-infrared diffusion in tissue: boundary condition and geometry analysis for finite-element image reconstruction. Appl Opt 40(4):588–600
25. Pogue BW, Patterson MS (2009) Review of tissue simulating phantoms for optical spectroscopy, imaging and dosimetry. J Biomed Opt 11(4):041102
26. Robertson FC, Douglas TS, Meintjes EM (2010) Motion artifact removal for functional near infrared spectroscopy: a comparison of methods. IEEE Trans Biomed Eng 57(6):1377–1387
27. Rolfe P (2000) In Vivo Near-Infrared Spectroscopy. Annu Rev Biomed Eng 02:715–754
28. Saleh BEA, Teich MC (2007) Fundamentals of photonics, 2nd edn. Wiley-Interscience, New York
29. Sato H, Kiguchi M, Maki A (2006) Wavelength dependence of effective pathlength factor in noninvasive optical measurements of human brain functions. Jpn J Appl Phys 45(12): L361–L363
30. Schweiger M, Arridge SR, Hiraoka M, Delpy DT (1995) The finite element method for the propagation of light in scattering media: boundary and source conditions. Med Phy 22(11):1779–1792
31. Sevick EM, Chance B, Leigh J, Nioka S, Maris M (1991) Quantitation of time- and frequency-resolved optical spectra for the determination of tissue oxygenation. Anal Biochem 195(2):330–351

32. Singh AK, Dan I (2006) Exploring the false discovery rate in multichannel NIRS. NeuroImage 33(2):542–549
33. Strangman G (2003) Factors affecting the accuracy of near-infrared spectroscopy concentration calculations for focal changes in oxygenation parameters. NeuroImage 18(4):865–879
34. Takatani S, Graham MD (1979) Theoretical analysis of diffuse reflectance from a two-layer tissue model. IEEE Trans Bio-med Eng 26(12):656–664
35. Takeuchi M, Hori E, Takamoto K, Tran AH, Satoru K, Ishikawa A, Ono T, Endo S, Nishijo H (2009) Brain cortical mapping by simultaneous recording of functional near infrared spectroscopy and electroencephalograms from the whole brain during right median nerve stimulation. Brain Topogr 22(3):197–214
36. Uludag K, Steinbrink J, Villringer A, Obrig H (2004) Separability and cross talk: optimizing dual wavelength combinations for near-infrared spectroscopy of the adult head. NeuroImage 22(2):583–589
37. Umeyama S, Yamada T (2009) New method of estimating wavelength-dependent optical path length ratios for oxy- and deoxyhemoglobin measurement using near-infrared spectroscopy. J Biomed Opt 14(5):1–6
38. Villringer A, Planck J, Hock C, Schleinkofer L, Dirnagl U (1993) Near infrared spectroscopy (NIRS): a new tool to study hemodynamic changes during activation of brain function in human adults. Neurosci Lett 154(1-2):101–104
39. Wray S, Cope M, Delpy DT, Wyatt JS, Reynolds EOR (1988) Characterization of the near infrared absorption spectra of cytochrome aa3 and haemoglobin for the non-invasive monitoring of cerebral oxygenation. Biochim Biophys Acta 933:184–192
40. Wyatt JS, Cope M, Delpy DT, Richardson CE, Edwards AD, Wray S, Reynolds EOR (1990) Quantitation of cerebral blood volume in human infants by near-infrared spectroscopy. J Appl Physiol (Bethesda, MD: 1985) 68(3):1086–1091
41. Yamada T, Umeyama S, Matsuda K (2010) A multidistance probe arrangement NIRS for detecting absorption changes in cerebral gray matter layer. Imaging 7557 (0):75570X–75570X–12
42. Zhao H, Tanikawa Y, Gao F, Onodera Y, Sassaroli A, Tanaka K, Yamada Y (2002) Maps of optical differential pathlength factor of human adult forehead, somatosensory motor and occipital regions at multi-wavelengths in NIR. Phys Med Biol 47(12):2075–2093
43. Zijistra WG, Buursma A, van der Roest WPM (1991) Absorption spectra of human fetal and adult oxyhemoglobin, de-oxyhemoglobin. Clin Chem 37(9):1633–1638

Chapter 4
Diffuse Optical Tomography for Brain Imaging: Theory

Zhen Yuan and Huabei Jiang

4.1 Introduction

4.1.1 Recent Advances in Diffuse Optical Tomography

Due to its numerous advantages including low cost, portability, and nonionizing radiation [1], near-infrared (NIR) diffuse optical tomography (DOT) is emerging as a potential tool for imaging biological tissues. To date, DOT has made a considerable advance and is being translated from the laboratory to the clinic. DOT is a natural extension of near-infrared spectroscopy (NIRS), which has been used clinically and in basic research, particularly in physiological and psychological research [2].

NIR light, with wavelengths between 600 and 1,000 nm, utilizes noninvasive radiation for imaging biological tissues. DOT using NIR light has been an active area of research for the past two decades. The main advantage of NIR DOT lies in providing a variety of quantitative information of biological tissues with high sensitivity and specificity compared to other imaging modalities. It has primarily been applied to image both structural and functional parameters of brain and breast tissues [3–7]. Recent phantom and clinical studies show that DOT can also provide quantitative optical images of hand joints and associated bones for early detection of joint-related diseases [8–11]. In addition, the potential use of molecular-specific contrast agents is an active research area with tremendous promise [12–14]. Presently, breast DOT can be performed repeatedly due to its nonionizing and noninvasive nature of imaging. Along with this, ongoing therapeutic investigations are showing a promise for monitoring chemotherapy using DOT [15–17].

As a functional imaging modality, NIR DOT is appealing in terms of its intrinsic optical contrast due to hemoglobin in the blood which is the main absorber of NIR light in most tissues. Consequently, NIRS is capable of distinguishing oxy- and

---

Z. Yuan • H. Jiang (✉)
Department of Biomedical Engineering, University of Florida, Gainesville, FL 32611, USA
e-mail: hjiang@bme.ufl.edu

S.J. Madsen (ed.), *Optical Methods and Instrumentation in Brain Imaging and Therapy*, Bioanalysis: Advanced Materials, Methods, and Devices 3,
DOI 10.1007/978-1-4614-4978-2_4, © Springer Science+Business Media New York 2013

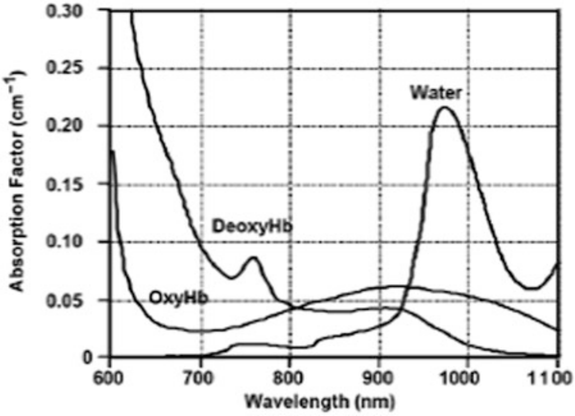

Fig. 4.1 Absorption spectra of hemoglobin and water, showing a spectral window in tissues in the NIR region (http://omlc.ogi.edu/spectra/)

deoxy-hemoglobin, which then provides total hemoglobin (HbT) and blood oxygen saturation (SO_2). In addition, tissue water and lipid contents can be estimated since there is a significant contribution of these contents to the NIR spectra. The distinct spectra for different chromophores make it possible to differentiate them in situ, which provides a powerful image-guided diffuse optical spectroscopy (DOS) technique for various applications including breast tissue imaging, brain functional imaging, finger joint imaging, molecular imaging, and photodynamic therapy monitoring [18–21] (Fig. 4.1).

DOT/DOS uses sophisticated image reconstruction techniques to generate images from multiple NIRS measurements. This generally involves solving both the forward problem and the inverse problem. In the forward problem, NIR light is delivered to the tissue surface and the transmitted and/or reflected light signal on the boundary is calculated based on the optical properties of tissue. Generally a diffusion model is used to approximate the propagation of NIR light in tissue. However, if the goal is to obtain the tissue property distribution from the measurement data, it is then defined as the inverse problem. With numerical methods, optimization algorithms, and regularization techniques, the distribution of the quantitative optical/physiological properties of tissue can be recovered using the assumed light transport model and measured boundary data [22–24].

Three typical signal measurement techniques using NIR light are currently being used for optical tissue imaging: continuous-wave (CW), time-domain (TD), and frequency-domain(FD) methods (Fig. 4.2) [19–21]. CW imaging systems directly measure the intensity of light transmitted and/or reflected through the tissue. The light source used in CW systems generally has a constant intensity or is modulated at a low frequency (a few kHz). TD systems use short laser pulses, with temporal spread below a nanosecond, and detect the increased spread of the pulse after passing through tissue. The time distribution of transmitted photons is known as the temporal point spread function (TPSF). By fitting the TPSF with a light propagation model such as the diffusion model, the medium parameters including absorption and scattering coefficients can be reconstructed. FD systems use an amplitude-modulated source at a high frequency (a few hundred MHz) and measure the attenuation of

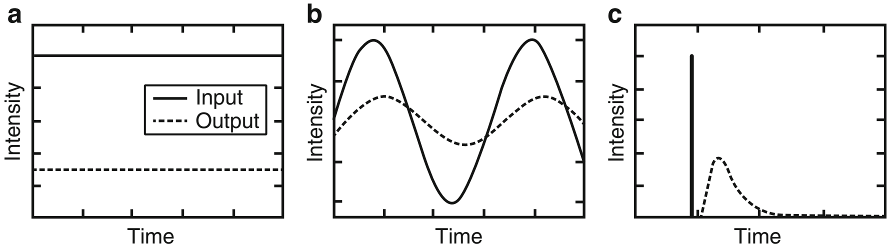

Fig. 4.2 Measurement approach: (**a**) CW, (**b**) FD, (**c**) TD modes (*solid line*: input light source, *dashed line*: output detected signal)

amplitude and phase shift of the transmitted signal. Typically in this approach, a radio-frequency oscillator drives a laser diode and provides a reference signal for phase measurement. Among the three methods, the CW approach is relatively cheap and easy to implement; however, the absorption and scattering coefficients can be distinguished only with the use of appropriate regularization techniques or a prior information in reconstruction. The other two methods provide complete information about scattering events from transmitted photons in tissue, so that both absorption and scattering properties of tissue can be estimated effectively. Avalanche photodiodes are widely used in optical signal detection due to the high dynamic range. Photomultipliers provide higher sensitivity, although with a limited dynamic range and higher cost. Single photon counting PMTs are used in TD to measure the photon flight time. Recently charge-coupled devices (CCDs) are commonly used in CW systems for spectroscopic investigation to improve the imaging accuracy and reduce the data acquisition time.

However, the major limitation of DOT is its low spatial resolution due to the multi-scattering events that occur along each photon path. One effective way to improve its resolution is to integrate it with currently accepted high-resolution clinical imaging systems, such as mammography, ultrasound, X-ray computed tomography or tomosynthesis, and magnetic resonance [25]. As a consequence, NIR DOT has undergone a transition from a stand-alone imaging modality towards hybrid-modality combinations with standard clinical imaging systems. Other strategies to improve NIR imaging accuracy generally include: (1) Taking advantage of more spectral information in the NIR range; (2) using more accurate forward model or robust reconstruction method; (3) building a reliable imaging system with high sensitivity and specificity; (4) using contrast agents to improve the imaging sensitivity and specificity. For example, the use of a priori spatial and spectroscopic information has been reported to achieve high-resolution DOT imaging with NIRS [21, 26].

4.1.2 Recent Advances in Neuroimaging Using DOT

Compared to other functional imaging modalities, such as functional magnetic resonance imaging (fMRI) and PET, DOT has the advantages of noninvasive, portable, convenience, and low cost, and, more importantly, it has unsurpassed high temporal resolution, which is essential for revealing rapid change of dynamic patterns of brain activities including change of blood oxygen, blood volume, and blood flow.

Since the mid-1990, most of the research work done in neuroscience using optical measurements has been focused on NIR spectroscopy or imaging of human and small animal brain function. They have utilized these optical techniques to localize or monitor the cerebral responses under different stimulus including visual [27–29], auditory [30], somatosensory [31], motor [32–34] and language [35]. Further, the researchers also investigated the neurological disorders using different measurement instrumentations and attempted to address neurovascular and neurometabolic coupling mechanisms for different diseases, such as seizure and epilepsy [36–39], depression [40–42], Alzheimer [43–45], and stroke rehabilitation [46–49]. In particular, most of the imaging work conducted was implemented with a sparse array, in which the sources and detectors were separated between 2 and 4 cm, providing low sensitivity and low spatial resolution [50]. Generally speaking, this is not DOT and has been termed optical topography (OT). So far most of the developed reconstruction methods in OT are limited to linear algorithms, which can only provide the change of optical or physiological properties of biological tissues with limited spatial resolution.

In contrast, DOT is generally implemented with a relatively dense array, which provides source and detector pairs with a number of separations [51]. The pairs that are close together will be more sensitive to superficial tissues (e.g., scalp, skull), whereas the pairs with a greater separation will be more sensitive to deeper tissues (e.g., cortex). As such, overlapping information from multiple detector pairs can be combined in the form of a model-based 3D image reconstruction. Reconstructing data can improve depth sensitivity and decrease physiological noise. Recent studies have demonstrated much higher resolution mapping of certain areas in the cortex using nonlinear or linear DOT reconstruction algorithms [52–54].

So far DOT is a relatively new addition to the field of functional neuroimaging, and there is little standardization. There is a growing effort within the optical imaging community to develop a more systematic framework for experimental design and data analysis. Additionally, multimodal imaging combining DOT with the existing brain imaging techniques in synergistic ways facilitates improved interpretation of data and provides brain functional map with excellent temporal and spatial resolution. In particular, MRI- or CT-guided DOT should have tremendous competitive power in future, which can provide 3D DOT of the whole brain based on the realistic head model.

4.2 Image Reconstruction Methods in DOT

In early days, OT reconstruction methods tried to recover the change in optical/physiological properties using the measured change in intensity. The spatial resolution provided by OT could not be better than the spacing between the sources and detectors [2]. One of the most significant improvements in image quality in OT came when a forward model was set up, which describes the geometry and the baseline optical properties of the head, and was used to calculate the amount by which each measurement would change given a small change in optical properties of each pixel. These values were assembled into a sensitivity matrix, which was then inverted and multiplied by the measured data to give an image. This process is not straightforward, as the sensitivity matrix is ill-posed and underdetermined [56–58]. In these OT reconstruction methods, linear algorithms are utilized and the sources and detectors are separated between 2 and 4 cm, providing low sensitivity and low spatial resolution.

DOT reconstruction algorithms allow multiple measurements to contribute to each pixel, leading to improvements in spatial resolution, and accuracy of quantitative tissue parameter reconstruction up to a factor of two [51, 59]. Various reconstruction schemes have been developed for DOT, such as analytical, back-projection, and linear and nonlinear methods. However, in this community regularization-based nonlinear methods have gained the highest attention since they can achieve highly accurate and quantitative image reconstruction. In the following sections, we focus on the description of the basic principles in nonlinear DOT reconstruction methods including the forward problem, the inverse problem, multi-modality imaging approach, spectral reconstruction, and vascular parameter recoveries.

4.2.1 Forward Problem

The development of a model to describe light migration in tissue is essential for the assessment of measurements in diagnostic NIRS and DOT. The equation of radiation transport (RTE) has been accepted as an accurate model to describe light migration in scattering media such as tissue [60, 61]. However, the RTE is difficult to solve, even in homogeneous media with simple boundaries. Additionally, solving the inverse problem with RTE is an even more daunting and time-consuming task. Present modeling of light propagation in scattering tissues is largely through the utilization of the diffusion approximation to the radiation transport equation, i.e., the photon diffuse equation which has the following form in the TD:

$$\nabla \cdot D(r)\nabla\Phi(r,t) - \mu_{\mathrm{a}}(r)\Phi(r,t) - \frac{\partial\Phi(r,t)}{v\partial t} = -S(r,t) \tag{4.1}$$

in which r is the position vector (mm), t is the time (s), v is the speed of light in the medium (mm/s), $\Phi(r,t)$ is the photon density (photon fluence rate: mW/mm^2), $D(r)$ the diffusion coefficient (mm^{-1}), $\mu_{\mathrm{a}}(r)$ is the optical absorption coefficient (mm^{-1}), $S(r,t)$ is the source strength (mW/mm^3), and the diffusion coefficient can be written as $D = 1/(3(\mu_{\mathrm{a}} + \mu_{\mathrm{s}}'))$, where μ_{s}' is the reduced scattering coefficients (mm^{-1}). Typically, the source is modeled as a single isotropic point source placed $1/\mu_{\mathrm{s}}'$ (1 mm) into the medium. The photon density near the boundary of turbid medium/tissue is generally described by the mixed Dirichlet–Neuman boundary condition (Type-III Boundary conditions) [24]:

$$D\nabla\Phi(r,t)\cdot\hat{n} = -\alpha\Phi(r,t) \tag{4.2}$$

in which $\hat{n}$ is the vector normal to measurement boundary, α is related to the refractive index (n) mismatch at the boundary via the following expression: $\alpha = \frac{1-R_{\mathrm{eff}}}{R_{\mathrm{eff}}}\frac{3}{2}\mu_{\mathrm{s}}'$, $R_{\mathrm{eff}} \approx \frac{-1.44}{n^2} + \frac{0.71}{n} + 0.668 + 0.63n$ and $n = \frac{n_{\mathrm{in}}}{n_{\mathrm{out}}}$.

The FD diffusion equation is obtained through the Fourier transform of (4.1):

$$\nabla\cdot D(r)\nabla\Phi(r,\omega) - \left(\mu_{\mathrm{a}}(r) + \frac{\mathrm{i}\omega}{c}\right)\Phi(r,\omega) = -S(r,\omega) \tag{4.3}$$

In FD, we have assumed that $\Phi(r,t) = \Phi(r)\mathrm{e}^{-\mathrm{i}\omega t}$, and the $\mathrm{e}^{-\mathrm{i}\omega t}$ terms have been factored out, since the detected signals are modulated at the same frequency as the light source (ω: light source modulation frequency). For a CW case where $\omega = 0$, the following photon diffusion equation and type-III boundary condition are derived,

$$\nabla\cdot D(r)\nabla\Phi(r) - \mu_{\mathrm{a}}(r)\Phi(r) = -S(r) \tag{4.4}$$

$$-D\nabla\Phi\cdot n = \alpha\Phi \tag{4.5}$$

The finite element (FE) method is the most widely used numerical method to solve the photon diffusion equation. To solve (4.4) and (4.5) using FE (a similar operation can be implemented for FD and TD cases), the weighted weak form for these two equations is stated as

$$\int_V \phi_i(\nabla\cdot D(r)\nabla\Phi - \mu_\alpha\Phi + S)\,\mathrm{d}V + \int_\Gamma \phi_i(-D\nabla\Phi\cdot n - \alpha\Phi)\,\mathrm{d}\Gamma = 0 \tag{4.6}$$

According to integration by parts, (4.6) is rewritten as follows:

$$\int_V (D(r)\nabla\phi_i\cdot\nabla\Phi(r) + \mu_{\mathrm{a}}\phi_i\Phi(r) - \phi_i S)\,\mathrm{d}V + \int_\Gamma \phi_i(\alpha\Phi)\,\mathrm{d}\Gamma = 0 \tag{4.7}$$

In addition, $\Phi(r)$, D and μ_{a} are spatially discretized as

$$\Phi = \sum_{i=1}^{N}\Phi_i\phi_i, \quad D = \sum_{i=1}^{N}D_i\phi_i, \quad \mu_{\mathrm{a}} = \sum_{i=1}^{N}(\mu_{\mathrm{a}})_i\phi_i \tag{4.8}$$

in which N is the node number of the finite element mesh and ϕ_i is the basis function. In consideration of (4.8), (4.7) can be written as

$$[A]\{\Phi\} = \{b\} \tag{4.9}$$

in which the elements of the matrix $[A]$ are $\alpha_{ij} = \int_V (-D\nabla\phi_j \cdot \nabla\phi_i - \mu_\mathrm{a}\phi_j\phi_i)\,\mathrm{d}V + \int_\Gamma (-\alpha\phi_j\phi_i)\,\mathrm{d}\Gamma$ where the integrations are performed over the problem domain (V) and boundary domain (Γ). $\{b\}$ is the source vector. Assuming a point source model, $S = S_0\delta(r - r_0)$ is used, where S_0 is the source strength and $\delta(r - r_0)$ is the Dirac delta function for a source at r_0.

4.2.2 Inverse Problem: Problem Statement for Nonlinear Reconstruction Methods

In solving the inverse problem for DOT, the goal is to recover the optical properties at each FE node using a finite number of measurements at the tissue surface. The objective function for regularized minimization statement is given [62] as follows:

$$\mathbf{F} = \min_{\chi}\left\{\sum_{i=1}^{M}(\Phi_i^\mathrm{m} - \Phi_i^\mathrm{c})^2 + \eta||\chi - \chi_0||^2\right\} \tag{4.10}$$

in which χ expresses D and μ_a, χ_0 is usually fixed, Φ_i^m is the measured photon density from a given scattering medium for $i = 1, 2,\ldots, M$ boundary locations, and Φ_i^c is the computed photon density with the same geometry as the scattering medium. In nonlinear and iterative-based reconstruction algorithms, χ_0 is set equal to χ_i determined by the recovered parameters at the previous iteration. This variation is termed the Levenberg–Marquardt algorithm [63, 64]. In this case, (4.10) is further simplified to

$$\text{Min: } F = \sum_{i=1}^{M}(\Phi_i^\mathrm{m} - \Phi_i^\mathrm{c})^2 \tag{4.11}$$

We can minimize the objective function by specifying $F = 0$. This is a typical optimization problem, where we are particularly interested in finding χ that makes F close to zero. Following a Taylor series expansion method, we obtain the approximated χ from nearby point χ_0 ($\Delta\chi = \chi - \chi_0$),

$$\frac{\partial F}{\partial\chi} = \frac{\partial F}{\partial\chi}(\chi_0) + \Delta\chi\frac{\mathrm{d}}{\mathrm{d}\chi}\left[\frac{\partial F}{\partial\chi}(\chi_0)\right] + \cdots \tag{4.12}$$

If the effect of the higher-order terms is ignored and $\partial F/\partial\chi = 0$ is assumed, (4.12) is rewritten as follows:

$$\chi = \chi_0 - \left\{\frac{\mathrm{d}}{\mathrm{d}\chi}\left[\frac{\partial F}{\partial\chi}(\chi_0)\right]\right\}^{-1}\frac{\partial F}{\partial\chi}(\chi_0) \tag{4.13}$$

The iterative form for (4.13) can be specified as

$$\chi_i = \chi_{i-1} - \left\{\frac{\mathrm{d}}{\mathrm{d}\chi}\left[\frac{\partial F}{\partial\chi}(\chi_{i-1})\right]\right\}^{-1}\frac{\partial F}{\partial\chi}(\chi_{i-1}) \tag{4.14}$$

Based on (4.11), we can solve for the first-order and second-order derivatives of F

$$\frac{\partial F}{\partial\chi} = 2\left(\frac{\partial\Phi^{\mathrm{c}}}{\partial\chi}\right)^{\mathrm{T}}(\Phi^{\mathrm{c}} - \Phi^{\mathrm{m}}) \tag{4.15}$$

$$\frac{\partial^2 F}{\partial\chi^2} = 2\left(\frac{\partial\Phi^{\mathrm{c}}}{\partial\chi}\right)^{\mathrm{T}}\frac{\partial\Phi^{\mathrm{c}}}{\partial\chi} + 2\left(\frac{\partial^2\Phi^{\mathrm{c}}}{\partial\chi^2}\right)^{\mathrm{T}}(\Phi^{\mathrm{c}} - \Phi^{\mathrm{m}}) \tag{4.16}$$

The contribution from the higher-order derivative terms in (4.16) is small and often discarded. Then inserting (4.16) into (4.14), we get

$$\chi_i = \chi_{i-1} + \left\{2\left(\frac{\partial\Phi^{\mathrm{c}}}{\partial\chi}\right)^{\mathrm{T}}\frac{\partial\Phi^{\mathrm{c}}}{\partial\chi}\right\}^{-1} 2\left(\frac{\partial\Phi^{\mathrm{c}}}{\partial\chi}\right)^{\mathrm{T}}(\Phi^{\mathrm{m}} - \Phi^{\mathrm{c}}) \tag{4.17}$$

in which $\partial\Phi/\partial\chi$ is the Jacobian matrix J, formed at the boundary measurement sites. It should be noted that the impact of the Hessian matrix $J^{\mathrm{T}}J$ in (4.17) is always ill-conditioned, which makes the iteration process unstable. A typical way to stabilize the inversion problem is through regularization to make $J^{\mathrm{T}}J$ more diagonally dominant. So the ultimate iterative updating equation for the optical properties in (4.17) becomes

$$(J^{\mathrm{T}}J + \lambda'\mathbf{I})\Delta\chi = J^{\mathrm{T}}(\Phi^{\mathrm{m}} - \Phi^{\mathrm{c}}) \tag{4.18}$$

in which, λ' is a scalar and $\mathbf{I}$ is the identity matrix. A very effective method for determining λ' is to set it equal to the trace of the Hessian matrix multiplied by an empirically determined factor σ, and the least-square error at each iteration,

$$\lambda' = \sigma(\Phi^{\mathrm{c}} - \Phi^{\mathrm{m}})^2 \times \mathrm{trace}[J^{\mathrm{T}}J] \tag{4.19}$$

Moreover, the adjoint sensitivity method is often implemented to calculate the Jacobian matrix, which is able to reduce the computational cost dramatically. Direct differentiation of both sides of (4.9) with respect to χ

$$[A]\left\{\frac{\partial\Phi}{\partial\chi}\right\} = -\left[\frac{\partial A}{\partial\chi}\right]\{\Phi\} \tag{4.20}$$

The Jacobian matrix $\partial\Phi/\partial\chi$ can be calculated through the following steps.

First, we define a N (node number) $\times$ M (measurement number) matrix Ψ, and let Ψ satisfy the following relationship:

$$[A]^{\mathrm{T}}[\Psi] = [\Delta_{\mathrm{d}}] \tag{4.21}$$

where the vector Δ_{d} has the unit value at the measurement sites/nodes and zero at other nodes. Then we left multiply (4.20) with the transposition of $[\Psi]$

$$[\Psi]^{\mathrm{T}}[A]\left\{\frac{\partial\Phi}{\partial\chi}\right\} = -[\Psi]^{\mathrm{T}}\left[\frac{\partial A}{\partial\chi}\right]\{\Phi\} \tag{4.22}$$

Equation (4.22) can be further written as follows:

$$\left\{\frac{\partial\Phi}{\partial\chi}\right\}^{\mathrm{T}}[A]^{\mathrm{T}}[\Psi] = -\{\Phi\}^{\mathrm{T}}\left[\frac{\partial A}{\partial\chi}\right]^{\mathrm{T}}[\Psi] \tag{4.23}$$

Inspecting (4.21) into (4.23), we get

$$\left\{\frac{\partial\Phi}{\partial\chi}\right\}^{\mathrm{T}} = -\{\Phi\}^{\mathrm{T}}\left[\frac{\partial A}{\partial\chi}\right]^{\mathrm{T}}[\Psi] \tag{4.24}$$

Now we can immediately tell that the left-hand side of the above equations actually gives the corresponding elements in the relative Jacobian matrix based on the adjoint sensitivity method

$$\left\{\frac{\partial\Phi}{\partial\chi}\right\} = -[\Psi]^{\mathrm{T}}\left[\frac{\partial A}{\partial\chi}\right]\{\Phi\} \tag{4.25}$$

The nonlinear reconstruction approach described so far is an iterative Newton method with combined Marquardt and Tikhonov regularizations that can provide stable inverse solutions. The Newton reconstruction process involves the iterative solution of the above equations (4.9) and (4.18), allowing an update of optical property distribution to be obtained at each iteration, i.e., $\chi_{\mathrm{new}} = \chi_{\mathrm{old}} + \Delta\chi$. However, to improve the reconstruction accuracy, the global convergence-based Newton method is often used using the following modified updating procedure [11]:

$$\chi_{\mathrm{new}} = \chi_{\mathrm{old}} + \zeta\Delta\chi \quad (0<\zeta \le 1) \tag{4.26}$$

where ζ is calculated from a backtracking line search. Thus the realization of the global convergence algorithm is quite straightforward: the algorithm starts with a full Newton step (i.e., $\zeta = 1$); if the updated χ are close enough to the final solution, a quadratic convergence is obtained; if not, the backtracking line search will provide a smaller value of ζ along the Newton direction; the reconstruction process continues until a quadratic convergence is achieved.

Finally, high quality image reconstruction based on the above iterative procedure depends on good choice of four initial parameters including the BC coefficient α, the source strength S, and the initial guesses of D and μ_α. As such, an optimization scheme was developed to find the best initial guesses based on the forward computation of the diffusion equation so that the following objective function is minimized [22]:

$$\text{Min: } \pi = \sum_{i=1}^{M} \left(\Phi_i^{\mathrm{m}} - \Phi_{i\ (calculated\ from\ optimized\ initial\ guesses)}^{\mathrm{c}}\right) \tag{4.27}$$

in which Φ_i^{m} is the measured photon density from a given experimental inhomogeneous medium, and Φ_i^{c} is the computed photon density from a homogeneous medium with the same geometry as the experimental medium.

4.2.3 Multi-Modality Image Reconstruction Method

It is widely accepted that DOT can provide high-contrast biological tissue imaging with quantitative optical properties. However, the limitation of tomographic NIRS and DOT is their low resolution due to the multi-scattering events that occur along each photon path. As mentioned in Sect. 4.1.2, an effective way to enhance its resolution is to integrate it with the existing high-resolution clinical imaging systems, such as mammography, ultrasound (US), X-ray computed tomography (CT) or tomosynthesis, and magnetic resonance (MR) [25].

While several methods are available in the area of high-resolution imaging modality-guided DOT reconstruction [5, 65–69], regularization-based schemes appear to be the most effective as they can flexibly handle the problems associated with incorrect initial estimation of optical properties and inaccurate domain segmentation that are required for a priori structural information guided DOT reconstruction. Several regularization-based schemes have been developed for high-resolution imaging (MR, US, and CT) guided DOT reconstruction. However, most of these schemes do not appear to be able to handle the cases where MR or CT is insensitive to the target tissues or lesions, resulting in inaccurate DOT reconstruction. To overcome these limitations, a modified Tikhonov or hybrid regularization technique has been conducted for spatial information guided DOT reconstruction [70].

The conventional Tikhonov-regularization sets up a weighted term as well as a penalty term to minimize the squared differences between computed and measured photon density values as follows:

$$\min_{\chi} : \{||\Phi^{\mathrm{c}} - \Phi^{\mathrm{o}}||^2 + \rho||\mathbf{L}\delta\chi||^2 = \{||\Phi^{\mathrm{c}} - \Phi^{\mathrm{o}}||^2 + \rho||\mathbf{L}(\chi^{\mathrm{c}} - \chi^{\mathrm{o}})||^2 \tag{4.28}$$

And the generated updating equation based on Newton iterative method can be expressed as

$$\Delta\chi = (J^{\mathrm{T}}J + \rho\mathbf{L}^{\mathrm{T}}\mathbf{L})^{-1}[J^{\mathrm{T}}(\Phi^{\mathrm{o}} - \Phi^{\mathrm{c}}) - \rho\mathbf{L}^{\mathrm{T}}\mathbf{L}\chi] \tag{4.29}$$

in which $\Phi^{\mathrm{o}} = (\Phi_1^{\mathrm{o}}, \Phi_2^{\mathrm{o}}, \ldots, \Phi_M^{\mathrm{o}})^{\mathrm{T}}$ and $\Phi^{\mathrm{c}} = (\Phi_1^{\mathrm{c}}, \Phi_2^{\mathrm{c}}, \ldots, \Phi_M^{\mathrm{c}})^{\mathrm{T}}$, and Φ_i^{o} and Φ_i^{c} are observed and computed photon intensity for $i = 1, 2, \ldots, M$ boundary locations; ρ is the weighted parameter; $\mathbf{L}$ is the regularization matrix or filter matrix.

In consideration of the fact that Tikhonov regularization can draw the solution towards the null space of the regularization matrix $\mathbf{L}$, that is $\mathbf{L}\chi^0 = 0$, we obtain the following updating equation when $\rho = 1$,

$$\Delta\chi = (J^{\mathrm{T}}J + \mathbf{L}^{\mathrm{T}}\mathbf{L})^{-1}[J^{\mathrm{T}}(\Phi^{\mathrm{o}} - \Phi^{\mathrm{c}})] \tag{4.30}$$

The most often used regularization matrices in DOT are the identity, in which $\mathbf{L}$ is a diagonal matrix and the prior information can be incorporated into the iterative process by using the spatially variant regularization parameter [67, 68]. The Laplacian-type filter matrix $\mathbf{L}$ is often used and its elements, L_{ij} are constructed according to the visible region or tissue type it was associated as follows [65]:

$$L_{ij} = \begin{cases} 1 & \text{if } i = j \\ -1/NN & \text{if } i,j \subset \text{one region} \\ 0 & \text{if } i,j \subset \text{different region} \end{cases} \tag{4.31}$$

where NN is the finite element node number within a tissue type.

However, the multi-modality imaging schemes expressed in (4.30) are not able to handle the cases where MR or X-ray is insensitive to the target tissues or lesions. For example, in the area of joint imaging, X-ray is not able to detect the cartilage and fluids as well as their changes in the finger joints, although the changes associated with the cartilage and fluids can be easily captured by low-resolution DOT alone. To resolve this issue, instead of imposing constraints on the magnitude of the solution or on its derivative as in Tikhonov regularization, the developed hybrid regularization method minimizes the difference between the desired solution and its approximate X-ray or MR estimate, as well as the residual error in the least square sense. Hence in hybrid regularization-based nonlinear reconstruction algorithm, the objective function becomes

$$\min_{\chi} : ||\Phi^{\mathrm{c}} - \Phi^{\mathrm{o}}||^2 + \beta\left\{||\Phi^{\mathrm{c}} - \Phi^{\mathrm{o}}||^2 + \lambda||\mathbf{L}\delta\chi||^2\right\} \tag{4.32}$$

where β is the hybrid regularization parameter. By minimizing Ω with respect to χ (i.e., $\partial\Omega/\partial\chi = 0$) and considering (4.30), we obtain the following updating equation for the hybrid regularization:

$$\Delta\chi = (J^{\mathrm{T}}J + \beta J^{\mathrm{T}}J + \lambda' I + \beta\mathbf{L}^{\mathrm{T}}\mathbf{L})^{-1}[J^{\mathrm{T}}(\Phi^{\mathrm{o}} - \Phi^{\mathrm{c}})] \tag{4.33}$$

If we specify the regularization parameter $\beta = 1$, (4.6) is further simplified as

$$\Delta\chi = (J^{\mathrm{T}}J + J^{\mathrm{T}}J + \lambda' I + \mathbf{L}^{\mathrm{T}}\mathbf{L})^{-1}[J^{\mathrm{T}}(\Phi^{\mathrm{o}} - \Phi^{\mathrm{c}})] \tag{4.34}$$

in which λ' is the Levenberg–Marquardt regularization parameter. It is noted from (4.34) that the hybrid regularization is actually a regularization scheme that combines both Levenberg–Marquardt and Tikhonov-regularization.

4.2.4 Diffuse Optical Spectral Reconstruction of Physiological Parameters of Tissues

DOS and DOT have more than 30-year history of being used to access tissue spectral parameters including HbT concentration, hemoglobin oxygen saturation, water and lipid concentration, scattering amplitude, and scattering power. Early work in the field of tomographic DOS focused on reconstruction of optical properties of tissue at several selected wavelengths. Then a least-square fitting algorithm was utilized to estimate the chromophore concentrations based on the recovered optical properties and Beer's Law [20, 71]. To date several methods are proposed to directly image the chromophore concentrations without first estimating the optical properties either in CW- or frequency-domain [26, 72]. An interesting study has shown that oxyhemoglobin (HbO_2), deoxyhemoglobin (Hb), water and scattering amplitude heterogeneities could be successfully recovered using CW measurements at four optimized wavelengths in the 650–930 nm range [73]. In particular, the use of a priori spatial and spectroscopic information has been reported to achieve high-resolution DOT imaging with NIRS [21, 26]. Chromophore concentrations can be reconstructed with high accuracy when spatial guidance from high-resolution imaging methods and spectral a priori information provided by NIRS are used [21, 26].

When the data acquisition at different wavelengths is finished, the following step is to generate the spectroscopic images based on a robust 3D reconstruction algorithm. For the forward problem, the photon density at different wavelengths can be calculated from the photon diffusion model using the finite element method. For CW cases, the spectra resolved forward model is written (similar operation can be conducted for FD and TD cases):

$$\nabla \cdot D(r,\lambda)\nabla\Phi(r,\lambda) - \mu_{\mathrm{a}}(r,\lambda)\Phi(r,\lambda) = -S(r,\lambda) \tag{4.35}$$

According to Beer's law, the wavelength-dependent tissue absorption is

$$\mu_{\mathrm{a}}(\lambda) = \sum_{i=1} \varepsilon_i(\lambda)c_i \tag{4.36}$$

in which c_i is the concentration, $\varepsilon_i(\lambda)$ is the extinction absorption coefficient of the ith chromophore (HbO_2, Hb, H_2O and lipid) at wavelength λ. Scattering properties (scattering amplitude a and scattering power b) are found by constructing a best fit to an empirical approximation to Mie scattering theory,

$$\mu_{\mathrm{s}}' = a\lambda^{-b} \tag{4.37}$$

Thus the forward model is further written as follows:

$$\nabla \cdot D\nabla\Phi(r,\lambda) - \sum_{i=1} \varepsilon_i(\lambda)c_i\Phi(r,\lambda) = -S(r,\lambda) \tag{4.38}$$

For the inverse problem, the following updating equation for the hybrid regularization is deduced [21],

$$\Delta\chi_\lambda = (J^{\mathrm{T}}J + J^{\mathrm{T}}J + \lambda'\mathbf{I} + \mathbf{L}^{\mathrm{T}}\mathbf{L})^{-1}[J^{\mathrm{T}}(\Phi^{\mathrm{o}}(\lambda) - \Phi^{\mathrm{c}}(\lambda))] \tag{4.39}$$

If no spatial guidance is incorporated, (4.39) is reduced to

$$\Delta\chi_\lambda = (J^{\mathrm{T}}J + \lambda'\mathbf{I})^{-1}[J^{\mathrm{T}}(\Phi^{\mathrm{o}}(\lambda) - \Phi^{\mathrm{c}}(\lambda))] \tag{4.40}$$

where $\Delta\chi_\lambda = (\,[\Delta c_1] \quad \cdots \quad [\Delta c_n] \quad [\Delta a] \quad [\Delta b]\,)^{\mathrm{T}}$ is the updating vectors for the absorbers and scatters. The Jacobian matrix $\boldsymbol{J}$ is denoted: $J = [\tilde{J}_{1,\lambda}, \ldots, \tilde{J}_{c,\lambda}, \tilde{J}_{a,\lambda}, \tilde{J}_{b,\lambda}]$, where $\tilde{J}_{c,\lambda}$ represent the Jacobian submatrices for different chromophores and is stated:

$$\tilde{J}_{c,\lambda} = \frac{\partial\Phi(\lambda)}{\partial\mu_{\mathrm{a}}} \frac{\partial\mu_{\mathrm{a}}}{\partial c_i} \tag{4.41}$$

When $D(\lambda)$ is expressed in terms of a and b using (4.37), the other Jacobian submatrices are written in consideration of $D = 1/(3(\mu_{\mathrm{a}} + \mu_{\mathrm{s}}'))$

$$\tilde{J}_{a,\lambda} = \frac{\partial\Phi(\lambda)}{\partial D}(-3D^2\lambda^{-b}), \quad \tilde{J}_{b,\lambda} = \frac{\partial\Phi(\lambda)}{\partial D}(3D^2\mu_{\mathrm{s}}' \ln\lambda) \tag{4.42}$$

Thus the image formation task for the spectral reconstruction is to update an optimized initial chromophore concentration distribution via iterative solution of (4.38) and (4.39) so that a weighted sum of the squared difference between the computed $\Phi^{\mathrm{c}}(\lambda)$ and measured photon density $\Phi^{\mathrm{o}}(\lambda)$ in (4.43) can be minimized:

$$\Omega = ||\Phi^{\mathrm{c}}(\lambda) - \Phi^{\mathrm{o}}(\lambda)||^2 \tag{4.43}$$

4.2.5 Calculation of Vascular Parameters (Cerebral Blood Flow Rate and Oxygen Consumption Rate) Based on the Recovered Physiological Responses

Analysis of the physiological responses of functional brain activation based on intrinsic signals has revealed new insights into the functional representations of areas such as the visual and somatosensory cortices [74, 75]. In addition to hemoglobin change, cerebral blood flow (CBF) and oxygen consumption rate (OC) changes resulting from functional activation are also important components of the hemodynamic response. Coupling between neuronal activity and the associated hemodynamic response is now becoming a hot topic in neuroscience [76, 77]. A clearer understanding of the neuro–metabolic–vascular relationship will enable greater insight into the functioning of the normal brain and will also have significant impact on diagnosis and treatment of neurovascular diseases such as stroke, Alzheimer's disease, brain injury, and epilepsy [78]. In order to achieve this goal, simultaneous monitoring of the spatiotemporal characteristics of OC, CBF, and the cerebral metabolic rate of oxygen is crucial.

Although numerous methods for assessment of cerebral OC and CBF have been explored including fMRI [79], arterial spin labeling MRI [80], PET [81], Fick's law-based optical systems [82], laser Doppler [83], diffuse correlation spectroscopy [84], and Doppler ultrasound [85], there remains a critical need for continuous, noninvasive instruments to measure CBF and OC in humans with intact skull. For example, the spatiotemporal resolution of PET is limited, and fMRI requires careful calibration of the scaling factor between the blood oxygen level-dependent signal and the relative changes of Hb concentration, as well as assumptions about the relationship between the changes in CBF and cerebral blood volume. Laser Doppler flow meter has limited penetration depth. Diffuse correlation spectroscopy has shown promising results, but it is still unclear whether it is practical enough to be used for continuous monitoring in humans. Fick's law-based systems are not entirely noninvasive, since they require the injection of a chromophore, and therefore cannot be used for continuous monitoring [86]. Laser speckle contrast imaging method can effectively recover the BF and OC parameters, but it is limited to superficial imaging [75].

NIR DOS and DOT have shown great potential to provide high spatiotemporal resolution and quantitative imaging of hemodynamic responses. In particular, dynamic optical imaging has allowed the exploration of time-resolved changes in tissue properties. The cerebral functional dynamics measured by DOT are due to the dynamical changes in blood volume and oxygenation in the scalp and brain where the hemodynamics are caused by CBF and OC change associated with heart beat, vasomotion, and vascular response to neuronal activity [87]. However, current dynamic DOT imaging techniques provide only the change of HbT and SO_2, which cannot give the change of CBF and OC due to the hemodynamic response to neuronal activation. As such, new mathematical models connecting changes in CBF and OC to observed changes in HbT and SO_2 are required to guide more quantitative interpretation of neuronal activity. The model should be able to provide indirect measurements of neuron-induced vascular parameters including blood flow rate (BF) and OC.

The principle of mass balance to the transport of oxygen in a blood vessel segment allows us to obtain quantitative information on how oxygen and blood are managed in tissue. To model oxygen transport in a blood vessel by this principle, we consider a one-dimensional cylindrical vessel (blood vessel) with R_i and R_o as the inner and outer radii, respectively, surrounded by other biological tissues. In addition, we assume all the oxygen (O_2) diffusing out the segment is consumed in a surrounding tissue region [88].

4.2.5.1 Mass Balance in Each Segment for Intravascular Flux

The law of mass conservation stipulates that the amount of O_2 lost from a vascular segment must be equal to the diffuse O_2 flux to the tissues, determined by the perivascular oxygen gradients. For a steady case, we have

$$Q_\mathrm{in}C_\mathrm{b}[\mathrm{HbT}]\mathrm{SO}_{2,\mathrm{in}} - Q_\mathrm{out}C_\mathrm{b}[\mathrm{HbT}]\mathrm{SO}_{2,\mathrm{out}} = l_i\pi d_i J_i \tag{4.44}$$

in which Q_in (mL/s) is the volumetric BF into the ith segment, Q_out the volumetric BF out of the segment, d_i is the diameter of the ith segment, l_i the length of the ith segment, HbT the total hemoglobin concentration in the blood (moles/mL), $\mathrm{SO}_{2,\mathrm{in}}$ the hemoglobin oxygen saturation flowing in the segment, $\mathrm{SO}_{2,\mathrm{out}}$ oxygen saturation flowing out of the segment, J_i the oxygen flux across the vessel wall (moles $O_2/\mathrm{cm}^2/\mathrm{s}$), and C_b is the oxygen binding capability of hemoglobin ($C_\mathrm{b} = 1.39$ mL O_2/gmHb; $C_\mathrm{b} = 1.$ if the concentration of O_2 dissolved in plasma is considered) [88]. In addition, (4.44) is rewritten in consideration of the mean BF:

$$Q_iC_\mathrm{b}[\mathrm{HbT}](\mathrm{SO}_{2,\mathrm{in}} - \mathrm{SO}_{2,\mathrm{out}}) = l_i\pi d_i J_i \tag{4.45}$$

where Q_i is the mean BF in the ith segment. For a transient case, (4.44) is further written as follows:

$$Q_\mathrm{in}(t)C_\mathrm{b}[\mathrm{HbT}]\mathrm{SO}_{2,\mathrm{in}}(t) - Q_\mathrm{out}(t)C_\mathrm{b}[\mathrm{HbT}]\mathrm{SO}_{2,\mathrm{out}}(t) - l_i\pi d_i J_i(t) = \frac{\partial M_{i,\mathrm{HbO}_2}(t)}{\partial t} \tag{4.46}$$

in which M_{i,HbO_2} is the moles of oxygenated hemoglobin in the ith segment. According to the principle of mass balance, the third term on the left-hand side of (4.46) is actually the OC_i of the ith segment (mole O_2/s). Considering the fact that each molecule of hemoglobin is able to carry four molecules of oxygen, (4.46) is stated as follows:

$$\begin{aligned} Q_{\text{in}}(t)C_{\text{b}}[\text{HbT}]\text{SO}_{2,\text{in}}(t) - Q_{\text{out}}(t)C_{\text{b}}[\text{HbT}]\text{SO}_{2,\text{out}}(t) \\ - \text{OC}_i(t)/4 = \frac{\partial M_{i,\text{HbO}_2}(t)}{\partial t} \end{aligned} \tag{4.47}$$

4.2.5.2 Mass Balance in Tissues Based on Global Analysis for Estimating Intravascular Flux

The oxygen consumed by the tissues (organs) is supplied from three blood vessel sources: capillaries, arterioles, and venules. As such, mass balance for O_2 in the whole tissues (organ) yields for a steady case

$$\sum_{i=1}^{M} (Q_{\text{in}}C_{\text{b}}[\text{HbT}]\text{SO}_{2,\text{in}} - Q_{\text{out}}C_{\text{b}}[\text{HbT}]\text{SO}_{2,\text{out}}) = \sum_{i=1}^{M} l_i \pi d_i J_i \tag{4.48}$$

and M is the number of blood vessels inside the tissues. Likewise, (4.48) can be stated as if all the O_2 is consumed

$$Q[\text{HbT}]_{\text{blood}}(\text{SO}_{2,\text{ti}} - \text{SO}_{2,\text{to}}) = \text{OC}/4 \tag{4.49}$$

For a dynamic case, (4.49) is further written as follows:

$$Q[\text{HbT}]_{\text{blood}}(\text{SO}_{2,\text{ti}} - \text{SO}_{2,\text{to}}) - \text{OC}/4 = \frac{\partial M_{\text{HbO}_2}}{\partial t} \tag{4.50}$$

where Q is the mean BF for all the blood vessels inside the tissues and is specified as the mean BF of tissues, $[\text{HbT}]_{\text{blood}}$ is the mean total blood hemoglobin concentration in the blood circulating through the tissues, OC is the mean oxygen consumption for the whole tissue volume V_{tissue}, M_{HbO_2} is the molar amount of oxygenated hemoglobin inside the measurement volume, and $\text{SO}_{2,\text{ti}}$, $\text{SO}_{2,\text{to}}$ is the averaged hemoglobin oxygen saturation at the inlet(artery) and outlet(vena) of the tissues, respectively. Moreover, it is noted that the molar amount of oxygenated hemoglobin concentration is expressed as

$$M_{\text{HbO}_2} = \text{SO}_2[\text{HbT}]_{\text{tissue}}V_{\text{tissue}} = [\text{HbO2}]V_{\text{tissue}} \tag{4.51}$$

Substituting (4.51) into (4.50), we obtain

$$\begin{aligned} & -\frac{\mathrm{OC}}{4V_{\mathrm{tissue}}}+\frac{Q}{V_{\mathrm{tissue}}}[\mathrm{HbT}]_{\mathrm{blood}}(\mathrm{SO}_{2,\mathrm{ti}}-\mathrm{SO}_{2,\mathrm{to}}) \\ & =\mathrm{SO}_2\frac{\mathrm{d}[\mathrm{HbT}]_{\mathrm{tissue}}}{\mathrm{d}t}+[\mathrm{HbT}]_{\mathrm{tissue}}\frac{\mathrm{dSO}_2}{\mathrm{d}t}=\frac{\mathrm{d}[\mathrm{HbO}_2]}{\mathrm{d}t} \end{aligned} \tag{4.52}$$

where V_{tissue} is the tissue volume and is assumed constant here, and SO_2 is the oxygen saturation. If the oxygen supply of tissues depends on the averaged oxygen saturation at the inlet and outlet of the tissues, tissue oxygen saturation should represent the weighted average of the arterial and venous saturation:

$$\mathrm{SO}_2=f\mathrm{SO}_{2,\mathrm{ti}}+(1-f)\mathrm{SO}_{2,\mathrm{to}} \tag{4.53}$$

Equation (4.53) can be rewritten as follows:

$$\mathrm{SO}_{2,\mathrm{to}}=(\mathrm{SO}_2-f\mathrm{SO}_{2,\mathrm{ti}})/(1-f) \tag{4.54}$$

Based on (4.54) and (4.52), we get

$$\begin{aligned} \frac{\mathrm{d}SO_2}{\mathrm{d}t}= & -\frac{\mathrm{OC}}{4V_{\mathrm{tissue}}[\mathrm{HbT}]}+\frac{Q}{V_{\mathrm{tissue}}[\mathrm{HbT}]}[\mathrm{HbT}]_{\mathrm{blood}}\left(\frac{\mathrm{SO}_{2,\mathrm{ti}}}{1-f}-\frac{\mathrm{SO}_2}{1-f}\right) \\ & -\frac{\mathrm{d}[\mathrm{HbT}]}{\mathrm{d}t}\frac{\mathrm{SO}_2}{[\mathrm{HbT}]} \end{aligned} \tag{4.55}$$

Equation (4.55) is the developed mathematical model that connects changes in BF and OC to known HbT and SO_2 captured by DOT. As such, mean OC and BF can be recovered by fitting (4.55) to time-resolved tissue oxygenation measurements. Equation (4.55) is an ordinary partial differential equation that can be solved iteratively by Runge–Kutta fourth order method coupled with the finite element method [89]. The fitting method is described as follows: with any given initial values for OC and BF within the specified range, this scheme is to optimize the OC and BF parameters based on the solution of (4.55) to reach the following minimized objective function:

$$\text{Min: }\mathbf{F}=\sum_{i=1}^{M}(\mathrm{SO}_{2i}^{\mathrm{m}}-\mathrm{SO}_{2i}^{\mathrm{c}})^2 \tag{4.56}$$

in which $\mathrm{SO}_{2i}^{\mathrm{m}}$ is the measured oxygenation parameter from M discrete time points, $\mathrm{SO}_{2i}^{\mathrm{c}}$ is the calculated oxygenation parameter from (4.52) for the same time points. Note the BF and OC are assumed constant during the measurements for the specified time range, due to the need for a sufficient time interval to obtain stable fitting results. Finally, it should be pointed out that Carp et al. also used a model similar to (4.52) to analyze the dynamic response of compressed breast tissues though it seems that their model has no strong theoretical basis [90].

4.3 Diffuse Optical Imaging Instrumentation

4.3.1 Introduction

According to the type of measured signal, DOT experimental systems are usually classified into three modes: TD, FD, and CW. In the TD mode, the source light is ultra-short-pulsed and the remitted light pulses are broadened. In the FD mode, the source light intensity is amplitude-modulated sinusoidally at typically hundreds of MHz, and in the CW mode, the source light is usually time-invariant. The TD and FD modes are information-rich, but slower in data acquisition and also more expensive than CW mode. It is not clear which method among CW, FD, and TD performs the best. Since CW mode is the most popular and dominant in the field to date, we focus on the introduction of CW imaging systems.

The goal of neuroimaging is to localize or measure the neural activity with different stimuli. We therefore need to use fast CW imaging systems. The most successful series of studies using CW have been performed by the Hitachi Medical Corporation (Tokyo, Japan) using their ETG-100 system [91], which includes eight laser diodes at 780 nm and eight at 830 nm and eight avalanche photodiode lock-in detectors. CW measurements are taken from 24 distinct source–detector pairs held in a regular grid pattern. Typically, two wavelengths at approximately 780 and 830 nm have been chosen, as they lie in the isosbestic point where the absorptions of Hb and HbO_2 are equal. However, recent studies have shown that it is possible to select the optimal wavelengths experimentally or theoretically [73]. It has also be shown that high connector density, for example, 24 sources and 28 detectors embedded in a small probe array, are able to provide the highest spatial resolution of DOT using CW measurements [92].

4.3.2 CW DOT Instrumentation

We describe a multi-spectral CW DOT system [93]. Briefly, this DOT system consisted of four main functional units: light generation and delivery unit, optical fiber probe/interface, detection units, and computer system with DAQ (data acquisition board) and Digital I/O (Input/output). CW laser modules (at 8 wavelengths) were used as light sources which delivered light to source optical fibers by means of multichannel optical switches. Optical fiber probe/interface was specially designed for animal study as shown in Fig. 4.3. Light diffused through the rat head was collected and the detected signals were digitalized and stored into the computer. This DOT system was not fast and the data acquisition time was about 1 min per frame (6×6 measurements).

To speed up the data acquisition, a CCD camera-based measurement system was set up for fast neuroimaging and spectroscopy analysis. As shown in Fig. 4.4,

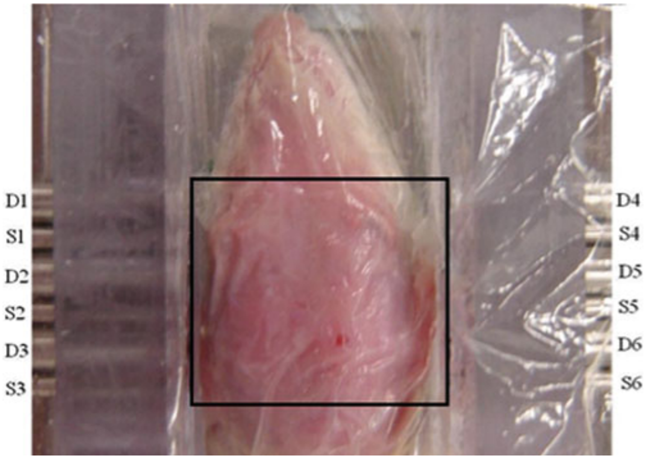

Fig. 4.3 Photograph of the fiberoptic/rat interface. *D* detection fibers; *S* source fibers. The imaging area is schematically shown as a *rectangle*

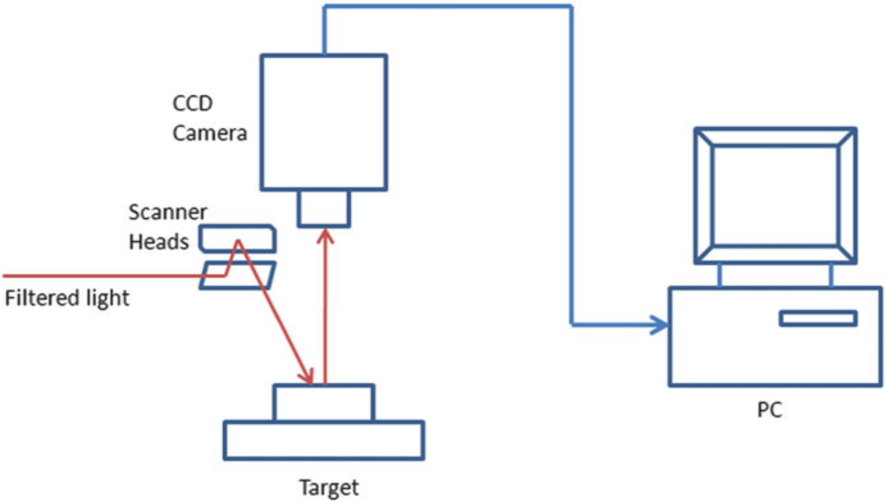

Fig. 4.4 CCD camera-based imaging setup

filtered light (700 and 750 nm) from a white light source was delivered through 2-axis open frame scanner heads to multiple source points, consequently on surface of the scalp area above the hippocampus. The screening site was imaged onto a CCD camera yielding a raw image of a ~12 × 12 mm area. Data acquisition time was about 750 ms per frame. This system is being used for imaging brain function in small animals.

4.4 In Vivo Application

As an example we demonstrate that DOT can be used to visualize the changes in local hemodynamics during seizures. The focal seizure was induced by microinjection 10 μL of 1.9 mM $GABA_A$ antagonist bicuculline methiodide (BMI) into the left parietal neocortex of a male Harlen Sprague–Dawley rat, which was imaged by a multi-spectral DOT system (Fig. 4.3). Functional images were obtained by the finite element-based nonlinear reconstruction algorithms described in Sect. 4.2. A series of dynamic 2D images were obtained to delineate the time course of changes of HbO_2, Hb, and HbT concentrations in the rat brain during seizure onset. The BMI-induced epileptic foci were localized and observed over time from the images obtained. The results suggest that DOT may be a promising modality for epilepsy imaging due to its ability to localize epileptic foci as well as its potential to map the functional activity in the area of human cerebral cortex in planning of epilepsy surgery.

4.4.1 Animals and the Focal Seizure Model

Animals used in this study were male Harlen Sprague–Dawley rats, weighing 50–60 g. A total of nine rats were used in this study, of which four were used for DOT and another five were used for electroencephalography (EEG) control study. The rats were housed in pairs in a controlled environment (Temperature: 21 ± 1°C; humidity: 60%; lights on at 8:00 A.M. to 8:00 P.M.; food and water ad lib). The experimental protocols and procedures involving animals and their care were conducted in conformity with NIH and IACUC committee at the University of Florida. Urethane 1 mg/kg was used to anesthetize the rats. A well-established animal model for focal seizures was used. The focal seizure was induced by microinjection $GABA_A$ antagonist BMI into the left parietal neocortex.

4.4.2 Experiment Method

As shown in Fig. 4.3, quadrate polycarbonate frames with six holes along each long side was used as an optic fiber holder. Anesthetized rats were mounted on a headset with ear bars and all hair on the scalp was shaved using hair removing lotion before a hole of 1 mm in diameter was drilled through the skull on the left parietal head region. A lab jack was used to adjust the height of the rat's head to a proper position (see Fig. 4.3). The top of the scalp was about 3–4 mm above the plane of the optical fiber array (imaging plane). A piece of clear polyethylene clingwrap was used to cover both the frame structure and the rat's head in order to load Intralipid 0.5% solution as coupling medium for filling the gap between the rat and the

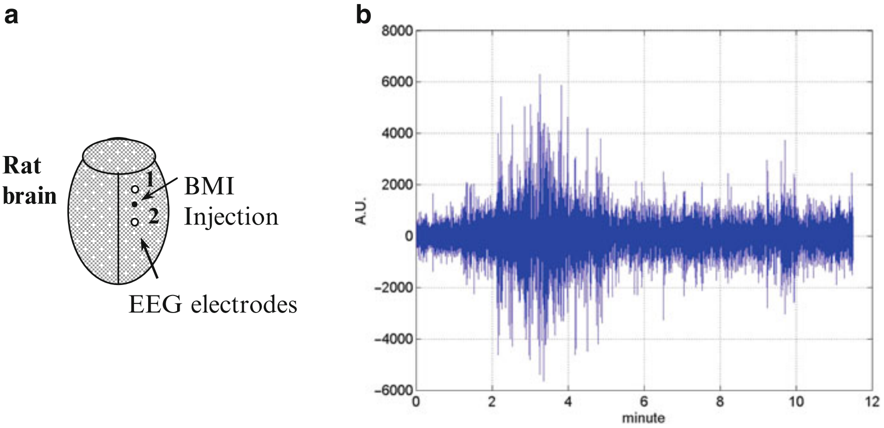

Fig. 4.5 (**a**) Locations of BMI injection (*solid dot*) and scalp EEG electrodes (*open circles*). (**b**) Twelve-minute scalp EEG recording after the injection of BMI on one rat

frame structure. Measurements were made before the BMI injection which was used as calibration data; 10 μL of BMI (1.9 mM) solution was injected by a syringe through the hole prepared before. DOT scans were conducted at several time points (1, 2, 4, 6, 8, and 25 min) after the BMI injection.

4.4.3 Electroencephalography Recording

Control experiments were conducted on five rats which were used for EEG recording in order to confirm the occurrence of focal seizure. Scalp EEG recording (two rats) from two electrodes 2.5 mm away from the BMI injection point (as shown in Fig. 4.5a) was recorded. In addition, multichannel EEG (Stellate EEG system) with four screw electrodes (three rats), which were advanced just below the skull and above the dura, was recorded to confirm the localization of seizures. As shown in Fig. 4.5a, two electrodes (#1 and #2) were on the same side of the injection point (left parietal neocortex), while the other two (#3 and #4) were on the opposite side. Distances from the injection point to the four electrodes were 3, 4, 6, and 7 mm, respectively. Rats were anesthetized with urethane (1 mg/kg), and the hairs were shaved with hair removing lotion. A hole of 1 mm in diameter was drilled through the skull on the left parietal head region before rats were put in a stereotaxic apparatus (Kopf), and the electrodes were put on or screwed in. Five-minute stabilized EEG was recorded before 10 μL of BMI (1.9 mM) solution was injected by a syringe through the hole prepared before. Thirty-minute EEG was recorded after the injection of BMI.

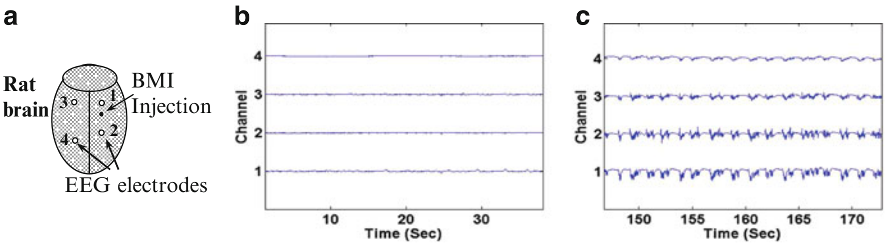

Fig. 4.6 (**a**) Locations of BMI injection (*solid dot*) and four EEG electrodes (*open circles*). (**b**, **c**) Four-channel EEG recordings from 0 to 40 s and 145 to 175 s on one rat after BMI injection, respectively

4.4.4 Results and Discussion

EEG was used to validate the seizure model. One sample of scalp EEG recording from 0 to 12 min after BMI injection is shown in Fig. 4.5b. Electrographic seizure onset occurs at 2 min following BMI injection as denoted by the rhythmic spiking and twofold increase in EEG amplitude from baseline EEG. Five minutes from the BMI injection time, the EEG postictal spikes are superimposed on the baseline activity. Four-channel EEG recordings from 0 to 40 s and 145 to 175 s on one rat after BMI injection are shown in Figs. 4.6b, c, respectively. Spikes show up in 145–175 s, which delineates the onset of seizures. The difference of amplitude among the signals recorded from four channels can be easily found, suggesting that the onset of seizure is localized.

Images of absolute absorption coefficient (μ_a/mm) at three wavelengths (633, 760 and 853 nm) were reconstructed at time points 1, 2, 4, 6, 8, and 25 min. Figure 4.7 presents the HbO_2, Hb, and HbT images derived from the absorption images at different time points. At the point of injection, localized increase of [HBO_2], [HB] and [HBT] (indicated by arrows) can be easily seen.

Here we also show the reconstruction results that demonstrate the feasibility of the recovery of mean BF and OC using the model described in Sect. 4.2.5. To reconstruct BF and OC, the initial parameters were given by: $HbT_{blood} = 0.72$ mM, $f = 0.2$, and $SO_{2,ti} = 0.98$. The dynamic HbT and SO_2 parameters were first calculated by fitting the reconstructed optical absorption coefficient using Beer's law at wavelengths 633, 760, and 853 nm. In addition, due to the highly nonlinear distribution of dynamic SO_2, the SO_2 distribution curve was separated into several approximated linear segments to improve the fitting accuracy of BF and OC. The mean BF and OC were fitted for each linear segment based on different initial values of HbT and SO_2. In this investigation, there were six measurements at 1, 2, 4, 6, 8, and 25 min after seizure onset. For each segment, only two discrete oxygenation measurements were used for the fitting calculation. We specified the fitted mean BF and OC for each segment as the values at the

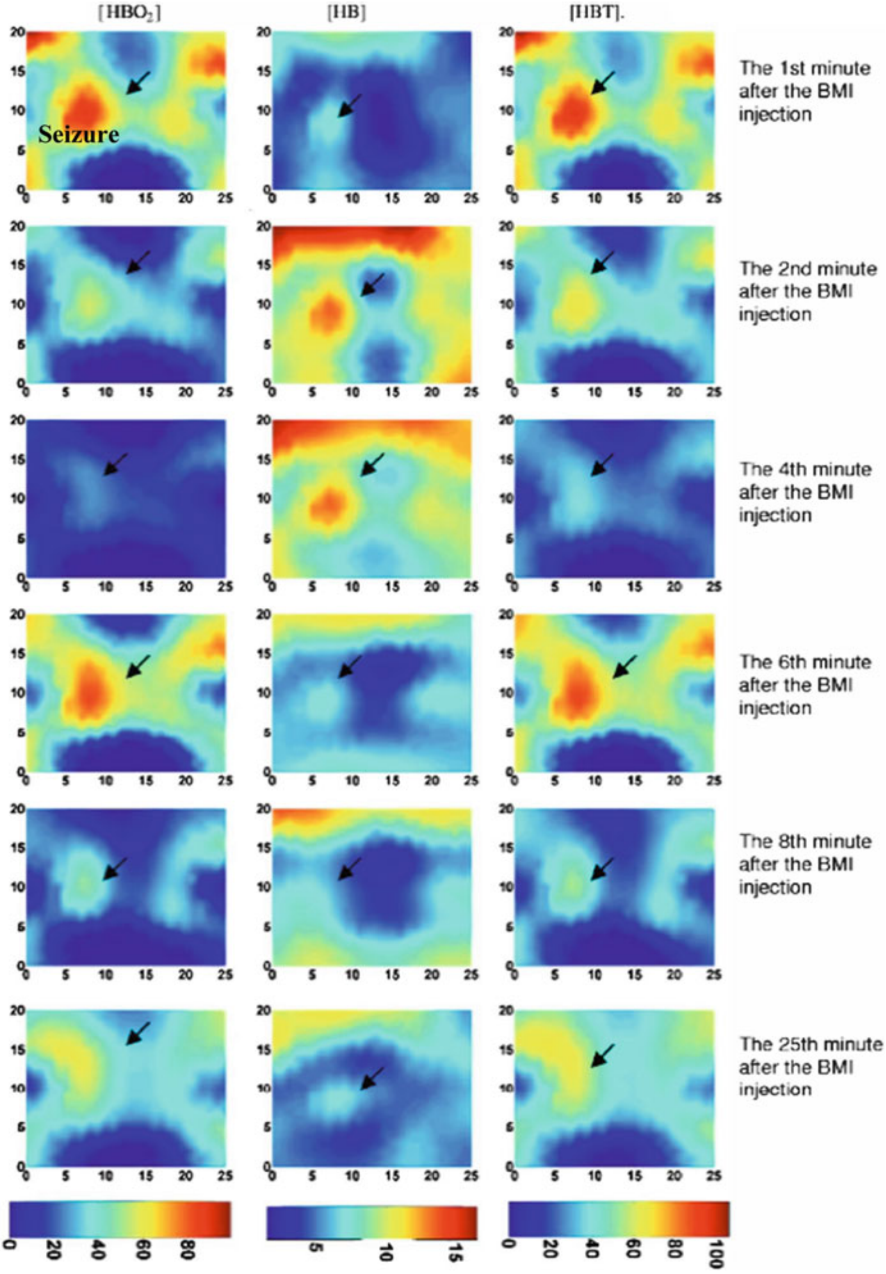

Fig. 4.7 Recovered HbO_2, Hb, and HbT (µM) images at different time points. *Left*: HbO_2, *middle*: Hb, *right*: HbT

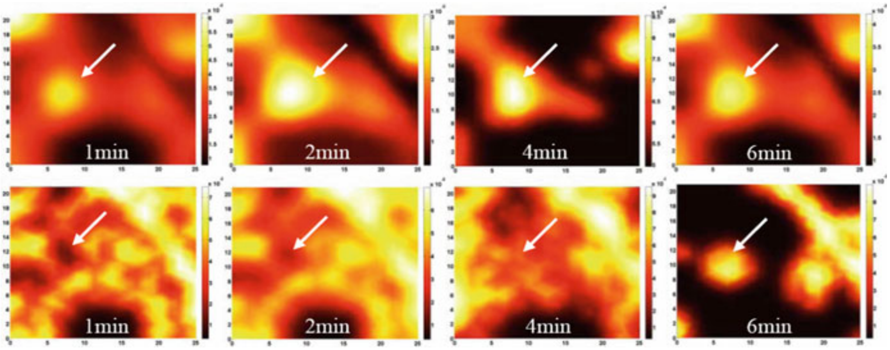

Fig. 4.8 Reconstructed volume normalized BF (mL/mL/s) (*top row*), and volume normalized OC (μmol/mL/s) (*bottom row*) images at different time points

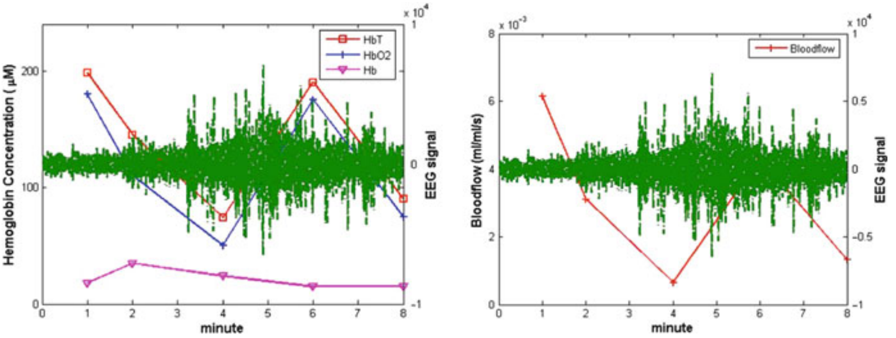

Fig. 4.9 The neurovascular and neurometabolic coupling. The *green line* shows the EEG signal

starting point of the segment. For example, we assumed the mean BF and OC fitted between minutes 1 and 2 as the BF and OC at minute 1.

Figure 4.8 presents the reconstructed volume normalized BF and OC images. We see that the seizure is clearly detected with the highest contrast in HbT, SO_2, and volume normalized BF. We note that the OC image is not effectively recovered due to the insufficient number of time points used to obtain stable fitting results. Further, it is observed from the peak values of BF shown in Fig. 4.8 that the recovered blood flow values (3.9–36.9 mL/100 mL/min) are in good agreement with the cerebral BF of rats (between 10 and 120 mL/100 mL/min) and humans (20–160 mL/100 mL/min) reported in the literature [94, 95]. The in vivo results shown here validate the merits of the mathematical model developed in Sect. 4.2.5.

Figure 4.9 shows that the hallmark of seizure onset correlates with the changes in blood volume, blood oxygenation, and blood flow. As revealed by the quantitative analysis, the auto-regulation of the brain was observed. From Fig. 4.9, we see that HbO_2 and BF oscillate from 1 to 8 min while Hb shows only a flat peak at 2 and 4 min after BMI injection. The fact that average BF, HbO_2 and Hb changed over time with different patterns indicates the auto-regulation which was the response of the seizure onset. Significant oscillation was found on the change of HbO_2 and BF instead of Hb which may also be due to auto-regulation. This is because Hb reflects the rate of metabolism while HbO_2 and BF are highly dependent on the vasomotion which can be contracted or dilated over time through auto-regulation. HbO_2 and BF in the seizure focus increased with oscillation and reached a peak at 6 min after BMI injection. Hb in the seizure focus increased slowly up to 4 min then decreased 6 min after the injection. These changes in HbO_2 and BF correlate well with the dynamics captured by the EEG measurements, which reveal the neurovascular and neurometabolic coupling mechanism in neural activity.

References

1. Yodh A, Chance B (1995) Spectroscopy and imaging with diffusing light. Phys Today 48:34–40
2. Gibson A, Dehghani H (2009) Diffuse optical imaging. Philos Trans R Soc A 367:3055–3072
3. Jiang H, Iftimia N, Xu Y, Eggert J, Fajardo L, Klove K (2002) Near-infrared optical imaging of the breast with model-based reconstruction. Acad Radiol 9:186–194
4. Srinivasan S, Pogue BW, Jiang S, Dehghani H, Kogel C, Soho S, Gibson JJ, Tosteson TD, Poplack SP, Paulsen KD (2003) Interpreting hemoglobin and water concentration oxygen saturation and scattering measured in vivo by near-infrared breast tomography. Proc Natl Acad Sci U S A 100:12349–12354
5. Zhu Q, Chen NG, Kurtzman SC (2003) Imaging tumor angiogenesis by use of combined near-infrared diffusive light and ultrasound. Opt Lett 28:337–339
6. Durduran T, Choe R, Culver JP, Zubkov L, Holboke MJ, Giammarco J, Chance B, Yodh AG (2002) Bulk optical properties of healthy female breast tissue. Phys Med Biol 47:2847–2861
7. Boas DA, Culver JP, Stott JJ, Dunn AK (2002) Three dimensional Monte Carlo code for photon migration through complex heterogeneous media including the adult human head. Opt Express 10:159–169
8. Hielscher AH, Klose AD, Scheel AK, Moa-Anderson B, Backhaus M, Netz U, Beuthan J (2004) Sagittal laser optical tomography for imaging of rheumatoid finger joints. Phys Med Biol 49:1147–1163
9. Pifferi A, Torricelli A, Taroni P, Bassi A, Chikoidze E, Giambattistelli E, Cubeddu R (2004) Optical biopsy of bone tissue: a step toward the diagnosis of bone pathologies. J Biomed Opt 9:474–480
10. Yuan Z, Zhang Q, Jiang HB (2007) 3D diffuse optical tomography imaging of osteoarthritis: initial results in finger joints. J Biomed Opt 12:034001
11. Yuan Z, Jiang H (2007) Image reconstruction schemes that combines modified Newton method and efficient initial guess estimate for optical tomography of finger joints. Appl Opt 46:2757–2768
12. Ntziachristos V, Bremer C, Graves EE, Ripoll J, Weissleder R (2002) In vivo tomographic imaging of near-infrared fluorescent probes. Mol Imaging 1:82–88
13. Cherry SR (2004) In vivo molecular and genomic imaging: new challenges for imaging physics. Phys Med Biol 49:R13–R48
14. Davis SC, Dehghani H, Wang J, Jiang S, Pogue BW, Paulsen KD (2007) Image-guided diffuse optical fluorescence tomography implemented with Laplacian-type regularization. Opt Express 15:4066–4082
15. Zhou C, Choe R, Shah N, Durduran T, Yu G, Durkin A, Hsiang D, Mehta R, Butler J, Cerussi A, Tromberg BJ, Yodh AG (2007) Diffuse optical monitoring of blood flow and oxygenation

in human breast cancer during early stages of neoadjuvant chemotherapy. J Biomed Opt 12:051903

16. Wilson BC, Patterson MS (1986) The physics of photodynamic therapy. Phys Med Biol 31:327–360
17. Pogue BW, Pitts JD, Mycek MA, Sloboda RD, Wilmot CM, Brandsema JF, O'Hara JA (2001) In vivo NADH fluorescence monitoring as an assay for cellular damage in photodynamic therapy. Photochem Photobiol 74:817–824
18. Cerussi A, Shah N, Hsiang D, Durkin A, Butler J, Tromberg BJ (2006) In vivo absorption, scattering, and physiologic properties of 58 malignant breast tumors determined by broadband diffuse optical spectroscopy. J Biomed Opt 11:044005
19. Dehghani H, Pogue BW, Poplack SP, Paulsen KD (2003) Multiwavelength three-dimensional near-infrared tomography of the breast: initial simulation, phantom, and clinical results. Appl Opt 42:135–145
20. Hebden JC, Yates TD, Gibson A, Everdell N, Arridge SR, Chicken DW, Douek M, Keshtgar MRS (2005) Monitoring recovery after laser surgery of the breast with optical tomography: a case study. Appl Opt 44:1898–1904
21. Yuan Z, Zhang Q, Sobel E, Jiang H (2010) Image-guided optical spectroscopy in diagnosis of osteoarthritis: a clinical study. Biomed Opt Express 1:74–86
22. Iftimia N, Jiang H (2000) Quantitative optical image reconstruction of turbid media by use of direct-current measurements. Appl Opt 39:5256–5261
23. Jiang H, Paulsen KD, Osterberg U, Pogue B, Patterson M (1996) Optical image reconstruction using frequency-domain data: simulations and experiments. J Opt Soc Am A 13:253–266
24. Paulsen KD, Jiang H (1995) Spatially-varying optical property reconstruction using a finite element diffusion equation approximation. Med Phys 22:691–701
25. Tromberg BJ, Pogue BW, Paulson KD, Yodh AG, Boas DA, Cerussi AE (2008) Assessing the future of diffuse optical imaging technologies for breast cancer management. Med Phys 35:2443–2452
26. Carpenter CM, Pogue BW, Jiang S, Dehghani H, Wang X, Paulson KD (2007) Image-guided optical spectroscopy provides molecular-specific information in vivo: MRI-guided spectroscopy of breast cancer hemoglobin, water, and scatter size. Opt Lett 32:933–935
27. Heekeren HR, Obrig H, Wenzel R, Eberle K, Ruben J, Villringer K, Kurth R, Villringer A (1997) Cerebral haemoglobin oxygenation during sustained visual stimulation—a near-infrared spectroscopy study. Philos Trans R Soc Lond B Biol Sci 352:743–750
28. Meek JH, Elwell CE, Khan MJ, Romaya J, Wyatt JS, Delpy DT, Zeki S (1995) Regional changes in cerebral haemodynamics as a result of a visual stimulus measured by near infrared spectroscopy. Proc R Soc Lond B Biol Sci 261:351–356
29. Ruben J, Wenzel R, Obrig H, Villringer K, Bernarding J, Hirth C, Heekeren H, Dirnagl U, Villringer A (1997) Haemoglobin oxygenation changes during visual stimulation in the occipital cortex. Adv Exp Med Biol 428:181–187
30. Sakatani K, Chen S, Lichty W, Zuo H, Wang YP (1999) Cerebral blood oxygenation changes induced by auditory stimulation in newborn infants measured by near infrared spectroscopy. Early Hum Dev 55:229–236
31. Franceschini MA, Fantini S, Thompson JH, Culver JP, Boas DA (2003) Hemodynamic evoked response of the sensorimotor cortex measured non-invasively with near infrared optical imaging. Psychophysiology 40:548–560
32. Colier WN, Quaresima V, Oeseburg B, Ferrari M (1999) Human motor-cortex oxygenation changes induced by cyclic coupled movements of hand and foot. Exp Brain Res 129:457–461
33. Hirth C, Obrig H, Villringer K, Thiel A, Bernarding J, Muhlnickel W, Flor H, Dirnagl U, Villringer A (1996) Non-invasive functional mapping of the human motor cortex using near-infrared spectroscopy. Neuroreport 7:1977–1981
34. Kleinschmidt A, Obrig H, Requardt M, Merboldt KD, Dirnagl U, Villringer A, Frahm J (1996) Simultaneous recording of cerebral blood oxygenation changes during human brain activation

by magnetic resonance imaging and near-infrared spectroscopy. J Cereb Blood Flow Metab 16:817–826

35. Sato H, Takeuchi T, Sakai KL (1999) Temporal cortex activation during speech recognition: an optical topography study. Cognition 73:B55–B66
36. Adelson PD, Nemoto E, Scheuer M, Painter M, Morgan J, Yonas H (1999) Noninvasive continuous monitoring of cerebral oxygenation periictally using near-infrared spectroscopy: a preliminary report. Epilepsia 40:1484–1489
37. Sokol DK, Markand ON, Daly EC, Luerssen TG, Malkoff MD (2000) Near infrared spectroscopy (NIRS) distinguishes seizure types. Seizure 9:323–327
38. Steinhoff BJ, Herrendorf G, Kurth C (1996) Ictal near infrared spectroscopy in temporal lobe epilepsy: a pilot study. Seizure 5:97–101
39. Watanabe E, Maki A, Kawaguchi F, Yamashita Y, Koizumi H, Mayanagi Y (2000) Noninvasive cerebral blood volume measurement during seizures using multichannel near infrared spectroscopic topography. J Biomed Opt 5:287–290
40. Eschweiler GW, Wegerer C, Schlotter W, Spandl C, Stevens A, Bartels M (2000) Left prefrontal activation predicts therapeutic effects of repetitive transcranial magnetic stimulation (rTMS) in major depression. Psychiatry Res 99:161–172
41. Matsuo K, Kato T, Fukuda M, Kato N (2000) Alteration of hemoglobin oxygenation in the frontal region in elderly depressed patients as measured by near-infrared spectroscopy. J Neuropsychiatry Clin Neurosci 12:465–471
42. Okada F, Takahashi N, Tokumitsu Y (1996) Dominance of the nondominant T hemisphere in depression. J Affect Disord 37:13–21
43. Frostig RD, Lieke EE, Tso DY, Grinvald A (1990) Cortical functional architecture and local coupling between neuronal activity and the microcirculation revealed by in vivo high-resolution optical imaging of intrinsic signals. Proc Natl Acad Sci U S A 87:6082–6086
44. Hanlon EB, Itzkan I, Dasari RR, Feld MS, Ferrante RJ, McKee AC, Lathi D, Kowall NW (1999) Near-infrared fluorescence spectroscopy detects Alzheimer's disease in vitro. Photochem Photobiol 70:236–242
45. Hock C, Villringer K, Muller-Spahn F, Hofmann M, Schuh-Hofer S, Heekeren H, Wenzel R, Dirnagl U, Villringer A (1996) Near infrared spectroscopy in the diagnosis of Alzheimer's disease. Ann N Y Acad Sci 777:22–29
46. Chen WG, Li PC, Luo QM, Zeng SQ, Hu B (2000) Hemodynamic assessment of ischemic stroke with near-infrared spectroscopy. Space Med Med Eng 13:84–89
47. Nemoto EM, Yonas H, Kassam A (2000) Clinical experience with cerebral oximetry in stroke and cardiac arrest. Crit Care Med 28:1052–1054
48. Saitou H, Yanagi H, Hara S, Tsuchiya S, Tomura S (2000) Cerebral blood volume and oxygenation among poststroke hemiplegic patients: effects of 13 rehabilitation tasks measured by near-infrared spectroscopy. Arch Phys Med Rehabil 81:1348–1356
49. Vernieri F, Rosato N, Pauri F, Tibuzzi F, Passarelli F, Rossini PM (1999) Near infrared spectroscopy and transcranial Doppler in monohemispheric stroke. Eur Neurol 41:159–162
50. Boas DA, Dale AM, Franceschini MA (2004) Diffuse optical imaging of brain activation: approaches to optimizing imaging sensitivity, resolution and accuracy. Neuroimage 23: s275–s288
51. Taber KH, Hillman E, Hurley R (2010) Optical imaging: a new window to the adult brain. J Neuropsychiatry Clin Neurosci 22(4):356–360
52. Koch SP, Habermehl C, Mehnert J et al (2010) High-resolution optical functional mapping of the human somatosensory cortex. Front Neuroenergetics 2:12
53. White BR, Culver JP (2010) Phase-encoded retinotopy as an evaluation of diffuse optical neuroimaging. Neuroimage 49:568–577
54. White BR, Snyder AZ, Cohen AL et al (2009) Mapping the human brain at rest with diffuse optical tomography. Conf Proc IEEE Eng Med Biol Soc 2009:4070–4072

55. White BR, Snyder AZ, Cohen AL, Petersen SE, Raichle ME, Schlaggar BL, Culver JP (2009) Resting-state functional connectivity in the human brain revealed with diffuse optical tomography. Neuroimage 47:148–156
56. Arridge SR (1999) Optical tomography in medical imaging. Inverse Probl 15:R41–R93
57. Boas DA, Brooks DH, Miller EL, Marzio CAD, Kilmer M, Gaudette RJ, Zhang Q (2001) Imaging the body with diffuse optical tomography. IEEE Signal Process Mag 18:57–75
58. Schweiger M, Gibson AP, Arridge S (2003) Computational aspects of diffuse optical tomography. IEEE Comput Sci Eng 5:33–41
59. Yamamoto T, Maki A, Kadoya T, Tanikawa Y, Yamada Y, Okada E, Koizumi H (2002) Arranging optical fibres for the spatial resolution improvement of topographical images. Phys Med Biol 47:3429–3440
60. Hielscher AH, Alcouffe RE, Barbour RL (1998) Comparison of finite-difference transport and diffusion calculations for photon migration in homogeneous and heterogeneous tissues. Phys Med Biol 43:1285–1302
61. Yuan Z, Hu X, Jiang H (2009) A higher-order diffusion model for three-dimensional photon migration and image reconstruction in optical tomography. Phys Med Biol 54:65–88
62. Tikhonov A (1977) Solutions of ill-posed problems. Wiley, New York
63. Levenberg K (1944) A method for the solution of certain nonlinear problems in least square. Q Appl Math 2:164–168
64. Marquardt DW (1963) An algorithm for least-squares estimation of nonlinear parameters. J Soc Ind Appl Math 11:431–441
65. Brooksby B, Dehghani H, Pogue B, Paulsen KD (2003) Near Infrared (NIR) tomography breast reconstruction with a prior structural information from MRI: algorithm development reconstruction heterogeneities. IEEE J Sel Top Quantum Electron 9:199–209
66. Barbour RL, Graber HL, Chang J, Barbour SS, Koo PC, Aronson R (1995) MRI-guided optical tomography: prospects and computation for a new imaging method. IEEE Comput Sci Eng 2:63–77
67. Zhang Q, Brukilacchio TJ, Li A, Scott J, Chaves T, Hillman E, Wu T, Chorlton M, Rafferty E, Moore RH, Kopans DB, Boas DA (2005) Coregistered tomography x-ray and optical breast imaging: initial results. J Biomed Opt 10:024033
68. Yuan Z, Jiang H (2010) High resolution x-ray guided three dimensional diffuse optical tomography of joint tissues in hand osteoarthritis: morphological and functional assessments. Med Phys 37(8):4343–4354
69. Konecky SD, Wienery R, Choe R, Corlu A, Lee K, Srinivasy SM, Saffer JR, Freifeldery R, Karpy JS, Yodh AG (2006) Diffuse optical tomography and position emission tomography of human breast. Biomedical Optics Topical Meeting and Tabletop Exhibit, Fort Lauderdale, FL
70. Yuan Z, Zhang Q, Sobel E, Jiang HB (2008) Tomographic x-ray-guided three-dimensional diffuse optical tomography of osteoarthritis in the finger joints. J Biomed Opt 13:044006
71. http://omlc.ogi.edu/spectra/hemoglobin/index.html
72. Li A, Zhang Q, Culver JP, Miller E, Boas DA (2004) Reconstructing chromosphere concentrations images directly by continuous-wave diffuse optical tomography. Opt Lett 29:256–259
73. Corlu A, Durduran T, Choe R, Schweiger M, Hillman EM, Arridge SR, Yodh AG (2003) Uniqueness and wavelength optimization in continuous-wave multispectral diffuse optical tomography. Opt Lett 28:2339–2341
74. Durduran T, Yu G, Burnett M, Detre J, Greenberg J, Wang J, Zhou C, Yodh AG (2004) Diffuse optical measurement of blood flow, blood oxygenation, and metabolism in a human brain during sensorimotor cortex activation. Opt Lett 29:1766–1768
75. Dunn A, Devor A, Bolay H, Andermann M, Moskowitz M, Dale A, Boas DA (2003) Simultaneous imaging of total cerebral hemoglobin concentration, oxygenation, and blood flow during functional activation. Opt Lett 28:28–30
76. Lauritzen M (2001) Relationship of spikes, synaptic activity, and local changes of cerebral blood flow. J Cereb Blood Flow Metab 21:1367–1383

77. Logothetis NK, Pauls J, Augath M, trinath T, Oeltermann A (2001) Neurophysiological investigation of the basics of the fMRI signal. Nature 412:150–157
78. Sakadzic S, Yuan S, Dilekoz E, Ruvinskaya S, Vinogradov A, Ayata C, Boas DA (2009) Simultaneous imaging of cerebral partial pressure of oxygen and blood flow during functional activation and cortical spreading depression. Appl Opt 48:169–177
79. Logothetis NK (2008) What we can do and what we cannot do with fMRI. Nature 453:869–878
80. Williams DS, Detre JA, Leigh JS, Koretsky AP (1992) Magnetic resonance imaging of perfusion using spin inversion of arterial water. Proc Natl Acad Sci 89:212–216
81. Mintun MA, Raichle ME, Martin WR, Herscovitch P (1984) Brain oxygen utilization measured with O-15 radiotracers and positron emission tomography. J Nucl Med 25:177–187
82. Patel J, Marks K, Roberts I, Azzopardi D, Edwards AD (1998) Measurement of cerebral blood flow in newborn infants using near infrared spectroscopy with indocyanine green. Pediatr Res 43:34–39
83. Fabricius M, Akgoren N, Dirnagl U, Lauritzen M (1997) Laminar analysis of cerebral blood flow in cortex of rats by laser-Doppler flowmetry, a pilot study. J Cereb Blood Flow Metab 17:1326–1336
84. Cheung C, Culver JP, Takahashi K, Greenberg JH, Yodh AG (2001) In vivo cerebrovascular measurement combining diffuse near-infrared absorption and correlation spectroscopies. Phys Med Biol 46:2053–2065
85. Kirkham FJ, Padayachee TS, Parsons S, Seargeant LS, House FR, Gosling RG (1986) Transcranial measurement of blood velocities in the basal cerebral arteries using pulsed Doppler ultrasound: velocity as an index of flow. Ultrasound Med Biol 12:15–21
86. Themelis G, D'Arceuil H, Diamond SG, Thaker S, Huppert TJ, Boas DA, Franceschini MA (2007) Near-infrared spectroscopy measurement of the pulsatile component of cerebral blood flow and volume from arterial oscillations. J Biomed Opt 12:014033
87. Tsai AG, Johnson PC, Intaglietta M (2003) Oxygen gradients in the microcirculation. Physiol Rev 83:933–963
88. Sharan M, Vovenko EP, Vadapalli A, Popel AS, Pittman RN (2008) Experimental and theoretical studies of oxygen gradients in rat pial micro vessels. J Cereb Blood Flow Metab 28:1597–1604
89. Michael M, William HP, Saul AT, William TV, Brian PF (1986–1992) Numerical recipes in Fortran 77. Cambridge University Press, Cambridge
90. Carp SA, Selb J, Fang Q, Moore R, Kopans DB, Rafferty E, Boas DA (2008) Dynamic functional and mechanical response of breast tissue to compression. Opt Express 16:16064–16078
91. Koizumi H, Yamamoto T, Maki A, Yamashita Y, Sato H, Kawaguchi H, Ichikawa N (2003) Optical topography: practical problems and new applications. Appl Opt 42:3054–3062
92. Zeff B, White BR, Dehghani H, Schlagger BL, Culver JP (2007) Retinotopic mapping of adult human visual cortex with high-density diffuse optical tomography. Proc Natl Acad Sci USA 104:12169–12174
93. Wang Q, Liang X, Zhang Q, Camey P, Jiang H (2008) Visualizing localized dynamic changes during epileptic seizure onset in vivo with diffuse optical tomography. Med Phys 35:21–224
94. Hernandez MJ, Brennan RW, Nowman GS (1978) Cerebral blood flow autoregulation in the rats. Stroke 9:150–154
95. Sharples PM, Stuart AG, Matthews DS, Aynsley-Green A, Eyre JA (1995) Cerebral blood flow and metabolism in children with severe head injury. Part 1: relation to age, Glasgow coma score, outcome, intracranial pressure, and time after injury. J Neurol Neurosurg Psychiatry 58:145–152

Chapter 5
Laser Speckle Imaging of Cerebral Blood Flow

Lisa M. Richards, Erica L. Towle, Douglas J. Fox, and Andrew K. Dunn

5.1 Introduction

The ability to visualize and monitor dynamic blood flow changes in tissue is of great importance for a wide range of applications and diseases, especially during surgical procedures. Vascular injury or irreversible tissue damage can result if a surgeon inadvertently occludes a vessel and does not repair the blockage quickly. This is particularly important when the tissue of interest is the brain, since prolonged ischemia can result in postoperative functional deficits. Thus, monitoring cerebral blood flow (CBF) during neurosurgery provides important physiological information and can help improve surgical outcomes for a wide variety of procedures. In order to minimize the amount of functional loss incurred by patients undergoing brain surgery, surgeons must be able to assess cortical function relative to the pathology to maintain a balance between sufficient resection of pathological tissue and preservation of motor, language, and sensory function. For procedures that require the removal of diseased brain tissue such as tumor resection or epilepsy, monitoring CBF can be used to localize areas of eloquent brain tissue and to assess postsurgical tissue viability. Monitoring CBF is particularly important during cerebrovascular procedures such as aneurysm clipping or vessel bypass, where the surgeon is operating directly on the blood vessels. The surgeon must be able to assess whether blood flow has returned to pre-surgical baseline levels in parent and branching vessels and identify residual stenosis or occlusion intraoperatively to reduce the risk of ischemic stroke and irreversible brain damage. Currently, surgeons rely on qualitative visual inspection under standard visible light, or use one of the clinically

---

L.M. Richards • E.L. Towle • A.K. Dunn (✉)
Department of Biomedical Engineering, The University of Texas at Austin, Austin, TX 78712, USA
e-mail: adunn@mail.utexas.edu

D.J. Fox
NeuroTexas Institute, St. David's Hospital, Austin, TX 78705, USA

S.J. Madsen (ed.), *Optical Methods and Instrumentation in Brain Imaging and Therapy*, Bioanalysis: Advanced Materials, Methods, and Devices 3,
DOI 10.1007/978-1-4614-4978-2_5, © Springer Science+Business Media New York 2013

available intraoperative vascular monitoring technologies. In most cases, vessel occlusions are not visible to the naked eye, making visual assessment an unreliable monitoring solution. Although there are multiple intraoperative vascular monitoring techniques available, none of them are dependable under all circumstances and improvement is still needed to address the existing shortcomings.

The most widely used intraoperative vascular monitoring tools include the gold standard intraoperative digital subtraction angiography (DSA) [1–4], electrophysiological monitoring [5–7], neuroendoscopy [8–10], microvascular Doppler sonography [11–13], and indocyanine green angiography (ICGA) [14–17]. Recently, Gruber et al. [18] evaluated these techniques for use during aneurysm clipping procedures, concluding that the techniques were "complementary rather than competitive in nature" and all had disadvantages when used as a stand-alone method. Relative to the other available techniques, near-infrared ICGA has emerged as a popular and important intraoperative tool only recently after integration into surgical microscope platforms from multiple manufacturers [19–21]. This provides a simple, real-time method for examining intravascular fluorescent activity in the operating field and allows the surgeon to visualize vascular blockages or stenosis. However, ICGA does not directly provide quantitative flow information and requires the injection of a fluorescent dye. This limits the use of the technique to only a few instances during a given surgery and requires a delay between repeat uses due to the presence of residual dye in the vasculature, meaning that perfusion cannot be continuously monitored. Also, patients who have an iodine allergy or have significant liver disease may be ineligible for safe use of the contrast agent [22]. Thus, the ability to obtain similar information provided by ICG fluorescence without the need for a contrast agent could be a major advantage, both for surgeons who will be able to continuously visualize perfusion during the procedure and for patients who are not a candidate for the ICG injection.

Optical techniques for monitoring flow in the clinical environment are based on dynamic light scattering and utilize either the Doppler Effect or time-varying laser speckle [23]. Laser Doppler techniques provide quantitative flow information, but are typically limited to single point measurements that require mechanical scanning to provide spatial information [24–26]. Full-field laser Doppler instruments have recently been developed with speeds up to 12 frames per second [27, 28] and Raabe et al. [29] used a system to image CBF intraoperatively, demonstrating functional activation areas consistent with fMRI and electrostimulation. Laser speckle imaging is based on the same phenomenon and provides a significant advantage in temporal resolution compared to laser Doppler systems. Because rapid processing techniques are available for computing and displaying the speckle contrast images [30], the temporal resolution of a laser speckle contrast imaging (LSCI) system is determined by the frame rate of the camera and may be >200 Hz for high-speed cameras available today. This method provides a relatively simple technique for visualizing detailed spatiotemporal dynamics of blood flow changes in real time with high spatial resolution. LSCI has been used for a large number of blood flow imaging applications in tissue, including the retina, skin, and brain. These tissues are particularly well suited for LSCI because the vasculature of interest is generally superficial. LSCI is unable to sense blood flow deeper than a few hundred microns because of the illumination and detection geometry, meaning that visual access to the vasculature is required. Although shallow penetration depth is a limitation of the technique, it makes LSCI ideal for use during surgery when the tissue is already exposed. LSCI has been used intraoperatively during neurosurgery with promising results, both with a commercially available system [31] and with a microscope-integrated design [32, 33]. This chapter reviews the physics behind LSCI and describes its utility as an intraoperative tool for monitoring blood flow during neurosurgical applications.

5.2 Laser Speckle Imaging Physics

Laser speckle is a random interference pattern produced when coherent light scatters from a random medium. The laser light scatters from different positions within the medium and travels slightly different path lengths, resulting in constructive and destructive interference. When the backscattered light is imaged onto a camera sensor, the interference produces a 2D randomly varying intensity pattern known as speckle. If the random medium is made up of individual moving scatterers, such as red blood cells within the vasculature of heterogeneous tissue, the speckle pattern fluctuates in time as a result of phase shifts in the backscattered light. By imaging the time-varying speckle pattern onto a camera with an exposure time (5–10 ms) greater than the time scale of the speckle intensity fluctuations (typically <1 ms for biological tissues), the camera integrates the temporal intensity fluctuations, resulting in blurring of the speckle pattern. Thus, areas of higher motion have more rapid intensity fluctuations and therefore more blurring of the speckles during the camera exposure. Since the motion of the scattering particles is encoded in the dynamics of the speckle pattern, a measure of blood flow can be obtained by quantifying the spatial blurring of the speckle pattern. This is accomplished by calculating the local speckle contrast, K, defined as the ratio of the standard deviation, σ_s, to the mean intensity of pixel values, $\langle I \rangle$, within small regions of the acquired image [34],

$$K(T) = \frac{\sigma_s(T)}{\langle I \rangle}, \tag{5.1}$$

where T is the exposure time of the camera. Thus, the speckle contrast is a measure of the local spatial contrast in the speckle pattern. The speckle contrast image is a spatially resolved map of the local speckle contrast and is calculated from the raw speckle image by computing this ratio at each pixel from the surrounding $N \times N$ pixel region (typically $N = 7$). Theoretically, the speckle contrast ranges between 0 and 1 when the speckle pattern is sampled properly [35], where $K = 1$ indicates no blurring and therefore no motion and $K = 0$ means that the scatterers are moving fast enough to average out all of the speckles.

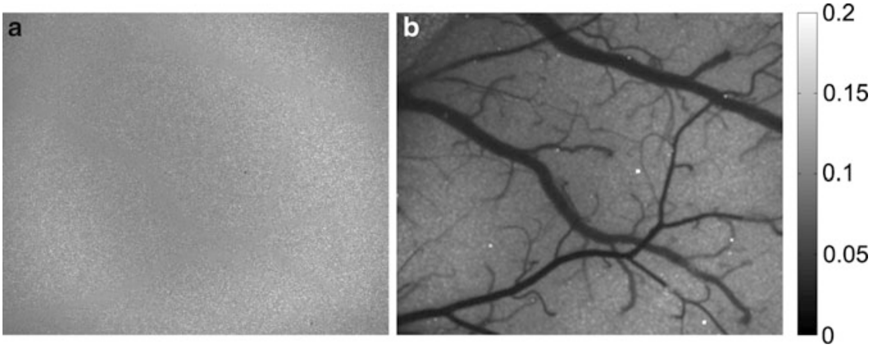

Fig. 5.1 (**a**) Example of a raw speckle image taken from a rat cerebral cortex with a 3 mm field of view, which shows a grainy pattern with some areas of spatial blurring visible. (**b**) The corresponding speckle contrast image is calculated using a 7 × 7 pixel sliding window, which shows the blood vessels on the surface of the brain with high spatial resolution. Although the raw image appears to contain little information, the speckle contrast image reveals a tremendous amount of information about the motion of the scattering particles in the sample

A typical example of a raw speckle image and the computed speckle contrast are shown in Fig. 5.1, which was taken from a rat cerebral cortex under normal conditions. The raw speckle image illustrates the grainy appearance of the speckle pattern. The speckle contrast image, computed directly from the raw speckle image using (5.1), represents a 2D map of motion occurring in the tissue, which is primarily due to blood flow. Areas of higher baseline flow, such as large vessels, have lower K values and appear darker in the speckle contrast image. Although speckle contrast values are indicative of the magnitude of motion in the sample, they are not linearly proportional to speed or flow. The exact quantitative relationship between speckle contrast and underlying flow is a complex function that is not completely understood for biological tissue and remains an active area of research [36].

The theory of correlation functions used in dynamic light scattering theory can be used to calculate the speckle correlation time τ_c from the speckle contrast values, which can then be related to the underlying flow or speed. The temporal fluctuations of speckles can be quantified using the electric field autocorrelation function $g_1(\tau)$. Because $g_1(\tau)$ is difficult to measure, the intensity autocorrelation function $g_2(\tau)$ is recorded and can be related to $g_1(\tau)$ using the Siegert relation [37]

$$g_2(\tau) = 1 + \beta |g_1(\tau)|^2, \tag{5.2}$$

where β is a normalization term that accounts for speckle averaging due to mismatch between speckle size and pixel size as well as polarization and coherence effects. The speckle correlation time τ_c is the characteristic decay time of the speckle autocorrelation function. The original relationship between $K(T)$ and τ_c was first proposed by Fercher and Briers in 1981 [38] and is given by

$$K(T, \tau_c) = \left(\frac{1 - \mathrm{e}^{-2x}}{2x} \right)^{1/2}, \tag{5.3}$$

where $x = T/\tau_c$. This expression has been widely used in the literature since its original introduction. Recently, a more accurate expression has been proposed by Bandyopadhyay et al. [39] to account for speckle averaging effects and is given by

$$K(T, \tau_c) = \left(\beta \frac{e^{-2x} - 1 + 2x}{2x^2}\right)^{1/2}. \tag{5.4}$$

Using simplifying assumptions, the speckle correlation time τ_c is assumed to be inversely proportional to blood flow, meaning that a smaller τ_c corresponds to a faster moving particles (red blood cells) in the tissue [23, 40]. Thus, the measured speckle contrast values are converted to correlation time using either (5.3) or (5.4) and relative blood flow changes can be calculated by computing the change in τ_c from a baseline value [41].

5.3 Instrumentation

One of the reasons LSCI has become widely adopted is the relative simplicity of the instrumentation required to image blood flow. The hardware for LSCI consists of a coherent light source such as a laser diode for illuminating the tissue, a camera for detection of the backscattered light, and imaging optics to focus the light onto the camera sensor. A traditional laboratory LSCI setup is shown in Fig. 5.2a. The laser beam is expanded and adjusted to illuminate the tissue area of interest, which may vary from a few millimeters in a small animal model to several centimeters in a clinical setting. The laser beam may be angled towards the tissue surface or have a near normal incidence and the wavelength of the laser is typically in the red to near infrared region to minimize effects from hemoglobin absorption. The camera specifications for LSCI vary widely in the literature, but generally a standard CCD or CMOS camera can be used. Because high light levels reach the camera, high dynamic range cooled cameras are usually not required for LSCI and inexpensive 8-bit cameras can provide excellent images of blood flow [42, 43].

To be clinically useful to surgeons, the LSCI technology must be integrated into the existing surgical platform. Although Hecht et al. [31] demonstrated intraoperative use with a standalone commercial LSCI instrument, the surgery must be interrupted to position the instrument over the surgical field of view. Thus, for use during neurosurgery, we integrated the LSCI hardware into the Zeiss Pentero neurosurgical microscope, which was convenient to use and allowed visualization of the tissue perfusion with minimal additional setup time [32, 33]. A schematic of the adapted microscope is shown in Fig. 5.2b. To illuminate the brain, the laser diode ($\lambda = 660$ nm, $P = 130$ mW) was incorporated into a microscope add-on laser adapter, which was attached to the bottom of the microscope head. A wavelength in the visible range was chosen due to the visible

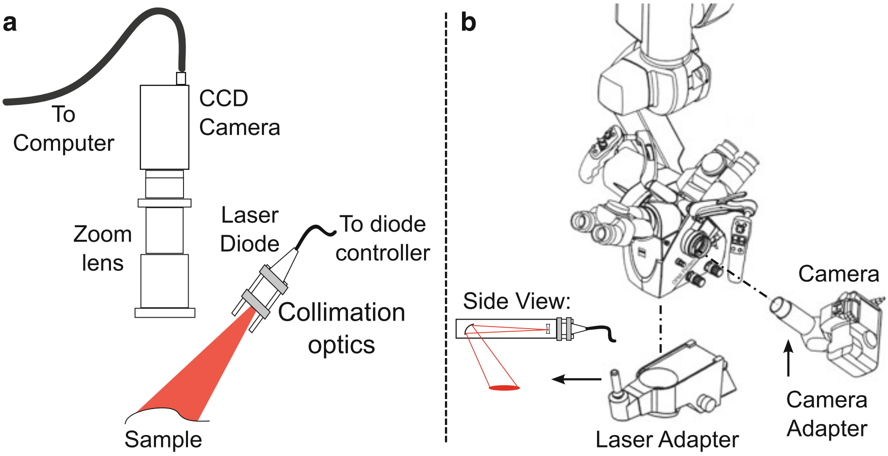

Fig. 5.2 (**a**) Traditional laboratory LSCI setup consisting of a laser diode, imaging optics, and a camera. (**b**) Intraoperative LSCI setup, where all components of the traditional setup are integrated into the Zeiss OPMI Pentero neurosurgical microscope (adapted from the Zeiss Pentero Manual version 9.3)

wavelength pass filters (400–700 nm) built-into the microscope. The laser beam travels linearly through the adapter until it encounters a curved mirror, which directs the beam towards the cortex as shown in the side view of Fig. 5.2b. The steering toggle on the laser adapter controls the angle of the mirror, which allows positioning of the laser beam on the tissue area of interest. The laser power was adjusted using a laser diode controller and was measured to be 28 mW/cm^2 for typical settings used, which is far below the ANSI standard of 200 mW/cm^2 for maximum permissible exposure to a visible laser beam [44]. An 8-bit camera (Basler 602f) was connected to one of the side viewing ports on the microscope using a c-mount camera adapter. This enabled the use of imaging optics built into the microscope to focus the camera and zoom into the area of interest on the tissue surface. The addition of the laser and camera did not interfere with the normal sterile draping of the microscope, meaning that the surgeon could use the microscope as desired during the operation. When the surgeon was ready to perform LSCI imaging, the microscope's built-in illumination was turned off and the laser was turned on for imaging. During the image acquisition, the patient's electrocardiogram (ECG) signal was also recorded from an existing anesthesia monitoring system in the operating room and was used during post-processing and analysis to help remove pulsatile motion artifacts. Integration of the equipment into an existing neurosurgical microscope allows real-time blood flow imaging with minimal interference to the procedure, which is an important consideration for intraoperative imaging applications.

5.4 Simultaneous Imaging of ICG Fluorescence and LSCI

As discussed previously, ICG fluorescence angiography has been widely examined in the neurosurgical community and has been integrated into the neurosurgical microscopes from multiple manufacturers. Thus, it is of great interest to compare LSCI and ICG fluorescence directly to examine the information obtained from both methods. In a rat model, we performed LSCI and ICG fluorescence imaging simultaneously, using two cameras and a 785 nm laser both as the excitation source for the ICG dye and the coherent source for LSCI. A dichroic beam splitter was used to direct the backscattered excitation light (785 nm) towards the LSCI camera and the ICG fluorescence emission light (820–835 nm) towards the ICG camera. The cameras were adjusted so that both imaged the same area of interest through an objective lens. Images were captured from a rat cerebral cortex after craniotomy and a change in physiology was introduced by occluding a vessel within the field of view. First, a comparison is illustrated for baseline normal physiological flow. In Fig. 5.3, baseline LSCI images are overlaid to show relative blood flow differences throughout the field of view as indicated by LSCI in (a) and ICG in (b). The LSCI overlay has been thresholded to show high flow areas where the flow rate is three times greater than the surrounding parenchyma tissue. The correlation time image was used to determine areas of high flow relative to the parenchyma tissue. The overlay identifies the largest vessels in the field of view, with dark red indicating fastest flow and yellow indicating slower flow. The ICG fluorescence can be quantified by the speed of the dye wash-in, measured by the time taken for the dye to reach maximum fluorescence (rise time). Thus, the ICG overlay has been thresholded to show the wash-in times of the ICG dye, with red indicating earlier wash-in (shorter rise time) and blue indicating later wash-in (longer rise time). This image allows separation of the arteries and veins in the field of view, which is important information during a surgical procedure [19]. By watching the wash-in of

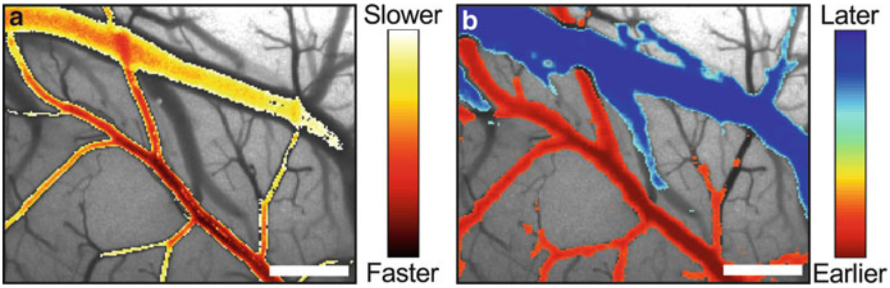

Fig. 5.3 Relative blood flow overlaid onto a baseline LSCI image from a rat cerebral cortex acquired during simultaneous imaging of LSCI and ICGA. (**a**) LSCI relative blood flow overlay, where *red* indicates faster flow and *yellow* indicates slower flow relative to surrounding parenchyma tissue. (**b**) ICG dye rise time overlay, where red indicates an earlier wash-in and *blue* indicates a later wash-in, allowing separation of arteries and veins. Scale bar represents 0.5 mm

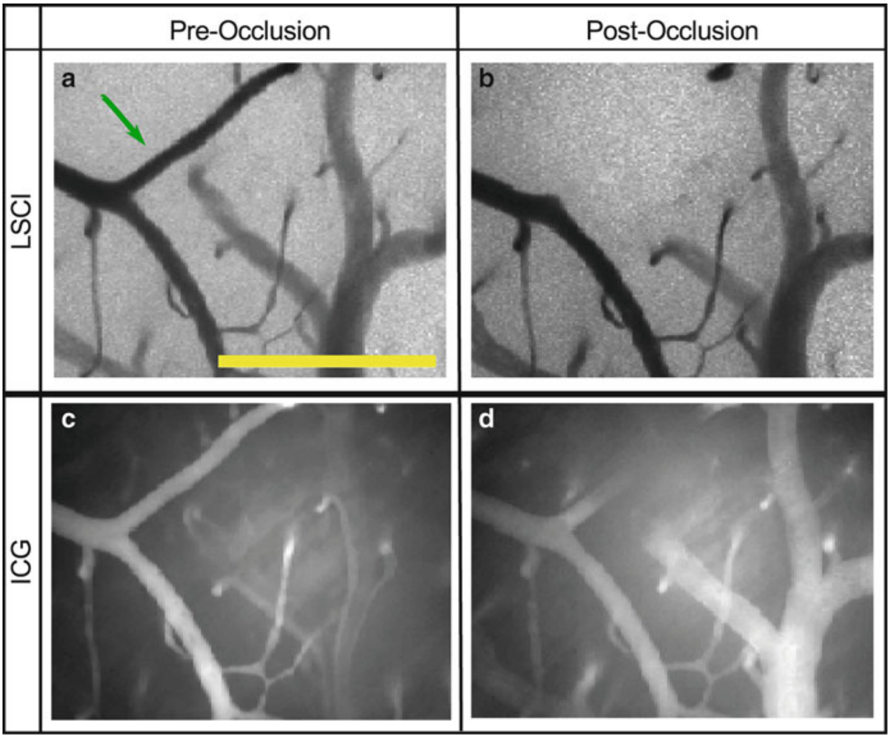

Fig. 5.4 Image set from a second animal in the study acquired using both LSCI (**a**, **b**) and ICG fluorescence imaging (**c**, **d**). Time points are shown for baseline physiological flow in (**a**) and (**c**) and after a localized vessel occlusion is induced using photothrombosis in (**b**) and (**d**). LSCI images appear darker in areas of higher flow, while ICG images appear brighter in areas where the ICG dye is present. Scale bar corresponds to 0.5 mm

the dye, the direction of flow can also be determined, which is one major advantage of ICG fluorescence. This figure demonstrates that both methods are capable of imaging the vasculature within the field of view with similar spatial resolution and that both techniques provide different information regarding blood flow in the field of view.

Images were also captured during a localized vessel occlusion induced using a rose-bengal photothrombotic clot model. The rose-bengal was injected after baseline images were acquired and a 532 nm laser was focused through the objective to activate the dye and induce a local clot on a vessel of interest in the field of view. An example from a second animal in the study is shown in Fig. 5.4, where LSCI and ICG fluorescence images are shown before and after the clot is formed. Although the images appear similar, the two techniques are providing different information. LSCI represents an overall blood flow map of the area, with darker areas representing higher flow and lighter areas indicating slower flow. The ICG images show the

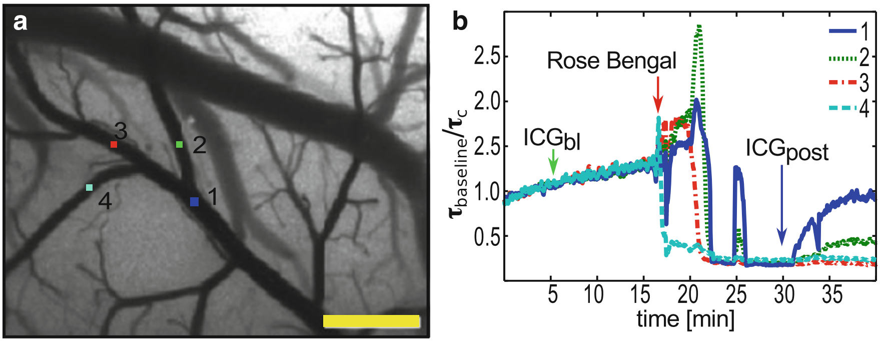

Fig. 5.5 Temporal blood flow changes measured from the first animal in the study at four regions of interest in different vessel branches. (**a**) Location of each region in the camera field of view shown on a representative baseline LSCI image. (**b**) Relative blood flow changes for all four regions measured by changes in correlation time relative to a baseline value. Temporal changes over 40 min are visualized, during baseline flow, occlusion, and after the clot has formed. *Arrows* indicate the time points of the baseline ICG injection, the rose-bengal injection to trigger clot formation, and the post-occlusion ICG injection. Scale bar corresponds to 0.5 mm

quantity of the fluorescent dye in the vessels, with larger vessels resulting in a brighter signal due to increased amount of dye present and darker areas indicating weaker fluorescent signal. In the pre-occlusion images, the vasculature is clearly visualized by both techniques. After the clot is formed, the upper branching vessel indicated by the arrow disappears from the field of view in the LSCI image, indicating that blood flow has reduced in the branched vessel to levels comparable to the surrounding parenchyma tissue. In the ICG image, the signal from the branched vessel is much dimmer, which results because the dye is being blocked from getting to that region. This demonstrates that both methods were able to identify the occluded vessel and also highlights the differences between the two techniques. While LSCI is truly measuring the motion within the tissue sample, ICG fluorescence allows visualization of blood volume rather than blood flow. This is clear since part of the branched vessel is still visible in the ICG images, which is due to dye becoming trapped inside the formed clot. Although it is still possible to identify the occlusion in this case, this may make ICG images more difficult for surgeons to interpret and could give misleading information.

One major advantage of LSCI is that it can be used to continuously monitor blood flow changes, both during baseline flow and during a clot formation. Figure 5.5 shows an example of a relative blood flow time course measured from the first animal in the study (same animal as Fig. 5.3). By calculating the correlation time within each region of interest and comparing to a baseline value, the relative blood flow changes can be calculated and easily visualized for four different vessel branches in the field of view. After the rose-bengal is injected, one vessel branch immediately clots, as shown by the sharp decrease in flow in region 4. The other vessel branches take a few minutes to fully clot, and then two of the branches re-perfuse briefly (regions 1 and 2), indicating that the clot broke free due to a pressure build-up. Because of the excess rose-bengal in the intravenous system, the clot reforms quickly and flow is again reduced in those regions. On the other hand, the ICG fluorescence provides the most useful information during the initial wash-in of the dye, which can be used to determine flow direction and separate arteries from veins. A reduction in maximum fluorescence reached during wash-in may also be used as an indicator of reduced blood flow, but quantitative results are difficult to interpret, especially if multiple injections of ICG are used during a single procedure.

This initial study in a rat model has demonstrated that LSCI and ICG fluorescence angiography provide complementary information about vessel perfusion. ICGA has distinct advantages of being able to identify flow direction and differentiate between feeding and draining vessels. LSCI has the advantages that it does not require an exogenous contrast agent and can provide continuous assessment of blood flow during surgical procedures. LSCI also provides a more direct measure of flow, while ICG fluorescence truly indicates blood volume. This study has also demonstrated that both techniques can be performed simultaneously using a single light source, meaning that the LSCI images can be acquired simultaneously with ICGA simply by adding a second camera to capture the excitation light.

5.5 Intraoperative Imaging During Neurosurgery

To examine the utility of LSCI as an intraoperative imaging tool during neurosurgery, we performed a pilot clinical study ($n = 10$) using LSCI to image CBF during brain tumor resection surgeries. The goal of the study was mainly to assess feasibility of the technique for intraoperative use and to examine performance both under baseline flow conditions and during an induced change in blood flow. Because the hardware has been integrated into the surgical workflow, the technique is minimally invasive and the hardware required is simply an add-on to an existing neurosurgical microscope.

5.5.1 Clinical Procedure

In this pilot clinical study, ten patients were imaged using LSCI during brain tumor resection procedures at the NeuroTexas Institute in St. David's Hospital, located in Austin, TX. The clinical study was approved by the Institutional Review Boards of the University of Texas at Austin and St. David's Hospital. The microscope-integrated LSCI instrument shown in Fig. 5.2b was used for all patients. Before each procedure, the camera and laser attachments were added to the microscope and a surgical staff member covered the modified microscope with a sterile standard microscope drape. The hardware attachments did not interfere with the draping procedure or with the normal function of the microscope, meaning that the surgeon

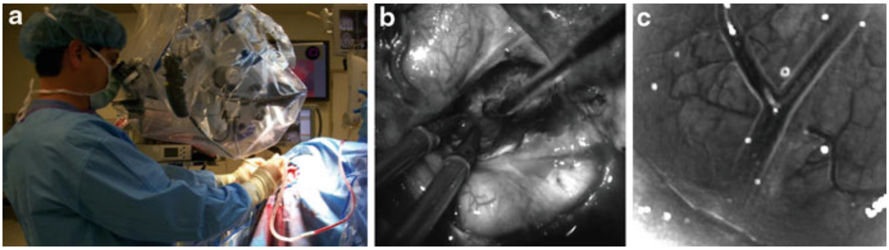

Fig. 5.6 Adapted Zeiss OPMI Pentero neurosurgical microscope in use during neurosurgery. (**a**) The surgeon uses the microscope to assist with the tumor resection procedure. (**b**) The surgeon's field of view as seen by our camera under the microscope's built-in xenon lamp illumination. (**c**) When the surgeon is ready to perform LSCI, the xenon lamp is turned off and the laser diode is turned on. LSCI images can be visualized instantaneously, with a representative speckle contrast image shown (averaged over ten frames)

could use the microscope during the procedure as needed. The LSCI imaging procedure was performed at the discretion of the surgeon, either before or after the tumor resection portion of the procedure.

For all cases, the surgeon performed the craniotomy and exposed the cortical tissue before imaging. If the microscope was not already being used in the procedure, the surgeon positioned the microscope over the cortical area of interest for imaging, using the built-in illumination to guide positioning and placement. Because the LSCI hardware was integrated into the neurosurgical microscope, the surgeon could easily control the location and angle of the microscope head. This provided the flexibility needed to accommodate for the variability in the craniotomy location of each patient and enabled fast setup, with positioning complete in less than 5 min. After positioning the microscope, the built-in illumination was turned off and the laser diode was turned on to perform LSCI imaging. The surgeon used the focus and zoom controls built into the microscope head to prepare for imaging and flushed the cortical tissue area of interest with sterile saline to reduce specular reflections in the camera field of view. LSCI images were acquired for ~10–15 min, while recording the camera exposure signal and the patient's ECG waveform simultaneously. An illustration of the microscope in use during surgery and the corresponding LSCI image is shown in Fig. 5.6.

Images of baseline blood flow conditions were recorded for all patients, in some cases over multiple tissue areas of interest. In two patients, the surgeon used bipolar cautery to perform surgical hemostasis within the camera field of view during LSCI imaging to induce a change in blood flow. After the surgical procedure, the LSCI hardware add-ons were removed from the microscope, leaving it exactly as it was before the surgery. Because the LSCI hardware is truly an add-on to an existing instrument, the system can be easily portable to different operating rooms and even different hospitals, as long as the surgical microscope is available.

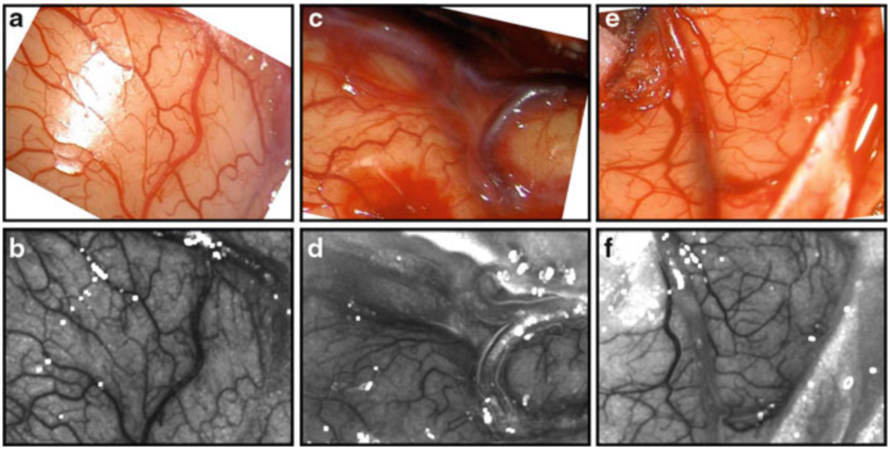

Fig. 5.7 (**a**, **c**, **e**) Color digital photographs taken from three different patients using the microscope's built-in illumination and color camera. These photographs have been registered to match the orientation of the corresponding representative speckle contrast images (**b**, **d**, **f**). The speckle contrast images are averaged over ten frames. The *bright white areas* in both the color images and the speckle contrast images are regions of specular reflection. The camera field of view is ~2 cm × 1.5 cm

5.5.2 Clinical Study Overview

The results from the pilot clinical study are promising and have demonstrated the instrument's ability to visualize blood flow in a real time, minimally intrusive manner. For a subset of the patients, images were acquired with the microscope's built-in color camera for comparison with the speckle contrast images. Figure 5.7 shows the camera field of view seen by the color camera under the built-in illumination along with corresponding representative speckle contrast images recorded from the same areas for three patients. The color photographs have been registered to match the orientation of the speckle contrast images, showing excellent alignment of the anatomical vasculature visible in the color images and the blood flow maps seen in the LSCI images. The blood vessels appear dark in the speckle contrast images, indicating that the vasculature in the field of view is unobstructed. The large vein running down the center of Fig. 5.7f may be the exception. The vessel does not appear to be obstructed in the corresponding color image, but the LSCI image indicates that this vein is flowing slower than the darker vessels nearby. The color images in Fig. 5.7c, e show blood pools present in the surgical field that obscure the view of the local vasculature. The corresponding LSCI images in Fig. 5.7d, f illustrate that the blood pools present in the surgical field do not interfere with image visibility, as flow is still clearly observed in the LSCI images where the blood pools are present. The ability to identify potentially obstructed vessels and to "see through" blood pools in the surgical field are examples of improved visualization possible with LSCI.

5.6 Dealing with Motion Artifacts

One of the challenges involved with using an imaging technique that is highly sensitive to motion is dealing with physiological motion that does not originate from blood flow alone. The cardiac cycle leads to unavoidable pulsatile variation in CBF for any in vivo measurement. Using the recorded ECG signal for each patient, we can generate an ad hoc cardiac filter to reduce the blood flow fluctuations within each heartbeat. This allows for improved visualization of actual functional flow changes that may be occurring. Because the brain tissue is able to deform after a portion of the skull is removed during the craniotomy, there are also motion artifacts due to pulsation and respiration. This tissue deformation results in a constantly changing camera field of view, which makes it difficult to track a specific tissue region over time. Image registration was used to match the spatial location between images taken at different time points for a complete image set. This helped account for the physical motion of the brain visible in the original image sets and allowed more accurate tracking of tissue regions of interest over time.

5.6.1 Cardiac Filtering

To illustrate the magnitude of blood flow changes that occur within each heartbeat, the measured correlation time for a region of interest is plotted on the same timescale as the ECG waveform recorded for the patient. A representative result from the first patient is shown in Fig. 5.8a, using the average correlation time measured from region 1 over a large blood vessel in Fig. 5.8c. This time course illustrates that the measured changes in τ_c are synchronized in time with the cardiac cycle. These pulsatile changes in blood flow can be tolerated during basic visual inspection of CBF and would not hinder use during applications where large changes in blood flow are expected, such as aneurysm clipping or vessel bypass. However, these fluctuations in CBF within each heartbeat may mask small changes in blood flow. This would be an issue during procedures involving functional mapping of the cortex, where activation may induce a change in blood flow as small as 10% from baseline values [29]. The magnitude of the fluctuations observed in Fig. 5.8a would limit the ability to identify small changes in blood flow, which is the main motivation for eliminating the artificial rise and fall of blood flow observed within the cardiac cycle.

Because the fluctuations observed are synchronized with the heartbeat, we have designed an ad hoc ECG filter to reduce the beat-to-beat variability. This filter is similar to an adaptive filter technique for MRI data developed by Deckers et al. [45] and was first described by our group in Parthasarathy et al. [32]. The filter is designed to identify the time of the camera exposure relative to the ECG cycle and to account for the signal shape at that relative time. Because both the camera exposure signal and the ECG waveform are recorded during image acquisition,

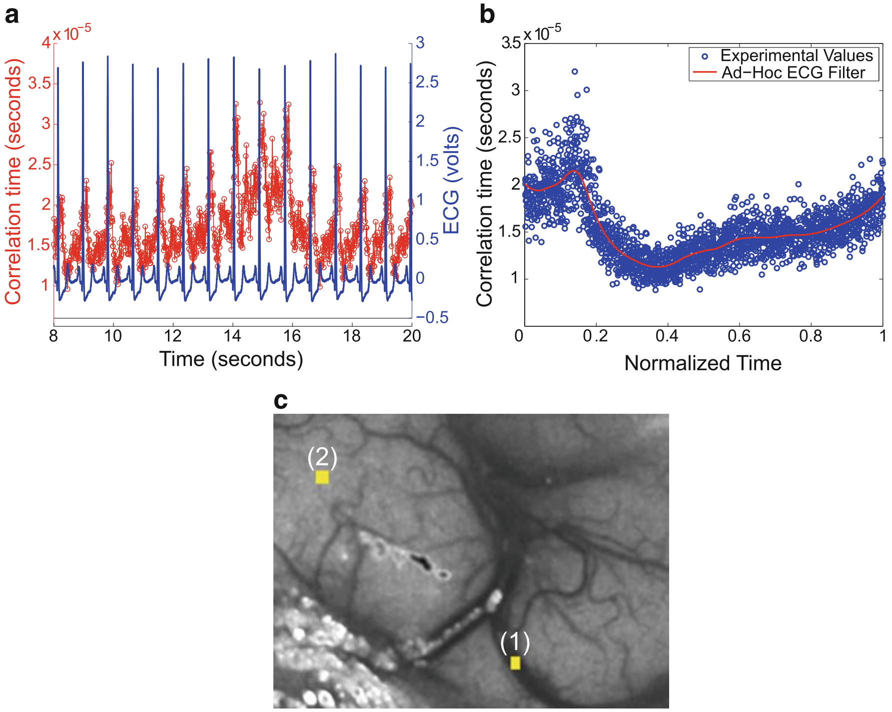

Fig. 5.8 (**a**) The average correlation time within a region of interest co-localized in time with the ECG waveform recorded for the patient. This illustrates clear fluctuations in correlation time that are synchronized with the cardiac cycle. (**b**) The ad hoc ECG filter produced using the average correlation times from the same region of interest during the time required for 25 heartbeats. (**c**) A representative speckle contrast image showing the locations of two regions of interest. Region 1, located in the vessel, is used for (**a**) and (**b**), while region 2, located in the parenchyma, will be used for analysis in Fig. 5.9

both the actual time of each speckle image and the actual time of each heartbeat are known. Thus, the correlation time measured from each speckle image can be assigned a "normalized time," which is defined as the time of image acquisition relative to the nearest heartbeat. The normalized time is defined in (5.5)

$$t_{\text{normalized}} = \frac{t_{\text{frame}} - t_{\text{beat}}}{t_{RR}}, \tag{5.5}$$

where t_{frame} is the time of the camera exposure, t_{beat} is the time of the nearest previous heartbeat, and t_{RR} is the duration of the heartbeat defined as the time between adjacent R peaks in the ECG waveform. Using the images acquired during the first 25 heartbeats in an image set, the average correlation time from a region of interest can be plotted against its normalized time to generate the ad hoc ECG filter function. An example for the same region is shown in Fig. 5.8b, where the blue

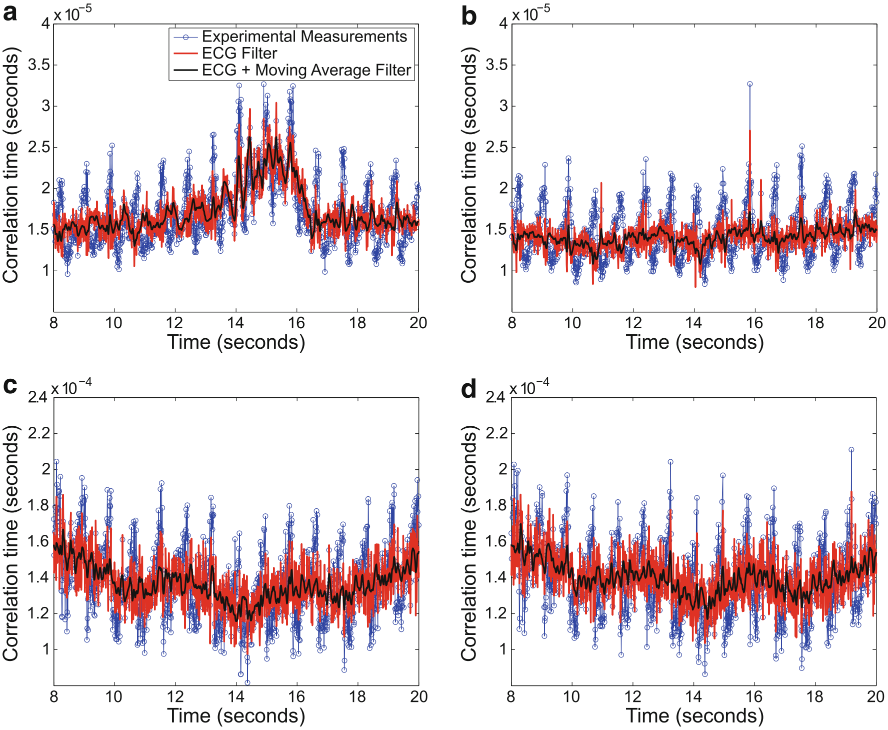

Fig. 5.9 (**a**) The ECG filtered result from the original dataset for region 1 over a large vessel in Fig. 5.8c. The *red curve* shows the ECG filtered output and the *black curve* shows the result after applying the small window moving average filter to the filtered output. (**b**) The ECG filtered result for the same vessel region after image registration has been applied to the image set. The registered filtered output is relatively flat, indicating that the registration process accounted for the large increase in τ_c observed in (**a**) between 14 and 16 s. (**c**) The ECG filtered result from the original dataset for region 2 in the tissue parenchyma from Fig. 5.8c, showing a slow oscillation in flow. (**d**) The ECG filtered result for the same parenchyma region after image registration has been applied to the image set, which is very similar to the original filtered output

circles are the measured τ_c values averaged from the region of interest in each image and the red line corresponds to the filter function generated by averaging the measured values with a large window moving average filter. Thus, each value of the filter function represents the average shape of the correlation time signal expected at a specific time in the ECG cycle. To apply the filter to the data, the normalized time of each image must be calculated. Then, the corresponding filter value for that normalized time is subtracted from the correlation time data point and the median correlation time value of the ECG filter is added back. To further reduce the noise in the filtered measurements, a small window moving average filter of width 0.05 s is applied to the ECG filtered result. The result after ECG filtering (red curve) and applying the small window moving average filter to the ECG filtered result (black curve) is shown for the same vessel region in Fig. 5.9a. This result illustrates that ECG filtering greatly reduces the variability within the cardiac cycle and gives a relatively smooth curve while preserving inherent physiological flow changes. One important detail to point out is that ECG filtering works very well for the specific region of interest used to generate the ad hoc ECG filter. However, the ECG filter shape varies greatly between different tissue regions and between patients, meaning that a general ECG filter cannot be used. Thus, each region of interest analyzed within each patient must have its own ECG filter shape to correct for beat-to-beat fluctuations in measured correlation time.

5.6.2 Image Registration

To account for large-scale tissue motion due to pulsation and respiration, image registration was performed in post-processing to align the camera field of view for each image set. Registration was performed using *Elastix*, an open-source software package for medical image registration based on the Insight Segmentation and Registration Toolkit (ITK) [46]. This program uses intensity-based image registration to adjust the position of a moving image to match a fixed image using the transformation type, similarity measure, and optimization procedure specified in a parameter file. The type of transformation used during registration is one of the most important parameters and must be chosen carefully. The transformation determines the types of deformations that are allowed to create the mapping between the fixed image and the moving image. Because the brain tissue is deforming, a nonrigid transform would be required for an exact mapping of the images to account for tissue distortion. However, LSCI records a 2D view of the 3D deformation and the microscope has a large enough depth of field to keep the image in focus during tissue motion. This limits the majority of tissue deformation in the recorded images to the x and y directions. Thus, a translation transform was used for initial analysis to preserve the image integrity and decrease the complexity of the image registration process. Mutual information was used as the similarity metric and adaptive stochastic gradient descent was used for the optimization procedure, as the developers of *Elastix* recommend both of these parameter choices for general medical image registration with good performance [46]. The speckle contrast images were provided to *Elastix* for registration, since the blood flow maps provided clear image features to improve registration performance. After image registration, the ECG filtering procedure was performed on the registered dataset and the filtered output was directly compared with the original results.

A side-by-side comparison of the filtered output from the two regions shown in Fig. 5.8c before and after registration is shown in Fig. 5.9. As shown by the fluctuations in the blue data points from the registered set in Fig. 5.9b, ECG filtering is still necessary as beat-to-beat variations are still clearly visible despite the image registration. Thus, the filtered results shown in the red and black curves were produced using an ECG filter function calculated using the first 25 heartbeats of the registered image set. Interestingly, the results from the region within the vessel shown in Fig. 5.9b indicate a relatively constant time course, while the result from the original dataset shown in (a) showed a large decrease in flow (increase in τ_c) between 14 and 16 s. After viewing the registered result, we can conclude that the decrease in flow was a result of the region of interest moving outside the vessel and into the surrounding tissue parenchyma, which has a slower flow than the vessel itself. This was confirmed in a video of the original image set with the vessel region of interest overlaid. The registered results from the tissue parenchyma region of interest shown in Fig. 5.9d appears remarkably similar to the original result in (c), indicating that the registration process did not have a large effect on the measured correlation time for the parenchyma tissue region. This suggests that the variation in blood flow within the tissue parenchyma where the capillary beds are located is higher than the variation produced from the tissue motion. Thus, there is a clear benefit to registering the images for regions of interest located in a vessel to ensure that the region remains inside the vessel throughout the time course of the analysis. This will eliminate any artificial changes in the time course due to movement of the spatial region into another tissue area, as observed with Fig. 5.9a. The benefit of image registration for analyzing tissue parenchyma regions is still being explored, but may be less important because of the inherent increase in variation observed in the parenchyma.

5.7 Conclusions

LSCI is a simple yet powerful tool for visualizing blood flow in real time with excellent spatiotemporal resolution and is ideal for use in a surgical setting. There is a clear need for monitoring CBF during neurosurgery and LSCI is a perfect candidate to overcome many of the disadvantages of currently available techniques. A direct comparison between LSCI and ICGA in an animal model demonstrated that the two techniques are complementary and provide different information to the surgeon. LSCI has the advantages that it does not require the use of an exogenous contrast agent, can be used continuously or repeated as often as needed, and provides a true measure of blood flow. The results from the 10-patient clinical study are promising and indicate the feasibility of using LSCI to monitor blood flow changes in a neurosurgical setting. The LSCI images showed excellent correlation with the anatomical vasculature captured by the microscope's built-in camera and were unobstructed by the presence of blood pools within the field of view. The microscope-integrated instrumentation proved to be convenient and easy to use for the surgeons, providing real time, full field blood flow maps with minimal interference to the surgical procedure. Both the ECG filtering and image registration helped account for variability observed in blood flow as a result of the cardiac cycle and tissue motion. Future work will include a larger clinical study to assess LSCI performance during a wider variety of neurosurgical procedures, including cerebrovascular repair and functional mapping.

Acknowledgments The authors would like to acknowledge the surgical staff at St. David's Hospital for their help during the intraoperative experiments. This work was supported by the Coulter Foundation, the National Science Foundation (CBET/0737731), the American Heart Association (0735136N), and the Consortium Research Fellowship Program.

References

1. Barrow DL, Boyer KL, Joseph GJ (1992) Intraoperative angiography in the management of neurovascular disorders. Neurosurgery 30(2):153–159
2. Vitaz TW, Gaskill-Shipley M, Tomsick T, Tew JM Jr (1999) Utility, safety, and accuracy of intraoperative angiography in the surgical treatment of aneurysms and arteriovenous malformations. AJNR Am J Neuroradiol 20(8):1457–1461
3. Chiang VL, Gailloud P, Murphy KJ, Rigamonti D, Tamargo RJ (2002) Routine intraoperative angiography during aneurysm surgery. J Neurosurg 96(6):988–992. doi:10.3171/jns.2002.96.6.0988
4. Tang G, Cawley CM, Dion JE, Barrow DL (2002) Intraoperative angiography during aneurysm surgery: a prospective evaluation of efficacy. J Neurosurg 96(6):993–999. doi:10.3171/jns.2002.96.6.0993
5. Symon L, Wang AD, Silva IECE, Gentili F (1984) Perioperative use of somatosensory evoked-responses in aneurysm surgery. J Neurosurg 60(2):269–275. doi:10.3171/jns.1984.60.2.0269
6. Little JR, Lesser RP, Luders H (1987) Electrophysiological monitoring during basilar aneurysm operation. Neurosurgery 20(3):421–427
7. Lopez JR, Chang SD, Steinberg GK (1999) The use of electrophysiological monitoring in the intraoperative management of intracranial aneurysms. J Neurol Neurosurg Psychiatry 66 (2):189–196. doi:10.1136/jnnp. 66.2.189
8. Kalavakonda C, Sekhar LN, Ramachandran P, Hechl P (2002) Endoscope-assisted microsurgery for intracranial aneurysms. Neurosurgery 51(5):1119–1126; discussion 1117–1126. doi:10.1227/01.NEU.0000031750.58301.67
9. Wang E, Yong NP, Ng I (2003) Endoscopic assisted microneurosurgery for cerebral aneurysms. J Clin Neurosci 10(2):174–176. doi:10.1016/S0967-5868(02)00320-X
10. Kinouchi H, Yanagisawa T, Suzuki A, Ohta T, Hirano Y, Sugawara T, Sasajima T, Mizoi K (2004) Simultaneous microscopic and endoscopic monitoring during surgery for internal carotid artery aneurysms. J Neurosurg 101(6):989–995. doi:10.3171/jns.2004.101.6.0989
11. Stendel R, Pietila T, Al Hassan AA, Schilling A, Brock M (2000) Intraoperative microvascular Doppler ultrasonography in cerebral aneurysm surgery. J Neurol Neurosurg Psychiatry 68 (1):29–35. doi:10.1136/jnnp. 68.1.29
12. Marchese E, Albanese A, Denaro L, Vignati A, Fernandez E, Maira G (2005) Intraoperative microvascular Doppler in intracranial aneurysm surgery. Surg Neurol 63(4):336–342; discussion 342. doi:10.1016/j.surneu.2004.05.031
13. Kapsalaki EZ, Lee GP, Robinson JS III, Grigorian AA, Fountas KN (2008) The role of intraoperative micro-Doppler ultrasound in verifying proper clip placement in intracranial aneurysm surgery. J Clin Neurosci 15(2):153–157. doi:10.1016/j.jocn.2006.11.006
14. Raabe A, Beck J, Seifert V (2005) Technique and image quality of intraoperative indocyanine green angiography during aneurysm surgery using surgical microscope integrated near-infrared video technology. Zentralbl Neurochir 66(1):1–6; discussion 7–8. doi:10.1055/s-2004-836223
15. Raabe A, Nakaji P, Beck J, Kim LJ, Hsu FP, Kamerman JD, Seifert V, Spetzler RF (2005) Prospective evaluation of surgical microscope-integrated intraoperative near-infrared indocyanine green videoangiography during aneurysm surgery. J Neurosurg 103 (6):982–989. doi:10.3171/jns.2005.103.6.0982

16. de Oliveira JG, Beck J, Seifert V, Teixeira MJ, Raabe A (2007) Assessment of flow in perforating arteries during intracranial aneurysm surgery using intraoperative near-infrared indocyanine green videoangiography. Neurosurgery 61(3 suppl):63–72; discussion 63–72. doi:10.1227/01.neu.0000289715.18297.08
17. Hanggi D, Etminan N, Steiger HJ (2010) The impact of microscope-integrated intraoperative near-infrared indocyanine green videoangiography on surgery of arteriovenous malformations and dural arteriovenous fistulae. Neurosurgery 67(4):1094–1103; discussion 1094–1103. doi:10.1227/NEU.0b013e3181eb5049
18. Gruber A, Dorfer C, Standhardt H, Bavinzski G, Knosp E (2011) Prospective comparison of intraoperative vascular monitoring technologies during cerebral aneurysm surgery. Neurosurgery 68(3):657–673; discussion 673. doi:10.1227/NEU.0b013e31820777ee
19. Raabe A, Beck J, Gerlach R, Zimmermann M, Seifert V (2003) Near-infrared indocyanine green video angiography: a new method for intraoperative assessment of vascular flow. Neurosurgery 52(1):132–139; discussion 139. doi:10.1097/00006123-200301000-00017
20. Dashti R, Laakso A, Niemela M, Porras M, Hernesniemi J (2009) Microscope-integrated near-infrared indocyanine green videoangiography during surgery of intracranial aneurysms: the Helsinki experience. Surg Neurol 71(5):543–550; discussion 550. doi:10.1016/j.surneu.2009.01.027
21. Khurana VG, Seow K, Duke D (2010) Intuitiveness, quality and utility of intraoperative fluorescence videoangiography: Australian Neurosurgical Experience. Br J Neurosurg 24(2):163–172. doi:10.3109/02688690903518247
22. Owens SL (1996) Indocyanine green angiography. Br J Ophthalmol 80(3):263–266. doi:10.1136/bjo.80.3.263
23. Briers JD (2001) Laser Doppler, speckle and related techniques for blood perfusion mapping and imaging. Physiol Meas 22(4):R35–R66. doi:10.1088/0967-3334/22/4/201
24. Wardell K, Jakobsson A, Nilsson GE (1993) Laser Doppler perfusion imaging by dynamic light scattering. IEEE Trans Biomed Eng 40(4):309–316. doi:10.1109/10.222322
25. Nielsen AN, Fabricius M, Lauritzen M (2000) Scanning laser-Doppler flowmetry of rat cerebral circulation during cortical spreading depression. J Vasc Res 37(6):513–522. doi:10.1159/000054084
26. Nakase H, Kaido T, Okuno S, Hoshida T, Sakaki T (2002) Novel intraoperative cerebral blood flow monitoring by laser-Doppler scanner. Neurol Med Chir (Tokyo) 42(1):1–4. doi:10.2176/nmc.42.1
27. Serov A, Steinacher B, Lasser T (2005) Full-field laser Doppler perfusion imaging and monitoring with an intelligent CMOS camera. Opt Express 13(10):3681–3689. doi:10.1364/OPEX.13.003681
28. Leutenegger M, Martin-Williams E, Harbi P, Thacher T, Raffoul W, Andre M, Lopez A, Lasser P, Lasser T (2011) Real-time full field laser Doppler imaging. Biomed Opt Express 2(6):1470–1477. doi:10.1364/BOE.2.001470
29. Raabe A, Van De Ville D, Leutenegger M, Szelenyi A, Hattingen E, Gerlach R, Seifert V, Hauger C, Lopez A, Leitgeb R, Unser M, Martin-Williams EJ, Lasser T (2009) Laser Doppler imaging for intraoperative human brain mapping. Neuroimage 44(4):1284–1289. doi:10.1016/j.neuroimage.2008.10.049
30. Tom WJ, Ponticorvo A, Dunn AK (2008) Efficient processing of laser speckle contrast images. IEEE Trans Med Imaging 27(12):1728–1738. doi:10.1109/TMI.2008.925081
31. Hecht N, Woitzik J, Dreier JP, Vajkoczy P (2009) Intraoperative monitoring of cerebral blood flow by laser speckle contrast analysis. Neurosurg Focus 27(4):E11. doi:10.3171/2009.8.FOCUS09148
32. Parthasarathy AB, Weber EL, Richards LM, Fox DJ, Dunn AK (2010) Laser speckle contrast imaging of cerebral blood flow in humans during neurosurgery: a pilot clinical study. J Biomed Opt 15(6):066030. doi:10.1117/1.3526368
33. Richards LM, Weber EL, Parthasarathy AB, Kappeler KL, Fox DJ, Dunn AK (2012) Intraoperative laser speckle contrast imaging for monitoring cerebral blood flow: results from a 10-patient pilot study. Proc SPIE 8207:82074L. doi:10.1117/12.909078

34. Briers JD, Webster S (1996) Laser speckle contrast analysis (LASCA): a nonscanning, full-field technique for monitoring capillary blood flow. J Biomed Opt 1(2):174–179. doi:10.1117/12.231359
35. Kirkpatrick SJ, Duncan DD, Wells-Gray EM (2008) Detrimental effects of speckle-pixel size matching in laser speckle contrast imaging. Opt Lett 33(24):2886–2888. doi:10.1364/OL.33.002886
36. Duncan DD, Kirkpatrick SJ (2008) Can laser speckle flowmetry be made a quantitative tool? J Opt Soc Am A 25(8):2088–2094. doi:10.1364/JOSAA.25.002088
37. Berne BJ, Pecora R (2000) Dynamic light scattering: with applications to chemistry, biology, and physics, Doverth edn. Dover Publications, Mineola, NY
38. Fercher AF, Briers JD (1981) Flow visualization by means of single-exposure speckle photography. Opt Commun 37(5):326–330. doi:10.1016/0030-4018(81)90428-4
39. Bandyopadhyay R, Gittings AS, Suh SS, Dixon PK, Durian DJ (2005) Speckle-visibility spectroscopy: a tool to study time-varying dynamics. Rev Sci Instrum 76(9). doi: doi:10.1063/1.2037987
40. Bonner R, Nossal R (1981) Model for laser Doppler measurements of blood flow in tissue. Appl Opt 20(12):2097–2107. doi:10.1364/AO.20.002097
41. Dunn AK, Bolay H, Moskowitz MA, Boas DA (2001) Dynamic imaging of cerebral blood flow using laser speckle. J Cereb Blood Flow Metab 21(3):195–201. doi:10.1097/00004647-200103000-00002
42. Boas DA, Dunn AK (2010) Laser speckle contrast imaging in biomedical optics. J Biomed Opt 15(1):011109. doi:10.1117/1.3285504
43. Draijer M, Hondebrink E, Van Leeuwen T, Steenbergen W (2009) Review of laser speckle contrast techniques for visualizing tissue perfusion. Lasers Med Sci 24(4):639–651. doi:10.1007/s10103-008-0626-3
44. American National Standard for the Safe Use of Lasers (2007). ANSI Z136.1-2007. Laser Institute of America
45. Deckers RH, van Gelderen P, Ries M, Barret O, Duyn JH, Ikonomidou VN, Fukunaga M, Glover GH, de Zwart JA (2006) An adaptive filter for suppression of cardiac and respiratory noise in MRI time series data. Neuroimage 33(4):1072–1081. doi:10.1016/j.neuroimage.2006.08.006
46. Klein S, Staring M, Murphy K, Viergever MA, Pluim JP (2010) elastix: a toolbox for intensity-based medical image registration. IEEE Trans Med Imaging 29(1):196–205. doi:10.1109/TMI.2009.2035616

Chapter 6
Photoacoustic Tomography of the Brain

Jun Xia and Lihong V. Wang

6.1 Introduction to Photoacoustic Tomography

Photoacoustic tomography (PAT) is based on the photoacoustic effect, in which the energy from a short laser pulse is absorbed by tissue chromophores, generating a local temperature rise which is subsequently converted into pressure waves via thermoelastic expansion. The emitted acoustic waves are detected by ultrasonic transducers. Based on the amplitude and arrival time of the acoustic signal, the distribution of optical absorption in the object can be computed.

As a hybrid technique, PAT combines the merits of both optical and ultrasonic imaging modalities. Since photoacoustic signals originate from optical absorption, tissue chromophores with different absorption characteristics can be spectrally separated. This enables PAT to provide label-free functional brain images of oxygen saturation (SO_2) and total hemoglobin concentration (HbT) based on the absorption spectra of oxyhemoglobin (HbO_2) and deoxyhemoglobin (Hb) [1, 2]. Optical contrast agents, such as organic dyes and nanoparticles, can also be used to improve the visibility of the neurovascular structures [3]. Taking advantage of the broad choice of fluorescent dyes and proteins, PAT can also image the brain at genetic and molecular levels [4], which will facilitate the understanding of tumor biology and brain diseases. Due to the low ultrasonic scattering in tissue, PAT provides high resolution images in the optical diffusive regime, with high depth-to-resolution ratios of more than 100 [5]. The spatial resolution of PAT in the optical diffusive regime is mainly determined by the properties of the ultrasonic transducer. Better resolutions are achieved by transducers with higher central frequencies and bandwidths. However, due to the strong ultrasonic attenuation (~1 dB/cm/MHz in tissue) at high frequencies, photoacoustic computed

---

J. Xia • L.V. Wang (✉)
Optical Imaging Laboratory, Department of Biomedical Engineering, Washington University in St. Louis, St. Louis, MO 63130, USA
e-mail: lhwang@biomed.wustl.edu

S.J. Madsen (ed.), *Optical Methods and Instrumentation in Brain Imaging and Therapy*, Bioanalysis: Advanced Materials, Methods, and Devices 3,
DOI 10.1007/978-1-4614-4978-2_6,

tomography (PACT) of deep tissues normally employs ultrasonic transducers with central frequencies ranging from 1 to 20 MHz [1]. Photoacoustic microscopy (PAM) works above this frequency range, generating high resolution images at a reduced penetration depth. The resolution of PAM can be defined by either the diffraction-limited optical focusing [optical-resolution (OR)-PAM] [6] or the frequency- and bandwidth-limited acoustic focusing [acoustic-resolution (AR)-PAM] [7]. OR-PAM can generate functional images of cortical microvasculature at single capillary levels to provide details of neurovascular coupling [8]. The photoacoustic Doppler effect can also be utilized in PAT to measure the speed of blood flow [9], which can be combined with other functional parameters to quantify the cerebral metabolic rate of oxygen [10]. In this chapter, we review all these different photoacoustic brain imaging techniques and highlight studies done in the past few years.

6.2 Photoacoustic Tomography Systems

6.2.1 Photoacoustic Computed Tomography

In PACT, the initial photoacoustic pressure $p_0(\overrightarrow{r})$ in the source is reconstructed from data received at multiple detecting positions. Several photoacoustic image reconstruction algorithms have been developed in the past few years [11–14], and reviews of the subject are available in references [15, 16]. For most of the studies reviewed in this chapter, images were reconstructed using the universal back-projection algorithm [11], whose time-domain formulation is expressed as

$$p_0(\overrightarrow{r}) = \frac{1}{\Omega_0}\int_s \mathrm{d}\Omega \left[2p(\overrightarrow{r_d},t) - 2t\frac{\partial p(\overrightarrow{r_d},t)}{\partial t}\right]\Bigg|_{t=\frac{|\overrightarrow{r}_d - \overrightarrow{r}|}{v_s}} \tag{6.1}$$

Here $p_0(\overrightarrow{r})$ is the initial pressure source, Ω_0 is the solid angle of the whole detection surface S with respect to a given source point at $\overrightarrow{r}$, $p(\overrightarrow{r_d},t)$ is the pressure received at detecting position $\overrightarrow{r_d}$ and time t, and v_s is the speed of sound. Equation (1) indicates that $p_0(\overrightarrow{r})$ is an integration to be conducted along the detection surface S, using $\mathrm{d}\Omega/\Omega$ as the weighting factor. The reconstructed $p_0(\overrightarrow{r})$ is proportional to the optical energy deposition $A(\overrightarrow{r})$, which is a product of the optical absorption coefficient $\mu_a(\overrightarrow{r})$ and the light fluence $F(\vec{r})$. Therefore, if the light fluence is homogeneous, the reconstructed image represents the distribution of μ_a in the source. Equation (1) can be used in three types of imaging geometries: cylindrical, planar, and spherical surfaces. The first two geometries are widely used in photoacoustic brain imaging.

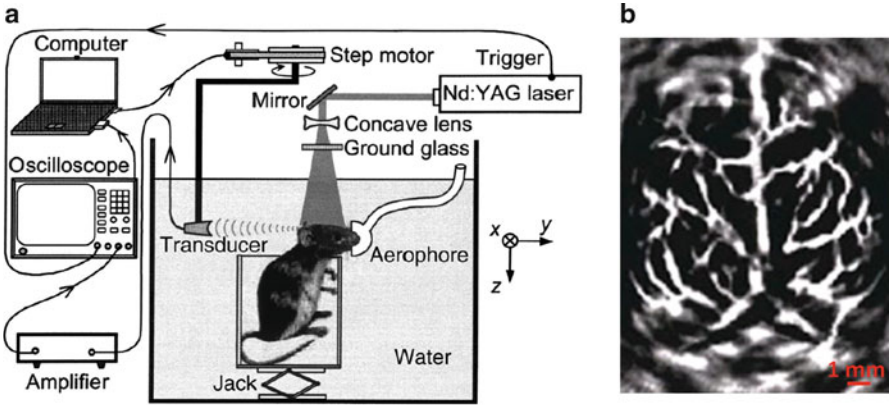

Fig. 6.1 (**a**) A schematic of a circular-view photoacoustic computed tomography (PACT) system based on a single element ultrasound transducer. (**b**) In vivo circular-view PACT image of the cortical vasculature of an adult rat with both the scalp and skull intact [1]. (reproduced from Wang et al. With permission)

6.2.1.1 Circular-View PACT

Figure 6.1 is a schematic of a circular-view PACT system based on a single element ultrasonic transducer [1]. The light source is a tunable pulsed laser with several nanoseconds pulse duration. Before reaching the animal brain, the laser beam is first expanded using a concave lens and then homogenized using a ground glass. This procedure ensures a uniform light illumination on the brain at a power intensity below the ANSI safety limit [17]. The animal is kept in an acoustic coupling medium and can breathe through a mask. The photoacoustic signals are detected by an ultrasonic transducer, which can scan circularly around the brain using a stepper motor. After a complete circular scan, a two-dimensional (2D) photoacoustic image of the brain can be reconstructed. Fig. 6.1b is an in vivo image of the cortical vasculature of a rat brain acquired noninvasively through the intact scalp and skull using a single-element circular-view PACT system [1]. Three-dimensional (3D) images can also be acquired by incrementally moving the animal or the transducer in the z direction [18]. Because of the mechanical scanning, the single-element circular-view PACT takes 15 min for a 2D scan and several hours for a 3D scan.

The imaging speed of circular-view PACT can be greatly improved by using an array of ultrasonic transducers [19–21]. Figure 6.2a is the top view of a 512-element full-ring transducer array [20]. The array was custom-made to form a complete circle with a 50 mm diameter. Each element in the array was curved in elevation (Fig. 6.2b) to produce a mechanical focal depth of 19 mm, without the loss and acoustic aberrations of external lenses. The combined foci of all elements form a 3D central imaging region of 12 mm in diameter and 2 mm in thickness, which closely fits the cross-section of an adult mouse brain. Due to the large number of transducer elements, the array output is first sampled by a receiver board. The board consists

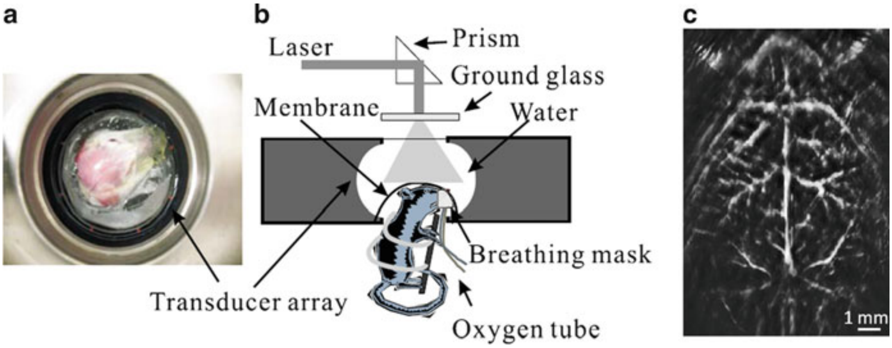

Fig. 6.2 Circular-view PACT with a full-ring ultrasonic transducer array. (**a**) Top view of the full-ring array and the animal head. (**b**) Side view of the array system and the position of the animal [21]. (reproduced from Li et al. With permission.) (**c**) In vivo full-ring array PACT image of the cortical vasculature of an adult mouse with both the scalp and skull intact

of 512 dedicated preamplifiers, 64 8:1 multiplexers, and 64 post-amplifiers [22]. The amplified and multiplexed signals are then digitized by a 64-channel data acquisition (DAQ) system. Due to the 8:1 multiplexing, a complete 512-element DAQ requires eight laser pulses. Data setup and transfer for results of a single acquisition can be performed at up to 8 Hz, leading to a maximum full-capture rate of 1 frame/s. The animal mounting scheme is also different from the one used in single-element PACT. Instead of being fully immersed in the coupling medium, the animal is supported from below, with the head being covered by a flexible membrane (Fig. 6.2b). Using the full-ring array PACT system, Fig. 6.2c is an in vivo photoacoustic image of the cortical vasculature of a 5–6-week-old mouse (~20 g) with both the scalp and skull intact.

The axial resolution of a circular-view PACT system is primarily determined by the bandwidth of the ultrasonic transducer [23]. For a wide bandwidth transducer, the axial resolution approximates to $0.8\lambda_c$, where λ_c is the acoustic wavelength at the high cutoff frequency. The lateral resolution is inversely related to the transducer's aperture and the distance between the imaging point and the scanning center.

6.2.1.2 Planar-View PACT

The photoacoustic signal can also be detected optically using a Fabry-Perot film sensing interferometer (FPI) [24, 25]. The sensor is transparent and can be placed on the surface of the animal's head without blocking the excitation laser. The excitation laser illuminates the animal brain in the same way as in circular-view PACT. The optical probe comes from a 1500 nm continuous-wave laser. The laser beam is focused and can raster scan over the surface of the sensor to map the distribution of the photoacoustic waves arriving at the sensing film. This configuration is equivalent to scanning a single-element piezoelectric transducer with an

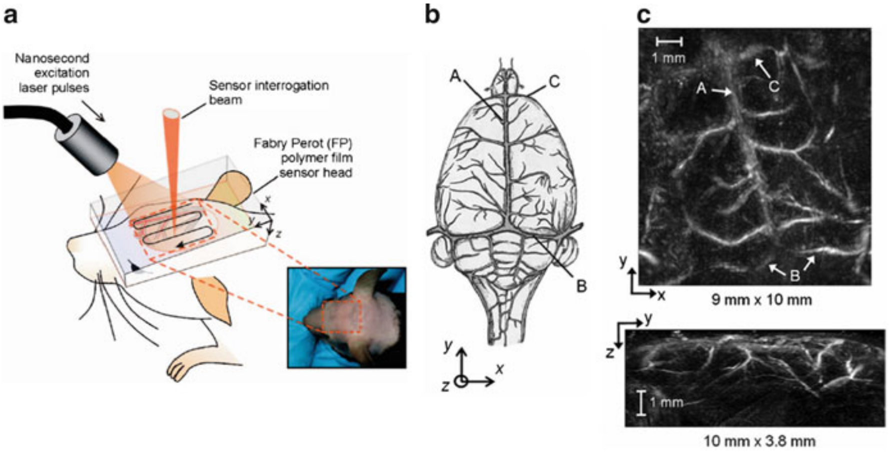

Fig. 6.3 (**a**) Experimental arrangement of a planar-view PACT system based on Fabry-Perot interferometry. The Fabry-Perot sensor head is placed on the surface of the mouse head over the region indicated on the photograph. (**b**) Schematic of superficial cerebral vascular anatomy: A, superior sagittal sinus; B, transverse sinus; C, inferior cerebral vein. (**c**) *x*-*y* (*top*) and *y*-*z* (*bottom*) maximum intensity projections of the 3D photoacoustic image [25]. (reproduced from Laufer et al. With permission)

active area equaling the size of the focal spot. Similar to the circular-view PACT, the axial resolution of a planar-view PACT is spatially invariant and determined mainly by the bandwidth and central frequency of the sensor. The lateral resolution depends on the detection aperture, the effective acoustic element size, and the bandwidth of the sensor [24]. Unlike piezoelectric transducers, the frequency response of an FPI sensor is defined primarily by the acoustic thickness of the polymer film spacer [24]. Figure 6.3c is an ex vivo image of a mouse brain with intact scalp and skull. In the experiment, 50 μm axial and lateral resolutions were achieved [24]. The scanning speed of the system is mainly limited by the pulse repetition rate (10 Hz) of the high power laser. Due to the long acquisition time (15 min), the mouse was scarified before the experiment to minimize motion artifacts [25].

6.2.2 *Photoacoustic Microscopy*

PAM employs a confocal design of optical illumination and acoustic detection. By using a spherically focused ultrasonic transducer, PAM receives signals primarily from the focal zone. Therefore, computational image reconstruction is not needed. After each laser pulse, PAM receives a depth-resolved temporal photoacoustic signal, and by raster scanning along the two transverse directions (B-scans), a 3D photoacoustic image can be acquired. Since the light irradiation area is relatively small, the laser used in PAM normally has much lower pulse power than the laser

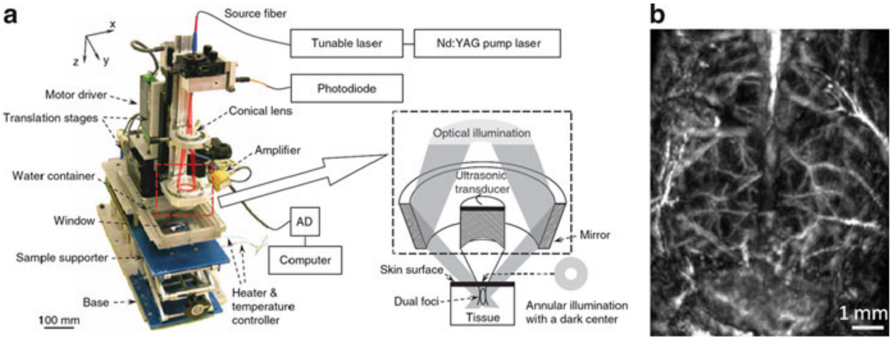

Fig. 6.4 (**a**) Experimental AR-Photoacoustic microscopy (PAM) system. The components within the *dashed* box in the photograph are mechanically translated along an x-y plane, with the bottom of the mirror and the ultrasonic transducer immersed in water. A window at the bottom of the water container is sealed with an optically and ultrasonically transparent disposable polyethylene membrane [26]. (reproduced from Zhang, Maslov, Stoica, and Wang. With permission.) (**b**) In vivo AR-PAM image of the cortical vasculature of an adult mouse with both the scalp and skull intact [28, 29]. (reproduced from Stein et al., Hu and Wang. With permission)

used in circular- and planar-view PACTs. The low power laser has a higher pulse repetition rate (>1 kHz), which enables PAM to raster scan at a high speed. Similar to PACT, the axial resolution of PAM is determined by the bandwidth and central frequency of the transducer. The lateral resolution can be determined by either the acoustic focus [acoustic-resolution (AR)-PAM [26] or the optical focus [optical-resolution (OR)-PAM] [6].

6.2.2.1 Acoustic-Resolution PAM

Figure 6.4a shows the experimental setup of an AR-PAM system. The laser beam passes through a conical lens to form a ring-shaped light, which is then focused on the imaging object by an optical condenser. The dashed box shows the schematic of the confocal light illumination and acoustic detection. The optical illumination on the tissue surface is donut shaped with a dark center, so that no strong photoacoustic signals are produced within the ultrasonic field of view. The ultrasonic transducer is placed in the center of the optical condenser. The whole setup for light delivery and acoustic detection can be moved along translation stages for alignment and raster scans. The lateral resolution of AR-PAM is determined by the focal diameter of the ultrasound transducer. This focal diameter approximately equals $0.7\lambda/\text{NA}$, where λ is the acoustic wavelength at the central frequency and NA is the numerical aperture of the transducer [27]. The system shown in Fig. 6.4a has a 0.44 acoustic NA and a 50 MHz central frequency with 70% bandwidth. It can image deeper than 3 mm in live animals, with axial and lateral resolutions of 15 and 45 μm, respectively [7]. Figure 6.4b is an in vivo AR-PAM image of the cortical vasculature of an adult mouse with both the scalp and skull intact [28].

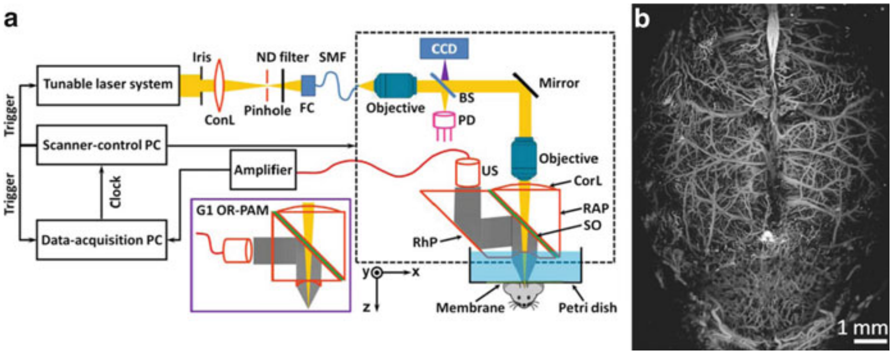

Fig. 6.5 (**a**) Schematic of the second-generation OR-PAM system. The *solid* boundary *inset* shows the configuration of the acoustic-optical combiner in the first-generation OR-PAM. ConL, condenser lens; ND, neutral density; FC, fiber collimator; SMF, single-mode fiber; CCD, charge-coupled device; BS, beam splitter; PD, photodiode; CorL, correction lens; RAP, right-angle prism; SO, silicone oil; RhP, rhomboid prism; US, ultrasonic transducer [8]. (reproduced from Hu et al. With permission.) (**b**) In vivo OR-PAM image of the cortical vasculature of an adult mouse with the scalp removed and the skull intact [29]. (reproduced from Hu and Wang. With permission)

6.2.2.2 Optical-Resolution PAM

As mentioned earlier, the lateral resolution of AR-PAM can be improved by using transducers with high central frequencies. However, high-frequency ultrasound also has strong attenuation in tissue, which limits the penetration depth of the system. For example, 5 μm lateral resolution can be achieved with an ultrasonic central frequency of 300 MHz. However, at such a high frequency, the penetration depth is only 100 μm, which is less than that of a pure optical microscope. Hence, instead of using high-frequency transducers, OR-PAM utilizes optical focusing to provide the lateral resolution.

Figure 6.5a is a schematic of a second-generation (G2) OR-PAM system [8]. The laser beam is first focused using an optical condenser and then spatially filtered by a pinhole. The filtered beam is launched into an optical fiber, whose output is collimated by a microscope objective. The collimated beam fills the back aperture of another identical objective, achieving nearly diffraction-limited optical focusing on the sample. A right angle prism and a rhomboid prism are used for acoustic-optical coaxial alignment. The gap between the two prisms is filled by silicone oil, so the light passes through while the ultrasound is reflected at the interface. Compared with the first-generation OR-PAM system, the G2 system replaces the lower right-angle prism with a rhomboid prism, which enhances the detection sensitivity by converting the shear-wave energy back into longitudinal waves, to which the ultrasonic transducer is more sensitive. Since the light illumination area is much smaller than the acoustic focus, bright-field illumination is utilized. The lateral resolution of the G2 OR-PAM is 2.1 μm, which is defined by the numerical aperture of the objective lens and the optical wavelength [8]. The axial resolution is still defined by the acoustic properties of the ultrasonic transducer. The high lateral resolution enables OR-PAM to resolve cortical microvasculature at single capillary levels (Fig. 6.5b) [8, 29]. Because of the limited penetration depth (~1 mm), the scalp needs to be removed in OR-PAM brain experiment [8].

6.3 Imaging Results

6.3.1 Real-Time Photoacoustic Tomography of Cortical Hemodynamics in Small Animals

Taking advantage of the full-ring array PACT system, the hemodynamics within the entire cerebral cortex of a Swiss Webster (23 g) mouse were studied in real-time by monitoring the wash-in process of a contrast dye [21]. After acquiring the control image (Fig. 6.6a), about 0.1 mL of Evans blue dye at 3% concentration was administered through tail vein injection. The entire cortical region was then continuously imaged at 620 nm (the peak absorption wavelength for the dye) at a temporal resolution of 1.6 s/frame. Since the optical absorption by blood is weak at 620 nm [30], the control image (Fig. 6.6a) misses many fine structures. With the increase in the optical absorption by Evans blue during the wash-in process,

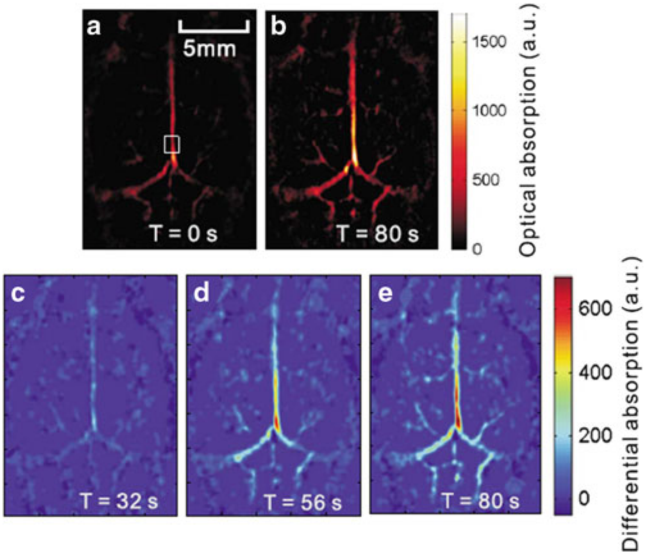

Fig. 6.6 Noninvasive imaging of the wash-in process of Evans blue in cortical vasculature. (**a**) and (**b**) PA images obtained before and after the dye injection. (**c**), (**d**), and (**e**) PA image difference relative to (**a**) at time 32, 56, and 80 s, respectively. All these images were obtained at 620 nm wavelength [21]. (reproduced from Li et al. With permission)

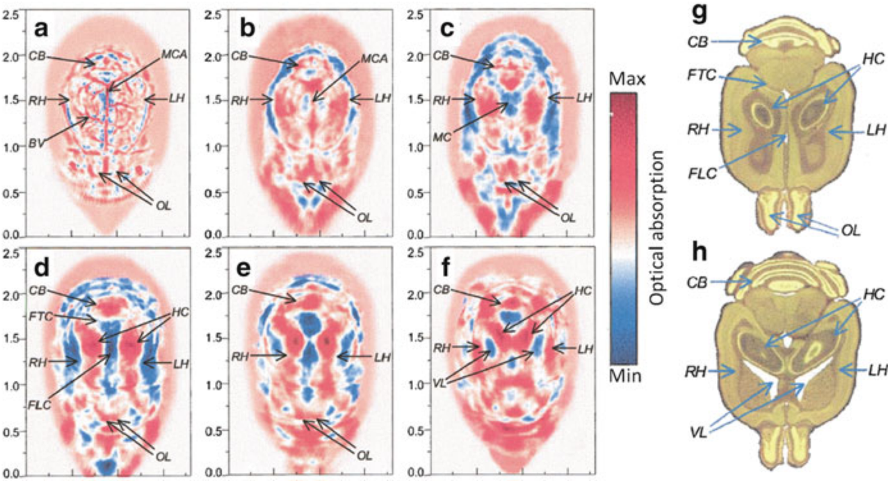

Fig. 6.7 Noninvasive 3D PACT of a mouse brain achieved with the skin and skull intact. The images show horizontal cross-sections from the dorsal to the ventral part of the brain, where the imaging depth is (**a**) 0.5 mm; (**b**) 2.0 mm; (**c**) 3.5 mm; (**d**) 5.0 mm; (**e**) 6.5 mm; and (**f**) 8.0 mm from the top surface of the mouse's head, with a constant interval of 1.5 mm. The size of each image is 1.8 cm × 2.5 cm. A color bar shows the magnitude of optical absorption, where the *red areas* (such as blood vessels) indicate tissues with comparatively higher optical absorption. The histological photographs in (**g**) and (**h**) are presented for comparison with the corresponding images in (**d**) and (**f**). In the PACT images and histological pictures, the major characteristic tissue structures in the mouse brain are indicated. BV, blood vessel; CB, cerebellum; FLC, fissura longitudinalis cerebri; FTC, fissura transversa cerebri; HC, hippocampus; LH, left hemisphere; MC, mesencephalon; MCA, middle cerebral artery; OL, olfactory lobes; RH, right hemisphere; VL, ventriculi lateralis [18]. (reproduced from Wang et al. With permission)

more vascular structures appeared, as shown in Fig. 6.6b. Figures 6.6c–e plot the differences between the pixel values in the subsequent images and the control image at three different times. Increases in the photoacoustic image values in both the hemispherical and the cerebellar vasculature can be clearly observed, demonstrating the increase in the dye concentration within the cortex blood vessels.

6.3.2 Three-Dimensional Structural Photoacoustic Tomography of a Mouse Brain

Three-dimensional structural PAT of a mouse (50 g) brain was achieved in situ with the skin and skull intact [18]. The experiment was performed using a circular-view PACT system equipped with a single-element unfocused transducer with 10 MHz central frequency. The circular scan, in combination with linear scans along the elevation, constitutes a cylindrical scan around the mouse head. An Nd:YAG laser operating at 532 nm was the excitation source. Figures 6.7a–f present

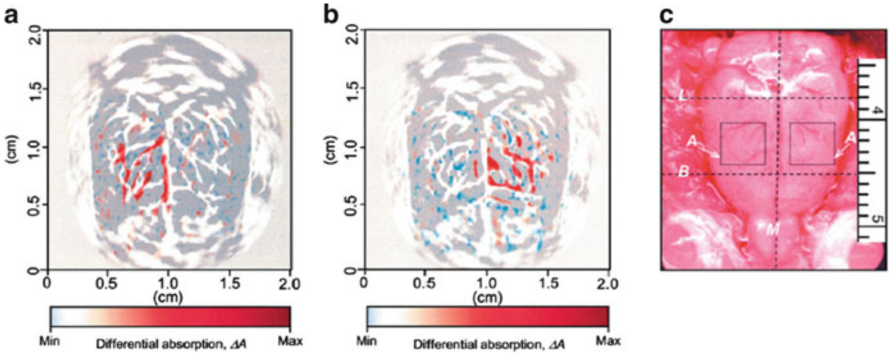

Fig. 6.8 Functional imaging of cerebral hemodynamic changes in response to whisker stimulation. (**a**) and (**b**) Noninvasive functional PACT images corresponding to *left*-side and *right*-side whisker stimulation, respectively, acquired with the skin and skull intact. The two maps of functional representations of whiskers are superimposed on the image of the vascular pattern in the superficial cortex. (**c**) Open-skull photograph of the rat cortical surface. B, bregma; L, lambda; M, midline; A, activated regions corresponding to whisker stimulation (4 mm × 4 mm) [1] (reproduced from Wang et al. With permission)

cross-sectional images of the brain at depths ranging from 0.5 to 8 mm, with an interval of 1.5 mm. Figure 6.7a shows the cortical surface of the mouse brain, where the vascular distribution in the superficial cortex can be seen clearly with high optical contrast. Figures 6.7b–f present the interior brain structures underneath the superficial cortex. For illustration, Fig. 6.7d, f are compared with their corresponding histological photographs in Fig. 6.7g, h, respectively [18]. Good matches can be observed, demonstrating that the characteristic tissue structures in the mouse brain can be imaged noninvasively using circular-view PACT. Since the optical absorption of blood is high at 532 nm [30], the image contrast is due to different hemoglobin concentrations in various brain tissues.

6.3.3 Functional Photoacoustic Brain Imaging

In the visible and near-infrared region, the dominant chromophores in the brain are HbO_2 and Hb, which have different absorption spectra. Therefore, when optical absorption from other chromophores can be neglected, spectral PAT can be utilized to separate the absorption contributions from HbO_2 and Hb, and provide functional information, such as SO_2 and HbT.

In vivo functional brain imaging using PAT was first demonstrated by Wang et al. in 2003 [1]. In that report, the neuronal activity due to whisker stimulation was studied on adult Sprague–Dawley rats (~350 g), using a single-element circular-view PACT system. To maximize the signal response, all whiskers on one side of the rat snout were deflected simultaneously at 10 Hz, with 8 mm oscillation amplitude. In the photoacoustic images (Fig. 6.8a, b) of whisker stimulation on

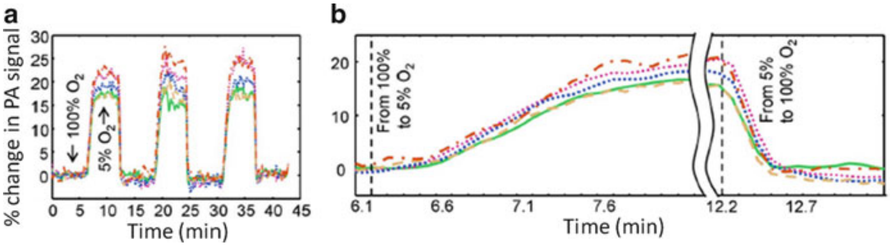

Fig. 6.9 Dynamic vessel response profiles. (**a**) Profile acquired through a hypoxic challenge and shown in percent change of radiometric PA signals. (**b**) Close-up of parts of the dynamic vessel responses shown in (**a**). Each colored trace corresponds to the response profile from a respective cortex vessel [28] (reproduced from Stein et al. With permission)

either side, the control image, where no stimulation was performed, was subtracted. Because the rat whisker-to-barrel system is lateralized, simulation on one side of the snout causes an increased neuroactivity accompanied by an increased blood flow on the contralateral side of the somatosensory cortex. The experimental findings (Fig. 6.8a, b) well agree with this mechanism, indicating that PAT can detect functional neuroactivity by imaging the changes in the local cerebral blood flow. The activated regions visualized by PACT are marked on the open-skull photograph of the brain cortical surface by two dotted frames (Fig. 6.8c). After the in vivo experiment, histological evaluation confirmed that the activated regions represented the whisker-barrel cortex.

Using a similar circular-view PACT system, the changes in HbT and SO_2 under three systemic physiological states—hyperoxia, normoxia, and hypoxia—were studied noninvasively in a rat model [2]. During the experiment, the oxygen concentration in the inhaled gas was adjusted through a gas proportioning meter, and the rat's global arterial blood oxygenation level was monitored in real-time using a pulse oximeter. In order to separate the absorptions from Hb and HbO_2, the brain was imaged using two wavelengths (584 and 600 nm) during each physiological state, generating six structural images. Before functional parameters were computed, the areas of cortical veins were segmented from the image background. It was found that the averaged SO_2 level in the segmented veins were 80, 70, and 57% in the hyperoxia, normoxia, and hypoxia states, respectively. The changes in HbT were also studied. The normoxia to the hypoxia transition induced a 12% increase in HbT, while the hyperoxia to normoxia transition induced a 4% increase in HbT. These observations agree well with the physiology of the brain [31].

In another study, AR-PAM was used to monitor the blood-oxygenation dynamics in response to controlled hypoxic and hyperoxic challenges in real-time [28]. After the entire cortical vasculature of an adult mouse was imaged (Fig. 6.4b), several somatosensory cortex vessels were identified. The cross-sections of these vessels were then studied in AR-PAM using B-scans, which can generate a depth-resolved cross-sectional image in less than 1 s. Instead of quantitatively calculating SO_2, the data was analyzed using a ratiometric procedure, which normalized the 561 nm image to the 570 nm image on a per-pixel basis. Because 570 nm is a hemoglobin

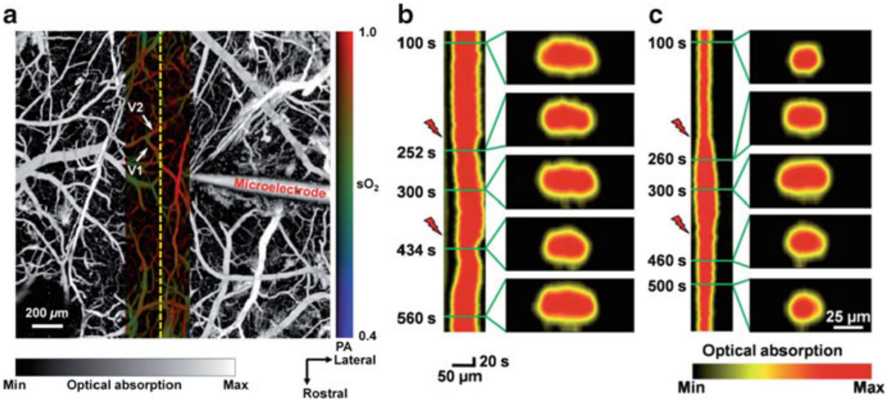

Fig. 6.10 (**a**) Superimposed open-skull photoacoustic images of the mouse cortical microvasculature. The maximum-amplitude projection image acquired at 570 nm is shown in *gray* scale, and the vessel-by-vessel hemoglobin oxygen saturation mapping of a smaller region calculated from dual-wavelength measurements is shown in color scale. (**b**) and (**c**) B-scan monitoring of vasoconstriction and vasodilatation induced by direct electrical stimulations at (**b**) 100 and (**c**) 150 μA. In each panel, the *left column* is the time course of the change in vessel diameter. The *right column* is the vessel cross-sectional image at different time points, indicated by the *green lines*. The *red* lightning symbol indicates the onset of the stimulation [32]. (reproduced from Tsytsarev et al. With permission)

isosbestic wavelength and 561 nm is a deoxyhemoglobin-dominant wavelength, the normalized result provides a time series of functional images whose magnitude is inversely proportional to the blood oxygenation level. The result shown in Fig. 6.9a is consistent with the aforementioned rat brain studies [2], i.e., hypoxia reduces the oxygenation level and hyperoxia increases the oxygenation level. Taking advantage of the fast scanning speed, Fig. 6.9b shows a close-up of the response curves, highlighting the response transition phases. A complete transition from hyperoxia to hypoxia took 63 s, while the subsequent recovery of hyperoxia took only 16 s.

Using high resolution OR-PAM, the vessel response to cortical electrical stimulation was monitored at the microscopic level [32]. The experiment was performed on a Swiss Webster mouse (~25 g). Before the experiment, a cranial opening ($4 \times 4\ \text{mm}^2$) was made using a dental drill. The exposed dura mater surface was then cleaned with artificial cerebrospinal fluid. To induce electrical stimulation, a 10-μm-diameter tungsten electrode was introduced into the cortex to a depth of 0.1–0.2 mm through the opening at about 2 mm lateral to the sagittal suture and 2 mm posterior to the bregma. The direct electrical stimulation caused reactions in cortical neurons, smooth muscle cells, and astrocytes, and subsequently drove the cortical vessels from the resting state to either vasoconstriction or vasodilatation. The experiment was first performed using two wavelengths (570 and 578 nm) to quantify the SO$_2$ within a small region of interest around the tip of the microelectrode (Fig. 6.10a). The dashed line in Fig. 6.10a was then chosen for hemodynamic monitoring at various stimulation intensities. Figure 6.10b, c demonstrate the vasoconstriction and vasodilatation of the same microvessel (V1 in Fig. 6.10a) in response to electrical stimulations at different current levels. At 100 μA, a distinct vasoconstriction appeared after each of the two stimuli. At 150 μA, the first stimulus produced a pronounced and prolonged vasodilatation, which prevented the vessel from recovering to the resting state before the arrival of the second stimulus. The study also found that 107 μA was the critical stimulation intensity corresponding to the transition from vasoconstriction to vasodilatations, indicating both coexistence and competition between the two responses.

6.3.4 Photoacoustic Tomography of the Brain Using Contrast Agents

Since photoacoustic signals originate from optical absorption, the vascular imaging contrast of PAT can be enhanced by using optical contrast agents. There are two main types of optical contrasts—organic dyes and metallic nanoparticles. Although nanoparticles normally have higher molar absorption coefficients and better wavelength tunability than organic dyes, the nanotoxicity of these materials is still unclear [33, 34]. On the other hand, organic dyes are generally nontoxic, and a few of them have already been approved by the US Food and Drug Administration (FDA) for human use [35–37]. Here we highlight a study using indocyanine green (ICG) [3] as the contrast agent. Reviews of various PAT contrast agents can be found in references [38, 39].

To prolong the dye circulation in blood, ICG was first stabilized by an FDA-approved polymer, polyethylene glycol (PEG). The conjugated ICG (ICG-PEG) had a peak absorption wavelength of 805 nm, which was also used as the laser irradiation wavelength. The experiment was performed on a Sprague–Dawley rat (~150 g) using the single-element circular-view PACT system. Figure 6.11a, b show noninvasive photoacoustic images acquired before and after ICG-PEG injection, respectively. The cortical structures in both images match well with the open-skull photograph (Fig. 6.11d) taken after the PA experiment. With the pre-injection image subtracted from the post-injection image, Fig. 6.11c shows increased photoacoustic signals due to the ICG-PEG injection. This differential image has a reduced background and shows detailed vasculature with small vessel branches (indicated as black arrows in Fig. 6.11c) that are not seen in Fig. 6.11a, b. Based on the signal amplitude, the dye detection sensitivity of the system was quantified to be 2 fmol per resolvable volume ($60 \times 60 \times 100\ \mu m^3$).

6.3.5 Simultaneous Functional and Molecular Photoacoustic Tomography of the Brain

Optical contrast agents can also be conjugated with bioactive materials to generate tissue-specific or molecular information. Taking advantage of this, Li et al. demonstrated that PAT can provide simultaneous functional and molecular brain

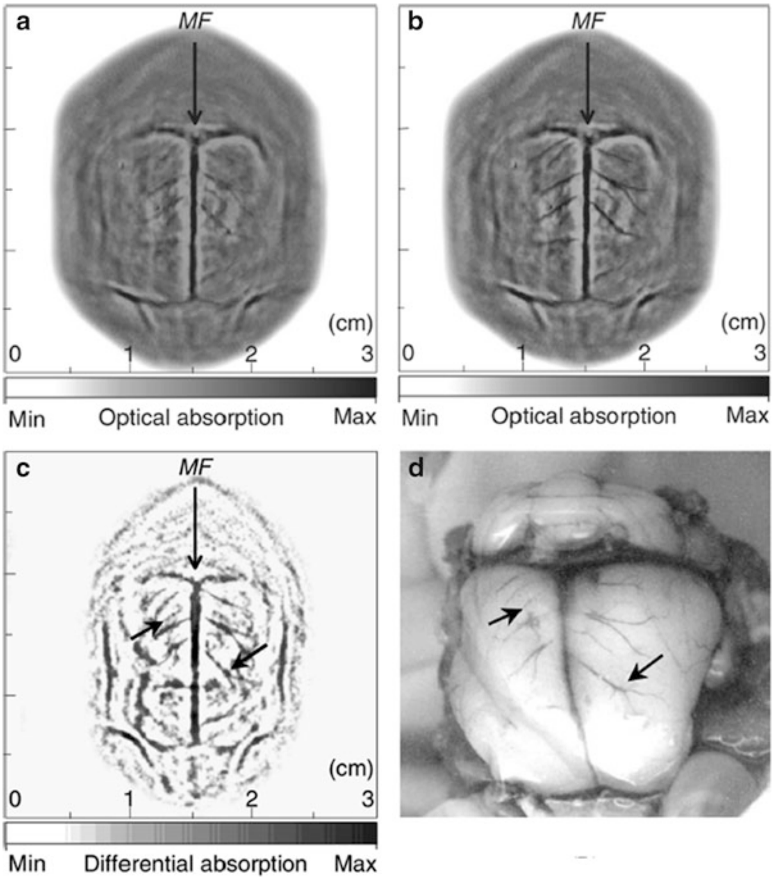

Fig. 6.11 In vivo noninvasive photoacoustic images of a rat brain. (**a**) and (**b**) Photoacoustic images acquired before and after the injection of ICG-polyethylene glycol (PEG), respectively, where the two *gray* scales are the same. MF, median fissure. (**c**) ICG-based angiograph of the rat brain (**c** = **b**−**a**). (**d**) Open-skull photograph of the rat brain obtained after the data acquisition (DAQ) for photoacoustic imaging. *Black arrows* indicate small vessel branches [3]. (reproduced from Wang et al. With permission)

imaging with high spatial resolution [40]. The contrast agent used in the study was an near-infrared dye named IRDye800-NHS (Li-Cor, Inc.) conjugated with a cyclic peptide, cyclo(Lys-Arg-Gly-Asp-phe) [c(KRGDf) for short]. IRDye800-c(KRGDf) targets $\alpha_v\beta_3$ integrin, which is over-expressed in the U87 glioblastoma tumor. Nude mice with implanted human U87 glioblastoma tumor cells in their brains were imaged using a circular-view PACT system at four wavelengths: 764, 784, 804, and 824 nm. These four wavelengths were chosen for separating the absorptions from Hb, HbO_2, and the molecular contrast. Figure 6.12a is a functional image of SO_2 in cortical vessels. The tumor region (red arrow, Fig. 6.12a) shows lower SO_2 than the surrounding normal tissue, indicating hypoxic tumor vasculature.

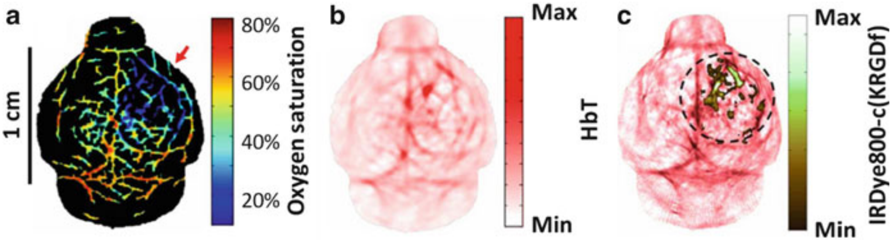

Fig. 6.12 In vivo molecular imaging of a nude mouse brain with a U87 glioblastoma xenograft. (**a**) SO_2 image. The *arrow* indicates the tumor region. (**b**) HbT image. (**c**) Composite of segmented molecular image of IRDye800-c(KRGDf) and structural image [40]. (reproduced from Meng-Lin et al. With permission)

Higher HbT (Fig. 6.12b) can also be observed around the same region due to tumor angiogenesis. Figure 6.12c is a composite image with the segmented molecular distribution superposed on the structural image of the brain cortex. It can be seen that the contrast agent mainly accumulates at the tumor region. After the in vivo experiment, the location and depth of the tumor observed in the photoacoustic images was confirmed by histological analysis [40].

6.3.6 Photoacoustic Tomography of Mouse Cerebral Edema Induced by Cold Injury

Taking advantage of the fact that water has a peak absorption coefficient around 975 nm, PAT was used to image a cold-induced cerebral edema in vivo [41]. The experiment was performed on adult mice (~25 g) using the full-ring array PACT system [20]. After the healthy brain was imaged, cold injury was induced by placing an aluminum tube filled with liquid nitrogen on the mouse scalp for 30 s. The mouse was then imaged 12, 24, and 36 h after the cold injury, using two wavelengths (610 and 975 nm) to track the changes in blood volume and water distribution at the edema site. Figure 6.13 shows the brain images acquired in vivo by the PACT system and subsequently acquired ex vivo by MRI. The imaging cross-section is approximately 1 mm beneath the brain surface. The 610 nm images (Fig. 13a, b) indicate the decreased amount of blood in the vessel during the first 24 h after the cold injury, while the 975 nm images (Fig. 13c, d) show an accumulation of water after the cold injury. These observations are consistent with brain cold injury studies [42]. Immediately after the PACT experiment, the mouse was sacrificed and scanned in a small-animal MRI scanner. The edema region indicated by MRI (Fig. 6.13e) agrees well with the PACT image in Fig. 6.13d.

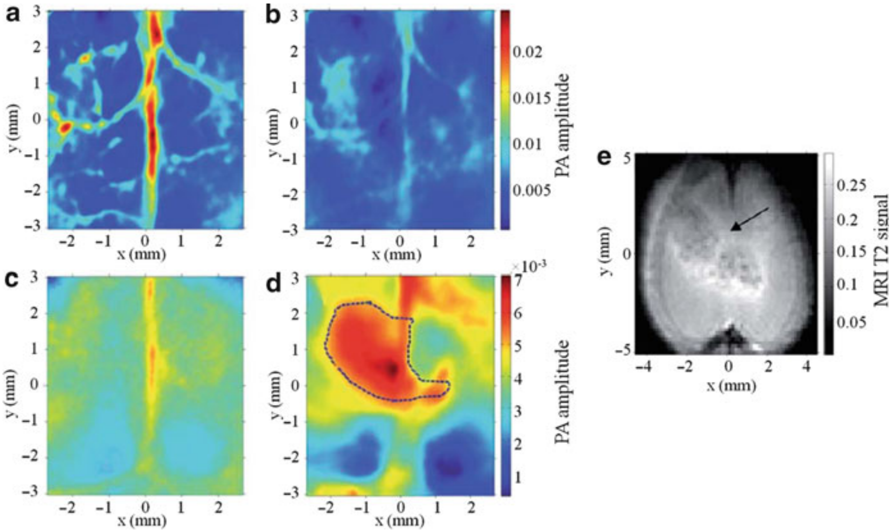

Fig. 6.13 Transcranial photoacoustic images of the mouse brain acquired noninvasively before cold injury (**a** and **c**) and 24 h after cold injury (**b** and **d**). The *upper* and *lower row* images were acquired at 610 and 975 nm wavelengths, respectively. (**e**) MRI image of the mouse cortex, taken immediately after the mouse was sacrificed. The edema is indicated by the *arrow*. The *dashed line area* in (**d**) outlines the contour area according to 60 % of the maximum water signal acquired at 975 nm [41] (reproduced from Xu et al. With permission)

6.3.7 *Photoacoustic Tomography of the Monkey Brain*

Besides small-animal brain imaging, PAT has also successfully imaged monkey brains [43]. The study was performed on a fresh head sample (9 × 7 cm in axial view) of a 20-month-old rhesus monkey, whose skull thickness was approximately 2 mm. Since the ultrasonic signals propagating through a skull are less distorted at lower frequencies (0.5–1 MHz) [44], the experiment utilized a 1 MHz central frequency transducer with 60% bandwidth and 12 mm diameter element size. A single-element circular-view PACT system was used to acquire images. The photoacoustic image (Fig. 6.14b) of the brain with the skull bone shows high correlation (0.7) with the photoacoustic image (Fig. 6.14c) of the exposed brain, indicating that the effect of the skull bone on PACT is not significant. However, the presence of the scalp degraded the photoacoustic image (Fig. 6.14a) significantly, probably because the scalp and dura mater severely reduced the laser penetration, and thus reduced the image's signal-to-noise ratio (SNR). Due to light attenuation in the scalp and dura meter, the vessels also look thicker in Fig. 6.14a. In a later study, Nie et al. [45]. demonstrated that the SNR and spatial resolution of the skull-only image (Fig. 6.14b) can be further improved by using the virtual point detector technique [27, 46].

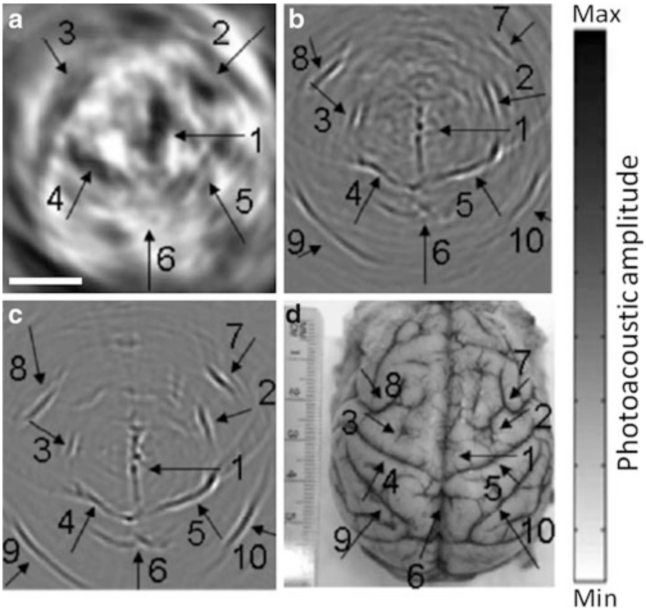

Fig. 6.14 (**a**) Photoacoustic image of a rhesus monkey brain with intact scalp and skull bone. Scale bar: 10 mm. (**b**) Photoacoustic image of the monkey brain with the skull bone only. (**c**) Photoacoustic image of the exposed monkey brain. (**d**) Photograph of the exposed monkey brain. The blood vessels that can be identified from photoacoustic images have matching numbers [43] (reproduced from Yang and Wang. With permission)

Ultrasound attenuation through the skull was also studied in detail by placing the skull between the detector and a human hair. The skull was then rotated to simulate different ultrasound incident angles. It was found that the PA signal from the hair decreased as the incident angle increased, and when the incident angle was larger than 35° the signal started to increase again. This observation can be explained by the fact that a PA signal contains both longitudinal and shear waves. When the incident angle reaches the critical angle for longitudinal waves, shear waves can still propagate and will convert into longitudinal waves at the exit boundary.

The monkey brain studies indicate that PAT can image through a relatively thick skull, and with proper modeling of the scalp and skull effects, PAT has great potential to be used in human neonatal brain imaging.

6.4 Discussion

Since the first demonstration of functional PAT in 2003 [1], the field has been growing rapidly. Neurovascular, functional, and molecular brain images at multiple spatial scales have been demonstrated on various animal models. While PAT has established itself as a promising tool for brain studies, more work needs to be completed to further improve the performance of this technique. In terms of imaging speed, the bottlenecks are the DAQ rate (for circular-view PACT) [20, 47], the laser pulse repetition rate (for both PACT and PAM) [48], and the raster-scanning speed (for PAM and planar-view PACT) [49–51]. Various solutions have been proposed to address these problems [47–51]. Quantitative photoacoustic studies also have challenges due to the fact that the photoacoustic signal is proportional to the product of the local light fluence and optical absorption coefficient. Therefore, optical heterogeneities in the brain need to be taken into account in spectral photoacoustic studies [52]. With a limited spatial resolution, diffuse optical tomography has been combined with PAT to estimate the local fluence [53, 54]. Absolute quantification of absorption coefficients using acoustic spectra has also been demonstrated [55]. As with optical heterogeneities, acoustic heterogeneities, such as variations in the speed of sound, also need to be considered, especially in computational image reconstruction [56–58]. This is important when implementing PAT on monkey or human brain studies, where the skull effect cannot be neglected. Nevertheless, despite these challenges, PAT, with its unique combination of optical absorption sensitivity and ultrasonic imaging depth and resolution scalability, has great potential to play an important role in brain imaging.

References

1. Wang X et al (2003) Noninvasive laser-induced photoacoustic tomography for structural and functional in vivo imaging of the brain. Nat Biotechnol 21:803–806
2. Wang X, Xie X, Ku G, Wang LV, Stoica G (2006) Noninvasive imaging of hemoglobin concentration and oxygenation in the rat brain using high-resolution photoacoustic tomography. J Biomed Opt 11:024015
3. Wang X et al (2004) Noninvasive photoacoustic angiography of animal brains in vivo with near-infraredlight and an optical contrast agent. Opt Lett 29:730–732
4. Razansky D et al (2009) Multispectral opto-acoustic tomography of deep-seated fluorescent proteins in vivo. Nat Photon 3:412–417
5. Wang LV (2009) Multiscale photoacoustic microscopy and computed tomography. Nat Photonics 3:503–509
6. Maslov K, Zhang HF, Hu S, Wang LV (2008) Optical-resolution photoacoustic microscopy for in vivo imaging of single capillaries. Opt Lett 33:929–931
7. Maslov K, Stoica G, Wang LV (2005) In vivo dark-field reflection-mode photoacoustic microscopy. Opt Lett 30:625–627
8. Hu S, Maslov K, Wang LV (2011) Second-generation optical-resolution photoacoustic microscopy with improved sensitivity and speed. Opt Lett 36:1134–1136
9. Fang H, Maslov K, Wang LV (2007) Photoacoustic Doppler effect from flowing small light-absorbing particles. Phys Rev Lett 99:184501
10. Yao J, Maslov KI, Zhang Y, Xia Y, Wang LV (2011) Label-free oxygen-metabolic photoacoustic microscopy in vivo. J Biomed Opt 16(7):076003
11. Xu M, Wang LV (2005) Universal back-projection algorithm for photoacoustic computed tomography. Phys Rev E Stat Nonlin Soft Matter Phys 71:016706

12. Burgholzer P, Matt GJ, Haltmeier M, Paltauf G (2007) Exact and approximative imaging methods for photoacoustic tomography using an arbitrary detection surface. Phys Rev E Stat Nonlin Soft Matter Phys 75:046706
13. Cox BT, Beard PC (2005) Fast calculation of pulsed photoacoustic fields in fluids using k-space methods. J Acoust Soc Am 117:3616–3627
14. Rosenthal A, Ntziachristos V, Razansky D (2011) Model-based optoacoustic inversion with arbitrary-shape detectors. Med Phys 38:4285–4295
15. Xu MH, Wang LHV (2006) Photoacoustic imaging in biomedicine. Rev Sci Instrum 77:22
16. Mark A, Peter K, Leonid K (2009) On reconstruction formulas and algorithms for the thermoacoustic tomography. In: Wang LV (ed) Photoacoustic Imaging and Spectroscopy. CRC Press, Boca Raton, FL, pp 89–101
17. American National Standard Institute (2000) American National Standard for safe use of lasers, ANSI Z136.1. American National Standard Institute, New York
18. Wang X, Pang Y, Ku G, Stoica G, Wang LV (2003) Three-dimensional laser-induced photoacoustic tomography of mouse brain with the skin and skull intact. Opt Lett 28:1739–1741
19. Gamelin J et al (2008) Curved array photoacoustic tomographic system for small animal imaging. J Biomed Opt 13:10
20. Gamelin J et al (2009) A real-time photoacoustic tomography system for small animals. Opt Express 17:10489–10498
21. Li C et al (2010) Real-time photoacoustic tomography of cortical hemodynamics in small animals. J Biomed Opt 15:010509
22. Gamelin J et al (2009) Design and characterization of an array-based photoacoustic tomographic system for small animal imaging. In: Wang LV (ed) Photoacoustic imaging and spectroscopy. CRC Press, Boca Raton, FL, pp 309–328
23. Xu MH, Wang LV (2003) Analytic explanation of spatial resolution related to bandwidth and detector aperture size in thermoacoustic or photoacoustic reconstruction. Phys Rev E Stat Nonlin Soft Matter Phys 67:15
24. Zhang E, Laufer J, Beard P (2008) Backward-mode multiwavelength photoacoustic scanner using a planar Fabry-Perot polymer film ultrasound sensor for high-resolution three-dimensional imaging of biological tissues. Appl Opt 47:561–577
25. Laufer J, Zhang E, Raivich G, Beard P (2009) Three-dimensional noninvasive imaging of the vasculature in the mouse brain using a high resolution photoacoustic scanner. Appl Opt 48: D299–D306
26. Zhang HF, Maslov K, Stoica G, Wang LV (2006) Functional photoacoustic microscopy for high-resolution and noninvasive in vivo imaging. Nat Biotechnol 24:848–851
27. Li C, Wang LV (2008) High-numerical-aperture-based virtual point detectors for photoacoustic tomography. Appl Phys Lett 93:033902
28. Stein EW, Maslov K, Wang LV (2009) Noninvasive, in vivo imaging of blood-oxygenation dynamics within the mouse brain using photoacoustic microscopy. J Biomed Opt 14:020502
29. Hu S, Wang LV (2010) Neurovascular photoacoustic tomography. Front Neuroenergetics 2:10
30. Li C, Wang LV (2009) Photoacoustic tomography and sensing in biomedicine. Phys Med Biol 54:R59–R97
31. Duong TQ, Iadecola C, Kim S-G (2001) Effect of hyperoxia, hypercapnia, and hypoxia on cerebral interstitial oxygen tension and cerebral blood flow. Magn Reson Med 45:61–70
32. Tsytsarev V et al (2011) Photoacoustic microscopy of microvascular responses to cortical electrical stimulation. J Biomed Opt 16:076002
33. Gwinn MR, Vallyathan V (2006) Nanoparticles: health effects - pros and cons. Environ Health Perspect 114:1818–1825
34. Lovell JF et al (2011) Porphysome nanovesicles generated by porphyrin bilayers for use as multimodal biophotonic contrast agents. Nat Mater 10:324–332
35. He YL, Tanigami H, Ueyama H, Mashimo T, Yoshiya I (1998) Measurement of blood volume using indocyanine green measured with pulse-spectrophotometry: its reproducibility and reliability. Crit Care Med 26:1446–1451

36. Haglund MM, Berger MS, Hochman DW (1996) Enhanced optical imaging of human gliomas and tumor margins. Neurosurgery 38:308–317
37. Hochheimer BF (1971) Angiography of rentina with indocyanine green. Arch Ophthalmol 86:564–565
38. Kim C, Favazza C, Wang LHV (2010) In vivo photoacoustic tomography of chemicals: high-resolution functional and molecular optical imaging at new depths. Chem Rev 110:2756–2782
39. Oraevsky A (2009) Gold and silver nanoparticles as contrast agents for optoacoustic tomography. In: Wang LV (ed) Photoacoustic imaging and spectroscopy. CRC Press, Boca Raton, FL, pp 373–386
40. Meng-Lin L et al (2008) Simultaneous molecular and hypoxia imaging of brain tumors in vivo using spectroscopic photoacoustic tomography. In: Proceedings of the IEEE, vol 96, pp 481–489
41. Xu Z, Zhu Q, Wang LV (2011) In vivo photoacoustic tomography of mouse cerebral edema induced by cold injury. J Biomed Opt 16:066020
42. Frei HJ et al (1973) Regional cerebral blood flow and regional metabolism in cold induced oedema. Acta Neurochir 29:15–28
43. Yang X, Wang LV (2008) Monkey brain cortex imaging by photoacoustic tomography. J Biomed Opt 13:044009
44. Fry FJ (1977) Transkull transmission of an intense focused ultrasonic beam. Ultrasound Med Biol 3:179–184
45. Nie L, Guo Z, Wang LV (2011) Photoacoustic tomography of monkey brain using virtual point ultrasonic transducers. J Biomed Opt 16:076005
46. Yang XM, Li ML, Wang LHV (2007) Ring-based ultrasonic virtual point detector with applications to photoacoustic tomography. Appl Phys Lett 90:3
47. Buehler A, Herzog E, Razansky D, Ntziachristos V (2010) Video rate optoacoustic tomography of mouse kidney perfusion. Opt Lett 35:2475–2477
48. Shi W, Hajireza P, Shao P, Forbrich A, Zemp RJ (2011) In vivo near-realtime volumetric optical-resolution photoacoustic microscopy using a high-repetition-rate nanosecond fiber-laser. Opt Express 19:17143–17150
49. Wang L, Maslov K, Yao J, Rao B, Wang LV (2011) Fast voice-coil scanning optical-resolution photoacoustic microscopy. Opt Lett 36:139–141
50. Rao B et al (2011) Real-time four-dimensional optical-resolution photoacoustic microscopy with Au nanoparticle-assisted subdiffraction-limit resolution. Opt Lett 36:1137–1139
51. Zemp RJ, Song L, Bitton R, Shung KK, Wang LV (2008) Realtime photoacoustic microscopy of murine cardiovascular dynamics. Opt Express 16:18551–18556
52. Beard P, Arridge S, Cox B, Laufer J (2009) Quantitative photoacoustic imaging. In: Wang LV (ed) Photoacoustic imaging and spectroscopy. CRC Press, Boca Raton, FL, pp 121–143
53. Yin L, Wang Q, Zhang Q, Jiang H (2007) Tomographic imaging of absolute optical absorption coefficient in turbid media using combined photoacoustic and diffusing light measurements. Opt Lett 32:2556–2558
54. Bauer AQ (2011) Quantitative photoacoustic imaging: correcting for heterogeneous light fluence distributions using diffuse optical tomography. J Biomed Opt 16:096016
55. Guo Z, Hu S, Wang LV (2010) Calibration-free absolute quantification of optical absorption coefficients using acoustic spectra in 3D photoacoustic microscopy of biological tissue. Opt Lett 35:2067–2069
56. Anastasio MA et al (2005) Half-time image reconstruction in thermoacoustic tomography. IEEE Trans Med Imaging 24:199–210
57. Cox BT, Kara S, Arridge SR, Beard PC (2007) k-space propagation models for acoustically heterogeneous media: application to biomedical photoacoustics. J Acoust Soc Am 121 (6):3453–64
58. Jin X, Wang LV (2006) Thermoacoustic tomography with correction for acoustic speed variations. Phys Med Biol 51:6437

Chapter 7
Optical Coherence Tomography for Brain Imaging

Gangjun Liu and Zhongping Chen

7.1 Introduction

Optical coherence tomography (OCT) is an imaging modality that takes advantage of the short coherence length of broad-band light sources to perform micrometer-scale, cross-sectional imaging of biological tissues [1]. In OCT, imaging contrast originates from variations in tissue scattering due to inhomogeneities in the sample's optical refractive indices. OCT offers axial resolution of 1–15 μm and penetration depth of around 2–3 mm. OCT was first used clinically in ophthalmology for the imaging and diagnosis of retinal disease. It has been applied to image subsurface structure in skin, vessels, and oral cavities as well as respiratory, urogenital, and gastrointestinal tracts [2].

Recently, there has been growing interest in using OCT for brain imaging. A feasibility study of OCT for guiding deep brain probes has found that OCT can differentiate the white matter and gray matter because the white matter tends to have a higher peak reflectivity and steeper attenuation rate compared to gray matter [3]. In vivo 3D visualization of the layered organization of a rat olfactory bulb with OCT has been demonstrated [4]. OCT has been used for single myelin fiber imaging in living rodents without labeling [5]. The refractive index in the rat somatosensory cortex was also measured with OCT [6]. In addition, functional extension of OCT, such as Doppler-OCT (D-OCT), polarization sensitive-OCT (PS-OCT), and phase-resolved-OCT (PR-OCT), can image and quantify physiological parameters in addition to the morphological structure image. Based on the scattering changes during neural activity, OCT has been used to measure the functional activation in neuronal tissues [7–12]. PS-OCT, which combines polarization sensitive detection with OCT to determine tissue birefringence, has been used for the localization of nerve fiber bundles and the

---

G. Liu • Z. Chen (✉)
Department of Biomedical Engineering, Beckman Laser Institute, University of California,
Irvine, CA, USA
e-mail: z2chen@uci.edu

S.J. Madsen (ed.), *Optical Methods and Instrumentation in Brain Imaging and Therapy*, Bioanalysis: Advanced Materials, Methods, and Devices 3,
DOI 10.1007/978-1-4614-4978-2_7, © Springer Science+Business Media New York 2013

mapping of micrometer-scale fiber pathways in the brain [13–15]. D-OCT, also named optical Doppler tomography (ODT), combines the Doppler principle with OCT to obtain high resolution tomographic images of moving constituents in highly scattering biological tissues [16–19]. D-OCT has been successfully used to image cortical blood flow and map the blood vessel network for brain research [20–25].

In this chapter, we review the principles and technology of OCT and D-OCT and describe a few examples of potential applications of OCT and D-OCT.

7.2 Principles of OCT and Doppler OCT

7.2.1 Principle of OCT

OCT uses coherent gating to discriminate single scattered photons from multiple scattered photons. OCT is based on a Michelson interferometer with a broadband light source (Fig. 7.1). Light from the source is split into a reference path and a sample path. The reference path light, after reflecting from the reference mirror interferes with the sample path light reflected or scattered back from the sample, and the interference pattern is detected by a photodetector. For the OCT system, short coherence broadband light sources are used, and the interference pattern is only observed when the reference and sample path lengths are matched to within the coherence length of the source. The axial resolution of an OCT system is determined by the coherence length of the light source, which is related to the central wavelength of the light source and the wavelength bandwidth. The lateral resolution is determined by the numerical aperture of the objective used to focus the light and the beam diameter incident on the objective.

To illustrate the coherence gating of the broadband light source, we consider the interference fringe generated in the Michelson interferometer with a broadband light source as in Fig. 7.1. The time-average, total power detected by the detector can be expressed as a sum of three terms representing reference (I_r), sample (I_s), and the interference fringe intensity ($\Gamma_{\text{oct}}(\tau)$),

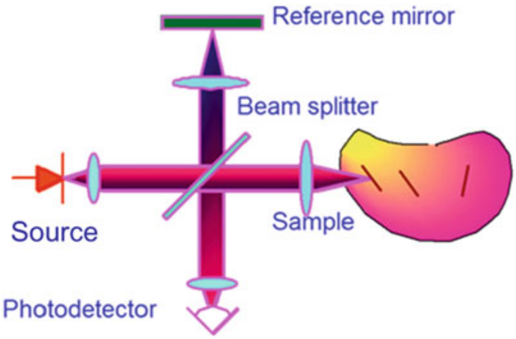

Fig. 7.1 Schematic of the OCT system

$$P_{\mathrm{d}}(v) = \int_{0}^{\infty} (P_{\mathrm{r}}(v) + P_{\mathrm{s}}(v) + P_{\mathrm{oct}}(v))\mathrm{d}v = I_{\mathrm{r}} + I_{\mathrm{s}} + \Gamma_{\mathrm{oct}}(\tau), \tag{7.1}$$

where v is the optical frequency, τ is the time delay between light traveled in the sample and reference arms and

$$P_{\mathrm{r}}(v) = S_0(v)|K_{\mathrm{r}}(v)|^2 \tag{7.2}$$

$$P_{\mathrm{s}}(v) = S_0(v)|K_{\mathrm{s}}(v)|^2 \tag{7.3}$$

$$P_{\mathrm{oct}}(v) = 2P_{\mathrm{oct}}(v)K_{\mathrm{r}}(v)K_{\mathrm{s}}(v)\cos[2\pi v(\Delta_{\mathrm{d}}/c + \tau)] \tag{7.4}$$

$$I_{\mathrm{r}} = \int_{0}^{\infty} P_{\mathrm{r}}(v)\mathrm{d}v \tag{7.5}$$

$$I_{\mathrm{s}} = \int_{0}^{\infty} P_{\mathrm{s}}(v)\mathrm{d}v \tag{7.6}$$

$$\Gamma_{\mathrm{oct}}(\tau) = \int_{0}^{\infty} P_{\mathrm{oct}}(v)dv \tag{7.7}$$

where Δ_{d} is the optical path length difference between light traveled in the sample and reference arms, $S_0(v)$ is the source power spectral density, $K_{\mathrm{r}}(v)$ and $K_{\mathrm{s}}(v)$ are the amplitude reflection coefficients of light backscattered from the reference mirror and turbid sample. Equation (7.7) shows that there is a Fourier transformation relation between the spectral domain signal $P_{\mathrm{oct}}(v)$ and time domain signals $\Gamma_{\mathrm{oct}}(\tau)$. Consequently, there are two methods to acquire the OCT signal: the spectral domain method and the time domain method.

Since the introduction of OCT in the 1990s, OCT has evolved from early time domain to Fourier domain systems. In a time domain OCT system, the source is typically a superluminescent diode (SLD), and the photodetector is a single element photovoltaic detector. The reference path length is rapidly changed by translating the reference mirror or by a rapid scanning optical delay (RSOD) line. The data processing consists of detecting the envelope of the detected fringe pattern corresponding to interference. In a Fourier domain-OCT (FD-OCT) system, the reference arm is kept stationary, and the interference fringes in the spectral domain are measured. Two methods have been developed to employ the Fourier domain technique: a spectrometer-based system [26, 27] and a swept laser source-based system [28, 29]. In a spectrometer-based OCT system, the photodetector in Fig. 7.1 is replaced with a spectrometer and the spectral interference pattern is detected by the spectrometer that spatially disperses different wavelengths onto different pixels of the line scan camera. In a swept laser source-based OCT system, the source in Fig. 7.1 is replaced with a wavelength sweeping laser, and the spectral interference pattern is detected by the single element photodetector as a function of time. The depth information for the FD-OCT system is encoded in the interference spectral fringe, and Fourier transform for the spectral fringe is used to obtain the depth information. FD-OCT systems have been shown to have better signal to noise ratio (SNR) and faster imaging speed than the time domain system. The faster speed and the higher SNR of the FD-OCT [30–32] make it promising for some high-speed and in vivo applications.

7.2.2 Principle of D-OCT

D-OCT combines the Doppler principle with OCT to obtain high resolution tomographic images of static and moving constituents simultaneously in highly scattering biological tissues [17, 18]. The first two-dimensional in vivo D-OCT imaging was reported using the spectrogram method [16–18]. The spectrogram method uses a short time fast Fourier transformation (STFFT) or wavelet transformation to determine the power spectrum of the measured fringe signal [16–18]. Although spectrogram methods allow simultaneous imaging of in vivo tissue structure and flow velocity, the velocity sensitivity is limited for high speed imaging. Phase-resolved D-OCT was developed to overcome these limitations [19]. This method uses the phase change between sequential A-line scans for velocity image reconstruction [19]. Phase-resolved D-OCT decouples spatial resolution and velocity sensitivity in flow images and increases imaging speed by more than two orders of magnitude without compromising spatial resolution and velocity sensitivity [19]. The significant increase in scanning speed and velocity sensitivity makes it possible to image in vivo tissue microcirculation in human skin [19, 33, 34]. Combination of the high speed and high sensitivity FD-OCT with the phase-resolved method has been demonstrated by a number of groups [35–37]. Because the dynamic range of the phase-resolved D-OCT depends on the speed of the line scans, FD Doppler OCT has an advantage over the time domain method in terms of imaging speed and velocity dynamic range.

In phase-resolved D-OCT, the Doppler frequency shift Δf is obtained by measuring the phase difference between sequential A-scans. The phase information of the fringe signal can be determined from the complex analytical signal $A_{j,z}$, where $A_{j,z}$ is the complex data at j_{th} A-scan and depth of z. The Doppler frequency shift Δf can be expressed as:

$$\Delta f = \frac{1}{2\pi}\frac{\mathrm{d}\phi}{\mathrm{d}t} = \frac{\Delta\phi}{2\pi T} = \frac{1}{2\pi\Delta T}\left[\tan^{-1}\left(\frac{\mathrm{Im}A_{j+1,z}}{\mathrm{Re}A_{j+1,z}}\right) - \tan^{-1}\left(\frac{\mathrm{Im}A_{j,z}}{\mathrm{Re}A_{j,z}}\right)\right] \tag{7.8}$$

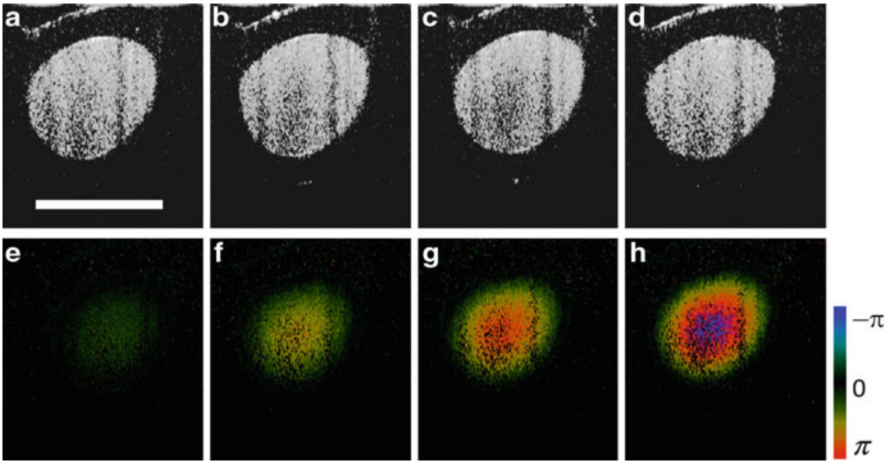

Fig. 7.2 (**a**–**d**) are OCT structure images of the flow phantom pumped at, respectively, 20, 40, 60, and 80 μL/min; (**e**–**h**) are D-OCT images of the flow phantom pumped at, respectively, 20, 40, 60, and 80 μL/min. Scale bar: 500 μm

where ΔT is the time difference between j_{th} A-scan and $(j+1)_{\text{th}}$ A-scan. In the time domain D-OCT system, the complex analytical signal $A_{j,z}$ is determined through analytic continuation of the measured interference fringes function by use of a Hilbert transformation. In FD-OCT systems, the complex signal $A_{j,z}$ is obtained through the Fourier transformation of the acquired fringe.

Alternatively, the phase change can also be calculated by the cross-correlation method [19]. In addition, averaging can improve the SNR [19, 38]. Averaging could be performed in both lateral and depth directions and the Eq (7.8) becomes [19, 38]:

$$\bar{f} = \frac{1}{(2\pi \cdot \Delta T)} \cdot \arctan\left\{ \frac{\sum_{j=1}^{J}\sum_{z=1}^{N}\left[\mathrm{Im}(A_{j+1,z})\mathrm{Re}(A_{j,z}) - \mathrm{Im}(A_{j,z})\mathrm{Re}(A_{j+1,z})\right]}{\sum_{j=1}^{J}\sum_{z=1}^{N}\left[\mathrm{Re}(A_{j,z})\mathrm{Re}(A_{j+1,z}) + \mathrm{Im}(A_{j+1,z})\mathrm{Im}(A_{j,z})\right]} \right\} \tag{7.9}$$

where J is the number of A-lines that are averaged, and N is the number of depth points that are averaged. The choice of J and N are dependent on application. Generally, a larger J and N will increase SNR. However, it also increases the computing time and decreases resolution.

Figure 7.2a–d are OCT structure images of the flow phantom pumped at, respectively, 20, 40, 60, and 80 μL/min. Figure 7.2e–h are phase-resolved D-OCT images of flow phantom pumped at, respectively, 20, 40, 60, and 80 μL/min. It should be noted that the phase is wrapped in Fig. 7.2h. It can be clearly seen from the D-OCT images that the Doppler frequency shift increases with increasing pumping speed.

In addition to the Doppler shift, Doppler variance can also be used to map the flow. Doppler variance has the benefit of being less sensitive to the pulsatile nature of the blood flow, less sensitive to the incident angle, and may be used to obtain the transverse flow velocity [33]. If σ denotes the standard deviation of the Doppler spectrum, the Doppler variance σ^2 can be obtained [33]:

$$\sigma^2 = \frac{\int (f - \bar{f})^2 P(f) \mathrm{d}f}{\int P(f) \mathrm{d}f} = \overline{f^2} - \bar{f}^2 \tag{7.10}$$

where $\bar{f}$ is the Doppler frequency and $P(f)$ is the power spectrum of the Doppler frequency shift. Using autocorrelation theory, the variance can be expressed as [33]:

$$\sigma^2 = \frac{1}{(2\pi \cdot \Delta T)^2} \left[1 - \frac{\left| \sum_{j=1}^{J} \sum_{z=1}^{N} (A_{j+1,z} A_{j,z}^*) \right|}{\sum_{j=1}^{J} \sum_{z=1}^{N} (A_{j,z} A_{j,z}^*)} \right] \tag{7.11}$$

where $A_{j,z}^*$ is the complex conjugate of $A_{j,z}$, J is the number of A-lines that are averaged, and N is the number of depth points that are averaged.

7.3 Brain imaging with OCT and D-OCT

7.3.1 Brain Anatomy

The cerebral cortex is generally believed to be composed of functional units called “columns” that are arranged in clusters perpendicular to the surface. Each column is comprised of neurons that respond preferentially to a specific feature of a stimulus that differs from its neighboring columns. Furthermore, perpendicular to the functional columns and parallel to the surface, the cortex is composed of six anatomical “layers,” with layer I being the outermost and VI, the innermost. Each anatomic layer is different by virtue of its connectivity pattern and/or cellular composition. Throughout the cortex, capillaries form a dense network near neurons. Changes in brain blood flow are known to be coupled to regions of neuronal activity. However, it is poorly understood whether there are layer differences in blood flow changes that occur within a column. Changes in blood flow within a cortical column are clinically important because disruption of this coupling is likely related to certain types of neuropathology, such as dementia [39].

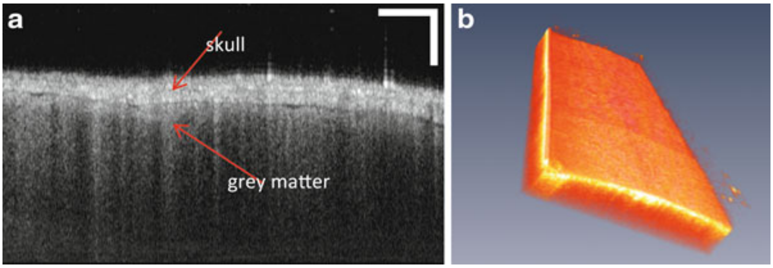

Fig. 7.3 In vivo OCT imaging of mouse brain. (**a**) One single OCT image of the mouse brain. (**b**) 3D volume rendering of the acquired mouse brain data

7.3.2 OCT Imaging of Brain

Imaging of internal brain structure has been performed with magnetic resonance imaging (MRI), positron emission tomography (PET), and near-infrared imaging with millimeter resolution [40, 41]. However, these methods have limited spatial resolution [5]. Multiphoton microscopies, such as coherent anti-Stokes-Raman scattering (CARS) microscopy, two photon-excited fluorescence (TPEF), second harmonic generation (SHG) microscopy, and third harmonic generation (THG) microscopy have also been demonstrated to image brain tissue with high spatial resolution. These nonlinear optical microscopes have limited penetration depth, typically a few hundred micrometers, and cannot provide quantitative information on large volumes of brain tissue. The micrometer resolution, millimeter penetration depth, and label-free nature make OCT one of the promising techniques for in vivo, large volume imaging of brain.

Figure 7.3 shows in vivo OCT images of a young mouse cortex with an intact skull. The OCT system is a swept source-based FD-OCT system with a central wavelength of 1,310 nm. The interface between the skull and gray matter can be clearly seen in Fig. 7.3a. Quantitative information, such as skull thickness, can be obtained from this image. A single A-line profile can also be used to quantify tissue properties and differentiate the tissue content [3]. Figure 7.3b shows the reconstructed 3D volume rendering of the acquired data.

OCT can also be used to provide surgical guidance in laser treatment of an epilepsy lesion. Epilepsy is a debilitating neurological disorder affecting 2.3 million people in the United States and an estimated 50 million people worldwide. Many types of brain lesions can trigger epilepsy. Although medical treatments are available, one in four patients continue to have seizures even under optimized antiepileptic drug regimens. For these patients who do not respond to medications, the removal of the lesion by surgical method is the only way to control the seizure. However, one of the challenges for surgical removal of the epileptic lesion is the accurate determination of the depth/boundary of the lesion during surgery. Currently, there is no noninvasive method to determine the depth/boundary of the lesion during surgery. In collaboration with Dr. Pearltson of Duke University, we

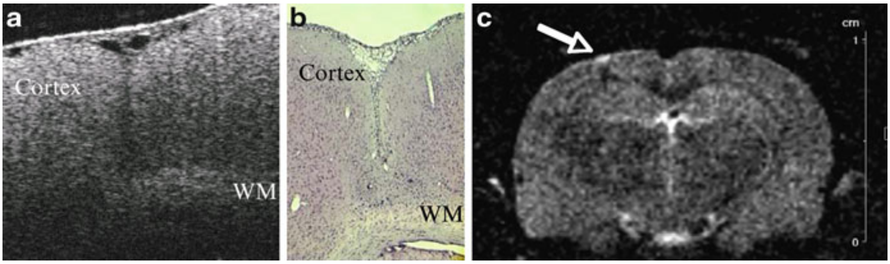

Fig. 7.4 Images of epileptogenic brain lesion in the neonatal rat model: (**a**) OCT image, (**b**) histology, (**c**) MRI image

have imaged rat brain from a neonatal rat model that has an epileptogenic brain lesion that is similar to developmental brain lesions observed in certain epileptic patients. Figure 7.4a shows an OCT image of the epileptogenic brain lesion in the neonatal rat model. We can clearly identify the depth/boundary of the lesion in the OCT image. Furthermore, we can also identify white matter in the brain that matches what we see in the histology (Fig. 7.4b). For comparison, we also include the MR image (Fig. 7.4c). Although MRI can identify the location of the lesion, the spatial resolution of MRI is too poor to determine the depth/boundary of the lesion. These results clearly demonstrate the value of an OCT image for surgical guidance for laser treatment of epilepsy lesions.

Another exciting field of OCT for brain imaging is neuroendovascular OCT. Endoscopic- or catheter-based probes enable access of internal structures of the brain with no or minimal invasion. Our group has developed a neuroendovascular OCT device that enables imaging of patients with brain aneurysms. Brain aneurysms are localized, blood-filled dilations of arteries in the brain that occur most commonly in the circle of Willis at the base of the brain. Aneurysms rupture causing subarachnoid hemorrhage (SAH) with high associated morbidity and mortality. SAH affects over 30,000 patients every year in the USA. Microscopic study of cerebral blood vessels shows that aneurysm walls have a different structure from normal blood vessels, especially at branch sites. These branch sites are the most probable sites for the formation of berry aneurysms. Currently, there is no existing technique to assess the structural composition of the aneurysm wall in the living body or to predict the stability of the aneurysm. In addition, the cerebral aneurysm is treated by either clipping or coiling. Due to its minimal invasiveness, endovascular coil embolization has become increasingly popular in the treatment of brain aneurysms. However, patients treated using this method require multiple follow-up angiographies to monitor healing. Imaging modalities with sufficient resolution to visualize healing across the aneurysm neck is currently not available clinically. Neuroendovascular OCT can image and reveal structure across the aneurysm neck with micrometer resolution. OCT can assess the structural composition and stability of the aneurysm wall before treatment, provide guidance during the endovascular coil embolization procedure, and evaluate the healing process

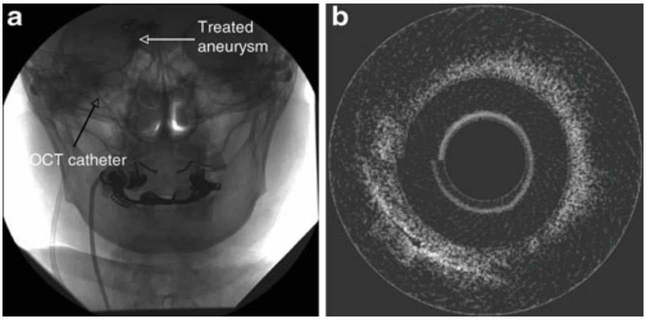

Fig. 7.5 In vivo posttreatment aneurysm imaged by OCT: (**a**) angiogram of a patient with an OCT catheter in a cerebral vessel; (**b**) in vivo OCT image obtained from patient that received endovascular coil embolization treatment. (From ref. [43])

posttreatment. To demonstrate the clinical feasibility of OCT for imaging cerebral vessels, we have developed an endovascular OCT catheter with a probe diameter of 0.7 mm [42]. We have demonstrated, to the best of our knowledge, the first OCT image of cerebral vasculature in human subjects [42, 43]. During the patient's follow-up angiography examination, an OCT endovascular catheter was inserted into the femoral artery where the angiography sheath was already present. The catheter was advanced to the intracranial aneurysm lesion under fluoroscopic guidance using standard endovascular techniques. Figure 7.5a shows an angiogram of an aneurysm patient with an OCT catheter in a cerebral vessel. Figure 7.5b shows an OCT image obtained from the same brain aneurysm patient who received endovascular coil embolization treatment. The aneurysm treated lesion is clearly visible in Fig. 7.5b. Our pilot clinical studies in four patients have shown that OCT imaging of the cerebral vasculature is feasible in a safe and effective manner.

7.3.3 Depth-Resolved Intrinsic Scattering Signal Changes During Functional Brain Activation

Intrinsic signal optical imaging (ISI) is a well-established optical imaging method which maps the clustered activation of neurons with a camera [44]. ISI is noninvasive and does not require dyes. It is based on a small change in the absorption (or reflection) of light that occurs in neuronal tissue when neurons are activated. The scattering or reflection property changes of neural tissue has been attributed to two factors: (1) the local refractive index change of the membrane or the cytoplasm due to the alteration of the ionic composition; (2) the cellular geometry change due to osmotically induced volume changes, as well as other physical forces [11]. The OCT signal originates from sample inhomogeneous scattering properties which are related to the sample's refractive indices. Different from the ISI technique, which integrates the back scattering or reflection signal from all depths and cannot provide depth-resolved information, OCT can offer a micrometer resolution, depth-resolved intrinsic scattering signal. A typical OCT system utilizes a near-infrared wavelength light source for imaging which penetrates deeper than the visible wavelength light source typically used in ISI.

Several groups have demonstrated the investigation of functional activation in neuronal tissues with the OCT technique. OCT has been used to visualize depth-resolved scattering property changes in a cat cortex in response to a visual stimulus [7]. Scattering properties of nerve fibers from the abdominal ganglion of the sea slug *Aplysia californica* before, during, and after electrical stimulation have been measured with OCT and the results show that the scattering during stimulation showed localized reversible increases compared with those acquired before stimulation [11]. The high-resolution, cross-sectional measurement of functional hemodynamic response to electrical stimulation in the rat cortex model was demonstrated with OCT [9]. The correlation between OCT and ISI has been demonstrated. By integrating all the depth signals from a single A-line, the depth-integrated OCT profile was compared with the ISI profile, and a clear and remarkable agreement between the profiles was found [8]. The spatial and temporal correlations of OCT and ISI are also verified with a rat somatosensory cortex through a thinned skull during forepaw electrical stimulation [10]. These results clearly indicate that OCT is a promising new technique for monitoring dynamic changes in the neural system under stimulation.

7.3.4 D-OCT of Cortical Blood Flow Dynamics in Animal Models

D-OCT has also been used to image brain hemodynamics in the cerebral cortex of the brain. As previously mentioned, the cerebral cortex is believed to be composed of functional units, called “columns,” that are arranged in clusters perpendicular to the surface of the cortex. High spatial resolution, on the order of micrometers, is necessary to distinguish different vascular components (arterioles, capillaries, venules) and individual columns, which are about 100–200 μm^2 in tangential size. Several different techniques have been used to study the coupling of blood flow within localized regions of brain activity, such as PET, near infrared spectroscopy (NIS), ISI, laser Doppler perfusion imaging (LDPI), laser speckle imaging (LSI), functional magnetic resonance imaging (fMRI), and two photon microscopy. However, the resolutions of PET, LDPI, and fMRI are too low to distinguish these components. Although ISI can map *en face* cortical hemodynamics and columns, depth resolution is not available [45, 46]. Two photon microscopy has been used for mapping cortical activity. However, this technique requires the injection of a fluorescent dye and has limited penetration depth [47]. The noninvasive high resolution tomographic capabilities of D-OCT make it a promising technique for mapping depth-resolved cortical blood flow.

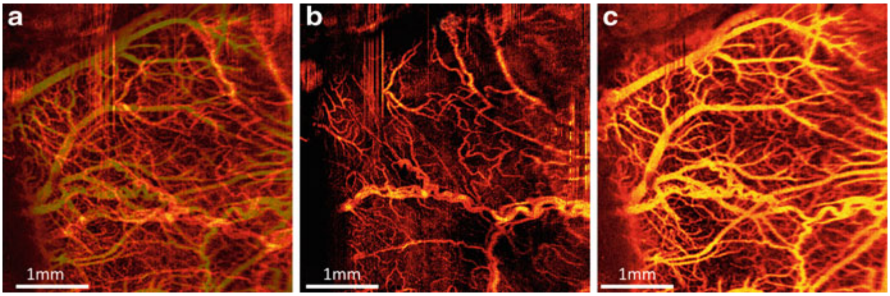

Fig. 7.6 *En face* projection view of Doppler variance images of rat cortex blood perfusion. (**a**) Projection view from the full imaging depth; (**b**) projection view from the skull; (**c**) projection view from the cortex

We reported the first D-OCT image of blood flow in the rat cerebral cortex in 1997 with time domain OCT [20]. Recent advances of Fourier domain phase-resolved D-OCT have significantly improved imaging speed and velocity sensitivity. These improvements have made the imaging of a full map of the cortex neurovascular structures down to the capillary level possible [22, 24, 25, 48]. Figure 7.6a shows an *en face* projection view of a D-OCT image of rat cortex blood vessels that reveals the detailed blood perfusion network over the cortex at capillary level resolution. The parietal cortex of an anesthetized rat was imaged through a dural incision. The D-OCT system is a swept source-based OCT system with an A-line rate of 50,000 Hz at a central wavelength of 1,310 nm. The image has a size of 5 mm by 5 mm and it takes 80 s to capture the whole 3D data volume. The image shown in Fig. 7.6 is obtained with the Doppler variance method which shows high sensitivity for mapping the blood vessel network. Because 3D information of the blood vessel network is mapped, one can separate the vascular network from different anatomical layers. For example, we can separate the blood vessel network in the skull from that in the cortex as shown in Fig. 7.6b, c. Figure 7.6b shows the *en face* projection view of the blood vessel network in the skull, and Fig. 7.6c shows the *en face* projection view of the blood vessel network in the cortex. In order to separate the skull from the cortex, the boundary between the skull and the cortex was found first based on the OCT image. This boundary was then applied to the Doppler variance tomography image. This preliminary investigation demonstrated that D-OCT can map blood flow in the cortex with high spatial resolution.

D-OCT shows great promise in brain research for imaging the entire depth of the cortex. D-OCT has been used to measure stimulus-induced changes in blood flow [20], evaluate and monitor brain ischemia and trauma [23, 49], and quantify blood circulation and flow resistance before and after a localized ischemic stroke in a mouse model [23]. Repeated D-OCT scans across a few selected vessels have been performed to get 2D Doppler flow maps as a function of time, which provide an accurate estimation of 2-D flow dynamics across the vessels. Spectral Doppler waveforms can be obtained by performing spectral analysis of the time sequences of Doppler images [50]. The quantitative information, such as maximum velocity envelope, mean velocity envelope, and flow-volume rate envelope, can be derived accordingly [50]. Doppler-angle-independent flow indices, such as flow resistance and flow pulsatility, can be determined from this measurement [50].

We have used spectral D-OCT for quantitative evaluation of dynamic blood circulation before and after a localized ischemic stroke in a mouse model [23]. Ischemic stroke is the third leading cause of death in the United States and has a tremendous impact on subsequent quality of life for the victim. One of the biggest limitations to this development is the lack of understanding of the mechanisms by which cerebral blood flow adapts and the cerebral vessel reacts to environmental insults (such as ischemia, inflammation, trauma, blood pressure changes, and metabolic stressors). Imaging modalities that can provide in vivo evaluation of flow dynamics in an ischemic stroke animal model is essential to the understanding and development of more effective intervention.

To demonstrate the use of spectral D-OCT for quantitative evaluation of blood circulation and flow resistance before and after a localized ischemic stroke, Rose Bengal photodynamic therapy (PDT) was used as a noninvasive means for inducing localized ischemia in the cortical microvasculature. Both LSI and spectral D-OCT were taken before and 15 min after each PDT trial. Spectral Doppler imaging (SDI) provided the temporal blood flow information, which is complementary to the spatially distributed flow information of 3D angiography. For comparison, in vivo laser-speckle images of the mouse brain cortex through a moistened, intact skull were also recorded. Figure 7.7a–c show the qualitative laser speckle images of the intact mouse skull and clearly demonstrate the overall reduced vascular blood flow with laser coagulation by the irradiation of Rose Bengal. The reduction was localized to the site where laser irradiation was delivered. Figure 7.7d shows the spectral D-OCT velocity as a function of time of vessel 1 before the PDT and Fig. 7.7e, f show the same after each of the two PDT irradiations. To calculate the Doppler-angle-independent resistive index (RI), the maximum velocity envelope curves were derived from spectral Doppler waveforms, as shown in Fig. 7.7f. For each cardiac cycle in Fig. 7.7f, symbol S represents the peak systolic maximum velocity and symbol D represents the end diastolic maximum velocity. The Doppler-angle-independent RI is calculated as $\mathrm{RI} = (S-D)/S$ for each cardiac cycle and then averaged for all 14 complete cycles covered in Fig. 7.7f. Statistical analysis of the velocity distributions of continuous Doppler images demonstrates how the velocity components and longitudinally projected flow-volume rate change over time for scatterers within the imaging volume. Similarly, Fig. 7.7g–i show the spectral D-OCT change of vessel 2 before and after PDT irradiation.

The Doppler-angle-independent RI can be used to quantify the vasculature resistance of the examined microvasculature [50]. Table 7.1 summarizes the quantitative changes of the RIs of the two vessels before and after PDT. For instance, a resistive index of ~0.47 was measured before the photoactivation of Rose Bengal in vessel 1. An increased RI of 0.60 was measured after the first laser irradiation and then ~0.7 after the second laser irradiation. The increase of RI is in agreement with the LSI results shown in Fig. 7.5a–c. The increase of RI can be

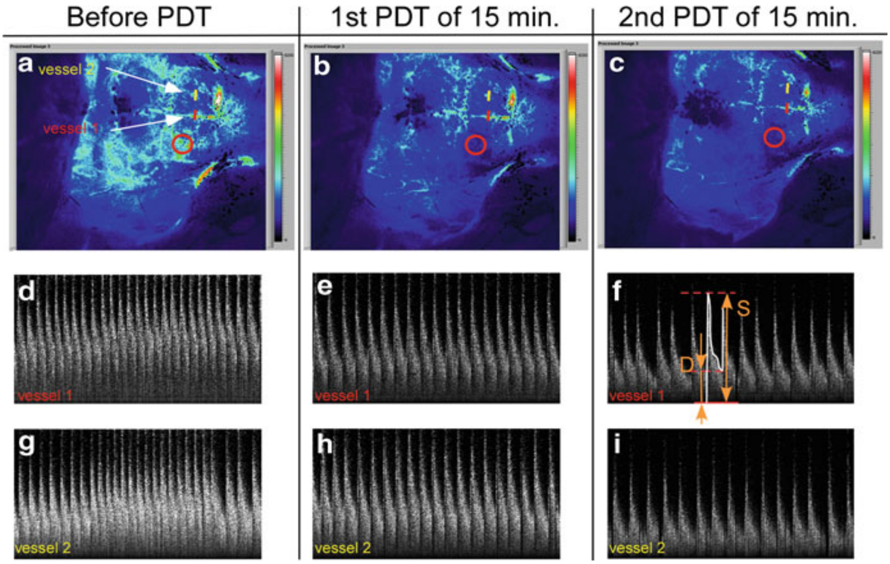

Fig. 7.7 Laser speckle flow index maps of the mouse skull (**a**) before PDT, (**b**) 15 min after the first PDT, and (**c**) 15 min after the second PDT, respectively. Spectral Doppler imaging of vessel 1 (*red line* in **a**) (**d**) before PDT, (**e**) after first PDT of 15 min, and (**f**) after second PDT of 15 min are shown in figure (**d**–**f**), respectively. Figures (**g**–**i**) show the spectral Doppler imaging of vessel 2 (*yellow*) before PDT, after first PDT of 15 min, and after second PDT of 25 min, respectively. (From ref. [23])

Table 7.1 The flow indices for each cardiac cycle, their average values, and standard deviation values for the maximum velocity envelope curve

Flow RI	Before PDT	After 1st PDT	After 2nd PDT
Vessel 1	0.47	0.60	0.69
Vessel 2	0.56	0.65	0.76

explained as increased vascular resistance that was caused by the localized ischemic stroke. The resistive index changes clearly showed the blockage of the cortical blood vessels.

7.4 Summary

OCT is a rapidly developing imaging technology with many potential applications in the field of brain imaging. Through different contrast enhancement mechanisms, functional OCT provides clinically important physiological information of the brain in addition to the structural image. OCT and its functional extension can greatly enhance potential applications of this technology in brain research. Given the noninvasive nature with exceptionally high spatial resolution and velocity sensitivity, functional OCT that can simultaneously provide tissue structure, blood perfusion, and other physiological information has great potential to become a powerful brain imaging tool for basic biomedical research and clinical medicine.

Acknowledgments The authors wish to acknowledge Dr. Christopher Lay, Dr. Melissa Davis, and Prof. Ron Frostig for preparing the rat used in the manuscript. Dr. Chen also acknowledges grant support from the National Institutes of Health (R01EB-10090, R01EY-021529, P41EB-015890, R01HL-103764, and R01HL-105215), Air Force Office of Scientific Research (F49620-00-1-0371, FA9550-04-0101), and the Beckman Laser Institute Endowment.

References

1. Huang D, Swanson EA, Lin CP, Schuman JS, Stinson WG, Chang W, Hee MR, Flotte T, Gregory K, Puliafito CA, Fujimoto JG (1991) Optical coherence tomography. Science 254:1178–1181
2. Drexler W, Fujimoto JG (2008) Optical coherence tomography: technology and applications. Springer, Berlin
3. Jeon SW, Shure MA, Baker KB, Huang D, Rollins AM, Chahlavi A, Rezai AR (2006) A feasibility study of optical coherence tomography for guiding deep brain probes. J Neurosci Methods 154:96–101
4. Watanabe H, Rajagopalan UM, Nakamichi Y, Igarashi KM, Madjarova VD, Kadono H, Tanifuji M (2011) In vivo layer visualization of rat olfactory bulb by a swept source optical coherence tomography and its confirmation through electrocoagulation and anatomy. Biomed Opt Express 2:2279–2287
5. Arous JB, Binding J, Léger J-F, Casado M, Topilko P, Gigan S, Boccara AC, Bourdieu L (2011) Single myelin fiber imaging in living rodents without labeling by deep optical coherence microscopy. J Biomed Opt 16:116012
6. Binding J, Arous JB, Léger J-F, Gigan S, Boccara C, Bourdieu L (2011) Brain refractive index measured in vivo with high-NA defocus-corrected full-field OCT and consequences for two-photon microscopy. Opt Express 19:4833
7. Maheswari RU, Takaoka H, Kadono H, Homma R, Tanifuji M (2003) Novel functional imaging technique from brain surface with optical coherence tomography enabling visualization of depth resolved functional structure in vivo. J Neurosci Methods 124:83–92
8. Rajagopalan UM, Tanifuji M (2007) Functional optical coherence tomography reveals localized layer-specific activations in cat primary visual cortex in vivo. Opt Lett 32:2614–2616
9. Aguirre AD, Chen Y, Fujimoto JG, Ruvinskaya L, Devor A, Boas DA (2006) Depth-resolved imaging of functional activation in the rat cerebral cortex using optical coherence tomography. Opt Lett 31:3459–3461
10. Chen Y, Aguirre AD, Ruvinskaya L, Devor A, Boas DA, Fujimoto JG (2009) Optical coherence tomography (OCT) reveals depth-resolved dynamics during functional brain activation. J Neurosci Methods 178:162–173
11. Lazebnik M, Marks DL, Potgieter K, Gillette R, Boppart SA (2003) Functional optical coherence tomography for detecting neural activity through scattering changes. Opt Lett 28:1218–1220
12. Maheswari RU, Takaoka H, Homma R, Kadono H, Tanifuji M (2002) Implementation of optical coherence tomography (OCT) in visualization of functional structures of cat visual cortex. Opt Commun 202:47–54

13. de Boer JF, Srinivas SM, Park BH, Pham TH, Chen Z, Milner TE, Nelson JS (1999) Polarization effects in optical coherence tomography of various biological tissues. IEEE J Sel Top Quant Electron 5:1200–1204
14. Nakaji H, Kouyama N, Muragaki Y, Kawakami Y, Iseki H (2008) Localization of nerve fiber bundles by polarization-sensitive optical coherence tomography. J Neurosci Methods 174:82–90
15. Wang H, Black AJ, Zhu JF, Stigen TW, Al-Qaisi MK, Netoff TI, Abosch A, Akkin T (2011) Reconstructing micrometer-scale fiber pathways in the brain: multi-contrast optical coherence tomography based tractography. Neuroimage 58:984–992
16. Chen Z, Milner TE, Dave D, Nelson JS (1997) Optical Doppler tomographic imaging of fluid flow velocity in highly scattering media. Opt Lett 22:64–66
17. Chen Z, Milner TE, Srinivas S, Xiaojun W, Malekafzali A, van Gemert MJC, Nelson JS (1997) Noninvasive imaging of in vivo blood flow velocity using optical Doppler tomography. Opt Lett 22:1119–1121
18. Izatt JA, Kulkarni MD, Yazdanfar S, Barton JK, Welch AJ (1997) In vivo bidirectional color Doppler flow imaging of picoliter blood volumes using optical coherence tomography. Opt Lett 22:1439–1441
19. Zhao Y, Chen Z, Saxer C, Shaohua X, de Boer JF, Nelson JS (2000) Phase-resolved optical coherence tomography and optical Doppler tomography for imaging blood flow in human skin with fast scanning speed and high velocity sensitivity. Opt Lett 25:114–116
20. Chen Z, Zhao Z, Srinivas SM, Nelson JS, Prakash N, Frostig RD (1999) Optical Doppler tomography. IEEE J Sel Top Quant Electron 5:1134–1142
21. Wang RK, Hurst S (2007) Mapping of cerebro-vascular blood perfusion in mice with skin and skull intact by Optical Micro-AngioGraphy at 1.3 μm wavelength. Opt Express 15:11402–11412
22. Jia Y, An L, Wang RK (2010) Label-free and highly sensitive optical imaging of detailed microcirculation within meninges and cortex in mice with the cranium left intact. J Biomed Opt 15:030510
23. Yu L, Nguyen E, Liu G, Choi B, Chen Z (2010) Spectral Doppler optical coherence tomography imaging of localized ischemic stroke in a mouse model. J Biomed Opt 15:066006
24. Srinivasan VJ, Sakadžić S, Gorczynska I, Ruvinskaya S, WuW FJG, Boas DA (2009) Depth-resolved microscopy of cortical hemodynamics with optical coherence tomography. Opt Lett 34:3086–3088
25. Srinivasan VJ, Sakadzic S, Gorczynska I, Ruvinskaya S, WuW FJG, Boas DA (2010) Quantitative cerebral blood flow with optical coherence tomography. Opt Express 18:2477–2494
26. Fercher AF, Kitzenberger CK, Kamp G, El-Zaiat SY (1995) Measurement of intraocular distances by backscattering spectral interferometry. Opt Commun 117:43–48
27. Wojtkowski M, Leitgeb R, Kowalczyk A, Bajraszewski T, Fercher AF (2002) In vivo human retinal imaging by Fourier domain optical coherence tomography. J Biomed Opt 7:457–463
28. Chinn SR, Swanson EA, Fujimoto JG (1997) Optical coherence tomography using a frequency-tunable optical source. Opt Lett 22:340–342
29. Golubovic B, Bouma BE, Tearney GJ, Fujimoto JG (1997) Optical frequency-domain reflectometry using rapid wavelength tuning of a Cr4+:forsterite laser. Opt Lett 22:1704–1706
30. Leitgeb R, Hitzenberger CK, Fercher AF, Kulhavy M (2003) Performance of fourier domain vs. time domain optical coherence tomography. Opt Express 11:889–894
31. de Boer JF, Cense B, Park BH, Pierce MC, Tearney GJ, Bouma BE (2003) Improved signal-to-noise ratio in spectral-domain compared with time-domain optical coherence tomography. Opt Lett 28:2067–2069
32. Choma MA, Sarunic MV, Yang C, Izatt JA (2003) Sensitvity advantage of swept source and Fourier domain optical coherence tomography. Opt Express 11:2183–2189

33. Zhao Y, Chen Z, Saxer C, Shen Q, Xiang S, de Boer JF, Nelson JS (2000) Doppler standard deviation imaging for clinical monitoring of in vivo human skin blood flow. Opt Lett 25:1358–1360
34. Zhao Y, Chen Z, Ding Z, Ren H, Nelson JS (2001) Three-dimensional reconstruction of in vivo blood vessels in human skin using phase-resolved optical Doppler tomography. IEEE J Sel Top Quant Electron 7:931–935
35. Leitgeb RA, Schmetterer L, DrexlerW FAF, Zawadzki RJ, Bajraszewski T (2003) Real-time assessment of retinal blood flow with ultrafast acquisition by color Doppler Fourier domain optical coherence tomography. Opt Express 11:3116–3121
36. Wang L, Wang Y, Bachaman M, Li GP, Chen Z (2004) Frequency domain Phase-resolved optical Doppler and Doppler variance tomography. Opt Commun 242:345–347
37. Zhang J, Chen Z (2005) In vivo blood flow imaging by a swept laser source based Fourier domain optical Doppler tomography. Opt Express 13:7449–7457
38. Yang VX, Gordon ML, Mok A, Zhao Y, Chen Z, Cobbold RSC, Wilson BC, Vitkin IA (2002) Improved phase-resolved optical Doppler tomography using the Kasai velocity estimator and histogram segmentation. Opt Commun 208:209–214
39. Ichimiya A (1998) Functional and structural brain imagings in dementia. Psychiatry Clin Neurosci 52:S223–S225
40. Laule C, Vavasour IM, Kolind SH, Li DK, Traboulsee TL, Moore GR, MacKay AL (2007) Magnetic resonance imaging of myelin. Neurotherapeutics 4:460–484
41. Stankoff B, Wang Y, Bottlaender M, Aigrot MS, Dolle F, Wu C, Feinstein D, Huang GF, Semah F, Mathis CA, KlunkW GRM, Lubetzki C, Zalc B (2006) Imaging of CNSmyelin by positron-emissiontomography. Proc Natl Acad Sci USA 103:9304–9309
42. Mathews MS, Su J, Heidari E, Levy EI, Linskey ME, Chen Z (2011) Neuroendovascular optical coherence tomography imaging and histological analysis. Neurosurgery 69:430–439
43. Su J, Mathews MS, Nwagwu CI, Edris A, Nguyen NV, Nguyen BV, Heidari M, Linskey ME, Chen Z (2008) Imaging treated brain aneurysms in vivo using optical coherence tomography. Proc SPIE 6847:684732
44. Grinvald A, Lieke E, Frostig RD, Gilbert CD, Wiesel TN (1986) Functional architecture of cortex revealed by optical imaging of intrinsic signals. Nature 324:361–364
45. Frostig RD, Lieke EE, Ts'o DY, Grinvald A (1990) Cortical functional architechture and local coupling between neuronal activityand the microcirculation revealed by in vivo high-resolution optical imaging of intrinsic signals. Proc Natl Acad Sci USA 87:6082–6086
46. Frostig RD, Masino SA, Kwon MC, Chen CH (1995) Using light to probe the brain: intrinsic signal optical imaging. Int J Imaging Syst Technol 6:216–224
47. Kleinfeld D, P. P. M., Helmchen F, Denk W (1998) Fluctuations and stimulus-induced changes in blood flow observed in individual capillaries in layers 2 through 4 of rat neocortex. Proc Natl Acad Sci USA 95:15741–15746
48. Vakoc BJ, Lanning RM, Tyrrell JA, Padera TP, Bartlett LA, Stylianopoulos T, Munn LL, Tearney GJ, Fukumura D, Jain RK, Bouma BE (2009) Three-dimensional microscopy of the tumor microenvironment in vivo using optical frequency domain imaging. Nat Med 15:1219–1223
49. Jia Y, Grafe MR, Gruber A, Alkayed NJ, Wang RK (2010) In vivo optical imaging of revascularization after brain trauma in mice. Microvasc Res 81:73–80
50. Rao B, Yu L, Jiang HK, Zacharias LC, Kurtz RM, Kuppermann BD, Chen Z (2008) Imaging pulsatile retinal blood flow in human eye. J Biomed Opt 5:040505

Chapter 8
Delineating Normal from Diseased Brain by Aminolevulinic Acid-Induced Fluorescence

Herbert Stepp and Walter Stummer

8.1 Introduction

This chapter deals with an intraoperative, fluorescence-based optical guidance tool to recognize brain tumor using 5-aminolevulinic acid (5-ALA). After the first scientific report of this technique in 1998 for its use in high-grade glioma (WHO grades III and IV), including glioblastoma (GBM), 5-ALA has since been approved by the European Medical Agency (EMA) and is now commercially available as Gliolan®. Augmental studies in the United States are ongoing with the aim of approval in this country also. The procedure involves application of a fluorochrome precursor (5-ALA), which is taken up by the cells of central nervous system tumos and of other primary brain tumors, metastases and spinal cord tumors results in synthesis and selective accumulation of red-fluorescent protoporphyrin IX (PpIX). This red fluorescence is excited with violet–blue light from a surgical microscope adapted for fluorescence visualization and observed through appropriate filters either with the naked eye of the surgeon or by sensitive cameras.

Other primary brain tumors and a variety of brain metastases are currently being investigated for their ability to produce PpIX fluorescence. More sensitive equipment is being developed with the aim of extending the applicability of the procedure to low-grade gliomas and poorly fluorescent metastases. The procedure also shows promise for guiding the resection of spinal cord tumors.

The overall aim is to maximize the extent of surgical removal of tumor tissue while maintaining safety, that is, minimizing the risk of producing functional

---

H. Stepp (✉)
Laser-Forschungslabor, LIFE Center, Klinikum der Universitaet Muenchen,
Marchioninistr. 23, 81377 Munich, Germany
e-mail: herbert.stepp@med.uni-muenchen.de

W. Stummer
Klinik fuer Neurochirurgie, Universitaetsklinikum Muenster, Albert-Schweitzer-Campus 1,
48149 Muenster, Germany

S.J. Madsen (ed.), *Optical Methods and Instrumentation in Brain Imaging and Therapy*, Bioanalysis: Advanced Materials, Methods, and Devices 3,
DOI 10.1007/978-1-4614-4978-2_8,

deficits or worsening the quality of life. A brief discussion of the clinical aspects of maximum resections in certain brain tumors is followed by a description of the biological and technical concepts of 5-ALA-based fluorescence-guided resection (FGR) of malignant glioma. The current status of clinical experience is presented, including some of the international efforts to improve the procedure and extend indications.

8.2 Importance of Gross Total Resection

The prognosis of patients suffering from high-grade glioma is among the worst of all cancers [1]. GBM carries the worst prognosis: despite surgery and chemotherapy or radiotherapy, median survival ranges from 6 to 21 months, being significantly longer for young patients (18–21 months) than for older patients (6–9 months) [2]. One of the essential aims of therapy is to extend recurrence-free and symptom-free survival. As far as surgery for intrinsic brain tumors is concerned, it may be trivial to assume that symptom-free survival should correlate with the extent of surgery. However, simply increasing resection carries the risk of side effects since glioma tissue is difficult to identify due to its similarity to normal brain. With standard surgical approaches, therefore, all of the contrast-enhancing tumor is usually removed in approximately 35–50% of cases, as judged by post-operative magnetic resonance imaging (MRI) [3, 4].

Neurosurgeons have long debated whether there is really hard proof for prolonged survival with nonimpaired quality of life following so-called “gross total resection” (GTR), as there are many possible biasing effects that have to be considered and excluded [5]. There is increasing evidence in support of a beneficial effect of GTR [4, 6–11]. Statistically, GTR has been shown to be of prognostic value in a large series of 788 patients by Laws et al. [11], although the extent of resection was not precisely measured. Such measurements are important and may be accomplished using post-operative MRI. Lacroix et al. [8] found that more than 98% of the contrast-enhancing tumor volume should be removed in order for GTR to be an independent predictor of survival in multivariate analysis. In a re-evaluation of data from a phase III clinical trial on FGR, Stummer et al. [9] demonstrated level 2b evidence (prospective cohort study) in favor of a dependence of survival on the completeness of resection. This is the clearest evidence obtained so far to show the benefit of safe GTR. Level 1 evidence would require a trial in which patients are randomized to be treated by different degrees of resection. Such a trial would be unfeasible, both from an ethical and from a technical point of view. In terms of quality of life, Brown et al. [6] showed improvement for patients with GTR.

Recently, it has been found that not only survival but also the efficacy of adjuvant therapies may be improved by GTR [12]. In this case, Stummer et al. have analyzed data from three phase III trials, two of them for the approval of new therapies. The first was designed for intracavitary chemotherapy with carmustine (BCNU) wafers (versus placebo) in malignant glioma patients and the second for concomitant radiochemotherapy (with temozolomide) followed by adjuvant sequential temozolomide (versus radiotherapy alone) in glioblastoma patients. In both cases, patients with prior GTR benefited most from the additional therapy. This concept is strongly supported by another recent multicenter prospective cohort study focusing on resection followed by adjuvant radiochemotherapy. In patients with no residual tumor (as determined from post-operative MRI), followed by concomitant radiochemotherapy, median survival exceeded the follow-up period of 24 months. If small volumes of residual tumor were visible on early post-operative MRI, survival was approximately 18 months [13].

Finally, the prognostic significance of age may be diminished because complete resections can be safely performed in older patients as recently reported [14, 15].

8.2.1 Surgical Techniques for Achieving Gross Total Resection

8.2.1.1 Neuronavigation

From pre-operative imaging alone, it is hard to achieve GTR safely [4, 8]. Neuronavigation provides a tool which relates pre-operative 3D imaging to the patient's head. Images can be MRI, CT, positron emission tomography (PET), or any combined overlay of these. Thus, the surgeon can determine the margins of the tumor as visible on the pre-operative images. There is a significant concern, however, regarding the accuracy of the match between the 3D data set and the actual tumor site. Intracranial pressure changes and tissue removal influence the form of the brain so that preoperative images loose their accuracy in providing information about the intraoperative anatomy. This phenomenon is called brain-shift and indeed limits the reliability of the procedure [16, 17]. Shifts of several millimeters are normal, and up to 2.5 cm must be considered [17]. Under these circumstances, a "maximum safe resection" is possible in only a very few cases.

8.2.1.2 IntraOperative MRI

In order to circumvent the limitations of neuronavigation, intraoperative MRI (iMRI) has frequently been employed and shown to improve the surgical precision in comparison with or in addition to neuronavigation [18]. iMRI has been studied for additional benefit concerning increased extent of resection, quality of life, or recurrence-free survival. A review by Kubben et al. [19] discusses limitations and bias found in most studies but concludes that there is level 2 evidence in favor of iMRI-guided surgery compared to conventional neuronavigation-guided surgery for GBM. A recent, prospectively randomized study compared iMRI + neuronavigation-guided versus conventional surgery (with and without neuronavigation) and found significant advantages for iMRI with a small number of, 24 and 25, patients in each group [20]. iMRI identified otherwise unresected tumor remnants in 8 of 24 patients and resulted in 23 of 24 patients with complete resections in the iMRI-group versus only 17 of 25 patients in the control group. Neuronavigation alone was used in 12 of the 25 patients of the control group and resulted in four incomplete resections. With regard to progression-free survival, the iMRI group marginally failed to show statistically significant superiority ($p = 0.083$), possibly on account of the small patient numbers. Neurological deficits occurred in five patients; however, no deficits were found in patients where iMRI led to extended resection. Due to its high cost and the additional time required for scanning, iMRI is as yet not broadly employed.

8.2.1.3 IntraOperative Ultrasound

Ultrasound imaging is easily adapted to intraoperative indications and is a technologically advanced and comparatively cost-effective method. Nevertheless, it has not gained broad acceptance in the context of glioma surgery. It has been found valuable for the delineation of low-grade gliomas, although iMRI appeared to be more accurate in a study by Gerganov et al. [21]. The limitation was most evident at the tumor borders. The same group has reported similar findings in an earlier study including high-grade glioma patients [22]. Rygh et al. [23] also report on similar limitations of intraoperative 3D ultrasound during and immediately after glioma resection with mainly limited specificity during resection (42%) and poor sensitivity when judging the resection cavity (26%).

8.2.1.4 Other Methods

Based on the clinical experience with intraoperative navigation and imaging, one may conclude that iMRI is the most reliable method to achieve safe gross total or even “complete” resection. This is, however, not surprising, because contrast enhancement in MRI is the criterion that measures the macroscopic extent of resection in most cases. It is obvious from the infiltrative nature of the disease and from the low cure rates observed that even a “complete resection,” as judged by post-operative MRI, is not sufficient to remove the malignant cells of a high-grade glioma. For this reason additional methods, based on truly microscopic imaging (as opposed to the macroscopic imaging afforded by surgical “microscopes”), have therefore been proposed to delineate the safe resection borders more precisely.

One of these is mass spectrometry analysis, a method that is frequently used in laboratory research for the molecular characterization of a tissue, which has now been proposed as an intraoperative tool to guide brain tumor surgery [24, 25].

Another is Optical Coherence Tomography (OCT), a tool that delivers highly resolved structural information of small tissue volumes in real time [26]. An OCT device was successfully adapted to a surgical microscope providing promising tissue discrimination capability at glioma tissue borders [27].

Intraoperative high-resolution microscopy may also be helpful. In a clinical study, Eschbacher et al. [28] correctly classified 26 of 28 brain tumors by confocal endomicroscopy after *i.v.* application of Na-fluorescein. Two-photon excited autofluorescence has been studied preclinically. An initial investigation on biopsy samples demonstrated the capability to determine cell density that correlated well with standard histopathology [29].

Autofluorescence spectroscopy has been studied and initially considered to be promising as a surgical guidance tool [30, 31], but there are no reports on further clinical studies. Instead, fluorescence lifetime of endogenous fluorophores was investigated as an additional parameter and a classification algorithm could be found, which worked well for the recognition of low-grade gliomas, but had a somewhat disappointing accuracy for high-grade gliomas [32].

As tumors have a different type of vasculature and an altered degree of oxygen metabolism, methods that are sensitive to such parameters might also be useful for tumor-border delineation. Recently, photoacoustics demonstrated the ability to measure blood flow and blood oxygenation parameters and showed evidence for increased oxygen saturation in an experimental transplanted early stage U87 tumor [33].

The application of exogenous fluorophores promises stronger and clearer contrast than relying on autofluorescence. Indocyanine green (ICG) is a clinically approved infrared absorbing and fluorescent dye (absorption/excitation at ca. 780 nm, emission at ca. 830 nm). When intravenously injected, it is confined primarily in the vasculature, as it readily binds to plasma (lipo)proteins. As early as 1993, it was found that the disturbed blood–brain barrier (BBB) of gliomas leaks ICG and leads to blue–green staining in an experimental glioma model [34]. Promising results were reported in a group of nine patients [35], but the technique was not developed further. The use of ICG in angiography during aneurysm surgery has rekindled interest in ICG flourescence imaging of tumors in the neurosurgical community. Martirosyan et al. [36] have found that at around 15 min after ICG injection, when vessel-confined ICG has already disappeared, GL261 tumors transplanted in mouse brains showed distinct ICG fluorescence. By adapting a confocal endomicroscopic probe for ICG-fluorescene, even cellular fluorescence could be detected that correlated well with histopathology.

Perhaps the oldest report on selective fluorochrome staining of primary brain tumors goes back to Moore et al. [37], who published the use of sodium-fluorescein for delineating tumor in 1947–1948. The method has been adopted in a simplified form in Japan and Europe, using nonmodified white light surgical microscopy with a high dose of fluorescein to make its fluorescence, or at least the tissue coloring, visible even without special spectral filtering [38, 39]. Macroscopically, the staining is tumor selective and GTR efficacy could be increased. Nevertheless, the possibility of fluorochrome diffusion into peritumoral tissue, for example, peritumoral edema, might lead to false-positive staining as was reported for other potentially tumor-selective fluorochromes [40]. This concern is, of course, also valid for ICG-staining. Furthermore, a high dose of fluorescein can lead to severe side effects by inducing an anaphylactic reaction [41, 42].

A promising variant of fluorescein staining is obtained by coupling this compound to albumin to exploit a similar selectivity mechanism as observed for ICG. Kremer et al. [43] have investigated 5-aminofluorescein-labeled albumin and report clinical results on 13 patients where they found an accuracy of 83.3% for fluorescence detection.

All these fluorochrome-based methods discussed so far rely on a passive kind of targeting. Tumor selectivity is presumably due to the disrupted blood–brain barrier, which is a hallmark of malignant brain tumors. Active molecular fluorescent targeting may, on the other hand, be obtained by functionalized nanoparticles, fluorochrome-labeled antibodies or peptides, or "smart probes" monitoring enzyme reactions or recognizing specific RNA sequences. Such methods will not be available clinically within the near future and the interested reader is referred to a review by Pogue et al. [44].

Last but not least, it should be mentioned that the probability of achieving GTR may also be increased by pre-operative employment of multimodal functional neuroradiologic imaging. Such methods include PET, MRI spectroscopy, and special MRI sequencing, such as diffusion tensor imaging and fMRI (BOLD sequences for perfusion imaging) [45, 46]. As some of these methods also highlight potentially functional normal brain (e.g., cortical fiber tracts), they might be especially helpful to avoid overly aggressive resection in the vicinity of eloquent areas [47].

The rest of this chapter will focus on the use of 5-ALA for the intraoperative guidance of brain tumor resection. The procedure uses fluorescence imaging, but it differs from the fluorescence-based procedures described above, because it involves a fluorochrome precursor rather than the administration of the fluorochrome itself. This makes a great difference in at least two regards: (1) during the phase of tissue distribution, 5-ALA produces no signal, whereas preformed fluorochromes will produce unspecific background signal, (2) 5-ALA requires active intracellular metabolization to be synthesized to the target fluorochrome PpIX, which potentially brings about additional cellular specificity in contrast to passively diffusing preformed fluorochromes, where tumor selectivity depends on parameters like selective vessel leakage, pH, and lymph drainage.

8.3 5-ALA Heme Biosynthesis and Tumor Selectivity of PpIX Accumulation

5-ALA is an endogenous molecule, synthesized in mitochondria and a precursor for heme synthesis. Figure 8.1 schematically illustrates the synthesis of 5-ALA and the further synthesis to PpIX and heme B [48, 49]. Eight molecules of 5-ALA are used to form the tetrapyrrolic structure, typical for porphyrins. Heme B molecules, also slightly modified in side chains to give heme A or C, are then incorporated into cytochromes to perform their task in the cellular respiratory chain. Each metabolically active cell is therefore equipped with this synthetic pathway.

The photophysical and photochemical properties of PpIX (its fluorescence and phototoxicity) are mediated by the conjugated bonds of the tetrapyrrolic porphyrin skeleton, stretching over 18 electrons that form a large π-electron system. With the

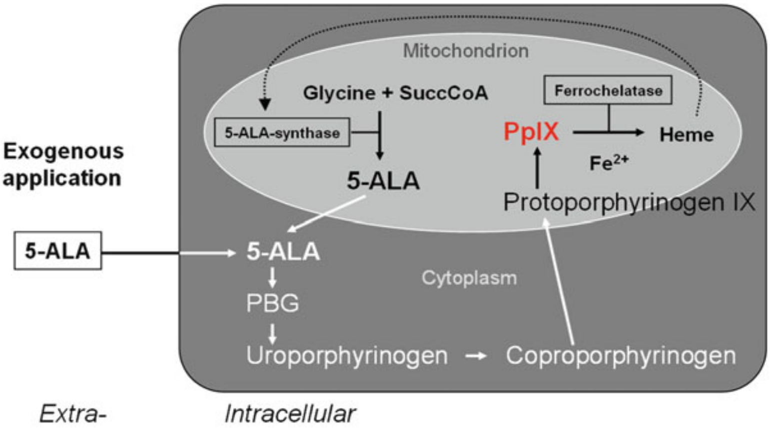

Fig. 8.1 Simplified schematic of the biosynthesis of heme. Protoporphyrin IX (PpIX) is the immediate precursor of heme. It accumulates, if the inhibitory feedback of heme concentration to the enzyme 5-ALA-synthase (*dotted arrow*) is bypassed by extracellular delivery of excess 5-ALA

insertion of the ferrous ion (Fe^{2+}), these properties are lost. PpIX is therefore the only molecule in heme synthesis which exhibits these interesting properties. It should be noted that inherited mutations in one of the enzymes involved in heme biosynthesis leads to the different variants of a disease called Porphyria [50]. "Vampires" such as the heme-deficient and light-sensitive Count Dracula probably were historical victims of this disease [51].

PpIX is normally not accumulated, as 5-ALA-synthase is regulated by free heme and iron. This inhibitory feedback can be bypassed by extracellular supply of 5-ALA. The uptake of 5-ALA through the cell membrane is mostly an active transport mediated by amino acid or di/tri-peptide transporters in a cell-type-dependent manner [52–57]. In case of a cancer-specific overexpression of membrane transport, this contributes to a tumor selectivity of the accumulation of PpIX.

The factors that lead to a tumor selectivity of PpIX accumulation are not fully elucidated. Selectivity depends on the cell or tissue type and is a multifactorial phenomenon [48]. On the level of heme synthesis, selective PpIX accumulation can occur when either the activity of enzymes leading to PpIX is increased or the activity of ferrochelatase is diminished, either by the enzyme itself or by a reduced availability of ferrous ions. Ferrochelatase and the enzyme porphobilinogen-deaminase (PBG-D) are the most discussed candidates for tumor selectivity in PpIX accumulation. Ferrochelatase activity was found reduced in liver tumors [58] and diverse cell lines [59, 60]. By further reducing iron availability by incubating cells with iron chelators, a higher PpIX accumulation can be observed, which is, as might be expected, dependent on the concentration of 5-ALA-incubation and cell line [61]. Interestingly, ferrochelatase-transfected cells may accumulate less PpIX [62]. PBG-D was found increased in some reports [63, 64]. Interestingly, one group found evidence for a second function of PBG-D, as it could be localized in the cell nucleus of glioma cell lines [65, 66]. It was speculated that PBG-D has a nuclear role related to cell transformation and differentiation. This may explain PpIX accumulation in proliferation induced tissue, for example, "false-positive" fluorescence found in inflammatory tissue. The definite relative role of PBG-D activity compared to ferrochelatase, however, remains unresolved [59], and there is definitely also a role of the other enzymes involved in heme synthesis, for example, ALA-dehydratase (ALA-D) [67].

To make things even more complicated, intracellular PpIX accumulation can be modified by efflux of PpIX through the mitochondria and the outer cell membrane. Although PpIX is produced inside mitochondria, soon after application it is found in the cytosol [68, 69]. The efflux from mitochondria might be mediated primarily by transport through the peripheral benzodiazepine receptor (PBR), a potential additional source for tumor selectivity, as PBR has been found to be overexpressed in cancer cell lines and its blocking has been shown to reduce PpIX accumulation [70]. Sustaining the PpIX efflux from mitochondria thus increases the cellular PpIX content. In contrast, PpIX efflux through the outer cell membrane leads to PpIX reduction. In cell cultures, the efflux of PpIX is connected with the presence of proteins in the culture medium. The presence of fetal bovine serum, which is a common constituent of cell culture media leads to PpIX efflux [71]. The hypothesis that PpIX may be transported via multidrug resistance membrane transporters was shown not to be the case for *P*-glycoprotein P-gp [72], but ABCG2 might be the relevant transporter, which reacts in the presence of extracellular serum proteins [73]. This is an interesting finding, because ABCG2 expression might be associated with stem cell properties [74]. In this case, caution is indicated, as such cancer stem cells may accumulate less PpIX with corresponding negative implications for the efficacy of photodynamic therapy (PDT) [75].

In the brain, there is an additional explanation for tumor selectivity, the BBB. The BBB is formed by the blood capillaries in the brain. The endothelial cells are very tightly connected and govern the transport of substances from blood to the brain interstitial fluid mostly by active membrane transport systems. The capillaries are surrounded by a thick basement membrane and astrocytes. It is well established that with increasing dedifferentiation, the neo-vessels growing in glioma tissue show increasing defects of the function and morphology of the BBB. This is the reason for the selective uptake of the contrast agent gadolinium-diethylenetriaminepentaacetic acid (Gd-DTPA) in contrast-enhanced MRI [76]. The intact BBB of normal brain represents a certain barrier for 5-ALA. Terr and Weiner [77] could not detect uptake of ^{14}C and ^{3}H radioactive-labeled 5-ALA in most brain structures of i.v. injected mice, except those which are connected to the cerebral spinal fluid via peri-ventricular structures, such as the choroid plexus bearing capillaries with a reduced barrier function.

Obwegeser et al. [78] have injected ^{14}C-labeled 5-ALA into rats bearing a C6 glioma and sampled tissue from the glioma, ipsi- and contralateral normal brain. Radioactivity measured in the glioma tissue was approximately threefold higher compared to normal tissue. As the investigators likely sampled larger tissue volumes from normal brain, probably containing structures connected to vessels without BBB, the effect of the BBB of normal brain and its deficiency in the glioma tissue is probably underestimated in this investigation.

Further investigations on model membranes [79] and isolated capillaries [80] also indicate that the BBB is quite efficient in preventing 5-ALA from entering into normal brain. If 5-ALA is encapsulated into liposomes and administered systemically to mice, the porphyrin content found in normal brain is significantly higher compared to nonencapsulated 5-ALA, a finding also supporting a barrier function for 5-ALA [81]. Finally, Ennis et al. [82] determined ^{14}C-labeled 5-ALA uptake into normal rat brains and concluded that this occurs via a diffusion process with a low influx rate except at the choroid plexus into the cerebrospinal fluid, which confirms the findings reported by Terr and Weiner [77].

After application, 5-ALA might induce a significant accumulation of PpIX in the endothelial cells of the blood vessels, even in normal ones. Madsen and Hirschberg [83] could induce a transient and localized opening of the BBB in normal rat brains by low-dose light treatment, indicating a photosensitized endothelium. While the authors propose to use this effect for the controlled administration of chemotherapeutics, it also indicates that some unspecific PpIX accumulation in normal brain might occur.

The extent to which the BBB is responsible for PpIX tumor selectivity in malignant glioma is unknown. In the context of FGR, the clinical observations made so far (see below) indicate that the BBB plays a significant role, although PpIX accumulation may extend into contrast MRI negative tumor. This has also been shown in an experimental tumor model [84] consisting of infiltrating human glioma cells (U251), transfected to produce green fluorescent protein (GFP) and implanted into the brains of nude mice. PpIX accumulation showed a better correlation with GFP staining and H&E histopathology than contrast MRI. However, on a microscopic scale, the possibility exists that infiltrating malignant cells may have migrated deeper into the brain, that is, into regions supplied by fully intact vessels (intact BBB) and might therefore not be exposed to sufficient amounts of 5-ALA to produce sufficient amounts of PpIX. That this may indeed be the case has been shown in a rat tumor model [85]. The inoculated BT_4C tumor cells grew to a bulk tumor with finger-like extensions and occasional isolated detached cell clusters invading normal brain. H&E staining clearly identified tumor on an almost single cell level. PpIX staining was strong in the bulk tumor and many of the extensions were stained with a slightly reduced intensity but PpIX fluorescence was almost absent in the completely detached tumor cell clusters. It is likely, however, that in order for 5-ALA to cross the BBB, the necessary perturbations in BBB integrity could be much smaller than those necessary for, for example, albumin or contrast-media to cross into the brain, because 5-ALA is a very small molecule (131 g/mol) compared to albumin (60,000 g/mol).

In summary, the following conclusions can be made regarding the clinical application of PpIX fluorescence for resection guidance:

- The applied drug (5-ALA) is not a fluorochrome, and therefore its distribution within the target organ is not a source of unspecific background
- 5-ALA availability in normal brain is limited due to the BBB
- 5-ALA uptake through the cell membrane occurs predominantly via active transport with a potential for tumor cell selectivity
- PpIX synthesis involves multiple enzymes, some of which show tumor-selectively increased or decreased (ferrochelatase) activity
- Intracellular redistribution of PpIX might be another source of tumor selectivity
- PpIX efflux from the cell depends on the extracellular milieu (proteins)

It may thus be expected that PpIX fluorescence has the potential to outline the macroscopic borders of the tumor at least as precisely as the contrast agents used for MRI, as the latter only marks the BBB deficiencies, whereas PpIX accumulation depends on several additional steps with a potential for tumor selectivity. One may speculate at this point that PpIX staining may correlate better with PET staining than with contrast-MRI (see below).

Once the bulk tumor has been surgically resected, it is difficult to determine how much tissue should be resected from the infiltration zone. In this regard, PpIX fluorescence may not be very helpful since it is often diminished due to (1) a reduced density of fluorescent tumor cells and (2) a reduced PpIX content and fluorescence from tumor cells as a function of distance from BBB-deficient vessels. The degree of resection will ultimately depend on tumor location. If the tumor is in an eloquent area, the resection may be incomplete; however, if there are no critical structures nearby, the resection may continue until all faintly fluorescent tissue has been resected. Neurophysiological monitoring techniques provide a helpful guide during resection in critical brain regions.

Technical equipment designed for intraoperative imaging of PpIX fluorescence of malignant glioma has to take these considerations into account. The equipment should clearly demarcate bulk tumor tissue from the infiltration zone and should suppress any potentially unspecific fluorescence from normal brain, be it due to unspecific PpIX accumulation in the adjacent peri-tumoral tissue or due to autofluorescence.

8.4 Instrumentation for Fluorescence-Guided Resection

The aim of any instrumentation for intraoperative fluorescence-based PpIX detection is to select the appropriate wavelength ranges for excitation and detection. Figure 8.2 shows excitation and emission spectra of freshly resected glioblastoma tissue containing PpIX. Most efficient excitation occurs in the violet–blue wavelength range around 410 nm, whereas PpIX fluorescence emission can be detected in the red wavelength range from 620 to 720 nm.

From the experience of PpIX fluorescence imaging for bladder cancer, it was decided to modify a standard surgical microscope to switch between normal white

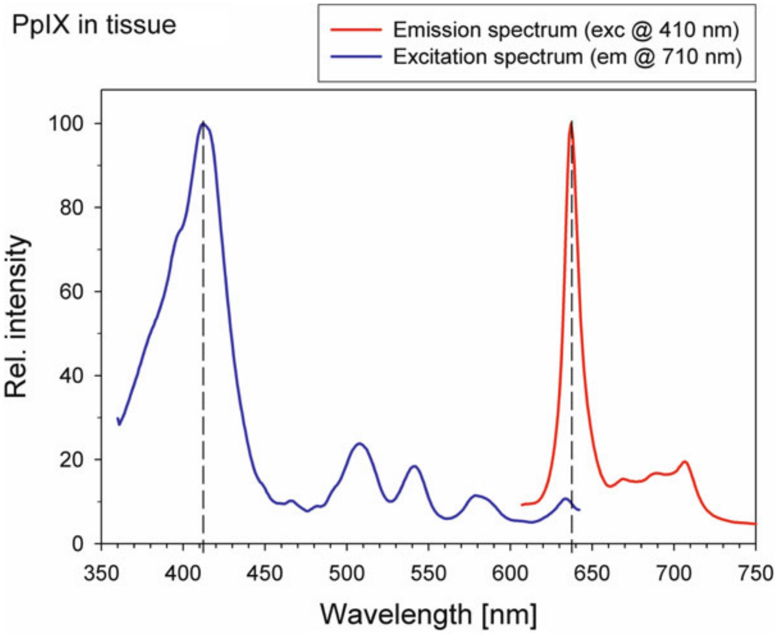

Fig. 8.2 Excitation (*blue curve*) and emission (*red curve*) spectra of PpIX fluorescence measured from a thin slice of human glioblastoma tissue shortly after resection. The patient received 20 mg/kg 5-ALA prior to surgery. Note that there is some background caused by endogenous fluorophores (autofluorescence) in both spectra

light mode and fluorescence mode by the simple activation of a foot pedal or a button on the microscope control panel. The spectral filtering was also adopted from the fluorescence endoscopes for bladder cancer [86]. It has proven advantageous not only to display PpIX fluorescence but also to overlay some remitted light in the blue wavelength range. This technical detail serves several important purposes. Firstly, the blue light allows visualization of nonfluorescent brain, thus giving tissue detail which is required to continue surgery even under blue light. Secondly, the remitted light overrides any unspecific weak red fluorescence emitted from normal brain tissue, be it due to minor amounts of PpIX synthesized in normal brain or residual autofluorescence in this wavelength range. It is also useful to set the threshold of detection a little higher to avoid the risk of resecting extensively into the infiltration zone, where the tumor cell density is already very low and functional brain tissue is the main component. Obviously, there is always a trade-off between sensitivity and specificity [87] as will be discussed below. The wavelength of the remitted blue light was chosen to overlap with the local minimum of blood absorption at 450 nm. Figure 8.3 shows the spectral filter characteristics of the excitation filter in the light source and the emission filter in the microscope objective. A considerable part of the excitation light is diffusely backscattered (remitted) from the tissue. Most of it is blocked by the emission filter, especially

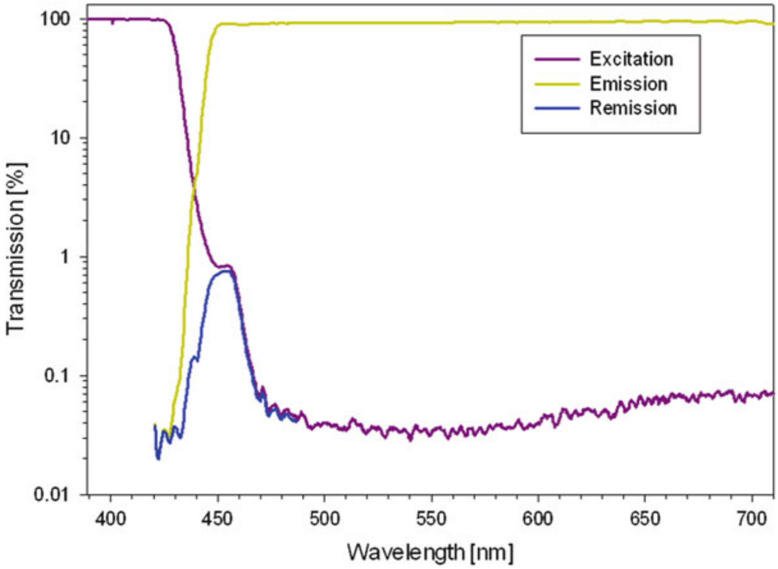

Fig. 8.3 Spectral transmission characteristics of excitation and emission filters and calculated product of both (*blue curve*), which determines the spectral bandwidth of light remitted from the tissue to the observer. Note the logarithmic scaling of the transmission axis

the short wavelength component. The small amount around 450 nm is transmitted to the observer and causes normal brain tissue to appear blue with a slight greenish hue, caused by tissue autofluorescence (Fig. 8.4, image 33). The blue light at this wavelength is also optimal to compensate for varying blood absorption: areas with high or low vascularity (especially capillaries) would otherwise cause any red fluorescence to appear increased or reduced just because of the different absorption of the excitation light. The remitted blue light, however, is also increased or reduced, and the ratio of red fluorescence versus blue remission is then rather constant. Because the tissue absorption at the excitation and emission wavelengths is very different, it turns out that light at 450 nm—having intermediate absorption—is the optimal choice for this purpose [88].

With increasing amounts of fluorescent PpIX in the tissue, there is a color change from blue to red, with the infiltration zone showing vague red fluorescence only, appearing in purple color due to the overlay of blue light of comparable intensity. GBM tissue usually accumulates sufficient PpIX to appear in bright red color under these conditions (Fig. 8.4), with very few exceptions caused by a lack of significant PpIX accumulation [89].

An excitation light intensity of the filtered broadband light source (ca. 390–440 nm) of approximately 10 mW/cm^2 is sufficient to observe the fluorescence through the surgical microscope with the naked eye. However, standard cameras are not well suited to record the fluorescence images for three reasons: (1) insufficient overall sensitivity, (2) insufficient sensitivity in the red PpIX

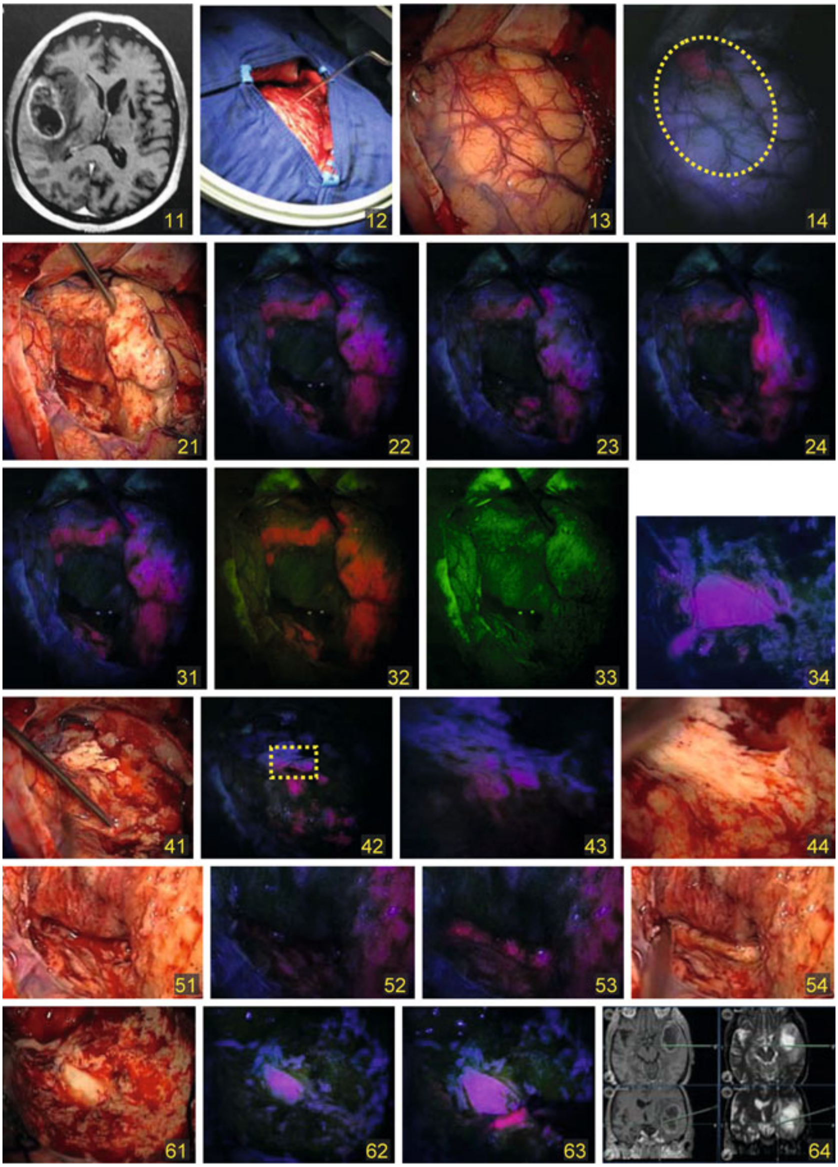

Fig. 8.4 Illustration of FGR of a GBM situated in the right temporal lobe in a 70 years old patient. 11: contrast MRI, 12: operation site after preparation of the dura, 13: close-up view through the surgical microscope, 14: *yellow dotted line* delineates the approximate extension of the tumor at depth; at the temporal polar site, the tumor approaches the cortical surface and PpIX fluorescence is visible. 21: first phase of resection. 22: same in fluorescence mode, central necrosis is void of PpIX fluorescence, whereas the periphery of the tumor is strongly fluorescent. 23: effect of photobleaching after 3.5 min: significant fading of red fluorescence. 24: deeper lying tissue readily shows strong fluorescence after removal of photobleached tissue layer. 31: same as 22. 32: removal of blue channel and enhancement of red channel to demonstrate a slight increase in

emission range, and (3) variable gain settings of the color channels. The latter causes variable thresholds for the recognition of PpIX-positive tissue. For this reason, the cameras are switched between white light and fluorescence modes simultaneously with the light source. Fixed gain settings for each color channel in the "fluorescence mode" and increased sensitivity, for example, by increasing the integration time of the sensor chip, enable the generation of reproducible and bright fluorescence images [87, 90].

There are, however, drawbacks associated with the use of such camera systems: (1) the dynamic range—the number of different gray levels that can be displayed—is rather limited, (2) the sensitivity setting employs a nonlinear curve, and (3) noise and blooming are far from minimized. These drawbacks may be reduced by employing scientific grade cameras, but one has to keep in mind other limitations, such as ambient light conditions and the fact that the spectral resolution of cameras is inherently limited by the band pass characteristics of the color channels (typically only three). It is therefore impossible to assign the red channel exclusively to PpIX emission, even if autofluorescence is considered from the green channel and subtracted by a correction algorithm. In order to maximize sensitivity for the detection of PpIX in tissue, spectral resolution has to be employed as discussed below. For the detection of resection limits of GBM, however, such ultimate sensitivity is not necessary, not even desirable, as it increases the risk of resecting into functional brain interweaved with infiltrating tumor. This aspect, as well as some other practical issues, including photobleaching of PpIX, is discussed in more detail by Tonn and Stummer [87].

8.5 Clinical Results

In this section, the focus is on FGR for high-grade gliomas. Low-grade gliomas are generally considered "fluorescence negative." This is true for the surgical fluorescence microscope, but might be different when applying a more sensitive technique as discussed later. Other brain tumors are discussed in a separate section.

◀

Fig. 8.4 (continued) sensitivity of PpIX recognition. 33: additional removal of red channel and enhancement of green channel demonstrating that autofluorescence is not a reliable indicator of tumor tissue. 34: after opening the ventricle, one can observe unspecific PpIX accumulation in the ependyma. 41: following resection of approximately half of the tumor mass. 42: same in fluorescence mode. 43–44: close-up view of the infiltration zone marked in 42. 51–54: demonstration of how blood conceals the PpIX fluorescence, but can easily be restored by suction of the blood layer (53). 61: resection cavity at the end of tumor surgery. 62: same in fluorescence mode, showing unspecific PpIX fluorescence of the ventricle wall. 63: careful suction of the blood layer reveals a residual fluorescent area that was also removed. 64: final neuronavigation confirms successful GTR. Images: courtesy of Dr. O. Schnell, Department of Neurosurgery, University Hospital of Munich

The European approval procedure passed through several stages of clinical trials. The pivotal phase III trial was a prospective randomized multicenter trial that demonstrated the safety and efficiency of 5-ALA-based FGR [91]. In this study, 5-ALA was randomly applied as a drinking solution at a dose of 20 mg/kg bodyweight to 139 patients with suspected malignant Glioma amenable to GTR. One hundred and thirty-one control patients were assigned to standard white light resection. The primary end points were "complete resection of contrast-enhancing tumor" as assessed by early post-operative MRI and "6-month progression-free survival." Both end points were reached: complete resections were observed in 65% (5-ALA group) versus 36% (white light group) and 6 months progression-free survival was 41% for the 5-ALA group vs. 21% for the white light group. There was no statistically significant difference in the frequency of adverse events. Additionally, "median residual tumor volume"—a secondary end point—was significantly lower in the 5-ALA group compared to the white light group, whereas statistical significance was not reached for the secondary end point "overall survival" (15.2 vs. 13.5 months ($p = 0.1$)). It was noteworthy that when complete resections were compared with incomplete resections irrespective of the treatment arm assignment, the complete resection group showed significantly prolonged survival (17.9 vs. 12.9 months, $p < 0.0001$) [92]. The study thus confirmed the previously discussed assumption of a significant benefit of GTR and also demonstrated that the overall risk was not increased. Although extended resections are associated with an increase in early adverse events, this must be balanced with a reduced need for secondary treatments and their associated side effects.

8.5.1 Sensitivity and Specificity

When aiming for a minimal risk of inducing side effects, such as functional deficits due to extended resection caused by false-positive staining of normal brain, PpIX specificity should be as close to 100% as possible. Indeed, the first reported clinical data indicated that all macroscopically fluorescent tissue contained malignant tumor [93]. This investigation was performed from an analysis of 89 biopsies sampled at the tumor borders of nine patients. In a later report, spectroscopically determined PpIX signal was correlated with tumor cell density, also indicating a very high specificity (Fig. 8.5, [94]): none of the samples that were histologically free of tumor (0% tumor cell density) showed PpIX fluorescence to a degree above 10% of that found in the brightest biopsy taken from the same patient. In the majority of these samples, PpIX was not detectable at all. A report with significantly more false-positive biopsies was published by Panciani et al. [95]: these authors found 5 false positives of 46 positive samples obtained from 54 patients with primary GBM.

Nabavi et al. [96] addressed the question of whether the high specificity found in primary malignant glioma is also found in recurrent tumor and under the condition of various pretreatments. In their biopsy-based evaluation, 342 of 354 biopsies

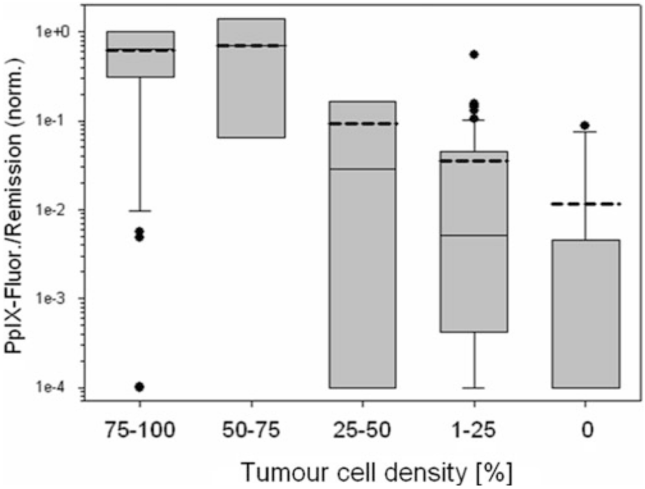

Fig. 8.5 Boxplot representation of the ratios of 635-nm PpIX fluorescence to the 450-nm remission vs. tumor cell density. The values are normalized with respect to the highest ratio obtained within the "75–100 % tumor cell density" group for each individual patient in order to account for patient-specific PpIX kinetics. Note logarithmic scaling. Values with no PpIX detectable are set to 1e-4. The median of the 0 % group is at 1e-4. *Dashed lines* represent the mean values (adapted from [94] with kind permission)

from fluorescent tissue (strong or weak) showed tumor histopathologically. One hundred and fifty-seven biopsies had been taken from intraoperatively normal appearing brain under white light. Eleven of the 12 false-positive findings originated from such areas, mostly weakly fluorescent. It is hypothesized that false positives may be due to infiltration of reactive astrocytes and macrophages or leakage of PpIX into surrounding edema. This interpretation is supported by findings of Utsuki et al. [97] and Ando et al. [98], where the latter performed their investigation on cryosections and identified differences in autofluorescence between true-positive and false-positive areas. Nabavi et al. [96] found no alteration of tumor fluorescence caused by radio- or chemotherapy pretreatment. With the possible occurrence of false positives, predominantly in recurrent GBM, caution is recommended when resecting fluorescent areas of uncertain white light appearance. Nevertheless, in initially diagnosed malignant gliomas, patients in whom strongly and weakly fluorescing tissue was resected completely demonstrated the best prognosis, followed by patients in whom some weakly fluorescing tissue was unresected. Prognosis was worst in patients in whom strongly fluorescent tissue was left behind [93]. These data suggest that if eloquent functions are not at jeopardy, resection should extend to encompass weak fluorescence.

When judging the sensitivity of FGR, three questions may be interesting to address: (1) do all malignant gliomas show comparable fluorescence? (2) How many false negatives are encountered on a biopsy basis? And (3) how does FGR perform in comparison with post-operative MRI or PET imaging?

The first question may be answered best on a per patient basis and relying on tissue samples, where PpIX can be extracted and quantitatively determined. In such investigations, it must be considered that large parts of the tumor may be necrotic and can therefore not be expected to show PpIX fluorescence. In view of the heterogenous nature of a malignant glioma, it is expected that PpIX accumulation is very different from patient to patient. Initial indication of such heterogeneity in PpIX accumulation was reported by Eleouet et al. [99]. Further investigations confirmed this finding [89, 100]. In the most recent investigation [100] of 19 patients with GBM, two showed no or only marginal PpIX in tissue specimens obtained during resection, and one showed below 1 μM PpIX. All others showed maximum PpIX levels ranging from 2.4 to 27.6 μM. Inter-patient variability appeared to be larger than intra-patient variability. Hefti et al. [101] judged sensitivity and specificity by comparing intraoperative fluorescence ("solid" or "vague" or none) with histopathology on a per patient basis. Seventy-one patients had received 5-ALA, among which 47 had GBM. There was only one GBM patient with a tumor not exhibiting fluorescence. Sensitivity was therefore 98%. In 38 of 42 cases with intended gross total removal, PpIX fluorescence correctly identified residual tumor. Tsugu et al. [102] reported about three fluorescence-negative glioblastomas among 20 investigated. It should be noted, however, that they used nonstandard equipment for fluorescence imaging. As a conclusion from these reports, one has to expect that not all malignant gliomas, even grade IV, will accumulate high concentrations of PpIX. A key to understanding this variability might be found in the widely varying proliferation activity of malignant gliomas. There are indeed several reports that find a good correlation between PpIX accumulation and the Ki67 proliferation index [89, 103–106], even within a single tumor [105].

The second question was first addressed by Stummer et al. [93]. The sensitivity reported was 85%, where the nine false-negative samples comprised four with predominantly necrosis and five with low-density infiltrates of tumor cells. Valdes et al. [107] used a calibrated fiber-optic probe to determine PpIX concentrations and correlated these findings to histopathology, resulting in a sensitivity of 95% for high-grade glioma, whereas the visual judgment through the surgical microscope appeared to have resulted in a much lower sensitivity. In an earlier study, a sensitivity of only 75% was reported for visually assessed fluorescence [108].

The third question is probably the most interesting one, as it compares the performance of FGR with the "gold standards" for the assessment of a successful GTR, namely, early post-operative contrast-enhanced MRI, and other clinically well-established assessment methods such as neuronavigation and PET. In the first larger patient series of Stummer et al. [109], it was shown that, of 17 patients whose tumors could be resected without leaving residual intraoperative fluorescence, only one exhibited residual contrast enhancement on post-operative MRI. On the other hand, 9 of 12 patients with residual "vague" fluorescence were MRI negative and even 8 of 23 with residual "solid" fluorescence were MRI negative. At least in the latter case, there is little doubt that vital tumor tissue had been left in the resection cavity.

This investigation suggests that FGR is significantly more sensitive than post-operative MRI. This is confirmed from a single center study published by Idoate et al. [106]. After having achieved a GTR rate of 83% with FGR in 30 patients, of the remaining patients with residual contrast enhancement, none was unexpected, as fluorescent tissue had to be left in the resection cavity due to safety concerns.

It has been shown that PET imaging using amino acids is potentially more sensitive than MRI [110, 111] and in that context it would be interesting to compare FGR with PET. Such studies have been performed [105, 112–116] albeit with somewhat inconsistent results. Arita et al. [112] found no correlation between PpIX fluorescence and ^{11}C-methionine-PET, although both correlated with tumor cell density and PpIX also with proliferation. Conversely, all other reports found a correlation. Ewelt et al. [113] and Floeth et al. [114] performed neuronavigation surgery after MRI-PET fused imaging and concluded that PpIX fluorescence is well suited to identify anaplastic foci in low-grade gliomas. They also demonstrated that all PpIX-fluorescent areas were ^{18}F-FET-PET positive, indicating a higher sensitivity for FET-PET compared to PpIX staining. Ewelt et al. [113] found an astonishingly low specificity for the PET results (46.1%) for high-grade gliomas. Widhalm et al. [105] focussed on tumors with nonsignificant contrast enhancement in MRI. Whereas none of the low-grade gliomas showed PpIX fluorescence, 8 of 9 grade III gliomas showed focal PpIX fluorescence, which was localized at the site with the highest preoperative methionine-PET signal. All these investigations are subject to some risk of mis-localization of the preoperative PET-signal due to brain shift. This was excluded in the investigation of Roessler et al. [115] by performing post-operative FET-PET. Eleven glioblastoma operations were included and areas with vague fluorescence had to be left in all cases. Post-operative MRI was negative in five cases and post-operative FET-PET was negative in three cases. From this finding, the authors concluded that 5-ALA is more sensitive for the detection of infiltrative tumor at the resection margins, possibly to such a degree that caution is indicated when using FGR in the vicinity of eloquent regions.

Low-grade diffuse gliomas have generally been considered not to accumulate sufficient fluorescence to render them amenable for FGR as previously performed on a macroscopic basis. Recently, Sanai et al. [117] demonstrated single cell fluorescence by confocal microscopy in these tumors and Valdes et al. [118] were able to measure fluorescence by spectroscopy. Thus, using the appropriate technology, even low-grade glioma may be amenable to visualization in the near future, as detailed below.

8.5.2 Conclusions for the Neurosurgeon

The available literature indicates quite consistently that 5-ALA is at present not able to guide surgery for low-grade gliomas on a macroscopic basis as afforded by the standard surgical microscope. In secondary grade III and IV gliomas, that is, initially low-grade gliomas containing areas of malignant degeneration, the intraoperative localization of anaplastic foci can quite reliably be performed using PpIX fluorescence. Grade IV gliomas show strong PpIX fluorescence in the proliferating parts of the tumor outside necrotic tissue. The intensity of fluorescence correlates with tumor cell density and proliferation index. The infiltrative parts of the glioblastomas show reduced fluorescence intensity, often described as "vague" or "pink." The positive predictive value of such tissue is still high, but may be below 100%, especially in recurrent tumors. Still, weakly fluorescing tissue should be resected, unless safety concerns dictate otherwise. FGR borders are potentially wider than indicated by contrast-enhanced MRI and correlate better with amino acid PET. Safe GTR is achieved more frequently than with conventional microsurgery. Since fluorescence appears more sensitive for identifying tumor than gadolinium uptake with MRI, surgery using FGR may be more extensive compared to intraoperative MRI. However, the surgical strategy at the resection borders requires careful consideration of possible risks, especially when PpIX fluorescence becomes "vague" and if eloquent brain regions are endangered. Under these circumstances neurosurgeons should incorporate intraoperative monitoring and mapping techniques into their neurosurgical strategy. Most clinical studies on FGR employ surgical microscopes by Carl Zeiss Company (Oberkochen) equipped with a fluorescence mode which features the spectral characteristics previously described. These are set to enable unambiguous identification of tissue with significant PpIX accumulation. Trace amounts of PpIX cannot be readily identified due to the remitted blue light. This serves to override any unspecific endogenous fluorescence in the red spectral part and to set the recognition threshold to a tumor cell density significantly above zero. In view of this, "no fluorescence" as judged from the surgical microscope does not exclude specific PpIX accumulation at low concentrations or distributed in single cells scattered among nonfluorescent normal cells. One has to bear in mind that, although a surgical microscope is used, the scale of observation is still macroscopic compared to the higher magnification used with dedicated microscopes used by histopathologists. We will briefly discuss the conditions under which a more sensitive PpIX detection makes sense and how it can be achieved.

The big advantage of the current embodiment is its simplicity in an intraoperative setting compared to all other available technologies [19]. Neuronavigation based on pre-operative imaging did not fulfill expectations in the context of glioma surgery, and intraoperative MRI is somewhat complex, impedes surgery, and is expensive. The diagnostic accuracy of FGR may exceed that of MRI, at least for glioblastoma surgery.

Surgery by itself will not cure diffusely infiltrating malignant gliomas and all tumors will inevitably recur, despite more extended resections using FGR. Thus, additional therapies are necessary that might serve to prolong survival in these patients. To this end, 5-ALA may provide an additional therapeutic perspective since PpIX, as derived from 5-ALA, is not only a fluorochrome but also a potent photosensitizer. This implies that cells with sufficient levels of PpIX accumulation can be destroyed by employing a sufficiently high, albeit nonthermal, light dose.

As long as the photosensitizer is selectively accumulated in tumor cells, light irradiation has the potential to selectively destroy invading tumor cells, while leaving adjacent functional brain undisturbed. This procedure is called PDT and is being explored for the treatment of glioblastoma either post-FGR [119] or in a stereotactic approach with implanted light diffusing fibers [94, 120]. Intriguing long-term survivors have been reported [121, 122].

Most of the clinical experience with FGR available to date is from Europe or Japan. FDA approval has not yet been obtained. However, there are a series of ongoing clinical trials in North America (refer to clinicaltrials.gov with search terms "aminolevulinic AND glioma"). Among 13 recruiting centers, 11 are located in North America, mostly conducting phase II studies, but also one phase III study. In the near future, new results can be expected concerning the reliability of FGR, its contribution to overall therapeutic outcome, optimal drug dosing, and the implementation of new technologies, such as point spectroscopy and confocal fluorescence microscopy. Some studies are investigating 5-ALA doses (10–50 mg/kg bodyweight), while others are evaluating different types of brain tumors or comparing FGR to other intraoperative tumor identification technologies. The only ongoing phase III study aims at testing a newly developed confocal endomicroscopic probe and also includes low-grade glioma [117]. As with most trials, the primary end point is the extent of resection compared to a placebo arm. Secondary end points are overall survival, time to progression, and side effects.

8.5.3 Spectroscopic and Microscopic Detection of PpIX-Fluorescence

The commercial surgical microscopes equipped with "5-ALA mode," as described above, have been developed for FGR of malignant gliomas. Disregarding large individual differences in PpIX accumulation, in the vast majority of cases, the fluorescence intensity is strong enough to discriminate vital tumor from infiltration, necrosis, and normal brain. Low-grade gliomas are usually declared "nonfluorescent" in investigations performed using available surgical microscopes. This may be due in part to the insufficient sensitivity of the equipment for detecting low concentrations of PpIX.

Optical spectroscopy is a very sensitive method for detecting PpIX in tissue. PpIX fluorescence is characterized by a distinct emission spectrum (Fig. 8.2), whereas brain tissue autofluorescence usually has no characteristic emission in the wavelength range of PpIX (610–730 nm). Only blood absorption can reduce fluorescence at 585 nm, which can make the emission spectrum appear to have a small peak at 610–630 nm. With state-of-the-art data processing, however, the contribution of PpIX emission can very reliably be detected or excluded. As long as the process to be detected, for example, low-grade glioma or metastasis, produces significantly more PpIX than adjacent normal brain, such a spectroscopic technique should be able to specifically detect considerably lower amounts of PpIX than would be possible with a surgical microscope. Several groups have developed corresponding devices, based on fiber-optic point spectroscopy [107, 118, 121, 123]. An ambitious method has been presented by Valdes et al. [107], where intraoperative fluorescence spectroscopy was performed with the aim of quantifying absolute tissue PpIX concentrations. As already mentioned, the fluorescence intensity is influenced by the optical properties of the sampled tissue, independently of PpIX concentration. In order to disentangle the different factors that influence spectral measurements, different algorithms have been suggested [124–128]. Valdes et al. [107] have used alternating fluorescence and white light remission spectroscopy to quantify PpIX concentrations. Consistent with their report on PpIX concentration measurements by chemical extraction [129], they find a considerable number of tumor-positive biopsies with significant PpIX accumulation, which were negative in intraoperative fluorescence imaging. This increase in sensitivity, however, comes at the price of a slightly reduced specificity and associated risk of unintentional tissue resection. As for the pertinent question of whether low-grade gliomas might be detectable by a high sensitivity technique, Valdes et al. [107] found a sensitivity of 75% and a specificity of 80% with their quantitative fiber-optic probe. These were the lowest values among the tumor types tested (low- and high-grade gliomas, meningiomas, and metastases).

Sanai et al. [117] have applied a new confocal fluorescence endomicroscopic technique to investigate 5-ALA-induced PpIX fluorescence in low-grade gliomas. None of the ten tumors showed macroscopic fluorescence but they were all positive in intraoperative confocal microscopy.

A drawback of point spectroscopy or confocal endomicroscopy is its clinical applicability, especially in cases where the entire surface of a resection cavity is to be evaluated. Even though raw fluorescence spectra can be displayed and evaluated in real time, it appears impractical to scan larger areas repetitively. On the other hand, if the area under suspicion is restricted, a contact fiber-optic measurement may be advantageous compared to noncontact imaging, because blood would not as easily obscure tissue fluorescence. It would be more reliable and would yield objective and quantitative data.

Hitherto, 5-ALA-based fluorescence guidance was mostly used for open surgical tumor resection. It may, however, also be very beneficial to use it during stereotactic biopsy procedures. Some groups have suggested that, given the high specificity for the detection of high-grade glioma, any tissue biopsy that shows PpIX fluorescence would indicate the presence of vital tumor tissue, rendering further tissue sampling obsolete. Only fluorescent tissue needs to be submitted to the histopathologist. Widhalm et al. [130] have demonstrated strong PpIX fluorescence in 43 of 50 patients, identifying 52/53 samples of glioblastomas, 9/10 grade III gliomas, and 14/16 lymphomas with a positive predictive value of 100%. The fluorescence was judged visually as “strong,” “vague,” or “none” under a fluorescence microscope. Unfortunately, no spectral recordings were performed. Nevertheless, they conclude that the sampling of representative biopsies is significantly enhanced, obviating the need for intraoperative histopathology in such cases. On the other hand, if no fluorescence is observed, a technical failure of the targeting may be the reason and intraoperative histology is crucial. A similar experience in 13 patients was reported by von Campe et al. [131], who stopped taking additional biopsies, once a fluorescent one had been obtained along the target trajectory during frameless stereotactic biopsy, thereby considerably shortening intervention time. Moriuchi et al. [132] report on two cases of stereotactic biopsy with exsitu fluorescence assessment, both cases showing fluorescence of representative tumor tissue. Due to the deep-seated tumors investigated, they argued that it was important to minimize the risks of inducing deficits, which would have increased by taking serial biopsies. The development of an optical stereotactic needle for in situ PpIX spectroscopy and endomicroscopic imaging was presented by Stepp et al. [100]. While this methodology bears merit, it must be remembered that various non-glioma lesions might have unspecific fluorescence in adjacent tissue, for instance abscesses or metastases [133]. Thus, fluorescence may not be specific for the lesion, possibly leading to nondiagnostic tissue sampling.

8.6 Beyond High-Grade Glioma: FGR for Other Primary Brain Tumors and Metastases

Apart from malignant gliomas, FGR has been described for resection of a variety of CNS tumors, including brain metastases, spinal cord lesions, and meningiomas. The experience is still very limited and therefore the implications for future application of 5-ALA based-FGR are uncertain.

An area of particular clinical interest has been FGR of meningiomas [107, 134–138]. Although the vast majority of meningiomas are benign, strong PpIX accumulation is frequently observed. Whereas the usefulness of FGR for low-grade convexity meningiomas can certainly be debated, there may be situations where knowledge of tumor extensions may be helpful, for instance in the delineation of cranial bone infiltration and for guiding resections when the tumor grows around vessels and nerve tracts. Furthermore, in heavily pre-treated atypical or anaplastic meningiomas with intraoperative scarring, improved delineation of the true extent of tumor infiltration would certainly be beneficial. However, not all meningiomas show fluorescence and, in some cases, the fluorescence is very heterogeneous. Coluccia et al. [135] report on 33 consecutive patients operated on after 5-ALA administration and fluorescence assessment. In 31 cases, fluorescence was detected and in 25 patients a total resection of the tumor was achieved. Interestingly, PpIX accumulation was not hampered by preoperative embolization of the feeding vessels of the tumor, which was performed in five cases. Valdes et al. [107] showed that from 20 biopsy sites in six patients, quantitative point spectroscopy detected high PpIX concentrations in the range of high-grade gliomas for eight biopsy sites; 11 sites were visible in fluorescence imaging. Spectroscopic PpIX quantification for meningioma in this study resulted in a sensitivity of 100% and a specificity of 93% for fluorescence indicating tumor infiltration. The other publications are case reports of atypical meningiomas with a high risk of recurrence, all concluding that FGR was helpful in identifying residual tumor. As presently available, surgical fluorescence microscopes are not sufficiently sensitive for detecting some regions of meningioma tissue. Modifications of the filter characteristics or of the camera gain settings might be considered, always bearing in mind that any increase in sensitivity might compromise specificity.

Reports on other primary brain tumors treated with FGR are rare, comprising a fluorescent chordoma [139], hemangioblastomas [140], ependymomas [141], lymphomas [141], and pituitary adenomas [141, 142].

More experience is available with *brain metastases* of various origins. The largest series was published by Kamp et al. [133] who retrospectively investigated 52 patients with metastatic lesions from a variety of primaries including breast, colorectal, small cell and nonsmall cell lung cancer, renal cell carcinoma, and malignant melanoma. In 32 cases, the metastatic tumor was fluorescent as judged with the surgical microscope used for FGR. No correlation was found with respect to the histopathological type or location of the primary tumor. With the exception of nondetectable fluorescence with all three small cell bronchial cancers, at least 50% of the other metastases showed fluorescence. After having completed white light resection, residual fluorescence was found in 24 patients, where 18 tissue samples were taken and tumor was confirmed in six of these. This indicates limited specificity. Nevertheless, FGR was considered helpful for detecting local invasion in the other cases. Eljamel [141] has also investigated FGR in a series of brain metastases, comprising lung, malignant melanoma, colon, and breast. Most of them were found fluorescence positive.

The limited specificity was also a concern in a publication of Utsuki et al. [143], who found 9 of 11 metastases fluorescent, but also “diffuse” fluorescence outside the borders of the tumor mass. They speculate that this unspecific fluorescence is due to propagation of PpIX produced in the tumor mass into the surrounding tissue by edema. Another possibility would be on-site production by inflammatory processes. An observation made by Schucht et al. [144] excludes diffusion of PpIX from the tumor since the malignant melanoma did not show fluorescence, whereas the surrounding tissue, devoid of tumor cells, did show fluorescence to a depth of 5 mm around the tumor. However, for the two nonfluorescent cases reported by Utsuki et al. [143], they explicitly state that peritumoral fluorescence was not observed. More single cases are reported by Potapov et al. [139] and Morofuji et al. [145]. Interesting studies have been performed by Aziz et al. [146] and Zilidis et al. [147], combining FGR and repetitive PDT for brain metastases. An excellent local control of the treated tumors (20 cases altogether) could be achieved, with only two deaths from recurrent brain metastases.

Fluorescence guidance may also be beneficial for the resection of spinal cord tumors. A malignant glioma was successfully removed during a cordectomy with the aim of minimal tissue removal but complete tumor resection, as reported by Ewelt et al. [148]. Shimizu et al. [149] detected tiny amounts of residual ependymoma after resection using fiber-optic spectroscopy. A larger series of spinal cord tumors resected with fluorescence guidance using fluorescence endoscopy and fiber-based spectroscopy was reported by Shevelev et al. [150]. Bright visible fluorescence was observed in 12 of 16 ependymomas, the remaining four ependymomas still showing a tumor/normal PpIX fluorescence ratio of 11 based on spectroscopic analysis. Two of three myxopapillary ependymomas showed visible fluorescence, one of four pilocytic astrocytomas showed moderate fluorescence, and two GBMs were brightly fluorescent, whereas no fluorescence could be detected in two cases of hemangioblastoma.

The currently available experience with PpIX accumulation in brain tumors other than malignant gliomas may be summarized as follows:

1. Low-grade glioma tissue does not show visible PpIX fluorescence
2. Low-grade gliomas may be detectable with high-sensitivity spectroscopy or confocal microscopy, but with limited accuracy
3. Low-grade gliomas are amenable to FGR for detecting anaplastic foci
4. There are no brain tumors that systematically accumulate or do not accumulate PpIX
5. The intra- and interpatient heterogeneity in PpIX accumulation is even greater than for high-grade gliomas
6. False-positive fluorescence has been found, especially around metastatic tumors
7. Particular caution in the interpretation of PpIX fluorescence is advised
8. FGR is helpful for achieving total resection in difficult cases of meningiomas or metastases, if the reduced positive predictive value is kept in mind
9. The use of high sensitive imaging or spectroscopy may be of value. Unfortunately, such devices are not available commercially for medical use
10. Investigating stereotactic biopsy samples with the fluorescence microscope may be promising (requires prior administration of 5-ALA to the patient)

8.7 Conclusions

The current clinical implementation of FGR using 5-ALA has proven its efficacy in enhancing the extent of safe resection of malignant glioma. It is a simple optical method, based on modified surgical microscopes which are commercially available. The application of 5-ALA as a drinking solution is straightforward. No drug-related side effects have been reported, as long as patients are shielded from intense light during the 24 h period after drug delivery. The surgical microscope can be switched between white light and fluorescence modes intraoperatively. The red PpIX fluorescence is readily observed and is a direct indication of suspicious tissue, without the concern of brain shift. Compared to other techniques for extended resections, such as intraoperative MRI and PET, FGR performs favorably. FGR is cost effective and does not impede the surgical procedure.

The technique cannot, however, replace careful decision making of the neurosurgeon, when approaching the infiltration zone or eloquent regions. FGR has been shown to enhance resections in malignant gliomas, resulting in improved progression-free survival. By reducing proliferating tumor cell load, FGR appears to improve the efficacy of adjuvant therapies.

As FGR is technically simple, some precautions and limitations have to be kept in mind, such as the need to reduce ambient light to a minimum during fluorescence mode and the limited sensitivity. Technical improvements are currently being developed to overcome these limitations. With increased sensitivity in detecting the presence of PpIX, other benign and malignant tumors in the brain may become amenable to FGR with a potential to significantly reduce recurrence rates. One has to consider, however, the likelihood of increased incidence of false-positive PpIX accumulation, for example, around metastases. Last, but not least, PpIX is a potent photosensitizer and clinical trials for brain tumor PDT are ongoing.

References

1. CBTRUS (2011) CBTRUS statistical report: primary brain and central nervous system tumors diagnosed in the United States in 2004–2007. Central Brain Tumor Registry of the United States, Hinsdale, IL. http:\crwww.cbtrus.org
2. Siker ML, Wang M, Porter K, Nelson DF, Curran WJ, Michalski JM, Souhami L, Chakravarti A, Yung WK, Delrowe J, Coughlin CT, Mehta MP (2011) Age as an independent prognostic factor in patients with glioblastoma: a Radiation Therapy Oncology Group and American College of Surgeons National Cancer Data Base comparison. J Neurooncol 104:351–356
3. McGirt MJ, Chaichana KL, Gathinji M, Attenello FJ, Than K, Olivi A, Weingart JD, Brem H, Quinones-Hinojosa AR (2009) Independent association of extent of resection with survival in patients with malignant brain astrocytoma. J Neurosurg 110:156–162
4. Sanai N, Berger MS (2008) Glioma extent of resection and its impact on patient outcome. Neurosurgery 62:753–764
5. Whittle IR (2002) Surgery for gliomas. Curr Opin Neurol 15:663–669
6. Brown PD, Maurer MJ, Rummans TA, Pollock BE, Ballman KV, Sloan JA, Boeve BF, Arusell RM, Clark MM, Buckner JC (2005) A prospective study of quality of life in adults with newly diagnosed high-grade gliomas: the impact of the extent of resection on quality of life and survival. Neurosurgery 57:495–504
7. Buckner JC (2003) Factors influencing survival in high-grade gliomas. Semin Oncol 30:10–14
8. Lacroix M, Abi-Said D, Fourney DR, Gokaslan ZL, Shi W, DeMonte F, Lang FF, McCutcheon IE, Hassenbusch SJ, Holland E, Hess K, Michael C, Miller D, Sawaya R (2001) A multivariate analysis of 416 patients with glioblastoma multiforme: prognosis, extent of resection, and survival. J Neurosurg 95:190–198
9. Stummer W, Reulen HJ, Meinel T, Pichlmeier U, Schumacher W, Tonn JC, Rohde V, Oppel F, Turowski B, Woiciechowsky C, Franz K, Pietsch T (2008) Extent of resection and survival in glioblastoma multiforme: identification of and adjustment for bias. Neurosurgery 62:564–576
10. Stummer W, Kamp MA (2009) The importance of surgical resection in malignant glioma. Curr Opin Neurol 22:645–649
11. Laws ER, Shaffrey ME, Morris A, Anderson FA Jr (2003) Surgical management of intracranial gliomas–does radical resection improve outcome? Acta Neurochir Suppl 85:47–53
12. Stummer W, van den Bent MJ, Westphal M (2011) Cytoreductive surgery of glioblastoma as the key to successful adjuvant therapies: new arguments in an old discussion. Acta Neurochir 153:1211–1218

13. Stummer W, Meinel T, Ewelt C, Martus P, Jakobs O, Felsberg J, Reifenberger G (2012) Prospective cohort study of radiotherapy with concomitant and adjuvant temozolomide chemotherapy for glioblastoma patients with no or minimal residual enhancing tumor load after surgery. J Neurooncol 108(1):89–97
14. Oszvald A, Guresir E, Setzer M, Vatter H, Senft C, Seifert V, Franz K (2012) Glioblastoma therapy in the elderly and the importance of the extent of resection regardless of age. J Neurosurg 116:357–364
15. Stummer W, Nestler U, Stockhammer F, Krex D, Kern BC, Mehdorn HM, Vince GH, Pichlmeier U (2011) Favorable outcome in the elderly cohort treated by concomitant temozolomide radiochemotherapy in a multicentric phase II safety study of 5-ALA. J Neurooncol 103:361–370
16. Willems PW, van der Sprenkel JW, Tulleken CA, Viergever MA, Taphoorn MJ (2006) Neuronavigation and surgery of intracerebral tumours. J Neurol 253:1123–1136
17. Trantakis C, Tittgemeyer M, Schneider JP, Lindner D, Winkler D, Strauss G, Meixensberger J (2003) Investigation of time-dependency of intracranial brain shift and its relation to the extent of tumor removal using intra-operative MRI. Neurol Res 25:9–12
18. Kuhnt D, Ganslandt O, Schlaffer SM, Buchfelder M, Nimsky C (2011) Quantification of glioma removal by intraoperative high-field magnetic resonance imaging: an update. Neurosurgery 69:852–862
19. Kubben PL, ter Meulen KJ, Schijns OE, ter Laak-Poort MP, van Overbeeke JJ, van Santbrink H (2011) Intraoperative MRI-guided resection of glioblastoma multiforme: a systematic review. Lancet Oncol 12:1062–1070
20. Senft C, Bink A, Franz K, Vatter H, Gasser T, Seifert V (2011) Intraoperative MRI guidance and extent of resection in glioma surgery: a randomised, controlled trial. Lancet Oncol 12:997–1003
21. Gerganov VM, Samii A, Giordano M, Samii M, Fahlbusch R (2011) Two-dimensional high-end ultrasound imaging compared to intraoperative MRI during resection of low-grade gliomas. J Clin Neurosci 18:669–673
22. Gerganov VM, Samii A, Akbarian A, Stieglitz L, Samii M, Fahlbusch R (2009) Reliability of intraoperative high-resolution 2D ultrasound as an alternative to high-field strength MR imaging for tumor resection control: a prospective comparative study. J Neurosurg 111:512–519
23. Rygh OM, Selbekk T, Torp SH, Lydersen S, Hernes TA, Unsgaard G (2008) Comparison of navigated 3D ultrasound findings with histopathology in subsequent phases of glioblastoma resection. Acta Neurochir 150:1033–1041
24. Eberlin LS, Norton I, Dill AL, Golby AJ, Ligon KL, Santagata S, Cooks RG, Agar NY (2012) Classifying human brain tumors by lipid imaging with mass spectrometry. Cancer Res 72:645–654
25. Agar NY, Golby AJ, Ligon KL, Norton I, Mohan V, Wiseman JM, Tannenbaum A, Jolesz FA (2011) Development of stereotactic mass spectrometry for brain tumor surgery. Neurosurgery 68:280–289
26. Bizheva K, Unterhuber A, Hermann B, Povazay B, Sattmann H, Drexler W, Stingl A, Le T, Mei M, Holzwarth R, Reitsamer HA, Morgan JE, Cowey A (2004) Imaging ex vivo and in vitro brain morphology in animal models with ultrahigh resolution optical coherence tomography. J Biomed Opt 9:719–724
27. Bohringer HJ, Lankenau E, Stellmacher F, Reusche E, Huttmann G, Giese A (2009) Imaging of human brain tumor tissue by near-infrared laser coherence tomography. Acta Neurochir 151:507–517
28. Eschbacher J, Martirosyan NL, Nakaji P, Sanai N, Preul MC, Smith KA, Coons SW, Spetzler RF (2012) In vivo intraoperative confocal microscopy for real-time histopathological imaging of brain tumors. J Neurosurg 116:854–860
29. Kantelhardt SR, Leppert J, Kantelhardt JW, Reusche E, Huttmann G, Giese A (2009) Multiphoton excitation fluorescence microscopy of brain-tumour tissue and analysis of cell density. Acta Neurochir 151:253–262

30. Croce AC, Fiorani S, Locatelli D, Nano R, Ceroni M, Tancioni F, Giombelli E, Benericetti E, Bottiroli G (2003) Diagnostic potential of autofluorescence for an assisted intraoperative delineation of glioblastoma resection margins. Photochem Photobiol 77:309–318
31. Toms SA, Lin WC, Weil RJ, Johnson MD, Jansen ED, Mahadevan-Jansen A (2007) Intraoperative optical spectroscopy identifies infiltrating glioma margins with high sensitivity. Neurosurgery 61:327–335
32. Butte PV, Mamelak AN, Nuno M, Bannykh SI, Black KL, Marcu L (2011) Fluorescence lifetime spectroscopy for guided therapy of brain tumors. Neuroimage 54(Suppl 1):S125–135
33. Yao J, Maslov KI, Zhang Y, Xia Y, Wang LV (2011) Label-free oxygen-metabolic photoacoustic microscopy in vivo. J Biomed Opt 16:076003
34. Hansen DA, Spence AM, Carski T, Berger MS (1993) Indocyanine green (ICG) staining and demarcation of tumor margins in a rat glioma model. Surg Neurol 40:451–456
35. Haglund MM, Berger MS, Hochman DW (1996) Enhanced optical imaging of human gliomas and tumor margins. Neurosurgery 38:308–317
36. Martirosyan NL, Cavalcanti DD, Eschbacher JM, Delaney PM, Scheck AC, Abdelwahab MG, Nakaji P, Spetzler RF, Preul MC (2011) Use of in vivo near-infrared laser confocal endomicroscopy with indocyanine green to detect the boundary of infiltrative tumor. J Neurosurg 115:1131–1138
37. Moore GE, Peyton WT et al (1948) The clinical use of fluorescein in neurosurgery; the localization of brain tumors. J Neurosurg 5:392–398
38. Shinoda J, Yano H, Yoshimura S, Okumura A, Kaku Y, Iwama T, Sakai N (2003) Fluorescence-guided resection of glioblastoma multiforme by using high-dose fluorescein sodium. Technical note. J Neurosurg 99:597–603
39. Koc K, Anik I, Cabuk B, Ceylan S (2008) Fluorescein sodium-guided surgery in glioblastoma multiforme: a prospective evaluation. Br J Neurosurg 22:99–103
40. Stummer W, Gotz C, Hassan A, Heimann A, Kempski O (1993) Kinetics of Photofrin II in perifocal brain edema. Neurosurgery 33:1075–1081
41. Dilek O, Ihsan A, Tulay H (2011) Anaphylactic reaction after fluorescein sodium administration during intracranial surgery. J Clin Neurosci 18:430–431
42. Tanahashi S, Lida H, Dohi S (2006) An anaphylactoid reaction after administration of fluorescein sodium during neurosurgery. Anesth Analg 103:503
43. Kremer P, Fardanesh M, Ding R, Pritsch M, Zoubaa S, Frei E (2009) Intraoperative fluorescence staining of malignant brain tumors using 5-aminofluorescein-labeled albumin. Neurosurgery 64:53–60
44. Pogue BW, Gibbs-Strauss S, Valdes PA, Samkoe K, Roberts DW, Paulsen KD (2010) Review of neurosurgical fluorescence imaging methodologies. IEEE J Sel Top Quantum Electron 16:493–505
45. Ballangrud AM, Lymberis S, Thakur SB, Karimi S, Huang W, Abrey LE, Beal K, Iwamoto FM, Brennan C, Gutin PH, Chang J (2011) Magnetic resonance spectroscopy imaging in radiotherapy planning for recurrent glioma. Medical Physics 38:2724–2730
46. Weber MA, Henze M, Tuttenberg J, Stieltjes B, Meissner M, Zimmer F, Burkholder I, Kroll A, Combs SE, Vogt-Schaden M, Giesel FL, Zoubaa S, Haberkorn U, Kauczor HU, Essig M (2010) Biopsy targeting gliomas: do functional imaging techniques identify similar target areas? Invest Radiol 45:755–768
47. Feigl GC, Ritz R, Moraes M, Klein J, Ramina K, Gharabaghi A, Krischek B, Danz S, Bornemann A, Liebsch M, Tatagiba MS (2010) Resection of malignant brain tumors in eloquent cortical areas: a new multimodal approach combining 5-aminolevulinic acid and intraoperative monitoring. J Neurosurg 113:352–357
48. Collaud S, Juzeniene A, Moan J, Lange N (2004) On the selectivity of 5-aminolevulinic acid-induced protoporphyrin IX formation. Curr MedChem Anti-Canc Agents 4:301–316
49. Layer G, Reichelt J, Jahn D, Heinz DW (2010) Structure and function of enzymes in heme biosynthesis. Protein Sci 19:1137–1161

50. Cappellini MD, Brancaleoni V, Graziadei G, Tavazzi D, Di Pierro E (2010) Porphyrias at a glance: diagnosis and treatment. Intern Emerg Med 5(Suppl 1):S73–80
51. Norman RA (2005) Past and future: porphyria and porphyrins. Skinmed 4:287–292
52. Anderson CM, Jevons M, Thangaraju M, Edwards N, Conlon NJ, Woods S, Ganapathy V, Thwaites DT (2010) Transport of the photodynamic therapy agent 5-aminolevulinic acid by distinct H + −coupled nutrient carriers coexpressed in the small intestine. J Pharmacol Exp Ther 332:220–228
53. Bermudez Moretti M, Correa Garcia S, Perotti C, Batlle A, Casas A (2002) Delta-aminolevulinic acid transport in murine mammary adenocarcinoma cells is mediated by beta transporters. Br J Cancer 87:471–474
54. Doring F, Walter J, Will J, Focking M, Boll M, Amasheh S, Clauss W, Daniel H (1998) Delta-aminolevulinic acid transport by intestinal and renal peptide transporters and its physiological and clinical implications. J Clin Invest 101:2761–2767
55. Neumann J, Brandsch M (2003) Delta-aminolevulinic acid transport in cancer cells of the human extrahepatic biliary duct. J Pharmacol Exp Ther 305:219–224
56. Novotny A, Xiang J, Stummer W, Teuscher NS, Smith DE, Keep RF (2000) Mechanisms of 5-aminolevulinic acid uptake at the choroid plexus. J Neurochem 75:321–328
57. Rud E, Gederaas O, Hogset A, Berg K (2000) 5-aminolevulinic acid, but not 5-aminolevulinic acid esters, is transported into adenocarcinoma cells by system BETA transporters. Photochem Photobiol 71:640–647
58. Van Hillegersberg R, Van den Berg JW, Kort WJ, Terpstra OT, Wilson JH (1992) Selective accumulation of endogenously produced porphyrins in a liver metastasis model in rats. Gastroenterology 103:647–651
59. Krieg RC, Fickweiler S, Wolfbeis OS, Knuechel R (2000) Cell-type specific protoporphyrin IX metabolism in human bladder cancer in vitro. Photochem Photobiol 72:226–233
60. Krieg RC, Messmann H, Rauch J, Seeger S, Knuechel R (2002) Metabolic characterization of tumor cell-specific protoporphyrin IX accumulation after exposure to 5-aminolevulinic acid in human colonic cells. Photochem Photobiol 76:518–525
61. Berg K, Anholt H, Bech O, Moan J (1996) The influence of iron chelators on the accumulation of protoporphyrin IX in 5-aminolaevulinic acid-treated cells. Br J Cancer 74:688–697
62. Ohgari Y, Nakayasu Y, Kitajima S, Sawamoto M, Mori H, Shimokawa O, Matsui H, Taketani S (2005) Mechanisms involved in delta-aminolevulinic acid (ALA)-induced photosensitivity of tumor cells: relation of ferrochelatase and uptake of ALA to the accumulation of protoporphyrin. Biochem Pharmacol 71:42–49
63. Navone NM, Polo CF, Frisardi AL, Andrade NE, Battle AM (1990) Heme biosynthesis in human breast cancer–mimetic “in vitro” studies and some heme enzymic activity levels. Int J Biochem 22:1407–1411
64. Hinnen P, de Rooij FW, van Velthuysen ML, Edixhoven A, van Hillegersberg R, Tilanus HW, Wilson JH, Siersema PD (1998) Biochemical basis of 5-aminolaevulinic acid-induced protoporphyrin IX accumulation: a study in patients with (pre)malignant lesions of the oesophagus. Br J Cancer 78:679–682
65. Greenbaum JF, Gozlan Y, Schwartz D, Katcoff DJ, Malik Z (2002) Nuclear distribution of porphobilinogen deaminase (PBGD) in glioma cells: a regulatory role in cancer transformation. Br J Cancer 86:1006–1011
66. Greenbaum L, Katcoff DJ, Dou H, Gozlan Y, Malik Z (2003) A porphobilinogen deaminase (PBGD) Ran-binding protein interaction is implicated in nuclear trafficking of PBGD in differentiating glioma cells. Oncogene 22:5221–5228
67. Schauder A, Feuerstein T, Malik Z (2011) The centrality of PBGD expression levels on ALA-PDT efficacy. Photochem Photobiol Sci 10:1310–1317
68. Liang H, Shin DS, Lee YE, Nguyen DC, Trang TC, Pan AH, Huang SL, Chong DH, Berns MW (1998) Subcellular phototoxicity of 5-aminolaevulinic acid (ALA). Lasers Surg Med 22:14–24

69. Inoue K, Karashima T, Kamada M, Shuin T, Kurabayashi A, Furihata M, Fujita H, Utsumi K, Sasaki J (2009) Regulation of 5-aminolevulinic acid-mediated protoporphyrin IX accumulation in human urothelial carcinomas. Pathobiology 76:303–314
70. Mesenholler M, Matthews EK (2000) A key role for the mitochondrial benzodiazepine receptor in cellular photosensitisation with delta-aminolaevulinic acid. Eur J Pharmacol 406:171–180
71. Wyld L, Burn JL, Reed MW, Brown NJ (1997) Factors affecting aminolaevulinic acid-induced generation of protoporphyrin IX. Br J Cancer 76:705–712
72. Li W, Zhang WJ, Ohnishi K, Yamada I, Ohno R, Hashimoto K (2001) 5-Aminolaevulinic acid-mediated photodynamic therapy in multidrug resistant leukemia cells. J Photochem Photobiol B 60:79–86
73. Ogino T, Kobuchi H, Munetomo K, Fujita H, Yamamoto M, Utsumi T, Inoue K, Shuin T, Sasaki J, Inoue M, Utsumi K (2011) Serum-dependent export of protoporphyrin IX by ATP-binding cassette transporter G2 in T24 cells. Mol Cell Biochem 358:297–307
74. Jin Y, Bin ZQ, Qiang H, Liang C, Hua C, Jun D, Dong WA, Qing L (2009) ABCG2 is related with the grade of glioma and resistance to mitoxantone, a chemotherapeutic drug for glioma. J Cancer Res Clin Oncol 135:1369–1376
75. Robey RW, Steadman K, Polgar O, Bates SE (2005) ABCG2-mediated transport of photosensitizers: potential impact on photodynamic therapy. Cancer Biol Ther 4:187–194
76. Galldiks N, Ullrich R, Schroeter M, Fink GR, Jacobs AH, Kracht LW (2010) Volumetry of [(11)C]-methionine PET uptake and MRI contrast enhancement in patients with recurrent glioblastoma multiforme. Eur J Nucl Med Mol Imaging 37:84–92
77. Terr L, Weiner LP (1983) An autoradiographic study of delta-aminolevulinic acid uptake by mouse brain. Exp Neurol 79:564–568
78. Obwegeser A, Jakober R, Kostron H (1998) Uptake and kinetics of 14 C-labelled meta-tetrahydroxyphenylchlorin and 5-aminolaevulinic acid in the C6 rat glioma model. Br J Cancer 78:733–738
79. Malakoutikhah M, Prades R, Teixido M, Giralt E (2010) N-methyl phenylalanine-rich peptides as highly versatile blood–brain barrier shuttles. J Med Chem 53:2354–2363
80. Garcia SC, Moretti MB, Garay MV, Batlle A (1998) Delta-aminolevulinic acid transport through blood–brain barrier. Gen Pharmacol 31:579–582
81. Fukuda H, Paredes S, Batlle AM (1992) Tumour-localizing properties of porphyrins. In vivo studies using free and liposome encapsulated aminolevulinic acid. Comp Biochem Physiol B 102:433–436
82. Ennis SR, Novotny A, Xiang J, Shakui P, Masada T, Stummer W, Smith DE, Keep RF (2003) Transport of 5-aminolevulinic acid between blood and brain. Brain Res 959:226–234
83. Madsen SJ, Hirschberg H (2010) Site-specific opening of the blood–brain barrier. J Biophotonics 3:356–367
84. Samkoe KS, Gibbs-Strauss SL, Yang HH, Khan Hekmatyar S, Jack Hoopes P, O'Hara JA, Kauppinen RA, Pogue BW (2011) Protoporphyrin IX fluorescence contrast in invasive glioblastomas is linearly correlated with Gd enhanced magnetic resonance image contrast but has higher diagnostic accuracy. J Biomed Opt 16:096008
85. Madsen SJ, Angell-Petersen E, Spetalen S, Carper SW, Ziegler SA, Hirschberg H (2006) Photodynamic therapy of newly implanted glioma cells in the rat brain. Lasers Surg Med 38:540–548
86. Jocham D, Stepp H, Waidelich R (2008) Photodynamic diagnosis in urology: state-of-the-art. Eur Urol 53:1138–1148
87. Tonn JC, Stummer W (2008) Fluorescence-guided resection of malignant gliomas using 5-aminolevulinic acid: practical use, risks, and pitfalls. Clin Neurosurg 55:20–26
88. Stepp H, Baumgartner R, Beyer W, Knuchel R, Korner TO, Kriegmair M, Rick K, Steinbach P, Stepp HG, Hofstetter A (1995) Fluorescence imaging and spectroscopy of ALA-induced protoporphyrin IX preferentially accumulated in tumour tissue. Optical Biopsies, Proceedings of SPIE 2627:13–24

89. Johansson A, Palte G, Schnell O, Tonn JC, Herms J, Stepp H (2010) 5-Aminolevulinic acid-induced protoporphyrin IX levels in tissue of human malignant brain tumors. Photochem Photobiol 86:1373–1378
90. Stummer W, Stepp H, Moller G, Ehrhardt A, Leonhard M, Reulen HJ (1998) Technical principles for protoporphyrin-IX-fluorescence guided microsurgical resection of malignant glioma tissue. Acta Neurochir 140:995–1000
91. Stummer W, Pichlmeier U, Meinel T, Wiestler OD, Zanella F, Reulen HJ (2006) Fluorescence-guided surgery with 5-aminolevulinic acid for resection of malignant glioma: a randomised controlled multicentre phase III trial. Lancet Oncol 7:392–401
92. Stummer W, Tonn JC, Mehdorn HM, Nestler U, Franz K, Goetz C, Bink A, Pichlmeier U (2010) Counterbalancing risks and gains from extended resections in malignant glioma surgery: a supplemental analysis from the randomized 5-aminolevulinic acid glioma resection study. J Neurosurg 114(3):613–623
93. Stummer W, Stocker S, Wagner S, Stepp H, Fritsch C, Goetz C, Goetz AE, Kiefmann R, Reulen HJ (1998) Intraoperative detection of malignant gliomas by 5-aminolevulinic acid-induced porphyrin fluorescence. Neurosurgery 42:518–525
94. Johansson A, Kreth FW, Stummer W, Stepp H (2010) Interstitial photodynamic therapy of brain tumors. IEEE Journal of selected topics in quantum electronics 16:841–853
95. Panciani PP, Fontanella M, Schatlo B, Garbossa D, Agnoletti A, Ducati A, Lanotte M (2012) Fluorescence and image guided resection in high grade glioma. Clin Neurol Neurosurg 114:37–41
96. Nabavi A, Thurm H, Zountsas B, Pietsch T, Lanfermann H, Pichlmeier U, Mehdorn M (2009) Five-aminolevulinic acid for fluorescence-guided resection of recurrent malignant gliomas: a phase ii study. Neurosurgery 65:1070–1076
97. Utsuki S, Oka H, Sato S, Shimizu S, Suzuki S, Tanizaki Y, Kondo K, Miyajima Y, Fujii K (2007) Histological examination of false positive tissue resection using 5-aminolevulinic acid-induced fluorescence guidance. Neurol Med Chir 47:210–213
98. Ando T, Kobayashi E, Liao H, Maruyama T, Muragaki Y, Iseki H, Kubo O, Sakuma I (2011) Precise comparison of protoporphyrin IX fluorescence spectra with pathological results for brain tumor tissue identification. Brain Tumor Pathol 28:43–51
99. Eleouet S, Rousset N, Carre J, Vonarx V, Vilatte C, Louet C, Lajat Y, Patrice T (2000) Heterogeneity of delta-aminolevulinic acid-induced protoporphyrin IX fluorescence in human glioma cells and leukemic lymphocytes. Neurol Res 22:361–368
100. Stepp H, Beyer W, Brucker D, Ehrhardt A, Fischer S, Goebel W, Goetz M, Guenther B, Hennig G, Herms J, Irion K, Johansson A, Kienast Y, Kniebuehler G, Li P, Ruehm A, Sandner S (2012) Fluorescence guidance during stereotactic biopsy. Proceedings of the SPIE 8207:in press
101. Hefti M, von Campe G, Moschopulos M, Siegner A, Looser H, Landolt H (2008) 5-aminolevulinic acid induced protoporphyrin IX fluorescence in high-grade glioma surgery: a one-year experience at a single institutuion. Swiss Med Wkly 138:180–185
102. Tsugu A, Ishizaka H, Mizokami Y, Osada T, Baba T, Yoshiyama M, Nishiyama J, Matsumae M (2011) Impact of the combination of 5-aminolevulinic acid-induced fluorescence with intraoperative magnetic resonance imaging-guided surgery for glioma. World Neurosurg 76:120–127
103. Ishihara R, Katayama Y, Watanabe T, Yoshino A, Fukushima T, Sakatani K (2007) Quantitative spectroscopic analysis of 5-aminolevulinic acid-induced protoporphyrin IX fluorescence intensity in diffusely infiltrating astrocytomas. Neurol Med Chir 47:53–57
104. Valle RD, Solis ST, Gastearena MAI, de Eulate RG, Echavarri PD, Mendiroz JA (2011) Surgery guided by 5-aminolevulinic fluorescence in glioblastoma: volumetric analysis of extent of resection in single-center experience. J Neurooncol 102:105–113
105. Widhalm G, Wolfsberger S, Minchev G, Woehrer A, Krssak M, Czech T, Prayer D, Asenbaum S, Hainfellner JA, Knosp E (2010) 5-Aminolevulinic acid is a promising marker

for detection of anaplastic foci in diffusely infiltrating gliomas with nonsignificant contrast enhancement. Cancer 116:1545–1552

106. Idoate MA, Diez Valle R, Echeveste J, Tejada S (2011) Pathological characterization of the glioblastoma border as shown during surgery using 5-aminolevulinic acid-induced fluorescence. Neuropathology 31:575–582
107. Valdes PA, Leblond F, Kim A, Harris BT, Wilson BC, Fan X, Tosteson TD, Hartov A, Ji S, Erkmen K, Simmons NE, Paulsen KD, Roberts DW (2011) Quantitative fluorescence in intracranial tumor: implications for ALA-induced PpIX as an intraoperative biomarker. J Neurosurg 115:11–17
108. Roberts DW, Valdes PA, Harris BT, Fontaine KM, Hartov A, Fan X, Ji S, Lollis SS, Pogue BW, Leblond F, Tosteson TD, Wilson BC, Paulsen KD (2010) Coregistered fluorescence-enhanced tumor resection of malignant glioma: relationships between delta-aminolevulinic acid-induced protoporphyrin IX fluorescence, magnetic resonance imaging enhancement, and neuropathological parameters. J Neurosurg 114(3):595–603
109. Stummer W, Novotny A, Stepp H, Goetz C, Bise K, Reulen HJ (2000) Fluorescence-guided resection of glioblastoma multiforme by using 5-aminolevulinic acid-induced porphyrins: a prospective study in 52 consecutive patients. J Neurosurg 93:1003–1013
110. Weber DC, Zilli T, Buchegger F, Casanova N, Haller G, Rouzaud M, Nouet P, Dipasquale G, Ratib O, Zaidi H, Vees H, Miralbell R (2008) [(18)F]Fluoroethyltyrosine- positron emission tomography-guided radiotherapy for high-grade glioma. Radiat Oncol 3:44
111. Tovi M, Lilja A, Bergstrom M, Ericsson A, Bergstrom K, Hartman M (1990) Delineation of gliomas with magnetic resonance imaging using Gd-DTPA in comparison with computed tomography and positron emission tomography. Acta Radiol 31:417–429
112. Arita H, Kinoshita M, Kagawa N, Fujimoto Y, Kishima H, Hashimoto N, Yoshimine T (2012) (11) C-methionine uptake and intraoperative 5-aminolevulinic acid-induced fluorescence as separate index markers of cell density in glioma: a stereotactic image-histological analysis. Cancer 118:1619–1627
113. Ewelt C, Floeth FW, Felsberg J, Steiger HJ, Sabel M, Langen KJ, Stoffels G, Stummer W (2011) Finding the anaplastic focus in diffuse gliomas: the value of Gd-DTPA enhanced MRI, FET-PET, and intraoperative, ALA-derived tissue fluorescence. Clin Neurol Neurosurg 113:541–547
114. Floeth FW, Sabel M, Ewelt C, Stummer W, Felsberg J, Reifenberger G, Steiger HJ, Stoffels G, Coenen HH, Langen KJ (2011) Comparison of (18)F-FET PET and 5-ALA fluorescence in cerebral gliomas. Eur J Nucl Med Mol Imaging 38:731–741
115. Roessler K, Becherer A, Donat M, Cejna M, Zachenhofer I (2012) Intraoperative tissue fluorescence using 5-aminolevolinic acid (5-ALA) is more sensitive than contrast MRI or amino acid positron emission tomography ((18)F-FET PET) in glioblastoma surgery. Neurol Res 34(3):314–317
116. Stockhammer F, Misch M, Horn P, Koch A, Fonyuy N, Plotkin M (2009) Association of F18-fluoro-ethyl-tyrosin uptake and 5-aminolevulinic acid-induced fluorescence in gliomas. Acta Neurochir 151:1377–1383
117. Sanai N, Snyder LA, Honea NJ, Coons SW, Eschbacher JM, Smith KA, Spetzler RF (2011) Intraoperative confocal microscopy in the visualization of 5-aminolevulinic acid fluorescence in low-grade gliomas. J Neurosurg 115:740–748
118. Valdes PA, Kim A, Leblond F, Conde OM, Harris BT, Paulsen KD, Wilson BC, Roberts DW (2011) Combined fluorescence and reflectance spectroscopy for in vivo quantification of cancer biomarkers in low- and high-grade glioma surgery. J Biomed Opt 16:116007
119. Eljamel MS, Goodman C, Moseley H (2008) ALA and Photofrin fluorescence-guided resection and repetitive PDT in glioblastoma multiforme: a single centre Phase III randomised controlled trial. Lasers Med Sci 23:361–367
120. Beck TJ, Kreth FW, Beyer W, Mehrkens JH, Obermeier A, Stepp H, Stummer W, Baumgartner R (2007) Interstitial photodynamic therapy of nonresectable malignant glioma

recurrences using 5-aminolevulinic acid induced protoporphyrin IX. Lasers Surg Med 39:386–393

121. Stepp H, Beck T, Pongratz T, Meinel T, Kreth FW, Tonn JC, Stummer W (2007) ALA and malignant glioma: fluorescence-guided resection and photodynamic treatment. J Environ Pathol Toxicol Oncol 26:157–164
122. Stummer W, Beck T, Beyer W, Mehrkens JH, Obermeier A, Etminan N, Stepp H, Tonn JC, Baumgartner R, Herms J, Kreth FW (2008) Long-sustaining response in a patient with non-resectable, distant recurrence of glioblastoma multiforme treated by interstitial photodynamic therapy using 5-ALA: case report. J Neurooncol 87:103–109
123. Haj-Hosseini N, Richter J, Andersson-Engels S, Wardell K (2010) Optical touch pointer for fluorescence guided glioblastoma resection using 5-aminolevulinic acid. Lasers Surg Med 42:9–14
124. Stepp H, Beck T, Beyer W, Pfaller C, Schuppler M, Sroka R, Baumgartner R (2007) Measurement of fluorophore concentration in turbid media by a single optical fiber. Med Laser App 22:23–34
125. Amelink A, Kruijt B, Robinson DJ, Sterenborg HJ (2008) Quantitative fluorescence spectroscopy in turbid media using fluorescence differential path length spectroscopy. J Biomed Opt 13:054051
126. Kanick SC, Robinson DJ, Sterenborg HJ, Amelink A (2012) Semi-empirical model of the effect of scattering on single fiber fluorescence intensity measured on a turbid medium. Biomed Opt Express 3:137–152
127. Müller MG, Georgakoudi I, Zhang Q, Wu J, Feld MS (2001) Intrinsic fluorescence spectroscopy in turbid media: disentangling effects of scattering and absorption. Appl Opt 40:4633–4646
128. Kim A, Khurana M, Moriyama Y, Wilson BC (2010) Quantification of in vivo fluorescence decoupled from the effects of tissue optical properties using fiber-optic spectroscopy measurements. J Biomed Opt 15:067006
129. Valdes PA, Kim A, Brantsch M, Niu C, Moses ZB, Tosteson TD, Wilson BC, Paulsen KD, Roberts DW, Harris BT (2011) delta-aminolevulinic acid-induced protoporphyrin IX concentration correlates with histopathologic markers of malignancy in human gliomas: the need for quantitative fluorescence-guided resection to identify regions of increasing malignancy. Neuro Oncol 13:846–856
130. Widhalm G, Minchev G, Woehrer A, Preusser M, Kiesel B, Furtner J, Mert A, Di Ieva A, Tomanek B, Prayer D, Marosi C, Hainfellner JA, Knosp E, Wolfsberger S (2012) Strong 5-aminolevulinic acid-induced fluorescence is a novel intraoperative marker for representative tissue samples in stereotactic brain tumor biopsies. Neurosurg Rev 35:381–391
131. von Campe G, Moschopulos M, Hefti M (2012) 5-Aminolevulinic acid-induced protoporphyrin IX fluorescence as immediate intraoperative indicator to improve the safety of malignant or high-grade brain tumor diagnosis in frameless stereotactic biopsies. Acta Neurochir 154(4):585–588
132. Moriuchi S, Yamada K, Dehara M, Teramoto Y, Soda T, Imakita M, Taneda M (2011) Use of 5-aminolevulinic acid for the confirmation of deep-seated brain tumors during stereotactic biopsy. Report of 2 cases. J Neurosurg 115:278–280
133. Kamp MA, Grosser P, Felsberg J, Slotty PJ, Steiger HJ, Reifenberger G, Sabel M (2012) 5-aminolevulinic acid (5-ALA)-induced fluorescence in intracerebral metastases: a retrospective study. Acta Neurochir 154:223–228
134. Bekelis K, Valdes PA, Erkmen K, Leblond F, Kim A, Wilson BC, Harris BT, Paulsen KD, Roberts DW (2011) Quantitative and qualitative 5-aminolevulinic acid-induced protoporphyrin IX fluorescence in skull base meningiomas. Neurosurg Focus 30:E8
135. Coluccia D, Fandino J, Fujioka M, Cordovi S, Muroi C, Landolt H (2010) Intraoperative 5-aminolevulinic-acid-induced fluorescence in meningiomas. Acta Neurochir 152:1711–1719
136. Kajimoto Y, Kuroiwa T, Miyatake S, Ichioka T, Miyashita M, Tanaka H, Tsuji M (2007) Use of 5-aminolevulinic acid in fluorescence-guided resection of meningioma with high risk of recurrence. Case report. J Neurosurg 106:1070–1074

137. Morofuji Y, Matsuo T, Hayashi Y, Suyama K, Nagata I (2008) Usefulness of intraoperative photodynamic diagnosis using 5-aminolevulinic acid for meningiomas with cranial invasion: technical case report. Neurosurgery 62:102–103
138. Whitson WJ, Valdes PA, Harris BT, Paulsen KD, Roberts DW (2011) Confocal microscopy for the histological fluorescence pattern of a recurrent atypical meningioma: case report. Neurosurgery 68:E1768–1772
139. Potapov AA, Usachev DJ, Loshakov VA, Cherekaev VA, Kornienko VN, Pronin IN, Kobiakov GL, Kalinin PL, Gavrilov AG, Stummer W, Golbin DA, Zelenkov PV (2008) First experience in 5-ALA fluorescence-guided and endoscopically assisted microsurgery of brain tumors. Med Laser App 23:202–208
140. Utsuki S, Oka H, Kijima C, Miyajima Y, Hagiwara H, Fujii K (2011) Utility of intraoperative fluorescent diagnosis of residual hemangioblastoma using 5-aminolevulinic acid. Neurol India 59:612–615
141. Eljamel MS (2009) Which intracranial lesions would be suitable for 5-aminolevulenic acid-induced fluorescence-guided identification, localization, or resection? A prospective study of 114 consecutive intracranial lesions. Clin Neurosurg 56:93–97
142. Eljamel MS, Leese G, Moseley H (2009) Intraoperative optical identification of pituitary adenomas. J Neurooncol 92:417–421
143. Utsuki S, Miyoshi N, Oka H, Miyajima Y, Shimizu S, Suzuki S, Fujii K (2007) Fluorescence-guided resection of metastatic brain tumors using a 5-aminolevulinic acid-induced protoporphyrin IX: pathological study. Brain Tumor Pathol 24:53–55
144. Schucht P, Beck J, Vajtai I, Raabe A (2011) Paradoxical fluorescence after administration of 5-aminolevulinic acid for resection of a cerebral melanoma metastasis. Acta Neurochir 153:1497–1499
145. Morofuji Y, Matsuo T, Toyoda K, Takeshita T, Hirose M, Hirao T, Hayashi Y, Tsutsumi K, Abe K, Nagata I (2007) Skull metastasis of hepatocellular carcinoma successfully treated by intraoperative photodynamic diagnosis using 5-aminolevulinic acid: case report. No Shinkei Geka 35:913–918
146. Aziz F, Telara S, Moseley H, Goodman C, Manthri P, Eljamel MS (2009) Photodynamic therapy adjuvant to surgery in metastatic carcinoma in brain. Photodiagnosis Photodyn Ther 6:227–230
147. Zilidis G, Aziz F, Telara S, Eljamel MS (2008) Fluorescence image-guided surgery and repetitive photodynamic therapy in brain metastatic malignant melanoma. Photodiagnosis Photodyn Ther 5:264–266
148. Ewelt C, Stummer W, Klink B, Felsberg J, Steiger HJ, Sabel M (2010) Cordectomy as final treatment option for diffuse intramedullary malignant glioma using 5-ALA fluorescence-guided resection. Clin Neurol Neurosurg 112:357–361
149. Shimizu S, Utsuki S, Sato K, Oka H, Fujii K, Mii K (2006) Photodynamic diagnosis in surgery for spinal ependymoma. Case illustration. J Neurosurg Spine 5:380
150. Shevelev I, Zelenkov P, Konovalov N, Nazarenko A, Gousha A, Rotin D, Shishkina L, Goraynov S, Kuszel J, Shehtman O, Potapov A, Golbin D, Kuzmin S, Loshenov V, Grachev P, Saveljeva T, Kholodtsova MN (2011) 5-ALA-fluorescence diagnosis in surgery of spinal cord tumors. Poster presented at European Congress of Neurosurgery, Rome, Italy, 9–14 Oct 2011

Chapter 9
Intracranial Photodynamic Therapy

Brian C. Wilson and Steen J. Madsen

9.1 Introduction

This chapter presents the use of photodynamic therapy (PDT) for clinical applications in the brain, particularly treatment of patients with solid brain tumors such as malignant gliomas. The principles and background of PDT are first described, followed by a summary of brain tumors and presentation of a heuristic model that serves to illustrate how PDT may be utilized. Subsequent sections will summarize what has been achieved to date in intracranial applications of PDT, and then the particular technical challenges that brain tumors pose for effective delivery of PDT treatment and some of the photophysical, photochemical, and photobiological strategies that have been explored to overcome these. The final section looks ahead to potential future needs and developments, both fundamental and practical.

PDT is a treatment technique that depends on the use of molecules (photosensitizers) that can be activated by light of an appropriate wavelength to generate other highly reactive molecules that interact with cellular structures, resulting in either cell death or functional modification [1]. The steps involved in PDT delivery are illustrated in Fig. 9.1a. While the concept of photodynamic treatment has been known for over a century [2], it has only been over the past 30 years that substantial penetration into clinical practice has occurred. PDT was initially developed to treat patients with solid tumors. This continues as a significant application and there have been multiple governmental approvals for a variety of tumor types and sites in different countries worldwide. In addition, a variety of oncological clinical trials are

---

B.C. Wilson (✉)
Department of Medical Biophysics, University of Toronto/Ontario Cancer Institute,
Toronto, ON, Canada
e-mail: wilson@uhnres.utoronto.ca

S.J. Madsen
Department of Health Physics and Diagnostic Sciences, University of Nevada,
Las Vegas, NV 89154-3037, USA

S.J. Madsen (ed.), *Optical Methods and Instrumentation in Brain Imaging and Therapy*, Bioanalysis: Advanced Materials, Methods, and Devices 3,
DOI 10.1007/978-1-4614-4978-2_9,

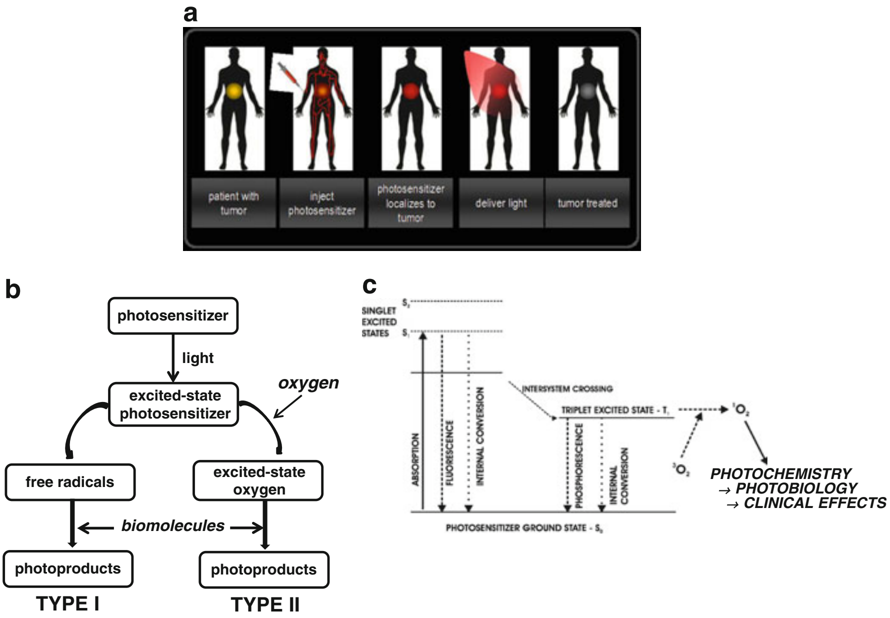

Fig. 9.1 (**a**) Schematic of the steps involved in photodynamic therapy (PDT) treatment, (**b**) Type I and II processes, (**c**) Simplified energy-level diagram for Type II activation

in progress and at different phases of development [1, 3]. These include PDT treatment of brain tumors, particularly malignant gliomas, which is the main focus of this chapter. In non-oncologic applications, about a decade ago PDT became the treatment-of-choice for the management of patients with wet-form age-related macular degeneration (AMD) and over two million patients have been treated worldwide. In this case, the objective is to shut down the abnormal choroidal neovasculature that is a leading cause of blindness in the elderly. For this, the so-called drug-light interval, i.e., the time between administering the photosensitizer (by intravenous injection) and administering the activating light, is short (~15 min), so that the photodynamic action is at the level of the vascular endothelial cells, leading to thrombotic occlusion. Other approved treatments include benign dermatological conditions and, most recently, treatment of localized bacterial infections such as periodontal disease, exploiting the ability of PDT with appropriate photosensitizers to kill even multidrug-resistant microorganisms. Other applications that have been explored include prevention of arterial restenosis following angioplasty, treatment of rheumatoid arthritis, and reduction of tumor cell burden in autologous bone marrow transplantation. Thus, PDT is, in principle, a highly versatile approach to a wide range of biomedical and clinical situations, all exploiting the same basic photophysical, photochemical, and photobiological principles. A major challenge in getting PDT adopted into widespread clinical use has been this very versatility, since it is necessary to "tailor" the treatment to be optimal for each application, in terms of the photosensitizer selection and doses and the light technologies and doses. As will be seen, this has remained a challenge for neuro applications also.

Figure 9.1b shows the two classes of photophysical process, termed Types I and II, that can take place. The latter is believed to be the most common interaction for the majority of photosensitizers that have been used clinically: unless otherwise stated, Type II interactions will be assumed throughout. The critical difference is that Type II processes require molecular oxygen to be present in the cells/tissues at adequate concentration. Figure 9.1c shows a simplified energy diagram for Type II activation.

The steps involved in Type II interactions are as follows:

1. A photon of light is absorbed by a photosensitizer molecule in its normal (ground) state, causing it to be raised to an electronically excited singlet energy state, which refers to how the spins of the valence electrons are oriented.
2. The singlet state can lose this excess energy in several different ways:
   (a) By so-called non-radiative transition back to the ground state, the result being heat generation. However, the light intensities used in PDT are usually limited in order to avoid any significant rise in the tissue temperature, so that this process has minimal biological consequences.
   (b) By emitting a longer wavelength (lower energy) photon in the form of fluorescence, with the photosensitizer again reverting to the ground state. This effect is the basis for fluorescence spectroscopy/imaging, which has developed in parallel with PDT, often in a codependent way: Chap. 8 discusses how, for example, this may be used in guiding resection of brain tumors, which (as discussed below) is synergistic with PDT.
   (c) By converting to the so-called triplet state by flipping one of the valence electron spins. This state is relatively long lived (e.g., approximately microsecond) compared with the singlet state (approximately nanosecond) and can either decay back to the ground state by emitting a photon (phosphorescence) or, most important for PDT, transferring the excess energy to ground-state molecular oxygen ($^3O_2$), raising this molecule to an excited singlet state ($^1O_2$). This singlet oxygen is highly reactive and interacts with nearby biomolecules, resulting in the biological effects such as cell kill.
3. The photosensitizer molecule returns to its ground state by one of the above routes, where it is available to undergo further excitations. Typically, during a PDT treatment each molecule goes through this cycle thousands of times, in effect acting as a catalyst to generate singlet oxygen from molecular oxygen. However, photosensitizers can also be destroyed or made inactive ("photobleached") in this process, for example, by the $^1O_2$ itself, so that, unless replenished by other molecules in the circulation, the reaction becomes self-limiting. Only rarely (~1 in 10^8 times) does the singlet oxygen decay back to its ground state, so that the photodynamic process depletes oxygen. Thus, if the rate of $^1O_2$ generation is too high, because of a combination of high photosensitizer concentration and high local light intensity (fluence rate, W cm^{-2}), it may exceed the natural

replenishment rate (related to local blood perfusion and the basal metabolic rate of the tissue) and limit the photodynamic process. This may be particularly the case in solid tumors that often have hypoxic regions. There are other complicating "dosimetry" factors, for example, the variations in tissue optical properties (see Chap. 1) can become important in delivering effective PDT treatment [4].

Singlet oxygen, because it is so highly reactive with biomolecules, is extremely short lived in cells and tissues ($\ll 1$ μs), so that it diffuses only a very short distance (tens of nanometers) from the point at which it is generated. Hence, the microlocalization of the photosensitizer is a major factor in determining which cellular structures are damaged, and thereby of the resulting mechanism(s) of cell death, namely necrosis, apoptosis, or autophagy. Since photosensitizers do not concentrate significantly in the cell nucleus unless specifically targeted, proliferative death due to DNA damage is not significant. Consequently, there is minimal mechanistic overlap with radiation therapy or most cancer chemotherapeutic drugs, so that PDT can be used prior to or following these standard modalities without contraindication. The downside is that PDT is energetically very inefficient, since it lacks the "biological amplification" conferred by damaging DNA, so that a high drug•light product is needed, which poses some practical challenges. On the other hand, the toxicity of PDT sensitizers in the absence of light ("dark toxicity") is very low compared to many chemotherapeutic agents at photodynamically effective doses.

At the tissue level, PDT induces primarily necrosis, either through direct killing of tumor or stromal cells or by causing vascular damage mediated by endothelial cell death that results in secondary tumor/stromal necrosis. In addition, PDT can induce significant immunomodulatory effects that can contribute to the tumor response, both locally and at distant (untreated) sites. This immune response has been reported in PDT of gliomas in an experimental model [5] and is associated with release of inflammatory factors.

9.2 Brain Tumors from the PDT Perspective

It is beyond the scope of this chapter to discuss the subject of brain tumors in depth, so that they will be considered only from the point of view of how PDT has been and could be used for clinical benefit. Intracranial tumors may be grouped into different categories according to whether they arise in the brain itself (primary lesions) or in other organs and then spread to the brain (metastatic lesions). Primary lesions may be genotypically and phenotypically malignant, with potential both to grow at the primary site and to spread both locally and to distant sites within or outside the brain, or they may be benign with no tendency to metastasize. Benign tumors such as meningiomas may nevertheless be life threatening, since the cranium is an enclosed space, so that continued tumor growth leads to displacement of normal brain structures and to increased intracranial pressure. Generally, these tumors are well encapsulated, which facilitates complete surgical resection, but

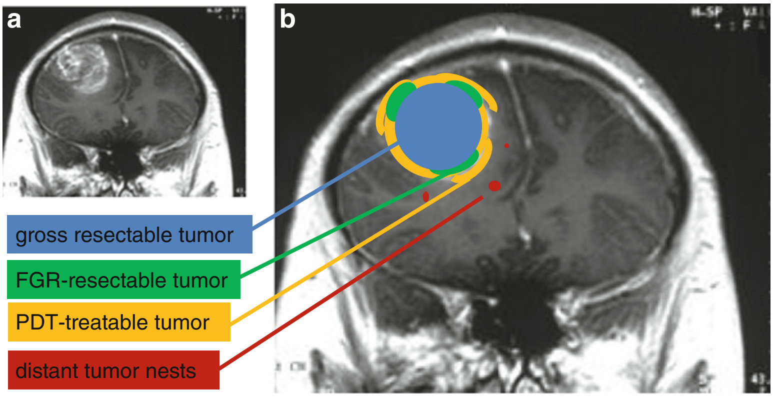

Fig. 9.2 (**a**) MR image of malignant brain tumor, (**b**) Schematic diagram of the four components into which such tumors may be grouped from a surgical, fluorescence-guided resection (FGR) and PDT perspective

this can still be challenging in some cases, for example, due to intimate attachment to normal tissues such as the dura.

The commonest forms of primary brain tumors are malignant gliomas that arise through genetic transformation of glial cells. Generally, these are very aggressive and the prognosis, even with best available treatments, is often grim, depending strongly on the stage of the tumor at diagnosis and on the patient's age and health status. Thus, for example, in the most advanced stages (glioblastoma multiforme and anaplastic astrocytoma) the standard treatment of maximal surgical resection followed by radiation therapy provides a mean survival from time of diagnosis of less than 12 months, with less than 10% of patients alive at 2 years. Adding best current chemotherapy (e.g., temozolomide) and antiangiogenic agents (e.g., bevacizumab) extends life only modestly, and most patients succumb due to local recurrence of tumor. It is in this scenario that PDT has been most investigated for its potential to extend life and/or improve the quality of life during remaining survival [6]. Typically, these tumors are locally infiltrative, with macroscopic, mesoscopic, and microscopic local invasion of normal brain tissue. There may also be distant "seeding" of tumor cells throughout large areas of the brain. These characteristics make complete destruction of the tumor, while avoiding damage to normal brain that would seriously affect neurological functions and hence the quality of life of these patients, extremely challenging.

Figure 9.2 presents a schematic view of such tumors, not from a biological perspective but rather in terms of the "components" that pose different technical challenges for which PDT and/or fluorescence image guidance may be useful.

These components are:

1. The bulk tumor that is visually distinct from the normal brain tissue and that can be successfully resected by conventional surgery (including the use of MRI or CT image guidance and the neurosurgical microscope)

2. The macroscopic tumor that is not normally visible but that can be detected using fluorescence (see below and Chap. 8) or other advanced optical imaging/ spectroscopy techniques
3. The mesoscopic/microscopic tumor tissue that is contiguous with or close to the bed of the bulk resection cavity is below the detection limit of existing intraoperative imaging techniques, and that can be selectively killed by PDT
4. Distant nests of tumor cells that may represent separate primary tumor foci and that are not currently reachable by PDT because of limited light penetration

The primary objective of PDT as used to date has been to selectively destroy tumor tissues in categories (1) and (3), immediately following surgical resection performed with or without fluorescence guidance. The key challenges in meeting this objective are:

(a) Achieving an adequate concentration of photosensitizer in the tumor cells and delivering enough light to the required tissue depth below the resection bed to cause clinically significant tumor cell kill (“sensitivity”)
(b) Achieving a high enough ratio of photosensitizer concentration in tumor compared to the adjacent regions of normal brain tissue that may also receive a significant light dose, so that collateral damage to critical normal brain structures and functions can be avoided or minimized (“specificity”)

Compared with solid tumors of other organs, successful PDT of intracranial tumors faces the additional issue of the blood–brain barrier (bbb), which is both a potential advantage and limitation. The purpose of the bbb in those normal brain structures possessing this feature (which include the white matter and cortex wherein most gliomas arise) is to serve as a barrier to “foreign” molecules and pathogens. In general tumors, including those in the brain, develop a “leaky” neovasculature as they grow, so that exogeneous drugs such as photosensitizers can be delivered to them, at least until they grow large enough to become locally hypoxic. This difference in vascularity should give a degree of intrinsic specificity, and indeed this has been observed for a number of different photosensitizers, which are mainly large molecules. However, an intact bbb means that photosensitizers cannot easily pass through the tight junctions between vascular endothelial cells in the normal blood vessels. The result is that, even though the volume-average photosensitizer concentration in normal brain tissue may be very small, the normal tissue can be exquisitely sensitive to microvascular damage, leading to edema and possibly ischemic necrosis [7]. Hence, there is a very narrow therapeutic window for PDT, and several different strategies have been directed to widen this, as discussed in Sect. 9.4.

9.2.1 Technical Aspects of Intracranial PDT

This section discusses the technical details of PDT treatment delivery, considering both the photosensitizers and the optical technologies for light generation and intracranial delivery. Many of these features are shared with PDT for other sites and pathologies, but there are also some unique aspects that will be indicated. The focus in this section will be on approaches used to date in clinical trials: other, sometimes more radical, strategies that are still at the preclinical research stage will be covered in Sect. 9.4.

9.2.1.1 Photosensitizers

To date, the majority of PDT studies, both clinically and preclinically, have used porphyrin-like photosensitizers. Porphyrins are a ubiquitous class of biomolecules (molecular weight of monomers ~600) that are synthesized by many cells and perform essential functions, including biosynthesis of hemoglobin, the oxygen-carrying molecule in blood. They are formed of large flat tetrapyrrol rings (see Table 9.1), with different side chains that are largely responsible for their different biochemical and pharmacological properties. In general, exogenously administered porphyrins accumulate in membrane structures in cells: initially in the plasma membrane and then at later times in mitochondria and other intracellular membranous organelles. Not all porphyrins are photodynamically active or fluorescent: for example the presence of a central metal atom may quench the photophysical pathways.

Following early observations of one of these molecules, hematoporphyrin (HP), and clinical tests in various tumor types, the first photosensitizer used in the modern era of PDT was a derivative, HpD (and its purified commercial versions, of which Photofrin® has been the most widely employed). HpD has been used in many of the brain tumor studies, including the most advanced clinical trials, as discussed in Sect. 9.3. HpD is derived from blood, rather than being chemically synthesized de novo like most other PDT photosensitizers, and so is a complex mix of many different porphyrin compounds of differing fluorescence and photosensitizing efficiencies. Typically, the volume-average maximum tumor-to-normal brain uptake ratio is about 10:1 (which is high compared with other tumor sites). However, the very high intrinsic sensitivity of normal brain to HpD-mediated PDT, due to microvascular damage, limits the photosensitizer and light doses that can be used in order to avoid the risk of collateral damage around the treatment site. HpD can be activated across the visible light spectrum but commonly red light at the longest-wavelength peak around 630 nm is used, since this has higher tissue penetration in tumor and normal brain (see Chap. 1). Typically, the drug-light time interval (DTI) between intravenously administering Photofrin and starting light irradiation is 24–48 h. Treatment causes primarily avascular necrosis of the tissue receiving a high enough drug•light product. A drawback of HpD is that it accumulates and is retained for several weeks in the skin, so that care must be taken to avoid bright light exposure for up to 1–2 months.

Several so-called second-generation synthetic photosensitizers have been investigated for intracranial PDT, as summarized in Table 9.1, some of which have been commercialized and formulated as pharmaceutical compounds. As in other applications, several are variations on the porphyrin theme, with different

Table 9.1 Representative photosensitizers and findings for brain tumor PDT (post 2000)

	Hematoporphyrin derivative, HpD (Photofrin$^{\circledR}$)	Aminolevulinic acid-induced protoporphyrin IX, ALA-PpIX	mTHPC (Foscan$^{\circledR}$)	Hypericin	Other
Preclinical	Damage to edematous tissue depends on laser dose, drug dose, and time point of irradiation [8]	Feasible to deliver photosensitizer and light over extended time period (mPDT) [11]	Intratumoral and systemic drug administrations are both effective [18]	PDT effective for small tumor nodules [19]	HPPH-PDT prolongs survival in rat gliomas [20]
	PDT enhances the efficacy of surgical resection of malignant gliomas [9]	Feasible to combine mPDT and FGR [12]			Apoptosis and necrosis observed in tumors following PC-4 PDT [21]
	Subclinical PDT promotes glioma growth [10]	Low fluence rates prolong survival of glioma-bearing animals [13]			PDT using SIM01 prolongs survival in C6 rat gliomas [22]
		PDT fails to eradicate implanted glioma cells, suggesting that ALA does not cross the blood–brain barrier (bbb) [14]			
		PDT-induced edema observed [15, 16] and bbb damage is light dose dependent [17]			
Clinical	Dose-dependent increase in survival in high-grade glioma [23, 24]	PDT and 3D treatment planning is feasible and safe in glioma patients [29]	Survival increases in high-grade glioma following FGR and PDT [30]		BOPP-PDT in high-grade glioma results in equivalent survival as standard treatment [31]

	ALA FGR and Photofrin PDT improve survival in GBM patients [25, 26] ALA FGR and Photofrin PDT improve survival in metastatic brain cancers [27, 28]		BPD-PDT safe in recurrent high-grade glioma [32]
Examples of molecular structures	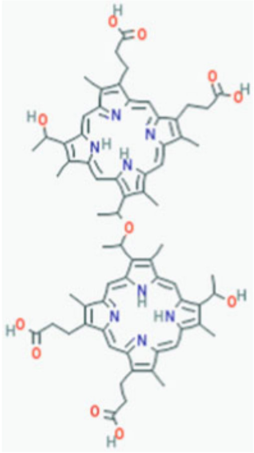	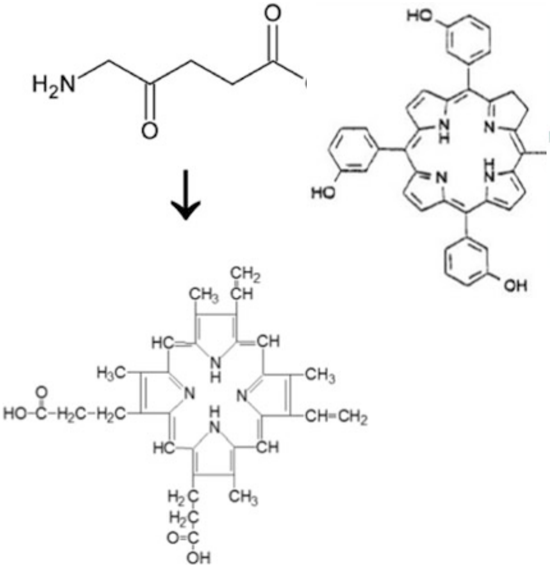	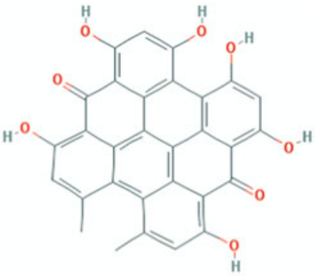

degrees of tumor selectivity and photodynamic efficacy. In some cases, the molecule has superior pharmacokinetic properties compared to HpD, for example, better water solubility or faster clearance from normal tissues, including skin. In other cases, longer wavelength activation confers somewhat deeper tissue penetration of the activating light, while other molecules such as mTHPC (activated at 652 nm) require a much lower drug•light product. Overall, however, none of these photosensitizers has shown remarkable advantages over HpD in terms of tumor-to-normal brain specificity, so that their selection depends on these other secondary properties, which nevertheless may be important from a practical perspective.

The "outlier" agent in brain-tumor PDT, as in several other applications, is the molecule aminolevulinic acid (5-ALA). This small molecule (molecular weight = 131) is not itself photoactive but, when administered locally or systemically, it is taken up by cells where it leads to increased heme biosynthesis: from an engineering perspective, ALA serves as a key feedback control in this complex multistep process. The penultimate step in this chain is the molecule protoporphyrin IX (PpIX), which is both fluorescent and photodynamically active (maximum wavelength of activation ~630 nm). The ability of ALA to penetrate the intact bbb has not been established unequivocally [14]. Hence, its tumor selectivity relies (also) on the tumor cells either synthesizing or accumulating more PpIX than normal brain cells, and this has been confirmed by ex vivo fluorescence spectroscopy and microscopy [33]. Several factors may be involved in this selectivity, including the high metabolic rate of tumor cells, and the relative lack of iron and the enzyme ferrochelatase in tumors: the latter means that the final step where an iron atom is inserted into the PpIX tetrapyrrole ring to convert it to the heme molecule is rate limited, so that PpIX differentially accumulates in these cells. Whatever the mechanism(s), the relative concentration of ALA in tumor compared to normal brain is very high: typically ~90:1 in white matter and >20:1 in cortex [33, 34]. Hence, there is a high intrinsic specificity in areas of the brain where most adult gliomas arise, which is greatly advantageous. (Note, however, that ALA-PpIX levels can also be high in areas of inflammation, due to either tumor or infection.) The level of PpIX in normal skin is also low, so that skin photosensitivity is much less of an issue than with Photofrin and even some second-generation agents such as mTHPC. The main limitation of ALA-PpIX is that PpIX is very photolabile, i.e., it is easily photobleached, which restricts the maximum effective drug•light product that can be achieved and, in turn, this limits the degree of tumor cell kill, especially in targeting bulk tumor.

9.2.1.2 Light Technologies

In other applications of PDT, there are three different classes of clinically useful light source, namely lasers, light emitting diodes (LEDs), and spectrally filtered lamps, and their advantages and limitations for different PDT applications have been discussed in detail elsewhere [4, 35]. For intracranial PDT the need to bring the light deeply into the brain is most commonly accomplished using optical fibers,

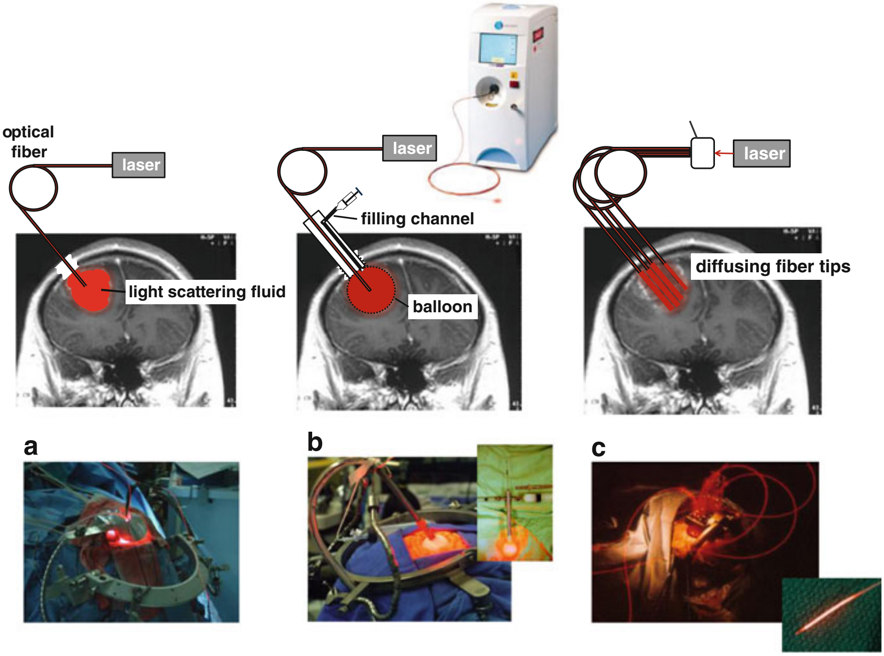

Fig. 9.3 Irradiation geometries for intracranial PDT. (**a**) Intracavitary treatment with an optical fiber placed within the scattering fluid-filled resection cavity following surgery and a reflective cover placed over the craniotomy, (**b**) as for (**a**) but with a balloon applicator filled with a light scattering fluid: the *insets* show a typical PDT laser and balloon applicator, (**c**) interstitial PDT pre-resection, showing multiple linear-diffuser fibers placed within the tumor mass: the *inset* shows one such diffusing fiber tip

for which the best light source is a laser, because of the high efficiency (>95%) with which the output can be coupled into single (multimode) fibers that typically have core diameters of 200–400 μm.

Intracavitary Irradiation

Most PDT clinical trials for gliomas have involved delivering treatment immediately following maximal surgical resection, with the objective of further reducing the residual tumor burden: the fact that residual tumor is present in virtually all high-grade glioma patients is evidenced by the extremely high local recurrence rates. The intent then is to irradiate the whole resection cavity as uniformly as possible and two main approaches have been used to achieve this, as illustrated in Fig. 9.3a, b.

In the first approach [36], the cavity is filled with a liquid, usually a 1 or 2% concentration of Intralipid® (or equivalent), which is a lipid-protein suspension routinely used for intravenous nutrition. This has micron-sized lipid droplets that efficiently scatter the light. By placing the distal end of the laser-coupled optical fiber into the cavity near its center, a uniform diffuse light distribution is generated. The primary light "dose" is then calculated from the total delivered light energy divided by the cavity surface area, assuming negligible absorption in the Intralipid. Care must be taken to ensure that there is no leakage of blood into the cavity during PDT irradiation, since this acts as an extremely efficient light attenuator, given the large optical pathlength of the multiply-scattered light. The simplest way to ensure this is by periodically flushing the cavity with fresh Intralipid. The second approach [37], first developed in 1986 [38], is to place an elastic balloon into the cavity and to fill this with Intralipid to the size of the cavity. This has the advantage of preventing the cavity from collapsing during irradiation and, since the shape is nearly spherical, the surface dose is better defined. The optical fiber is then brought close to the center of the volume through a channel in the applicator that holds the balloon. It has proven to be simplest to use the finger cut from a surgical glove as the balloon material, held by a pressure ring placed over it onto the applicator stem. A potential disadvantage of the balloon technique is that there is risk of pressure on the tissue due to the balloon, which could limit blood flow and, hence, tissue oxygenation, although this has never been explicitly demonstrated.

A variation on the balloon approach has been to replace the laser and optical fiber with a high-power LED source that is integrated into the end of the applicator [39]. This has the advantage of considerably lower cost than a high-power diode laser, but presents the problem of removing the heat generated in the LEDs, which are typically only about 10% efficient in electrical-to-optical conversion. To some extent the Intralipid scattering volume acts as a heat sink.

As indicated earlier, the total light energy required in PDT is large: for example, in irradiating the tumor resection cavity tissue surface, the incident energy density is typically up to several hundred Joules per square centimeter in order to deliver an adequate drug•light product. (Note that the necrotic response of tissues to PDT generally displays a threshold-type behavior, where there is a sharp demarcation between tissues receiving an adequate dose and the adjacent tissue that receives just below this dose. Hence, complete tumor destruction is highly dependent on achieving an above-threshold dose throughout the entire volume.) Thus, for example, with a 5 cm diameter resection cavity (~75 cm^2 surface area), a total energy of a few thousand Joules is needed. This has several implications. Firstly, since the surface intensity must be limited to less than about 200 mW cm^{-2} in order to avoid light-induced tissue heating, the irradiation time is at least tens of minutes. Secondly, the laser output should ideally be at least 5 W in order to keep the treatment time within an acceptable range, given that the treatment is delivered intraoperatively following surgery that may itself take several hours. Thirdly, since the wavelength must match the selected wavelength peak of the photosensitizer activation spectrum (typically in the range 630–760 nm), this high power requirement limits the types of laser that are commercially available and suitable for use in a clinical, especially operating room environment. It also has significant cost impact. The history of PDT lasers over the past 30 years has seen progression from the original argon ion-pumped dye lasers, metal vapor lasers, and frequency-doubled Nd:YAG (KTP)-pumped dye lasers to the diode lasers used currently, as in the example shown in Fig. 9.3b.

Interstitial Irradiation

Optical fibers may be placed directly into tissue to deliver the light to a local volume. For a standard cut-end fiber, this generates a nearly spherical light distribution because of the high intrinsic scattering of tissue. In this case the fluence rate (W cm^{-2}) falls off very rapidly with distance, r, from the fiber tip, approximately as $(1/r)\exp(-\mu_{\mathrm{eff}}r)$, where μ_{eff} is the effective optical attenuation coefficient of the tissue, which depends on both the absorption and scattering coefficients at the treatment wavelength [4]. In the 630–760 nm range, μ_{eff} is typically ~3–10 cm^{-1} in tumor tissue and is even higher in normal brain (see Chap. 1), so that the local fluence rate drops tenfold for every few mm of radial depth. The resulting diameter of treatment is reported as typically 1–2 cm, depending on the photosensitizer and target tissue. This single cut-end fiber approach has been used intracranially, for example, in destroying small metastatic lesions [27, 28].

Larger treatment volumes—*in principle arbitrarily large*—can be achieved by placing multiple fibers into the tissue at a suitable interfiber spacing, as has been reported for example in PDT treatment of prostate cancer to cover the whole gland (typically 6–8 fibers, each of several cm length to destroy 20–50 g of tissue in total) [40]. In practice, this requires either sequential activation of each fiber, with resulting long treatment times, or the use of beam splitters with a single laser or multiple lasers to deliver light simultaneously through several fibers. More efficient coverage of large tissue volumes can be achieved using fibers that emit light radially along the last few cm near the tip (see Fig. 9.3c), thereby generating a cylindrical volume of effective treatment from each fiber. Again, these fibers have been used commonly in other solid tumor applications and also to illuminate along the length of hollow organs such as the esophagus, bile duct or bronchus, or within arteries. This approach has been used in the past in glioma treatments [41], in which HpD-PDT was administered to the bulk tumor volume, including a margin of normal or mixed tumor-normal tissues, prior to surgical resection. The rationale was that this allowed more accurate geometric targeting of PDT to the tumor mass, based on pretreatment MRI or CT imaging.

Interstitial PDT is also possible using a linear array of small LED sources embedded within a flexible catheter [42] and again this has the advantage of being relatively inexpensive compared to the use of a diode laser source plus diffusing fibers. The limitation is that, because of the need to avoid overheating around the source, the optical power needs to be kept low, so that, in the absence of active cooling of the source (which adds complexity and makes it difficult to keep the catheter to a small diameter), prolonged treatment times are required in order to deliver the effective light dose. Currently, clinical trials (for tumors in other organs) use 20 mW cm^{-1} length and treatment times in excess of 1 h. On the other hand, very low dose-rate (or "metronomic") PDT may have specific biological advantages, particularly in the brain: see Sect. 9.4.2.

9.2.1.3 Connection to Fluorescence-Guided Surgery

Given the intrinsic fluorescent properties of many photosensitizers, and the historical development of the first-generation agent HpD, there have always been strong developmental and application linkages between PDT and fluorescence-based diagnostics, sometimes termed PDD [43]. In particular, fluorescence spectroscopy is a standard and very sensitive technique for measuring the concentration of photosensitizers in cells and tissues [44], while fluorescence microscopy is often used to determine their microdistribution [33, 45]. Clinically, in vivo fluorescence point spectroscopy and imaging with photosensitizers have been developed as diagnostic techniques, particularly for detection of early neoplastic lesions [46]. This has been particularly applied in the skin and in endoscopy of different hollow organs (bronchus, gastrointestinal tract, bladder, cervix), because of the importance of these as sites for cancer initiation and progression. ALA-PpIX has been particularly used for this purpose because of its high intrinsic specificity for malignant tissue, its low skin photosensitization and the fact that it may be administered either orally or topically (e.g., instilled in the bladder at the time of cystoscopic examination). In the context of PDT, in vivo fluorescence has been used to localize lesions for targeting the treatment light, to assess the uptake of photoactive drug in the target tissues and, through the phenomenon of photobleaching, to monitor the delivery and distribution of the treatment dose [43, 47].

The concept of using fluorescence of photosensitizers to guide surgical resection of tumors also has a long history and is predicated on there being a degree of selectivity between tumor-involved and adjacent tumor-free tissue. In the brain, it was first explored in 1991 in a preclinical glioma model in rats using a phthalocyanine photosensitizer, and was shown to give significant improvement in completeness of resection [48]. Similar findings were reported with Photofrin, and the first clinical studies were done in the late 1990s, using a stand-alone instrument designed specifically for this application, with a long working distance to allow good surgical access. This system used dual-wavelength excitation to correct for the attenuation of the light in the tissues and to subtract the background intrinsic (auto) fluorescence from the tissue [49].

An alternative technology approach, in which fluorescence imaging was integrated into a neurosurgical microscope, was evaluated using ALA-PpIX contrast in multicenter clinical trials of glioma. This demonstrated significant increase in tumor-free survival of patients with high-grade disease compared to surgery using only the standard white-light microscope [50]. Development continues along several lines in multiple groups worldwide, including exploration of alternative fluorophores, the use of time-resolved tissue autofluorescence, methods to make truly quantitative measurement of fluorophore concentration in tissues in vivo [51], and approaches to subsurface fluorescence imaging [52]. Chapter 8 addresses this topic more fully.

Referring again to Fig. 9.2, fluorescence guidance extends the completeness of surgical resection but does not remove all tumor, even locally, as evidenced by the continuing high recurrence rates, despite improved survival. If, however, this is followed by PDT (using either the same photosensitizer or a second agent), then it should be possible to reduce the residual tumor burden by another substantial fraction. As discussed below, initial clinical trials of this combined approach have been reported and one would expect this to be developed further, given the significant, albeit still subcurative, responses seen when either technique is used alone.

9.3 Clinical Studies

There are excellent recent reviews of the development and status of clinical trials of PDT of malignant glioma and other intracranial tumors, as well as the combination of PDT with fluorescence-guided tumor resection [6, 53], so we will not repeat these in detail here. During the 1990s and early 2000s the main effort was focused on HpD-PDT in high-grade gliomas, administered to the resection cavity bed immediately following maximum conventional tumor resection, using the intracavitary approaches described above (Fig. 9.3a, b). In all cases, patients were also given standard postsurgical radiation treatment and chemotherapy: the latter changed during this period, somewhat confounding the interpretation of the PDT responses. The photosensitizer doses were based largely on the limiting skin photosensitivity, and typically fixed at either 5 or 2 mg kg^{-1} body weight, depending on whether HpD itself or the purified commercial version Photofrin®, respectively, was used. In the 1980s and 1990s a handful of phase I and II trials in some 300+ patients demonstrated a significant improvement in mean survival of up to about 1 year compared with standard therapies (surgery + radiation + chemotherapy). It should be emphasized that these trials did not include prospective randomization of patients, but rather compared the results with historical controls. Nevertheless, an important observation was made was that survival post treatment appeared longer in patients receiving more than the median light dose (80 J cm^{-2}) than in those receiving less than this dose. This led to an FDA-registered prospective, multicenter, randomized phase III trial comparing 120 J cm^{-2} vs. 40 J cm^{-2} in recurrent tumors and 120 J cm^{-2} vs. no PDT in primary tumors. This study was terminated at interim analysis because no statistically significant differences in overall survival were detected. This contrasted with the positive findings of another cohort of several hundred patients treated in a single-center, non-randomized trial in Melbourne, Australia [24], in which the survival was markedly increased, but in which much higher doses, of up to 260 J cm^{-2}, were used. The 120 J cm^{-2} dose limit in the randomized trial was set by concern for PDT-induced edema and resulting increased intracranial pressure, which had been seen in earlier clinical studies [37] and also investigated in preclinical in vivo glioma models [15, 16]. However, the Melbourne study demonstrated that escalated postoperative administration of steroids controlled this problem satisfactorily, even for very high light doses. Clearly then, a prospectively randomized trial of intracavitary HpD-PDT is needed, with doses of at least 200 J cm^{-2} in order to validate this treatment option for high-grade glioma patients.

Phase I/II studies of PDT for glioma have also been reported with the photosensitizer mTHPC [30]: this is a very potent sensitizer that requires typically tenfold less drug dose than HpD. However, like Photofrin, it causes prolonged skin photosensitization and, to date, the clinical studies have not been extensive enough to know if it provides a significant advantage over HpD for glioma treatments, in terms of either improved tumor destruction or tumor-to-normal brain selectivity. The possibility of administering the photosensitizer directly into the tumor tissue has been explored with mTHPC, in order to limit the skin sensitization and, potentially, increase the effective drug dose in the target tissue.

In the above trials, PDT has been given simply as an adjuvant following standard surgical resection. More recently, groups in Europe have combined ALA-PpIX-based fluorescence-guided resection with PDT. Thus, Eljamel and colleagues found increased survival (52.8 weeks) relative to controls (24.6 weeks) in high-grade glioma patients receiving ALA-PpIX fluorescence-guided resection followed by repetitive Photofrin-PDT [54]. Patients in both groups had surgical debulking of tumor using standard techniques and all received postoperative radiation therapy, so that the study and control groups were comparable. Kostron et al. [30] reported increased survival (9 months) in recurrent malignant glioma patients receiving mTHpc-based FGR + PDT relative to matched controls (3.5 months). These are all encouraging early results. If the model posited in Fig. 9.2 is correct, then the additional reduction of the residual tumor provided by fluorescence guidance means that the subsequent application of PDT treatment should be more effective in reducing the burden of disease. This should translate into improved survival and, although not likely to be curative in high-grade glioma, would afford other biological approaches such as chemotherapy, gene therapy, or immunotherapy a better chance of complete tumor eradication.

As far as other intracranial uses of PDT are concerned, there have only been a few studies reported to date, with limited numbers of patients. These include ALA PpIX-based FGR and Photofrin-PDT in patients with metastatic brain tumors [27, 28], for which the early results suggest that PDT is effective in tumor destruction, so that this could represent a potentially viable minimally invasive approach, even for deep-seated tumors.

9.4 Emerging Techniques for Intracranial PDT

The major unsolved challenges in intracranial PDT, especially for gliomas, revolve around the need to achieve a higher level of tumor cell kill in deeper-lying areas of invasion and a greater degree of tumor-to-normal specificity so that more aggressive treatment, i.e., a higher drug•light product, can be administered safely to achieve a greater degree of tumor control. Increasing the specificity is not, however, simply restricted to increasing the concentration of photosensitizer in tumor vs.

normal cells. Other potential strategies involve manipulating the microlocalization of the photosensitizer and selecting for apoptotic tumor cell death in order to minimize secondary damage to normal brain. These approaches may also require development of novel light sources and delivery systems as well as on-line dose and treatment-response monitoring. Other strategies that have been investigated in preclinical glioma models are ways either to increase the antitumor effect or to reduce the potential damage to normal brain, and there are also emerging concepts to use PDT as a means to facilitate delivery of other antitumor agents in the brain.

9.4.1 Alternative Photosensitizers

As mentioned in the Introduction, a variety of photosensitizers have been explored for PDT of brain tumors in preclinical models in vitro and in vivo. Examples are given in Table 9.1, in which "conventional" PDT protocols have been used. In general, with the exception of ALA-PpIX, none has shown remarkably better specificity or efficacy than HpD, although individually they have other secondary advantages. As in other PDT applications, longer wavelengths are useful to increase the effective light penetration and, hence, the treatment depth for a given administered dose. However, the increased penetration depth is modest beyond about 650 nm in the case of brain, unlike more pigmented tissues (see Chap. 1). Unlike other PDT applications, little work has been done to date to explore options for targeted delivery of photosensitizers to brain tumors, such as the use of antibodies or nanoparticles [55, 56]. The issue of how the bbb will affect such delivery schemes will need to be addressed.

9.4.2 Low Dose-Rate/Metronomic PDT

There have been a number of studies in a variety of tumor models in which the photosensitizer and/or light are delivered at very low dose rates in order to achieve antitumor specificity through the different photobiological mechanism(s) that are selected. This has been termed "metronomic," mPDT [57], and must be distinguished from treatments in which the light dose rate is somewhat reduced—by perhaps a factor of 2 or 3—in order to avoid photochemical depletion of the tissue oxygenation that limits the effective PDT dose delivered [4, 58]. Metronomic PDT using ALA has been shown capable of producing (glioma) tumor cell killing through apoptosis (i.e., programmed cell death) without inducing any measurable damage to normal brain: this is illustrated in Fig. 9.4a, using a special stain for apoptosis. Furthermore, there was no necrotic cell death seens even in the tumor. This was an unexpected finding; its importance lies in the fact that necrotic cell death triggers an inflammatory response, which may result in further, secondary damage to normal brain. Subsequent in vitro studies [59] showed that specific genetic pathways are affected in mPDT compared with standard high dose-rate treatments, even with the same photosensitizer. It is not known whether these metronomic effects also occur with other photosensitizers of if they are unique to ALA-PpIX. A second rationale for mPDT is that single high dose-rate PDT treatments probably will not be able to deliver a tumoricidal dose beyond about 2 cm with current photosensitizers, due to inability to get a high enough light dose at depth in a clinically acceptable treatment time, especially when PDT is given intraoperatively to the surface of the surgical resection bed. However, delivering the light over a much longer period (hours, days, or even weeks) relaxes this constraint.

Madsen and colleagues have explored the low dose-rate PDT regime in detail in vitro, using multicell glioma spheroids in which several thousand tumor cells grow as a sub-millimeter diameter sphere. These cell aggregates have some of the characteristics of solid tumors, in particular oxygen, nutrient, and photosensitizer gradients that can affect the PDT response. Specifically, enhanced efficacy of ALA-PDT at ≤ 10 mW cm^{-2} was shown in human glioma spheroids, and repetitive low fluence rate treatments gave much higher tumor cell kill than single treatments, as illustrated in Fig. 9.4b [60].

ALA and light have also been administered in intracranial glioma models in vivo at very low dose rates [14, 61] and also demonstrated that mPDT is technically feasible, safe, and can provide a degree of tumor control, as illustrated in Fig. 9.4c, where the tumor cells were transfected with the luciferase (firefly) gene that allows noninvasive tracking of the tumor growth and treatment response over time. Typically, 100 mg kg^{-1} body weight day^{-1} of ALA and 0.5–2 μW of light (total energy of ~200 J) were administered over several days in these studies. These should be compared to the standard acute "high dose" regime of a single dose of 20–100 mg kg^{-1} of ALA, and 100 mW (100 J) of light. A particular advantage of ALA for mPDT is that it can be taken orally, which simplifies long-term delivery. It is seen in this particular response data that it is not the total amount of light that matters, so much as the rate at which it is given, since all three treatments (0.5 mW for 4 days, 1 mW for 2 days, 2 mW for 1 day) have the same total energy (86.4 J), but only the lowest dose rate for the extended period to killed the tumor cells at a rate that equaled or exceeded their proliferation rate.

Collectively, the photobiological findings to date provide a compelling rationale to investigate mPDT to treat high-grade gliomas in patients. True mPDT, with photosensitizer and light delivered continuously over an extended period, has not yet been reported clinically. While repetitive dosing of gliomas has been done using Photofrin-PDT following ALA-PpIX based fluorescence-guided resection in patients [54], this used high light dose rates and, as noted above, it is not known if ALA is the only agent that can achieve tumor cell-specific apoptosis at low dose rate.

Certainly, the continuous synthesis of PpIX through continuous or frequent low dose ALA administration means that the PpIX is likely to be activated when it is still in the mitochondria (the site of heme biosynthesis) and mitochondrial membrane damage is known to be the primary mechanism of PDT-induced apoptosis [1, 59].

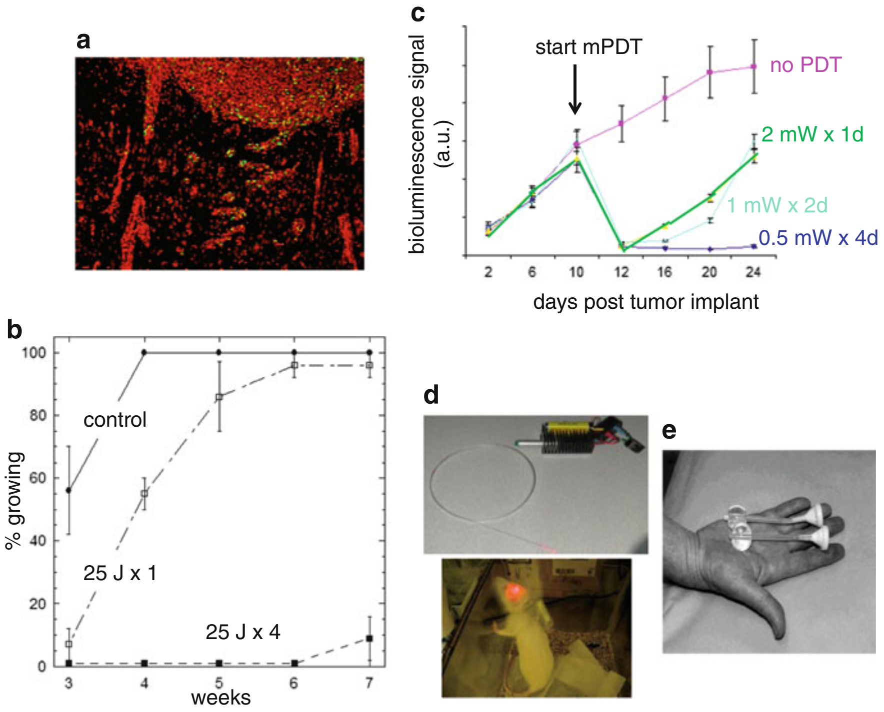

Fig. 9.4 Examples of low dose-rate/metronomic PDT. (**a**) Fluorescence microscopy of glioma and normal brain tissue in an intracranial rat tumor model following mPDT, showing apoptotic cells (*green*, TUNEL stain) confined to areas of tumor (*red*) [57], (**b**) in vitro ALA-PDT responses in glioma spheroids showing suppression of spheroid growth following single low dose-rate (2.5 mW cm^{-2}) treatment or repetitive treatments (at weeks 0, 1, 2, and 3) [60], (**c**) in vivo mPDT responses in an intracranial tumor model in rats [61] with the viable tumor monitored using bioluminescence, (**d**) tether-less "backpack" light source for mPDT developed for use in such preclinical models [62], (**e**) balloon applicators for extended light delivery to the surgical resection cavity: these would be fiber-optic coupled to a laser similar to the applicator in Fig. 9.3b but would be left in place following closure of the surgical wound [63]

The technical questions that need to be addressed in applying mPDT clinically are (a) can the ALA and light be administered such that rate of tumor cell death exceeds the proliferation rate but still remain below the threshold for tumor cell necrosis? and (b) how can the light be administered over a period of days or more? The limited preclinical studies to date are encouraging with respect to the first issue (see Fig. 9.4c). The same preclinical studies also showed that it is possible to implant and immobilize optical fibers in brain tumor and have these connected to an external diode laser or LED source through a burr hole in the skull (Fig. 9.4d). The option of a balloon implant into the brain has also been demonstrated in patients for the purpose of delivering brachytherapy [63], as illustrated in Fig. 9.4e, so that this should be feasible also for PDT light delivery. Nevertheless, the light delivery remains a biomedical engineering challenge, for which the solution may depend on whether or not the tumor has been surgically resected prior to mPDT being applied, since this changes the required irradiation geometry.

9.4.3 Precision PDT Light Targeting

With standard established techniques for PDT light delivery (open-beam irradiation of an accessible tissue surface or placement of interstitial fibers), and using continuous (CW) irradiation, the light distribution is defined by the irradiation geometry and by the tissue optical properties, and generally is highly diffuse (see Chap. 1). This limits the spatial precision that can be achieved in targeting specific tissue structures. One way in which the light delivery can be precisely targeted is to use 2-photon activation of the photosensitizer by an ultrashort (typically ~100 fs) near-infrared (NIR) laser pulse. The very high instantaneous intensity ($I > 10^9$ W cm^{-2}) means that there can be a significant probability of two photons being absorbed simultaneously by a photosensitizer molecule: thereafter, the photophysics and photochemistry are the same as for 1-photon PDT. However, since light is highly scattered, the intensity falls, and consequently the probability of 2-photon activation also falls, as $1/I^2$. Hence, efficient 2-photon activation only occurs within the focal spot of the laser beam. Photosensitizers can be designed to have very high 2-photon cross section and also very low 1-photon absorption at the NIR wavelength [64]. As a result, exquisite spatial confinement of the PDT effect can be achieved. This has been demonstrated both in vitro and in vivo, for example, to shut down single blood vessels [65]. The approach has not yet been explored for intracranial applications, but it could be of value, for example, in skull base tumors, in which the thin residual tumor layer could be safely ablated without damaging the underlying critical normal tissues. Specialized laser sources and optical fiber delivery would be required, as would image-guided robotic scanning in order to realize the full precision and to safely and completely scan the entire target area.

9.4.4 PDT Response Modifiers

Widening the therapeutic window for PDT remains a major challenge in general, but is particularly acute in the brain because of the functional consequences of damaging normal tissues, either through primary photodynamic killing of brain cells such as astrocytes and vascular endothelial cells (causing vascular shutdown), or by inducing an inflammatory response that results in secondary neuronal damage. Thus, either the responsivity of the tumor component needs to be enhanced and/or the brain adjacent to tumor (i.e., unavoidably exposed to the PDT light in order to destroy infiltrating tumor) needs to be protected. The former is in common with PDT for any tumor target, while the latter is highly specific to brain. One example of recent work in the neuroprotection is the use of a statin (Atorvastatin) that has been shown to reduce the functional deficits following stroke, intracranial hemorrhage, or traumatic injury. When given after Photofrin-PDT, this drug induced new blood vessel and synapse formation in damaged brain and promoted functional restoration [66].

9.4.5 Other Potential Intracranial Uses of PDT

Here, we will first mention two ideas to use sublethal PDT to enhance the delivery of other therapeutic agents in brain tumors. The first is based on the facts that the intact bbb limits the delivery of any therapeutic agent but that the normal brain may be exquisitely sensitive to PDT through damage to the vascular endothelial cells, arising also because the intact bbb prevents transport of exogenous agents. Hence, Hirschberg et al. [17] have proposed and demonstrated in a preclinical model that ALA-PDT at an appropriate low dose can cause transient opening of the bbb in a focal region defined by the light delivery· The bbb was found to be disrupted 2 h following PDT and was 80–100% restored 72 h later, with no long-term damage evident on histology. Enhanced delivery of the drug bleomycin, following PDT-induced disruption of the bbb, was demonstrated in a preclinical model.

The second approach is that of photochemical internalization (PCI), which is discussed fully in Chap. 11. Briefly, this is a novel approach in which photosensitizers are used to improve the therapeutic efficacy of macromolecules that accumulate in endocytic vesicles [67]. The concept is to localize the sensitizer and the macromolecule in vesicles of target cells, such as infiltrating glioma cells, followed by light excitation. This results in release of the endocytically bound macromolecules into the cytosol, with subsequent therapeutic impact. In this case, the rapid attenuation of light in the brain is an advantage, since restricting the macromolecule release to the vicinity of the light irradiation should limit any side effects to adjacent nontarget brain tissue. PCI requires the use of photosensitizers that localize in the plasma membrane and the most efficient photosensitizers for this purpose, such as disulfonated phthalocyanine ($AlPcS_{2a}$), are those that have an amphiphilic structure with a hydrophilic moiety that inhibits penetration through cell membranes.

The efficacy of PCI-mediated delivery of a chemotherapeutic agent (bleomycin) was recently demonstrated in vitro in F98 rat glioma monolayers and human glioma spheroids [68]. Treatment resulted in significant cell kill in both models using very low light dose (1.5 J cm^{-2}) and bleomycin concentration (0.25 μg mL^{-1}), with minimal toxicity from either treatment alone. This suggests that PCI could be a viable technique for enhancing the efficacy of drugs that have previously shown to be ineffective in the treatment of high-grade gliomas.

The use of PCI to enhance gene delivery represents another potential application for intracranial PDT. Specifically in glioma cells in vitro, $AlPcS_{2a}$-PDT has been shown to increase delivery of tumor suppressor genes (e.g., PAX-6, PTEN) [69] by a factor of 5–10 compared to controls. If this is translatable in vivo and to the clinic, it could prove valuable to accelerate the use of gene therapies in brain tumor control: one might then envisage this being used after cytotoxic PDT in order to "mop up" remaining tumor cells, both around the PDT treatment site and remote from it.

Finally, there has been a recent resurgence of interest in photochemical bonding of tissues, in which a photoactivatable dye is placed on the opposing tissue surfaces and light is applied locally [70]. This causes photochemical cross-linking of collagen, the main structural protein in tissues, resulting in immediate, mechanically strong and leak-free joining of tissue structures, with excellent healing and low fibrosis. Currently, this approach has focused mainly on the photosensitizer Rose Bengal, which is activated by green light and most likely operates predominantly through Type I photophysics. Successful, suture-less bonding has been demonstrated in a number of different tissues and for several distinct applications: general surgery, joining of severed nerves, joining of blood vessels, and corneal surgery. For some applications, e.g., joining blood vessels, the tissues may be wrapped in a dye-loaded membrane (commonly human amniotic membrane) to aid in alignment and stabilization before the light is applied. Clearly, these methods could be of value in neurosurgical applications where speed, precision, surgical wound integrity, and complication-free healing are paramount. Development of photosensitizer and light delivery tools for these specific applications that optimize the "geometry" of the bonding will pose interesting biophysical/bioengineering challenges.

9.5 Summary and Conclusions

The principle of PDT is the use of energy-activated molecules, in which each component alone has no effect but when combined can be used for targeted, mechanism-selective cell/tissue destruction or modification. This concept remains compelling and has led to exploration of a remarkable variety of potential clinical applications across many medical specialties. Some of these have already come to fruition, with substantial clinical and commercial impact, despite numerous false starts and, with the benefit of hindsight, strategic mistakes that have to date limited its adoption into widespread medical practice. Overall, progress in the development and clinical evaluation/optimization of intracranial PDT of brain tumors has been slow and limited to only a few centers and trials compared to other tumor sites and to non-oncological applications. In part this is due to special challenges of photosensitizer and light delivery in the brain compared to other tumor sites. However, this PDT work has undoubtedly helped inform and drive the parallel development of fluorescence-guided tumor resection, which is now emerging rapidly, not only in neurosurgery but also in a variety of other surgical specialties. It seems likely that, conversely, FGR will now drive further development of intracranial PDT for oncologic neurosurgery.

The many ongoing developments in PDT photosensitizers, photosensitizer delivery systems, optical technologies, and photobiology will likely impact also intracranial PDT applications, through improvements in photosensitizer selectivity/targeting, light delivery and dosimetry, and biological approaches to enhanced efficacy. At the same time, advances in other neurodiagnostic and neurointerventional technologies (intraoperative imaging, robotics, gene therapies, etc.) will undoubtedly facilitate and extend the applications of PDT. Thus, for example, the increasing use of minimally invasive image-guided surgical robotics is highly compatible and synergistic with the delivery of local selective treatments such as PDT.

In summary, intracranial tumors present very difficult technical, biological, and clinical challenges for PDT and its cousin fluorescence-guided surgery. Some of the solutions will come from "mainstream" PDT research and rigorous clinical trials, while others will either come from complementary areas of PDT or be enabled by other sciences and technologies. The challenges continue to be intellectually exciting and their solution, through interdisciplinary efforts, will ultimately be important in extending survival and improving the quality of life of brain tumor patients and in advancing the field of PDT, with concomitant benefit to other clinical applications.

References

1. Hamblin M, Mroz P (eds) (2008) Advances in photodynamic therapy: basic, translational and clinical. Artech, Boston
2. Moan J, Peng Q (2003) An outline of the hundred-year history of PDT. Anticancer Res 23:3591–3600
3. Agostinis P, Berg K, Cengel KA, Foster TH, Girotti AW, Gollnick SO, Hahn SM, Hamblin MR, Juzeniene A, Kessel D, Korbelik M, Moan J, Mroz P, Nowi D, Piette J, Wilson BC, Golab J (2011) Photodynamic therapy of cancer: an update. CA Cancer J Clin 61:250–281
4. Wilson BC, Patterson MS (2008) The physics, biophysics and technology of photodynamic therapy. Phys Med Biol 53:R61–R109
5. Li F, Cheng Y, Lu J, Hu R, Wan Q, Feng H (2011) Photodynamic therapy boosts anti-glioma immunity in mice: a dependence on the activities of T cells and complement C3. J Cell Biochem 112:3035–3043
6. Eljamil S (2010) Photodynamic applications in brain tumors: a comprehensive review of the literature. Photodiagnosis Photodyn Ther 7:76–85
7. Lilge L, Olivo M, Schatz S, Maguire J, Wilson BC (1996) The sensitivity of normal brain and intracranially implanted VX2 tumour to interstitial photodynamic therapy. Br J Cancer 73:332–343
8. Goetz C, Hasan A, Stummer W, Heimann A, Kempski O (2002) Experimental research photodynamic effects in perifocal, oedematous brain tissue. Acta Neurochir (Wien) 144:173–179
9. Zhang X, Jiang F, Kalkanis SN, Yang H, Zhang Z, Katakowski M, Hong X, Chopp M (2006) Combination of surgical resection and photodynamic therapy of 9L gliosarcoma in the nude rat. Photochem Photobiol 82:1704–1711

10. deCarvalho AC, Zhang X, Roberts C, Jiang F, Kalkanis SN, Hong X, Lu M, Chopp M (2007) Subclinical photodynamic therapy treatment modifies the brain microenvironment and promotes glioma growth. Glia 55:1053–1060
11. Bisland SK, Lilge L, Lin A, Rusnov R, Wilson BC (2004) Metronomic photodynamic therapy: rationale and preclinical evaluation of technical feasibility for treating malignant brain tumors. Photochem Photobiol 80:22–30
12. Bogaards A, Varma A, Zhang K, Zach D, Bisland SK, Moriyama EH, Lilge L, Muller PJ, Wilson BC (2005) Fluorescence image-guided brain tumour resection with adjuvant metronomic photodynamic therapy: pre-clinical model and technology development. Photochem Photobiol Sci 4:438–442
13. Angell-Petersen E, Spetalen S, Madsen SJ, Sun CH, Peng Q, Carper SW, Sioud M, Hirschberg H (2006) Influence of light fluence rate on the effects of photodynamic therapy in an orthotopic rat glioma model. J Neurosurg 104:109–117
14. Madsen SJ, Angell-Petersen E, Spetalen S, Carper SW, Ziegler SA, Hirschberg H (2006) Photodynamic therapy of newly implanted glioma cells in the rat brain. Lasers Surg Med 38:540–548
15. Ito S, Rachinger W, Stepp H, Reulen HJ, Stummer W (2005) Oedema formation in experimental photo-irradiation therapy of brain tumours using 5-ALA. Acta Neurochir (Wien) 147:57–65
16. Mathews MS, Chighvinadze D, Gach HM, Uzal FA, Madsen SJ, Hirschberg H (2011) Cerebral edema following photodynamic therapy using endogenous and exogenous photosensitizers in normal brain. Lasers Surg Med 43:892–900
17. Hirschberg H, Uzal FA, Chigvinadze D, Zhang MJ, Peng Q, Madsen SJ (2008) Disruption of the blood-brain barrier following ALA-mediated photodynamic therapy. Lasers Surg Med 40:535–542
18. Mannino S, Molinari A, Sabatino G, Ciafre SA, Colone M, Maira G, Anile C, Arancia G, Mangiola A (2008) Intratumoral vs systemic administration of meta-tetrahydroxyphenylchlorin for photodynamic therapy of malignant gliomas: assessment of uptake and spatial distribution in C6 rat glioma model. Int J Immunopathol Pharmacol 21:227–231
19. Cole CD, Liu JK, Sheng X, Chin SS, Schmidt MH, Weiss MH, Couldwell WT (2008) Hypericin-mediated photodynamic therapy of pituitary tumors: preclinical study in a GH4C1 rat tumor model. J Neurooncol 87:255–261
20. Lobel J, MacDonald IJ, Ciesielski MJ, Barone T, Potter WR, Pollina J, Plunkett RJ, Fenstermaker RA, Dougherty TJ (2001) 2-[1-hexyloxyethyl]-2-devinyl pyropheophorbide-a (HPPH) in a nude rat glioma model: implications for photodynamic therapy. Lasers Surg Med 29:397–405
21. George JE III, Ahmad Y, Varghai D, Li X, Berlin J, Jackowe D, Jungermann M, Wolfe MS, Lilge L, Totonchi A, Morris RL, Peterson A, Lust WD, Kenney ME, Hoppel CL, Sun J, Oleinick NL, Dean D (2005) Pc 4 photodynamic therapy of U87-derived human glioma in the nude rat. Lasers Surg Med 36:383–389
22. Olivier D, Bourre L, El-Sabbagh E, Loussouam D, Simonneaux G, Valette F, Patrice T (2007) Photodynamic effects of SIM01, a new sensitizer, on experimental brain tumors in rats. Surg Neurol 68:255–263
23. Muller P, Wilson B, Lilge L, Yang V, Hetzel F, Chen Q, Fullager T, Fenstermaker R, Selker R, Abrams J (2001) Photofrin-photodynamic therapy for malignant brain tumors. Proc SPIE 4248:34–45
24. Stylli SS, Kaye AH, MacGregor L, Howes M, Rajendra P (2005) Photodynamic therapy of high grade glioma—long term survival. J Clin Neurosci 12:389–398
25. Eljamel MS, Goodman C, Moseley H (2008) ALA and Photofrin fluorescence-guided resection and repetitive PDT in glioblastoma multiforme: a single centre phase III randomized control trial. Lasers Med Sci 23:361–367

26. Kaneko S (2008) A current overview: photodynamic diagnosis and photodynamic therapy using 5-ALA in neurosurgery. Jpn J Soc Laser Surg Med 29:135–146
27. Zilidis G, Aziz F, Telara S, Eljamel MS (2008) Fluorescence image-guided surgery and repetitive photodynamic therapy in brain metastatic malignant melanoma. Photodiagnosis Photodyn Ther 5:264–266
28. Aziz F, Telara S, Moseley H, Goodman C, Manthri P, Eljamel MS (2009) Photodynamic therapy adjuvant to surgery in metastatic carcinoma in brain. Photodiagnosis Photodyn Ther 6:227–230
29. Beck TJ, Kreth FW, Beyer W, Mehrkens JH, Obermeier A, Stepp H, Stummer W, Baumgartner R (2007) Interstitial photodynamic therapy of nonresectable malignant glioma recurrences using 5-aminolevulinic acid induced protoporphyrin IX. Lasers Surg Med 39:386–393
30. Kostron H, Fiegele T, Akatuna E (2006) Combination of FOSCAN® mediated fluorescence guided resection and photodynamic treatment as new therapeutic concept for malignant brain tumors. Med Laser Appl 21:285–290
31. Rosenthal MA, Kavar B, Uren S, Kaye AH (2003) Promising survival in patients with high-grade gliomas following therapy with a novel boronated porphyrin. J Clin Neurosci 10:425–427
32. Schmidt MH, Meyer GA, Reichert KW, Cheng J, Krouwer HG, Ozker K, Whelan HT (2004) Evaluation of photodynamic therapy near functional brain tissue in patients with recurrent brain tumors. J Neurooncol 67:201–207
33. Olivo M, Wilson BC (2004) Mapping ALA-induced PpIX fluorescence in normal brain and brain tumour using confocal fluorescence microscopy. Int J Oncol 25:37–45
34. Lilge L, Wilson BC (1998) Photodynamic therapy of intracranial tissues: a preclinical comparative study of four different photosensitizers. J Clin Laser Med Surg 16:81–91
35. Brancaleon L, Moseley H (2002) Laser and non-laser light sources for photodynamic therapy. Lasers Med Sci 17:173–186
36. Stylli SS, Kaye AH (2006) Photodynamic therapy of cerebral glioma—a review. Part II—clinical studies. J Clin Neurosci 13:709–717
37. Muller PM, Wilson BC (1995) Photodynamic therapy for recurrent supratentorial gliomas. Semin Surg Oncol 11:346–354
38. Wilson BC, Muller PJ, Yanche JC (1986) Instrumentation and light dosimetry for intra-operative photodynamic therapy (PDT) of malignant brain tumors. Phys Med Biol 31:125–133
39. Schmidt MH, Bajic DM, Reichert KW II, Martin TS, Meyer GA, Whelan HT (1996) Light-emitting diodes as a light source for intraoperative photodynamic therapy. Neurosurgery 38:552–556
40. Davidson SRH, Weersink RA, Haider MA, Gertner MR, Bogaards A, Giewercer D, Scherz A, Trachtenberg J, Wilson BC (2009) Treatment planning and dose analysis for interstitial photodynamic therapy of prostate cancer. Phys Med Biol 54:2293–2313
41. Origitano TC, Reichman OH (1993) Photodynamic therapy for intracranial neoplasms: development of an image-based computer-assisted protocol for photodynamic therapy of intracranial neoplasms. Neurosurgery 32:587–595
42. Video of interstitial LED source is viewable at http://www.lsoncology.com
43. Wilson BC, Weersink RA, Lilge L (2003) Fluorescence in photodynamic therapy dosimetry. In: Pogue B, Mycek M (eds) Fluorescence in biomedicine. Marcel Dekker, New York, pp 529–562
44. Lilge L, O'Carroll C, Wilson BC (1997) A solubilization technique for photosensitizer quantification in ex vivo tissue samples. J Photochem Photobiol B39:229–235
45. Mitra M, Foster TH (2008) In vivo confocal fluorescence imaging of the intratumor distribution of the photosensitizer mono-L-aspartylchlorin-e61. Neoplasia 10:429–438
46. Ardeshirpour Y, Chernomordik V, Capala J, Hassan M, Zielinsky R, Griffiths G, Achilefu S, Smith P, Gandjbakhche A (2011) Using in-vivo fluorescence imaging in personalized cancer diagnostics and therapy, an image and treat paradigm. Technol Cancer Res Treat 10:549–560

47. Dysart JS, Patterson MS (2005) Characterization of Photofrin photobleaching for singlet oxygen dose estimation during photodynamic therapy of MLL cells in vitro. Phys Med Biol 50:2597–2616
48. Poon WS, Schomacker KT, Deutsch TF, Martuza RL (1992) Laser-induced fluorescence: experimental intraoperative delineation of tumor resection margins. J Neurosurg 76:679–686
49. Bogaards A, Sterenborg HJ, Trachtenberg J, Wilson BC, Lilge L (2007) In vivo quantification of fluorescent molecular markers in real-time by ratio imaging for diagnostic screening and image-guided surgery. Lasers Surg Med 39:605–613
50. Stummer W, Pichlmeier U, Meinel T, Wiestler OD, Zanella F, Reulen HJ; ALA-Glioma Study Group (2006) Fluorescence-guided surgery with 5-aminolevulinic acid for resection of malignant glioma: a randomised controlled multicentre phase III trial. Lancet Oncol 7:392–401
51. Valdés PA, Leblond F, Kim A, Harris BT, Wilson BC, Fan X, Tosteson TD, Hartov A, Ji S, Erkmen K, Simmons NE, Paulsen KD, Roberts DW (2011) Quantitative fluorescence in intracranial tumor: implications for ALA-induced PpIX as an intraoperative biomarker. J Neurosurg 115:11–17
52. Kim A, Roy M, Dadani FN, Wilson BC (2010) Topographic mapping of subsurface fluorescent structures in tissue using multiwavelength excitation. J Biomed Opt 15:066026
53. Kostron H (2010) Photodiagnosis and therapy and the brain. Methods Mol Biol 635:261–280
54. Eljamil MS, Goodman C, Moseley H (2007) ALA and Photofrin fluorescence-guided resection and repetitive PDT in glioblastoma multiforme: a single centre phase III randomized controlled trial. Lasers Med Sci 23:361–367
55. Rai P, Mallidi S, Zheng X, Rahmanzadeh R, Mir Y, Elrington S, Khurshid A, Hasan T (2010) Development and applications of photo-triggered theranostic agents. Adv Drug Deliv Rev 62:1094–1124
56. Reddy GR, Bhojani MS, McConville P, Moody J, Moffat BA, Hall DE, Kim G, Koo Y-EL, Woolliscroft MJ, Sugai JV, Johnson TD, Philbert MA, Kopelman R, Rehemtulla A, Ross BD (2006) Vascular targeted nanoparticles for imaging and treatment of brain tumors. Clin Cancer Res 12:6677–6686
57. Bisland SK, Lilge L, Lin A, Rusnov R, Wilson BC (2004) Metronomic photodynamic therapy as a new paradigm for photodynamic therapy: rationale and pre-clinical evaluation of technical feasibility for treating malignant brain tumors. Photochem Photobiol 80:2–30
58. Wang KK, Mitra S, Foster TH (2007) A comprehensive mathematical model of microscopic dose deposition in photodynamic therapy [erratum in: Med Phys 35, 4278–4280, 2008]. Med Phys 34:282–293
59. Singh G, Alqawi O, Espiritu M (2010) Metronomic PDT and cell death pathways. Methods Mol Biol 635:65–78
60. Madsen SJ, Sun CH, Tromberg BJ, Hirschberg H (2003) Repetitive 5-aminolevulinic acid-mediated photodynamic therapy on human glioma spheroids. J Neurooncol 62:243–250
61. Davies N, Wilson BC (2007) Interstitial *in vivo* ALA-PpIX mediated metronomic photodynamic therapy (mPDT) using the CNS-1 astrocytoma with bioluminescence monitoring. Photodiagnosis Photodyn Ther 4:202–212
62. Davies N, Wilson BC (2007) Tetherless fiber-coupled optical sources for extended metronomic photodynamic therapy. Photodiagnosis Photodyn Ther 4:184–189
63. Madsen SJ, Sun CH, Tromberg BJ, Hirschberg H (2001) Development of a novel indwelling balloon applicator for optimizing light delivery in photodynamic therapy. Lasers Surg Med 29:406–412
64. Dahlstedt E, Collins HA, Balaz M, Kuimova MK, Khurana M, Wilson BC, Phillips D, Anderson HL (2009) One- and two-photon activated phototoxicity of conjugated porphyrin dimers with high two-photon absorption cross sections. Org Biomol Chem 7:897–904
65. Collins HA, Khurana M, Moriyama EH, Mariampillai A, Dahlstedt E, Balaz M, Kuimova MK, Phillips D, Drobizhev M, Yang VXD, Rebane A, Wilson BC, Anderson HL (2008) Blood vessel closure using photosensitisers engineered for two-photon excitation. Nat Photonics 2:420–424

66. Zheng X, Chopp M, Lu Y, Jiang J, Zhao D, Ding C, Yang H, Zhang L, Jiang F (2011) Atorvastatin reduces functional deficits caused by photodynamic therapy in rats. Int J Oncol 39:1133–1141
67. Berg K, Selbo PK, Prasmickaite L, Tjelle TE, Sandvig K, Moan J, Gaudernack G, Fodstad O, Kjolsrud S, Anholt H, Rodal GH, Rodal SK (1999) aned Hogset A., Photochemical internalization: a novel technology for delivery of macromolecules into cytosol. Cancer Res 59:1180–1183
68. Hirschberg H, Zhang MJ, Gach HM, Uzal FA, Peng Q, Sun CH, Chighvinadze D, Madsen SJ (2009) Targeted delivery of bleomycin to the brain using photo-chemical internalization of *Clostridium perfringens* epsilon prototoxin. J Neurooncol 95:317–329
69. Chou CH, Sun CH, Zhou YH, Madsen SJ, Hirschberg H (2011) Enhanced transfection of brain tumor suppressor genes by photochemical internalization. Proc SPIE 7883:2D1–2D9
70. O'Neill AC, Randolph MA, Bujold KE, Kochevar IE, Redmond RW, Winograd JM (2009) Photochemical sealing improves outcome following peripheral neurorrhaphy. J Surg Res 151:33–39

Chapter 10
Nanoparticle-Mediated Photothermal Therapy of Brain Tumors

Amani R. Makkouk and Steen J. Madsen

10.1 Introduction

10.1.1 Definition and History

The emerging field of nanotechnology has the potential to revolutionize diagnostic and therapeutic medical applications. With a diameter ranging from 10 to 1,000 nm, nanoparticles are solid colloidal particles with unique optical, chemical, and magnetic properties. The ability to tailor these properties by introducing material, shape, and size variations has led to flexibility and diversity in their biological applications [1–4].

Metallic nanoparticles were the first to unlock the nanotechnology field, following the discovery of the colloidal nature of gold solutions in 1857. Though colloidal gold has traditionally been used as a cure, its first application in nanotechnology was in the development of the immunogold labeling technique by Faulk and Taylor [5] in the early 1970s. Subsequently, the range of applications increased with improved insight into their quantum properties and their manipulation [6]. Although there are a wide variety of nanoparticles, this review focuses on gold-based particles since they have been used exclusively in photothermal therapy (PTT) of brain tumors.

Gold nanoparticles are highly appealing for cancer diagnostics and therapy due to the inert properties of gold (resistance to corrosion and low toxicity), in addition

---

A.R. Makkouk
Interdisciplinary Graduate Program in Immunology, University of Iowa, Iowa, IA 52242, USA

S.J. Madsen (✉)
Department of Health Physics and Diagnostic Sciences, University of Nevada, Las Vegas,
NV 89154-3037, USA
e-mail: steen.madsen@unlv.edu

S.J. Madsen (ed.), *Optical Methods and Instrumentation in Brain Imaging and Therapy*, Bioanalysis: Advanced Materials, Methods, and Devices 3,
DOI 10.1007/978-1-4614-4978-2_10,

to the ease with which biocompatible ligands can be conjugated to their surface. Ligands range from targeting agents that optimize tumor delivery, to chemotherapeutic drugs. Furthermore, the tunable optical properties of the gold core govern their applicability as diagnostic imaging or therapeutic thermoablative tools [7].

10.1.2 Advantages Over Fluorophores

Conventional fluorophores used in bioimaging include organic photoabsorbers such as indocyanine green. Although in common use, they suffer from photobleaching and low absorption cross-sections that require high irradiation energies [8]. In contrast, gold nanoparticles are highly photostable and have enhanced absorption cross-sections and high light-to-heat conversion efficiencies. Additionally, their optical absorption is variable and hence they can be tuned over a wide range of wavelengths [9–11].

10.1.3 Types of Gold Nanoparticles

Gold nanoparticles have been synthesized in various shapes, sizes, and forms with varying absorption wavelengths and cross-sections. These include gold nanospheres, nanorods and nanocages, gold–silica nanoshells, and gold–gold sulfide (GGS) nanoparticles. Gold nanospheres are particularly popular due to their small size (<100 nm) and ease of fabrication. Their absorption wavelength lies in the visible spectral region at 500–600 nm but can readily be extended into the near infrared (NIR) by increasing their size [12–14].

Gold nanorods have been widely studied in cancer applications because of their absorption cross-section which is superior to all other gold nanoformulations. They are similar in size to gold nanospheres but have two absorption wavelengths (longitudinal and transverse) due to their distinctive shape, whereby their aspect ratio (length/width) tunes their absorption within the NIR region [15]. For example, peak absorption wavelengths range from approximately 650 to 950 nm for aspect ratios of 2.4–5.6.

Gold–silica nanoshells were the first to be used in PTT of cancer. They consist of a spherical dielectric silica core (50–500 nm), and a thin layer of gold (5–20 nm). Their absorption wavelength can span both visible and NIR regions, and is easily manipulated by varying the core-to-shell ratio, whereby decreasing the gold shell thickness increases the wavelength (Fig. 10.1). Their ease of engineering within the NIR region, where optical radiation has significant penetration in biological tissues, makes them particularly attractive for in vivo studies [16, 17]. Most in vivo PTT studies have used gold–silica nanoshells with cores of 100–120 nm and shells of 10–20 nm since these size distributions result in peak absorption at approximately 800 nm.

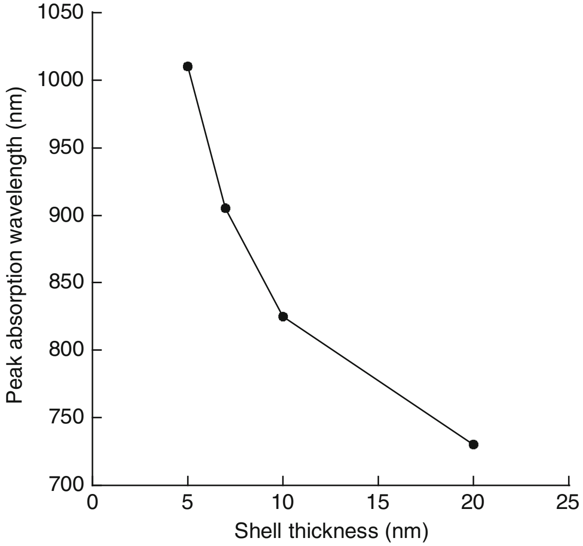

Fig. 10.1 Peak absorption wavelength of gold–silica nanoshells as a function of gold shell thickness for a silica core diameter of 60 nm. As the core-to-shell ratio increases, the peak absorption shifts to longer wavelengths

Other nanoparticle formulations include hollow gold nanocages [18] and GGS nanoparticles [19]. Gold nanocages are synthesized via galvanic replacement of silver cubes, while GGS are made of gold sulfide cores coated with a thin gold shell. Both are smaller in size than other gold nanoformulations, and therefore they are more likely to traverse the leaky tumor vasculature. These nanoparticles also have significant absorption in the NIR region which makes them ideally suited for PTT.

10.1.4 Applications in Cancer

Ongoing research has elucidated several advantages of gold nanoparticles over other biodiagnostic tools such as quantum dots (QDs) and organic dyes. The use of gold nanoparticles as thermoablative agents for various types of cancer, either directly or with functional targeting to enhance tumor delivery has been the subject of a number of in vitro and in vivo studies. A brief summary follows.

10.1.4.1 Diagnostic Applications

The use of gold nanoparticles has expanded rapidly in recent years to cover a wide range of cancer diagnostic applications such as immunolabeling and bioimaging. Detection techniques include, but are not limited to, light scattering, surface-enhanced Raman scattering (SERS) and laser diffraction, all of which offer excellent specificity and sensitivity [20].

Immunolabeling with gold nanoparticles conjugated to antibodies dates back to the 1980s, and ongoing research has shown promising results for the diagnosis of various cancer types, including lymphoma, leukemia, and cancers of the lung, liver, and breast. In addition to antibodies, other nanoparticle conjugates including aptamers and folates have also shown promise as diagnostic agents.

The use of gold nanoparticles as contrast agents for bioimaging applications is relatively recent, yet these particles have demonstrated potential in a number of clinical applications. So far, research has focused on QDs as contrast agents; however, gold nanoparticles are superior in that they display enhanced scattering and are immune from photobleaching. Cai et al. [21] successfully used polyethylene glycol (PEG)-conjugated colloidal gold nanoparticles to visualize microvasculature in mice using micro-CT imaging. Their results are promising for subsequent tumor applications such as studying tumor angiogenesis. Recently, Noreen et al. [22] employed bare gold nanospheres as contrast agents for investigating brain tumor angiogenesis. Mice implanted intracranially with glioma cells were injected intravenously with 25-nm gold nanospheres, which were able to diffuse through leaky blood vessels and reveal their fenestration. Fourier-transform infrared (FTIR) imaging was employed, which relies on the absorption of infrared radiation by covalent bonds, while nanoparticles served as inorganic contrast agents.

Other in vivo imaging studies have employed SERS to detect Raman signals emitted from specialized gold nanoparticles. In a similar fashion, nanoparticles have been used as contrast agents for tumor bioimaging through biomarker targeting, such as the EGFR [23]. This is particularly relevant for the imaging of gliomas since these tumor cells have been shown to overexpress EGFR [24].

10.1.4.2 Therapeutic Applications

Conventional cancer therapies include surgery, chemotherapy, and radiation therapy. While surgery is not an option for inaccessible tumors, and chemotherapy and radiotherapy have serious side effects, PTT represents an attractive alternative. In PPT, hyperthermia is induced following absorption of optical radiation by gold nanoparticles. Conversion of absorbed light into heat generates high temperatures and subsequent cell death. Due to the significant penetration of NIR light in biological tissues, nanoparticles with strong NIR absorption are preferred for PTT applications. The goal of PTT is to induce rapid heating in tumor tissues while minimizing thermal diffusion to surrounding tissues. The minimum temperature increase for effective PTT ranges from 10 to 20°C [25], but higher temperature elevations (30–40°C) may be required in hypoxic, low pH environments characteristic of many tumors. A number of in vivo studies have shown that 10–20° temperature elevations are achievable with gold nanoshell concentrations of $1–5 \times 10^9$ particles/mL, laser power densities of 1–5 W/cm^2, and treatment times of 1–5 min. It should be noted that failure to achieve adequate heating may result in adverse effects due to the production of heat shock proteins which confer resistance to tumor cells [26].

Gold nanospheres are suboptimal for PTT since their optical absorption lies in the visible region. Huang et al. [9] were able to successfully excite immunotargeted gold nanospheres in the NIR region with a femtosecond laser at 800 nm; however, the required high energy fluence was a major drawback.

Gold nanoshells, on the other hand, have been investigated extensively both in vitro and in vivo due to their tunable NIR absorption. Hirsch et al. [27] were the first to demonstrate PTT using gold–silica nanoshells. They showed that a 6-min exposure to an 820-nm continuous laser was efficient in activating gold nanoshells injected into subcutaneous tumors, resulting in irreversible thermal damage at a 4–6 cm depth. Using similar nanoshells, Stern et al. [28] observed 93% tumor necrosis in a subcutaneous prostate cancer model, while Gobin et al. [29] observed substantial tumor regression and a survival rate of >80% in nanoshell-treated mice.

Gold nanorods have been investigated by several groups for PTT of tumors, both in vitro [15, 30–31] and in vivo [32–36]. In one study, Dickerson et al. [33] demonstrated the feasibility of PTT of deep tissue tumors using pegylated gold nanorods with NIR absorption at 800 nm. The nanorods showed preferential accumulation in tumors resulting in tumor temperatures of approximately 45°C following 10 min of 1.7–1.9 W/cm^2 NIR laser irradiation. Not surprisingly, they observed better tumor resorption when the nanorods were administered intratumorally rather than intravenously.

10.2 Photophysics of Gold Nanoparticles

10.2.1 Photothermal Properties

When gold nanoparticles are exposed to light of a specific frequency, a resonant collective oscillation of the free surface electrons results—a process known as surface plasmon resonance (SPR) [12]. Gold nanoparticles optimally absorb incident light at their SPR wavelength, which is governed by their size, shape, and surface composition [13, 38]. Furthermore, their absorption cross-sections exceed by several orders of magnitude those of common organic dyes, such as indocyanine green [39]. Following light absorption, surface electrons are photoexcited and the resultant heated electron gas is dissipated within picoseconds to the surrounding medium [15]. The resultant photothermal damage in biological tissues includes cell membrane rupture, protein denaturation, impairment of DNA and RNA synthesis, and apoptosis.

PTT efficacy depends on a number of factors, including intratumoral light distribution. NIR penetration depths in normal and malignant human brain (ca. 0.5–1.0 cm) are relatively modest and hence effective PTT requires intratumoral light delivery via optical fibers. Additional factors affecting PTT efficacy include the distribution and concentration of nanoparticles within the tumor, which should be optimized so as to produce temperatures sufficient for effective ablation.

10.2.2 Effects of Size and Shape on Heating Efficiency

It has already been shown that the shape and size of gold nanoparticles govern their optical properties, i.e., the SPR wavelength and the absorption cross-section. For example, an increase in diameter results in absorption at longer wavelengths and therefore, gold nanospheres suitable for NIR activation are rather large and are thus less attractive for photothermal applications due to their limited passage through the leaky tumor vasculature and reduced cellular uptake. Gold nanoshells, on the other hand, can be kept at a constant overall diameter while adjusting the ratio of shell thickness to silica core diameter. As the ratio decreases, the SPR absorption shifts to the NIR region, thus facilitating control over their tunability within the optical spectrum [13, 20].

For gold nanorods, their shape dictates two absorption wavelengths: a stronger band in the NIR region along the longitudinal axis, and a weaker band in the visible region along the transverse axis. Their absorption, however, is easily tuned via their aspect ratio (length/width), and they have the highest absorption cross-sections of all the gold nanoparticle formulations [10, 12].

10.3 Production of Gold Nanoparticles

Different synthetic methods are employed for the fabrication of gold nanospheres, nanorods, and nanoshells. The basic method for synthesizing gold cores was first reported by Turkevitch et al. [40], which is based on using citrate to reduce gold in an $HAuCl_4$ solution. Subsequent modifications led to better size distribution and control, and one popular method is the Brust-Schiffrin bi-phasic technique. Briefly, it involves forming gold clusters via transfer of gold ions from water into toluene, followed by the addition of an organic thiol, which results in thiolated gold nanoparticles. This technique offers the additional advantage of multi-functionalization, whereby peptides and PEG can be easily introduced to the thiolated nanosphere surface [7].

The two primary methods for gold nanorod synthesis are the template method and the seed-mediated method. In the template method, gold is electrochemically deposited within the pores of template membranes. The pore diameter controls the nanorod's diameter, while the amount of gold deposited controls the length. Although this is a relatively simple technique, it results in low yields. The seed-mediated method involves producing gold seeds via chemical reduction of a gold salt solution. Nanorods are then grown from the seeds in a gold salt solution with a weak reducing agent, and can be produced in larger yields than the template method [23].

The synthesis of gold nanoshells was developed by Oldenburg et al. [41]. First, the dielectric silica cores are grown and functionalized with amine groups. Then, the gold shell is added to the silica core through a seeded growth method, whereby gold colloid is reduced on the surface from the $HAuCl_4$ solution and gradually grows into a complete shell. The shell thickness is controlled by the amount of $HAuCl_4$ added to the solution.

10.4 Biodistribution and Toxicity of Gold Nanoparticles

10.4.1 Biodistribution Profiles and Brain Accessibility

The biodistribution of nanoparticles is a function of their size, surface charge, and administration route. Not surprisingly, direct intratumoral injections result in the highest tumor concentrations; however, this route is feasible for only a small fraction of tumors. Consequently, research has focused on more clinically relevant routes of administration such as intravenous delivery [42].

Following intravenous injection, the negatively charged gold surface leads to opsonization, whereby the nanoparticles are bound to serum proteins (such as complement C3b). This results in rapid removal by the reticuloendothelial system of the liver and spleen, where the majority of nanoparticles accumulate regardless of size [43]. It has been shown that gold nanoshells have higher accumulation in the spleen compared to the liver [44], while the reverse is observed with gold nanorods [45, 46]. Smaller nanoparticles (ca. 15 nm) have a wider organ distribution that includes the kidney, heart, stomach, and brain. A number of studies, including those of Sonavane et al. [47], have shown that 50 nm is the maximum gold nanoparticle diameter for effective blood–brain barrier (BBB) penetration. Subsequently, it has been hypothesized that 20 nm is the critical size for passive penetration of the BBB, likely due to the 20-nm width of the gap between the capillary endothelium and the end-feet of overlying astrocytes. Larger nanoparticles may cross the BBB via receptor-mediated transport due to interactions between apolipoproteins adsorbed on their surface and scavenger receptors located at the BBB [42].

Gold nanoparticles have been shown to be internalized by cells in a shape and size-dependent manner. Chithrani et al. [48] reported that spherical gold nanospheres had better uptake than nanorods, and the optimal internalization size range of 25–50 nm has been reported by several groups. This is of particular interest for PPT, as greater internalization of nanoparticles by tumor cells is likely to induce more effective heating.

10.4.2 Tumor Specificity

10.4.2.1 Enhanced Permeability and Retention Effect

Following systemic administration, gold nanoparticles accumulate in tumors either passively or actively. Passive uptake occurs via enhanced permeability and retention (EPR). An expanding tumor mass induces rapid angiogenesis to supply the proliferating cells. The newly formed blood vessels (often within the tumor's outer shell) are structurally defective and leaky, with inconsistent diameters and large gaps (up to 600 nm) that allow nanoparticles to passively extravasate and accumulate in tumors. Due to faulty lymphatic drainage, nanoparticles are preferentially retained in tumor tissues, except for brain tumors since the brain does not have a lymph system [16, 38].

Other factors that influence intratumoral penetration include size and surface charge. Using gold nanoparticles conjugated with PEG, Perrault et al. [49] showed that smaller nanoparticles (<60 nm) had better dispersion into tumors, while larger nanoparticles (100 nm) remained within the perivascular tumor regions. Regarding surface charge, Kim et al. [37] have shown that negatively charged nanoparticles have better dispersion throughout tumor cylindroid models.

Though systemic administration routes allow for passive tumor targeting of nanoparticles through the EPR effect, high concentrations are nevertheless observed in the liver, spleen, and other organs. In a study by James et al. [44], it was shown that <5% of injected gold–silica nanoshells reached the tumor. Moreover, passive targeting allows very limited penetration to the tumor's hypoxic center (where resistant cells reside) because of the reduced blood flow to the tumor core [38]. Consequently, other approaches that enhance nanoparticle delivery have been employed, including functionalization and cellular delivery.

10.4.2.2 Enhancing Delivery

One of the simplest approaches to improve the tumor biodistribution of gold nanoparticles is to attach PEG to their surface, which provides steric stabilization. The so-called PEGylated nanoparticles have higher circulation half-lives as a result of reduced opsonization and phagocytosis, which has been shown to enhance efficacy in a number of tumor models. Other functionalization schemes have employed active targeting by attaching proteins (e.g., antibodies) that direct the particles to tumor cells overexpressing antigenic biomarkers, such as HER2 [16, 50, 51].

In an in vitro model of human oral squamous cell carcinoma (HSC) overexpressing alpha v beta 6 $\alpha(v)\beta(6)$ integrins, Kang et al. [52] used gold nanospheres bioconjugated with an arginine-glycine-aspartic acid peptide (RGD), which targets $\alpha(v)\beta(6)$ integrins on the tumor cell surface and allows nanoparticles to enter the cytoplasm via receptor-mediated endocytosis. The nanoparticles were also bioconjugated with a nuclear localization signal (NLS) peptide allowing nucleus-specific targeting that disturbed the division of cancer cells, causing cytokinesis arrest, DNA damage, and apoptosis.

Another promising delivery strategy, coined the "Trojan Horse," was recently developed by Choi et al. [53] for efficient delivery of gold nanoparticles into the hypoxic core of tumors. This method is based on exploiting the ability of macrophages to internalize nanoparticles and to migrate and accumulate within tumor tissue. Using an in vitro breast cancer spheroid model, gold nanoshell-loaded macrophages infiltrated tumor spheroids, reaching the hypoxic core within 3 days of co-incubation.

Macrophages as cellular delivery vehicles are particularly suited for the treatment of gliomas because of their ability to traverse the intact BBB. Attracted by chemokines secreted by tumor cells, circulating monocytes migrate towards

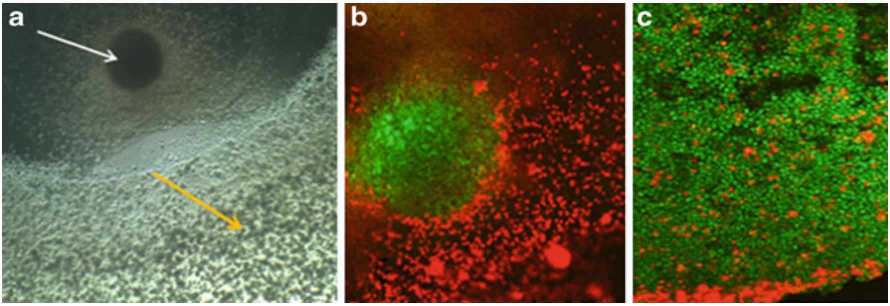

Fig. 10.2 (**a**) Light microscope image of collagen migration assay consisting of two collagen layers, one containing a single tumor spheroid (*white arrow*) and the other containing distributed macrophages (*yellow arrow*). (**b**) Two-photon fluorescence image demonstrating macrophage (*red cells*) migration from the macrophage collagen layer towards the spheroid consisting of glioma cells transfected with green fluorescent protein (GFP). (**c**) High-magnification tomographic image demonstrating penetration of macrophages (*red*) into the GFP spheroid (*green*) [55]

tumors and become tumor-associated macrophages (TAMs). In glioblastoma multiforme (GBM), TAMs can constitute up to a third of the tumor mass [54], and can thus serve as efficient carriers of nanoparticles through the BBB and the blood–brain tumor barrier (BBTB). The migratory potential of macrophages has been studied in vitro using a very simple model consisting of human glioma spheroids embedded in collagen ([55]; Fig. 10.2).

10.4.3 Toxicity

Numerous studies have shown that gold is safe and ideally suited for human use: it has relatively low toxicity and is highly biocompatible. In vitro cytotoxicity assays have shown that gold nanoparticle toxicity is size-dependent, with smaller nanoparticles ($<$5 nm) demonstrating higher toxicity. Furthermore, compatibility of gold nanoparticles with the immune system has been shown to be largely dependent on their surface chemistry. Nonetheless, biological applications commonly employ larger sized nanoparticles that are PEGylated, which improves stability and reduces both cytotoxicity and immunotoxicity [7, 14, 56, 57]. The clearance kinetics of gold nanoparticles has been studied in several animal models and, collectively, the results suggest that small ($<$5 nm) nanoparticles undergo renal excretion whereas larger particles are retained in the liver and spleen for up to 6 months without apparent deleterious effects [44, 46, 58, 59]. Goodrich et al. [45] observed regions of chronic inflammation corresponding to areas of PEG-coated gold nanorod aggregation in both the liver and spleen; however, the long-term side effects of these lesions are unclear. Acute toxic effects of gold nanoparticles have not been observed in any animal models thus far [14].

10.5 Photothermal Therapy of Brain Tumors

The standard therapy for malignant brain tumors such as GBM includes surgical resection followed by radiation and chemotherapy [60, 61]. While hyperthermia is not yet part of this standard therapy regimen, it has some advantages over conventional treatment modalities, most notably the low probability of cells developing thermal resistance. Although tumor cell selectivity is a major obstacle with conventional photothermal therapies, the use of gold nanoparticles as photothermal agents may overcome this limitation. Even though both healthy and tumor tissues are exposed to optical radiation, thermal damage will be confined to tumors containing high concentrations of nanoparticles [62].

Selective tumor damage can be achieved by controlling light irradiation parameters (wavelength, fluence rate, and irradiation time) and nanoparticle parameters (size concentration and tumor specificity) [25]. While different gold nanoparticle formulations have been investigated for various cancer therapies, applications to brain tumors have focused on gold nanoshells, probably because they have been extensively investigated and, as such, their properties are better known compared to other formulations. A summary of in vitro and in vivo gold nanoparticle PTT applications for brain tumors is listed in Table 10.1.

10.5.1 In Vitro PTT Studies

Bernardi et al. [60] were the first to study the use of nanoshells as PTT agents for brain tumors. In an effort to improve tumor cell selectivity, the authors tested targeted nanoshells in two in vitro cell lines overexpressing different antigenic biomarkers. Nanoshells bioconjugated to anti-HER2 antibody were tested in Daoy human medulloblastoma cells overexpressing HER2, while nanoshells bioconjugated to anti-IL13Rα2 were tested in U373 human high-grade glioma cells overexpressing IL13Rα2. Using NIR laser irradiation at 80 W/cm^2 for 2 min, the authors demonstrated in both settings that nanoshells selectively killed tumor cells overexpressing the targeted biomarker, but not control cells that lacked the expression. Furthermore, nanoshell toxicity was confined to areas exposed to the laser, which further confirms the specificity of PTT requiring both the nanoparticles and laser for efficient heating.

Baek et al. [63] used a different approach to improve nanoshell targeting to brain tumors by employing the ability of macrophages to migrate through the extracellular matrix of solid tumors. Macrophages can thus act as delivery vectors of nanoshells into the glioma microenvironment for subsequent NIR laser-induced thermoablation. This technique was investigated in an in vitro model consisting of multicell human glioma spheroids which are three-dimensional aggregates of tumor cells that provide a more accurate representation of tumors in vivo than cells in monolayer. Using visible and NIR absorption spectroscopy, it was shown that there

Table 10.1 In vitro and in vivo photothermal therapies of brain tumors using gold nanoparticles

Type	Cell line/animal model	Nanoparticle	Size (nm)	Wavelength (nm)	Incident power density	Irradiation time (min)	References
In vitro	Daoy overexpressing HER2	Targeted nanoshells (anti-HER2)	120	800	80 W/cm^2 (beam diameter = 2 mm)	2	[60]
	U373 overexpressing IL13Rα2	Targeted nanoshells (anti-IL13Rα2)					
	ACBT spheroids	PEG-coated nanoshells loaded into murine macrophages	134	810	2–28 W/cm^2 (beam diameter = 3 mm)	1–10	[63]
In vivo	cTVT in a canine brain model	I.V. PEG-coated nanoshells	150	808	3.5 W (beam diameter = 1 cm)	3	[64]
	U373 grown S.Q. in SCID mice	I.V. PEG-coated nanoshells	150	800	4 W/cm^2 (beam diameter = 9 mm)	3	[62]
	U87MGwtEGFR grown S.Q. in nu/nu mice	I.V. PEG-coated nanocages	45	808	0.7 W/cm^2 (beam diameter NM)	10 min	[56]

Cell lines: *Daoy*, human medulloblastoma; *U373*, human high-grade glioma; *ACBT*, human grade IV glioma; *cTVT*, canine transmissible venereal tumor; *U87MGwtEGFR*, human glioblastoma

HER-2 human epidermal growth factor receptor 2; *IL13Rα2* interleukin 13 receptor α2; *PEG* polyethylene glycol; *I.V.* intravenous; *S.Q.* subcutaneous; *SCID* severe combined immunodeficiency; *nu*/*nu* athymic; *NM* not mentioned

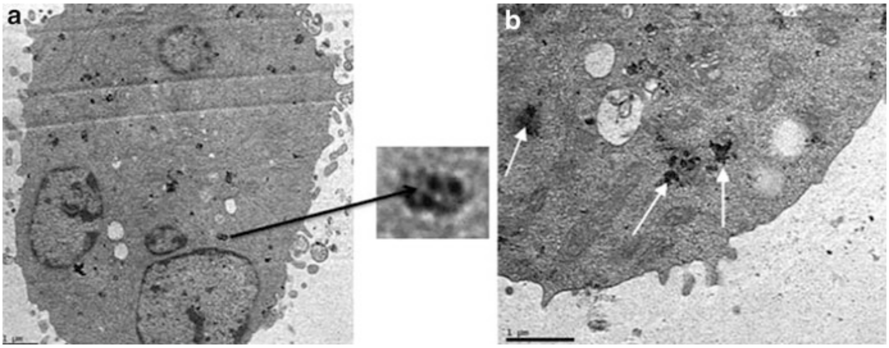

Fig. 10.3 TEM images of nanoshell-loaded murine macrophages. The nanoshells are aggregated in vacuoles dispersed throughout the cytoplasm (**a**, **b**). Magnification of a vacuole in (**a**) shows the high contrast nanoshells. *White arrows* in (**b**) indicate vacuoles containing nanoshells [63]

was no significant shift in the absorption peak of gold nanoshells in solution compared to aggregated nanoshells inside murine macrophages. Extensive uptake of gold nanoshells by murine macrophages was observed within 24 h as revealed by transmission electron microscopy (TEM; Fig. 10.3). Then, individual tumor spheroids were co-incubated with empty or nanoshell-loaded macrophages for 2 or 18 h, followed by NIR irradiation (2–28 W/cm^2) for 1, 5, or 10 min and follow-up for survival and growth for 2 weeks.

Human glioma spheroids containing nanoshell-loaded macrophages demonstrated significant growth inhibition following laser irradiation, unlike non-treated controls or laser-treated controls containing empty macrophages (Fig. 10.4). This was seen at laser irradiances as low as 7 W/cm^2. At 14 W/cm^2, complete growth inhibition was seen, whereas an irradiance of 28 W/cm^2 resulted in complete obliteration of spheroids within seconds of irradiation. The specificity of the approach was confirmed by the observation that ablation was observed only in regions containing the nanoshell-loaded macrophages, while the surrounding tumor cells remained viable ([63]; Fig. 10.5).

10.5.2 *In Vivo PTT Studies*

The three in vivo PTT brain tumor studies reported in the literature employed PEG-coated nanoshells/nanocages to improve accumulation in tumors following intravenous (i.v.) administration. In the first study, Day et al. [62], expanded on their earlier in vitro results [60] by employing a subcutaneous model of the high-grade glioma cell line U373, grown in immunodeficient mice. Following i.v. administration, the authors waited 24 h as shown in biodistribution studies to be sufficient for tumor accumulation of nanoshells. Then, NIR irradiation (4 W/cm^2)

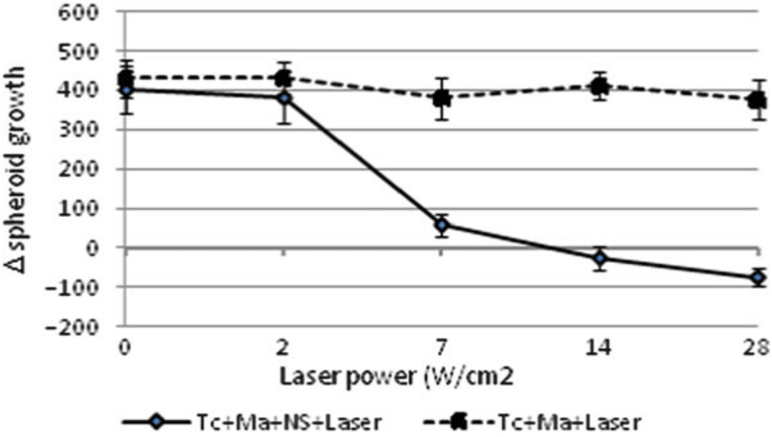

Fig. 10.4 Effects of laser irradiance on spheroid growth. Preformed spheroids incubated with either empty (Tc + Ma) or nanoshell-loaded macrophages (Tc + Ma + NS) for 24 h and subsequently irradiated with varying irradiances for 10 min. Δ spheroid growth represents the mean diameter 14 days postirradiation minus the initial pre-irradiation diameter

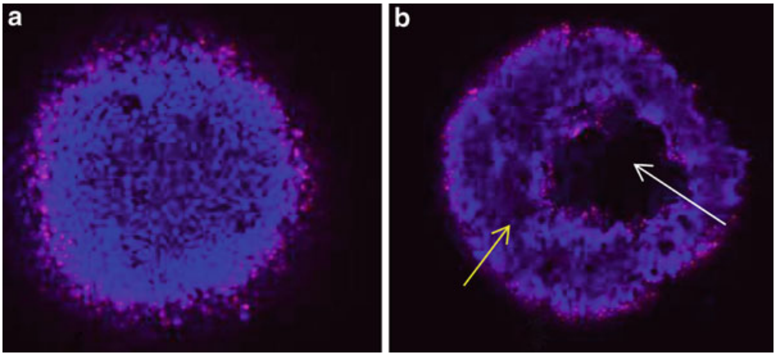

Fig. 10.5 Two-photon images of hybrid spheroids formed with 500 nanoshell-loaded macrophages concentrated in the core of the spheroid. (**a**) PTT: 7 W/cm^2, (**b**) PTT: 28 W/cm^2. Laser beam diameter 3 mm, spheroid diameter 0.7 mm, 1 min irradiation time. Images acquired 24 h following treatment. At high irradiance (**b**), the spheroid core was completely obliterated (*white arrow*). Live/dead assay of these spheroids revealed that the surrounding cells in the outer rim, which contained no nanosphere-loaded macrophages were largely unaffected by the irradiation (*yellow arrow*). Images were acquired at a depth of approximately 80 μm. The field of view for each image is 600 × 600 μm [63]

was applied for 3 min, and mice were monitored daily for 3 months for survival and tumor growth. PTT was able to induce complete responses in 57% of the mice, whereas tumor growth progressed in the control group, none of which survived beyond 24 days.

Schwartz et al. [64] investigated PTT in an orthotopic model, using a non-brain tumor cell line. The authors reported the successful use of passively delivered nanoshells for PTT of canine transmissible venereal tumor (cTVT) in a canine brain model. PEG-coated nanoshells were injected i.v. followed by a 24 h interval to allow for sufficient intracranial accumulation. TEM studies revealed that nanoshells accumulated along the capillary walls of the growing cTVT tumor. This implies that the tumor's leaky microvasculature allowed nanoshell passage, an important observation as primary brain tumors have been reported to have similar fenestrated vasculature. NIR irradiation was then delivered over 3 min at 3.5 W with an intratumoral optic fiber to ensure even heating. This resulted in temperatures of ~66°C in the tumor tissue compared to sublethal temperatures of ~49°C in the contralateral hemisphere (control). Subsequent postmortem histology revealed the effectiveness and selectivity of the applied PTT, as thermal ablation was seen only in the tumor tissue, with minimal damage to adjacent normal tissue.

Chen et al. [56] investigated PEGylated gold nanocages for their ability to induce hyperthermia in a bilateral subcutaneous model of human glioblastoma in athymic mice. Biodistribution studies conducted 96 h postinjection revealed efficient passive uptake of the nanocages by the tumors, reaching 5.7% of the injected dose per gram of tissue (ID/g). Additionally, the nanocages were distributed throughout the tumor, but at slightly higher concentrations at the periphery.

At 72 h postinjection, the authors irradiated tumors on the right flank for 10 min (0.7 W/cm^2), ensuring that the spot size covered the entire tumor. Surface temperatures of 54°C were measured in tumors of the nanocage-injected mice, while those of control mice (saline-injected) remained below 37°C.

PTT efficacy was evaluated noninvasively using functional [^{18}F]fluorodeoxyglucose positron emission tomography (^{18}F-FDG PET). Though performed at an early time point (24-h post-therapy), it nonetheless showed a significant reduction of tumor metabolic activity in nanocage-injected mice as compared to that of saline-injected mice. When normalized to untreated (contralateral) tumors, the decrease in metabolic activity was 70%. Finally, histological examination identified clear and extensive thermal damage to the nuclei of tumor cells and tumor interstitium that was absent in tumors not exposed to laser irradiation or from mice injected with saline.

10.6 Concluding Remarks

It is important to note that gold nanoparticles as PTT agents for tumors have already reached the stage of clinical trials. As of 2011, gold nanoshells (under the commercial name of AuroLase®) have an open Investigational Device Exemption (IDE) with the US FDA to evaluate their safety and efficacy for the treatment of refractory or recurrent head and neck cancers (www.nanospectra.com). While highly encouraging, additional studies will be required to assess the role of gold nanoparticles (and PTT) in the treatment of brain tumors.

References

1. Fadeel B, Kasemo B, Malmsten M, Stromme M (2010) Nanomedicine: reshaping clinical practice. J Intern Med 267(1):2–8
2. Gewin V (2009) Big opportunities in a small world. Nature 460(7254):540–541
3. Muthu MS, Singh S (2009) Targeted nanomedicines: effective treatment modalities for cancer, AIDS and brain disorders. Nanomedicine (Lond) 4(1):105–118
4. Roco MC (1999) Nanoparticles and nanotechnology research. J Nanopart Res 1(1):1–6
5. Faulk WP, Taylor GM (1971) An immunocolloid method for the electron microscope. Immunochemistry 8(11):1081–1083
6. Lead JR, Smith E (2009) Environmental and human health impacts of nanotechnology. Wiley, Chichester
7. Arvizo R, Bhattacharya R, Mukherjee P (2010) Gold nanoparticles: opportunities and challenges in nanomedicine. Expert Opin Drug Deliv 7(6):753–763
8. Boisselier E, Astruc D (2009) Gold nanoparticles in nanomedicine: preparations, imaging, diagnostics, therapies and toxicity. Chem Soc Rev 38(6):1759–1782
9. Huang X, Qian W, El-Sayed IH, El-Sayed MA (2007) The potential use of the enhanced nonlinear properties of gold nanospheres in photothermal cancer therapy. Lasers Surg Med 39 (9):747–753
10. Huang X, Jain PK, El-Sayed IH, El-Sayed MA (2008) Plasmonic photothermal therapy (PPTT) using gold nanoparticles. Lasers Med Sci 23(3):217–228
11. Kumar CSSR (2007) Nanomaterials for medical diagnosis and therapy. Wiley-VCH, Weinheim
12. Huang X, Jain PK, El-Sayed IH, El-Sayed MA (2007) Gold nanoparticles: interesting optical properties and recent applications in cancer diagnostics and therapy. Nanomedicine 2(5):681–693
13. Li JL, Gu M (2010) Gold-nanoparticle-enhanced cancer photothermal therapy. IEEE J Sel Topics Quantum Electron 16(4):989–996
14. Kennedy LC, Bickford LR, Lewinski NA, Coughlin AJ, Hu Y, Day ES et al (2011) A new era for cancer treatment: gold-nanoparticle-mediated thermal therapies. Small 7(2):169–183
15. Huang X, El-Sayed IH, Qian W, El-Sayed MA (2006) Cancer cell imaging and photothermal therapy in the near-infrared region by using gold nanorods. J Am Chem Soc 128(6):2115–2120
16. Hirsch LR, Gobin AM, Lowery AR, Tam F, Drezek RA, Halas NJ et al (2006) Metal nanoshells. Ann Biomed Eng 34(1):15–22
17. Lowery AR, Gobin AM, Day ES, Halas NJ, West JL (2006) Immunonanoshells for targeted photothermal ablation of tumor cells. Int J Nanomedicine 1(2):149–154
18. Chen JY, Wiley B, Li ZY, Campbell D, Saeki F, Cang H, Au L, Lee J, Li XD, Xia YN (2005) Gold nanocages: engineering their structure for biomedical applications. Adv Mater 17:2255–2261
19. Zhou HS, Honma I, Komiyama H, Haus JW (1994) Controlled synthesis and quantum size effect in gold-coated nanoparticles. Phys Rev B 50(16):12052–12056
20. Radwan SH, Azzazy HM (2009) Gold nanoparticles for molecular diagnostics. Expert Rev Mol Diagn 9(5):511–524
21. Cai QY, Kim SH, Choi KS, Kim SY, Byun SJ, Kim KW, Park SH, Juhng SK, Yoon KH (2007) Colloidal gold nanoparticles as a blood-pool contrast agent for x-ray computed tomography in mice. Invest Radiol 42(12):797–806
22. Noreen R, Pineau R, Chien C, Cestelli-Guidi M, Hwu Y, Marcelli A et al (2011) Functional histology of glioma vasculature by FTIR imaging. Anal Bioanal Chem 401:795–801
23. Cai W, Gao T, Hong H, Sun J (2008) Applications of gold nanoparticles in cancer nanotechnology. Nanotechnol Sci Appl 1:17–32
24. Libermann TA, Nussbaum HR, Razon N, Kris R, Lax I, Soreq H, Whittle N, Waterfield MD, Ulrich A, Schlessinger J (1985) Amplification, enhanced expression and possible

rearrangement of EGF receptor gene in primary human brain tumorus of glial origin. Nature 313:144–147

25. Terentyuk GS, Maslyakova GN, Suleymanova LV, Khlebtsov NG, Khlebtsov BN, Akchurin GG et al (2009) Laser-induced tissue hyperthermia mediated by gold nanoparticles: toward cancer phototherapy. J Biomed Opt 14(2):021016
26. Curley SA, Cherukuri P, Briggs K, Patra CR, Upton M, Dolson E, Mukherjee P (2008) Noninvasive radiofrequency field-induced hyperthermic cytotoxicity in human cancer cells using cetuximab-targeted gold nanoparticles. J Exp Ther Oncol 7:313–326
27. Hirsch LR, Stafford RJ, Bankson JA, Sershen SR, Rivera B, Price RE, Hazle JD, Halas NJ, West JL (2003) Nanoshell-mediated near-infrared thermal therapy of tumors under magnetic resonance guidance. Proc Natl Acad Sci U S A 100:13549–13554
28. Stern JM, Stanfield J, Kabbani W, Hsieh JT, Cadeddu JA (2008) Selective prostate cancer thermal ablation with laser activated gold nanoshells. J Urol 179(2):748–753
29. Gobin AM, Lee MH, Halas NJ, James WD, Drezek RA, West JL (2007) Near-infrared resonant nanoshells for combined optical imaging and photothermal cancer therapy. Nano Lett 7:1929–1934
30. Tong L, Zhao Y, Huff TB, Hansen MN, Wei A, Cheng JX (2007) Gold nanorods mediate tumor cell death by compromising membrane integrity. Adv Mater 19:3136–3141
31. Choi BJ, Yang J, Jang E, Suh JS, Huh YM, Lee K, Haam S (2011) Gold nanostructures as photothermal therapy agent for cancer. Anticancer Agents Med Chem 11(10):953–964
32. Choi WI, Kim J-Y, Kang C, Byeon CC, Kim YH, Tae G (2011) Tumor regression in vivo by photothermal therapy based on gold-nanorod-loaded, functional nanocarriers. ACS Nano 5:1995–2003
33. Dickerson EB, Dreaden EC, Huang X, El-Sayed IH, Chu H, Pushpanketh S, McDonald JF, El-Sayed MA (2008) Gold nanorod assisted near-infrared plasmonic photothermal therapy (PPTT) of squamous cell carcinoma in mice. Cancer Lett 269:57–66
34. von Maltzahn G, Park JH, Agrawal A, Bandaru NK, Das SK, Sailor MJ, Bhatia S (2009) Computationally guided photothermal tumor therapy using long-circulating gold nanorod antennas. Cancer Res 69:3892–3900
35. Li Z, Huang P, Zhang X, Lin J, Yang S, Liu B, Gao F, Xi P, Ren Q, Cui D (2010) RGD-conjugated dendrimer-modified gold nanorods for in vivo tumor targeting and photothermal therapy. Mol Pharm 7:94–104
36. Kim J-Y, Choi WI, Kim YH, Tae G, Lee SY, Kim K, Kwon IC (2010) In-vivo tumor targeting of pluronic-based nano-carriers. J Control Release 147:109–117
37. Kim B, Han G, Toley BJ, Kim CK, Rostello VM, Forbers NS (2010) Tuning payload delivery in tumour cylindroids using gold nanoparticles. Nat Nanotechnol 5(6):465–472
38. Lal S, Clare SE, Halas NJ (2008) Nanoshell-enabled photothermal cancer therapy: impending clinical impact. Acc Chem Res 41(12):1842–1851
39. O'Neal DP, Hirsch LR, Halas NJ, Payne JD, West JL (2004) Photo-thermal tumor ablation in mice using near infrared-absorbing nanoparticles. Cancer Lett 209:171–176
40. Turkevitch J, Stevenson PC, Hillier J (1951) A study of the nucleation and growth processes in the synthesis of colloidal gold. Discuss Faraday Soc 11:55–75
41. Oldenburg SJ, Jackson JB, Westcott SL, Halas NJ (1998) Infrared extinction properties of gold nanoshells. Appl Phys Lett 75:2897–2899
42. Khlebtsov NF, Dykman L (2011) Biodistribution and toxicity of engineered gold nanoparticles: a review of in vitro and in vivo studies. Chem Soc Rev 40(3):1647–1671
43. Cuenca AG, Jiang H, Hochwald SN, Delano M, Cance WG, Grobmyer SR (2006) Emerging implications of nanotechnology on cancer diagnostics and therapeutics. Cancer 107 (3):459–466
44. James WD, Hirsch LR, West JL, O'Neal PD, Payne JD (2007) Applications of INAA to the build-up and clearance of gold nanoshells in clinical studies in mice. J Radioanal Nucl Chem 271:455–459

45. Goodrich GP, Bao L, Gill-Sharp K, Sang KL, Wang J, Payne JD (2010) Photothermal therapy in a murine colon cancer model using near-infrared absorbing gold nanorods. J Biomed Opt 15 (1):018001
46. Niidome T, Yamagata M, Okamoto Y, Akiyama Y, Takahasi H, Kawano T, Katayama Y, Niidome Y (2006) PEG-modified gold nanorods with a stealth character for in vivo applications. J Control Release 114(3):343–347
47. Sonavane G, Tomoda K, Makino K (2008) Biodistribution of colloidal gold nanoparticles after intravenous administration: effect of particle size. Colloids Surf B Biointerfaces 66 (2):274–280
48. Chithrani BD, Ghazani AA, Chan WCW (2006) Determining the size and shape dependence of gold nanoparticle uptake into mammalian cells. Nano Lett 6(4):662–668
49. Perrault SD, Walkey C, Jennings T, Fischer HC, Chan WC (2009) Mediating tumor targeting efficiency of nanoparticles through design. Nano Lett 9(5):1909–1915
50. Everts M (2007) Thermal scalpel to target cancer. Expert Rev Med Devices 4(2):131–136
51. Lin AW, Lewinski NA, West JL, Halas NJ, Drezek RA (2005) Optically tunable nanoparticle contrast agents for early cancer detection: model-based analysis of gold nanoshells. J Biomed Opt 10(6):064035
52. Kang B, Mackey MA, El-Sayed MA (2010) Nuclear targeting of gold nanoparticles in cancer cells induces DNA damage, causing cytokinesis arrest and apoptosis. J Am Chem Soc 132(5):1517–1519
53. Choi MR, Stanton-Maxey KJ, Stanley JK, Levin CS, Bardhan R, Akin D et al (2007) A cellular Trojan Horse for delivery of therapeutic nanoparticles into tumors. Nano Lett 7 (12):3759–3765
54. Fleige G, Nolte C, Synowitz M, Seeberger F, Kettenmann H, Zimmer C (2001) Magnetic labeling of activated microglia in experimental gliomas. Neoplasia 3:489–499
55. Hirschberg H, Baek SK, Kwon YJ, Sun CH, Madsen SJ (2010) Bypassing the blood–brain barrier: delivery of therapeutic agents by macrophages. Proc SPIE 7548:3Z-1
56. Chen J, Glaus C, Laforest R, Zhang Q, Yang M, Gidding M, Welch MJ, Xia Y (2010) Gold nanocages as photothermal transducers for cancer treatment. Small 6(7):811–817
57. Dobrovolskaia MA, McNeil SE (2007) Immunological properties of engineered nanomaterials. Nat Nanotechnol 2(8):469–478
58. Hainfeld JF, Slatkin DN, Focella TM, Smilowitz HM (2006) Gold nanoparticles: a new x-ray contrast agent. Br J Radiol 79(939):248–253
59. Huang XL, Zhang B, Ren L, Ye SF, Sun LP, Zhang QQ, Tan MC, Chow GM (2008) In vivo toxic studies and biodistribution of near infrared sensitive Au-Au(2)S nanoparticles as potential drug delivery carriers. J Mater Sci Mater Med 19(7):2581–2588
60. Bernardi RJ, Lowery AR, Thompson PA, Blaney SM, West JL (2008) Immunonanoshells for targeted photothermal ablation in medulloblastoma and glioma: an in vitro evaluation using human cell lines. J Neurooncol 86(2):165–172
61. Sathornsumetee S, Rich JN (2008) Designer therapies for glioblastoma multiforme. Ann N Y Acad Sci 1142:108–132
62. Day ES, Thompson PA, Zhang L, Lewinski NA, Ahmed N, Drezek RA et al (2011) Nanoshell-mediated photothermal therapy improves survival in a murine glioma model. J Neurooncol 104(1):55–63
63. Baek SK, Makkouk AR, Krasieva T, Sun CH, Madsen SJ, Hirschberg H (2011) Photothermal treatment of glioma; an in vitro study of macrophage-mediated delivery of gold nanoshells. J Neurooncol 104(2):439–448
64. Schwartz JA, Shetty AM, Price RE, Stafford RJ, Wang JC, Uthamanthil RK et al (2009) Feasibility study of particle-assisted laser ablation of brain tumors in orthotopic canine model. Cancer Res 69(4):1659–1667

Chapter 11
Photo-activated Cancer Therapy: Potential for Treatment of Brain Tumors

Henry Hirschberg

11.1 Introduction

The resistance of high grade glioma (glioblastoma multiforme; GBM) to therapeutic intervention is due to a number of factors. Among the most important are significant genetic variations, including numerous deletions, amplifications, and point mutations to receptor and suppressor genes. Additionally, the diffuse and infiltrative nature of GBMs makes complete surgical resection virtually impossible. The propensity of glioma cells to migrate along white matter tracts makes it clear that a cure is only possible if the migratory cells can be eradicated. Despite the factors already mentioned, 80% of GBMs recur within 2 cm of the resection margin, and therefore a reasonable starting point for improving the prognosis of GBM patients would be the development of improved local therapies capable of eradicating glioma cells in the margin, or brain-adjacent-to-tumor (BAT). Complicating successful therapy further are variations in blood–brain barrier (BBB) patency throughout the tumor and BAT volume—it is intact in some regions, while leaky in others and this has significant implications for the delivery of therapeutic agents. The BBB controls the passage of blood-borne agents into the central nervous system (CNS) and, as such, it plays a vital role in protecting the brain against pathogens. Although this protective mechanism is essential for normal brain function, it also poses a significant hindrance to the entry of drugs into the brain. The protective function of the BBB is particularly problematic for the treatment of infiltrating gliomas. Although surgery is used to remove gross tumor, standard adjuvant therapies consisting of radiation and chemotherapy often fail to eliminate infiltrating glioma cells in or beyond the BAT region—a zone that commonly extends several centimeters from the resection margin [1]. Infiltrating tumor cells are supplied with nutrients and oxygen by the normal brain

---

H. Hirschberg (✉)
Beckman Laser Institute, University of California, Irvine, CA, USA
e-mail: hhirschb@uci.edu

S.J. Madsen (ed.), *Optical Methods and Instrumentation in Brain Imaging and Therapy*, Bioanalysis: Advanced Materials, Methods, and Devices 3,
DOI 10.1007/978-1-4614-4978-2_11,

vasculature and consequently, protected by the BBB: few anti-cancer drugs are capable of crossing this barrier. The efficacy of any drug treatment depends on the ability of the therapeutic agent to reach its target. Therefore, destruction of infiltrating tumor cells is a crucial step for curing malignant gliomas. This cannot be accomplished until methods are developed to: (1) deliver drugs or carriers across the BBB at a selected site, or (2) selectively disrupt in a site-specific manner this protective barrier. Eradication of gliomas is highly unlikely without addressing the problems posed by the BBB. Although a number of therapeutic strategies have been attempted, the most popular include the local delivery of: (1) chemotherapeutic agents using polymer wafers, and (2) ionizing radiation in the form of brachytherapy [2, 3]. Unfortunately, neither of these strategies has resulted in significant prolongation of survival.

One potential method to improve drug delivery would therefore be to induce increased vascular permeability to these agents in the local tumor environment. Photodynamic therapy (PDT) is a treatment modality combining a photosensitizing drug and light to activate the photosensitizer in an oxygen-dependent manner resulting in oxidation of biomolecules in the light-exposed region. Details of the mechanism and effects of PDT have been covered in Chap. 9.

PDT has been traditionally used to destroy tumor cells and surrounding vasculature using localized light delivery and a photosensitizing drug. In contrast, low fluence rate PDT has recently been shown to increase permeability of vasculature to chemotherapy agents in several animal models by modifying the cell's cytoskeleton. This in turn leads to alteration in the endothelial cell shape, the loss of tight junctions, and ultimately an increase of vascular permeability [4–8]. Although the use of PDT to selectively enhance the distribution of macromolecular therapeutics to tumors is attractive, it remains a double-edged sword since it depends on optimal PDT conditions in order to avoid vasospasm, vessel thrombosis, and tissue infarction. In this chapter, several experimental light-based therapeutic modalities that could potentially be employed in the treatment of gliomas are reviewed.

11.2 Photochemical Internalization

Photochemical internalization (PCI) is a special type of PDT that can be used to enhance the delivery of macromolecules in a site-specific manner [9–14]. The concept is based on the use of specially designed photosensitizers, which localize preferentially in the membranes of endocytic vesicles. The photosensitizer, aluminum phthalocyanine disulfonate ($AlPcS_{2a}$), a phthalocyanine derivative containing two charged sulfonate groups linked to phthalic subunits in adjacent positions on the Pc molecule and an Al metal ion coordinated at its center (Fig. 11.1), is well suited for PCI. The most important and distinguishable property of $AlPcS_{2a}$ is its amphiphilicity which refers to chemical compounds possessing both hydrophilic

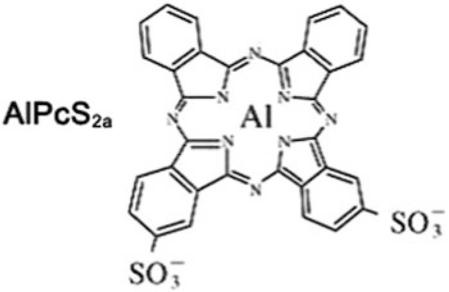

Fig. 11.1 Structure of the photosensitizer aluminum phthalocyanine dilsulphonate ($AlPcS_{2a}$)

and lipophilic properties. Most phthalocyanine photosensitizers are lipophilic and therefore insoluble in water, which makes them unsuitable for use in biological systems. This problem has been solved by sulfonation and by hydroxylation of the benzene rings in the phthalocyanine [15]. For example, while the phthalocyanine skeleton of $AlPcS_{2a}$ is lipophilic, the two adjacent sulfonate groups attached to the phthalocyanine molecule contribute to its hydrophilic nature. This amphiphilic photosensitizer is perfectly designed to localize in the cellular membrane [16]. This is achieved by inserting the lipophilic phthalocyanine skeleton of $AlPcS_{2a}$ in the lipophilic interior of the cellular membrane and dissolving the sulfonate groups in the hydrophilic outer layer of the membrane. $AlPcS_{2a}$ molecules first localize in the cell membrane. During endocytosis, a partial cell membrane with previously localized $AlPcS_{2a}$ molecules pinches inward to form an endocytic vesicle (endosome), and subsequently, the attached $AlPcS_{2a}$ molecules are transported into the cell via the endosomal membrane.

Although a number of small molecule drugs can readily enter cells, they have relatively low therapeutic specificity primarily due to their structural limitations. Since hydrophilic macromolecules are taken up by the cell body through endocytosis, they have to escape through the endosomal membrane into the cytosol in order to exert their full biological effects. Unfortunately, macromolecules are generally trapped in the endosome, and after endosome-lysosome fusion, are degraded by powerful lysosomal enzymes thereby losing their therapeutic effects.

Since the main target of PCI is the membranes of endocytic vesicles, the choice of membrane-localizing photosensitizer is important for effective PCI. In this respect, photosensitizers with an amphiphilic structure are the most efficient since the hydrophilic part of the photosensitizer prevents penetration through the cellular membrane. Once the photosensitizer is securely localized in the cell membrane, it will eventually be incorporated into the membranes of endocytic vesicles via the process of endocytosis. The photosensitizer must maintain its position within the endocytic vesicle, while the macromolecular drugs are trapped within the vesicle in order to avoid photochemical destruction of the macromolecules.

11.2.1 Mechanisms of PCI

While specific amphiphilic photosensitizers (e.g., $AlPcS_{2a}$) preferentially accumulate in the membranes of endosomes, upon light exposure the photosensitizer interacts with ambient oxygen to produce singlet oxygen. Since singlet oxygen has a very short range of action (< 20 nm), only the area of the vesicular membrane where the photosensitizer is localized will be damaged by singlet oxygen-mediated reactions with amino acids, unsaturated fatty acids, and cholesterol in the membrane bilayer. Although the exact structure of the damaged endosomes has not yet been elucidated, the results of vesicular membrane damage (either increased permeability or destructive opening depending on the light fluence and photosensitizer concentration) are easily demonstrated. The previously trapped macromolecular drugs can now be released from the endocytic vesicles into the cytosol in a fully functional form and are free to diffuse to their intended targets to exert their therapeutic effects. The PCI concept is illustrated in Fig. 11.2.

11.2.2 Advantages of PCI

PCI as a drug delivery technology has many advantages. (1) There are no restrictions on the size of the molecules that can be effectively delivered, making PCI highly suitable for a wide variety of molecules. (2) PCI also exhibits high site-specificity, which limits the biological effect to only illuminated areas and lowers the potential systemic side effects of the delivered drug. (3) PCI is a method that increases the therapeutic efficacy of a wide range of macromolecules allowing for the possibility of using lower drug doses to minimize morbidity. (4) PCI is well suited for combination with other modalities or strategies for targeted drug delivery, thus increasing the potential for further therapeutic improvements. PCI has also been shown to potentiate the biological activity of a large variety of macromolecules and other molecules that do not readily penetrate the plasma membrane, including proteins (e.g., protein toxins and immunotoxins), peptides, DNA delivered as a complex with cationic polymers or incorporated in adenovirus or adeno-associated virus, peptide-nucleic acids (PNA), and chemotherapeutic agents.

11.2.3 Blood Brain Barrier Opening

Localized opening of the BBB is a potentially useful application of both PDT and PCI as it could enhance the delivery of therapeutic agents for the treatment of a wide variety of brain diseases including cancer. Site-specific disruption of the BBB for drug delivery into the brain has been accomplished using a number of approaches including highly focused ultrasound [17] and laser-based techniques such as PDT

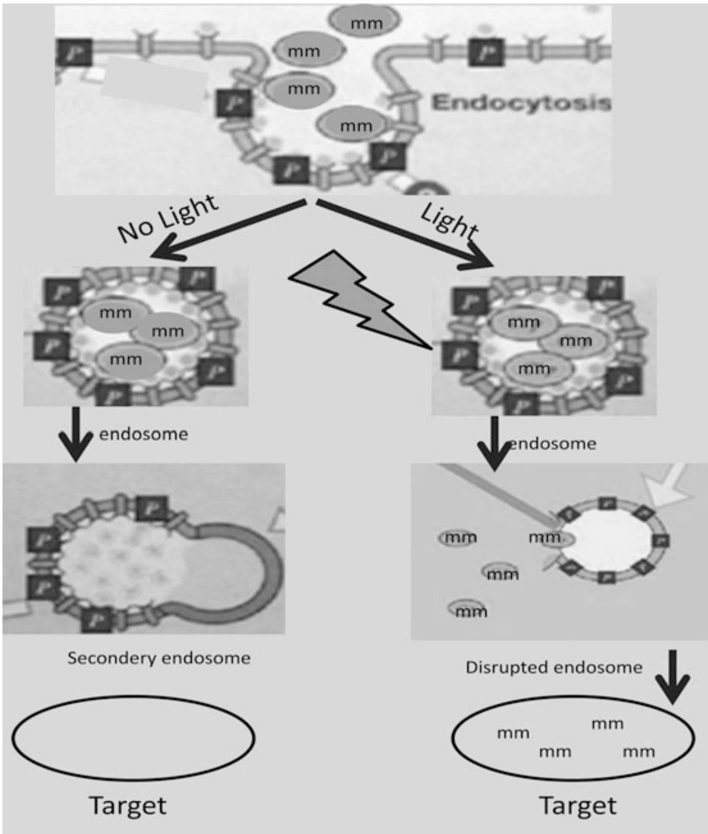

Fig. 11.2 Schematic illustration of PCI. Left panel; Macromolecules (mm) taken up through endocytosis and trapped in endosomes. Fusion with lysosomes (secondary endosomes) leads to their degradation before they have exerted their action. Right panel: PCI is based on accumulation of photosensitizer (PS) in endosomes. Light exposure causes rupture of the endo/lysosomal membrane and releases the mm into the cytosol where they can exert their biological activity

[18] and PCI [19].These approaches are appealing for a number of reasons including the highly localized nature of the BBB disruption: unlike the use of hyperosmolar solutions, the BBB is only disrupted at sites subjected to sufficient laser power densities which can be controlled by the user to coincide with the location of the pathology. Through judicious choice of beam parameters, the affected volume can be as small as a few mm^3. Equally important are observations showing that these highly focused approaches do not cause permanent damage to the BBB, as long as incident power densities remain below threshold levels. Under these conditions, the BBB may remain open for relatively long periods of time thus facilitating multi-fractionated drug delivery. In contrast, repeated injections of hyperosmotic compounds are required for extended treatment regimens since the BBB remains open for only a few minutes following bradykinin administration [20].

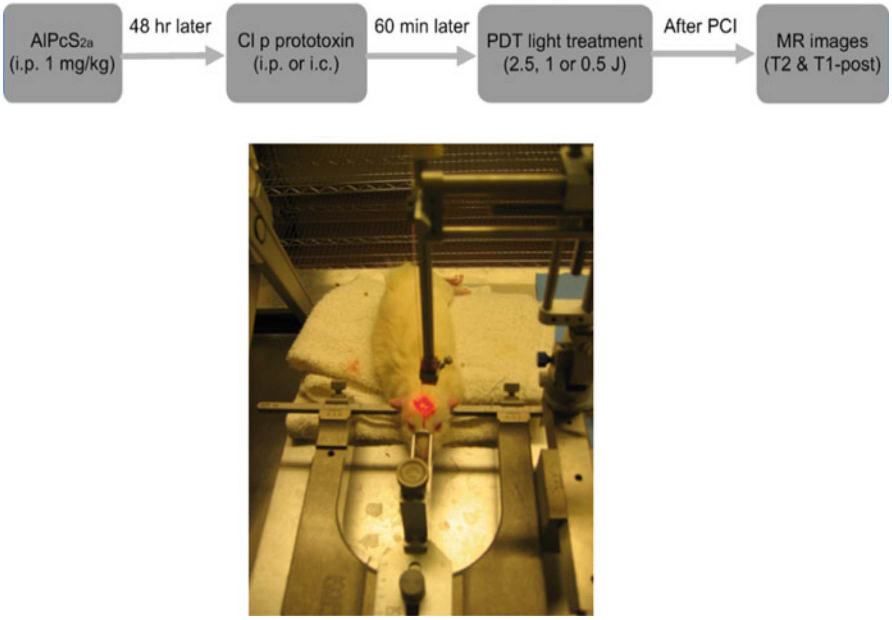

Fig. 11.3 Experimental protocol for Clp-PCI BBB disruption. Rats were fixed in the stereotactic frame and a skin incision was made exposing the skull. An optical fiber was placed in contact with the surface of the skull to the right of the midline. Surface light irradiation was given approximately 60 min after Clp ip administration

Localized BBB opening via PCI-mediated delivery of *Clostridium perfringens* epsilon prototoxin (Clp) was recently investigated in Fischer rats [19]. The rationale for using Clp is due to the ability of active toxin to cause widespread but reversible opening of the BBB [21–23]. Following systemic administration, Clp prototoxin is converted to fully active toxin by proteolytic cleavage. The experimental set up is shown in Fig. 11.3.

The results demonstrated that Clp-PCI was capable of causing localized BBB disruption at very low light fluences (1 J) as shown in Fig. 11.4.

Of particular interest was the time duration and evolution of the Clp-PCI BBB disruption since this represents the therapeutic window for drug delivery. Based on an analysis of MR images, enhancement volumes were observed to peak three days following Clp-PCI suggestive of maximum BBB opening at that time (Fig. 11.5). Thereafter, contrast volumes were observed to decrease, and by day 11, only trace amounts of contrast were observed.

In a follow-on study using an orthotopic brain tumor model consisting of F98 glioma cells in Fischer rats, newly implanted tumor cells were used to mimic the characteristics of infiltrating cells remaining in the resection margin usually found following surgical removal of bulk tumor. PDT or PCI localized BBB opening was performed 24 h after cell inoculation [24]. This is an insufficient time to allow for the development of bulk tumor and BBB degradation, but long enough for the cells

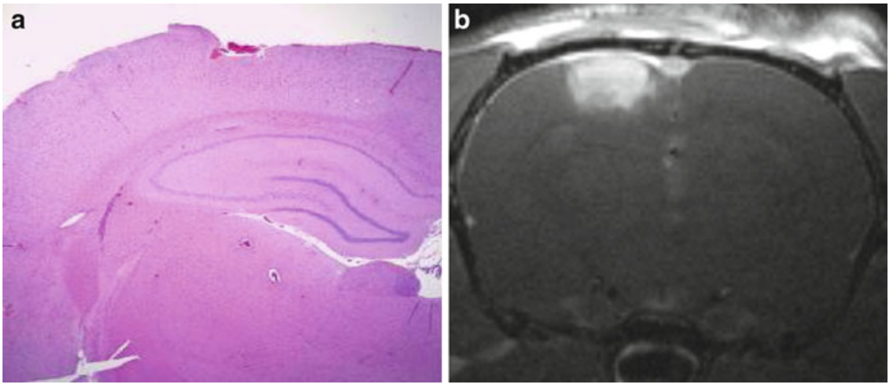

Fig. 11.4 Effects of Clp-PCI on BBB and tissue disruption. Coronal a: H&E sections from rat brains corresponding to T1 contrast MRI scans (b). The sections were taken 21 days post-treatment and the T1- weighted post-contrast images were acquired 3 days post-treatment

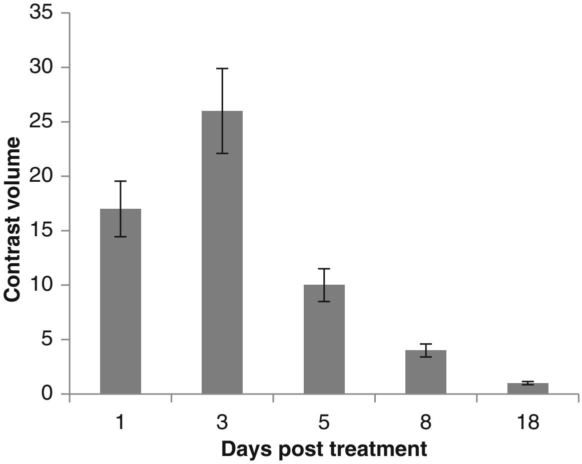

Fig. 11.5 Average time course of BBB opening induced by Clp-PCI. The animals (n = 4 per group) received i.p. injection of Clp at a concentration of 1:100, 1 mg kg^{-1} $AlPcS_{2a}$. and a light fluence of 1 J. Scanning was performed on days 1, 3, 5, 8 and 18 after treatment. All T1 post-contrast images were taken 15 min following i.p. contrast injection

(doubling time of approximately 18 h) to form small, sequestered, micro-clusters which are protected by an intact BBB. The survival of animals implanted with F98 tumor cells, as shown in Fig. 11.6, was significantly extended following BLM chemotherapy with PCI-mediated BBB opening compared to controls that received chemotherapy only.

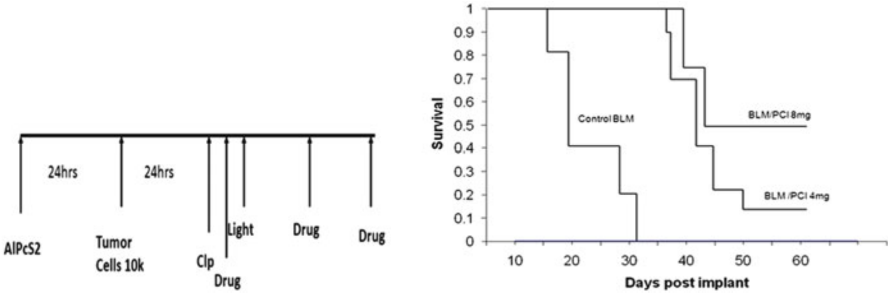

Fig. 11.6 Treatment protocol and Kaplan–Meier survival of tumor cell implanted animals. All animals received 1×10^4 cells i.c. Three groups were followed: BLM 8 mg/kg only, Clp-PCI BLM experimental groups ($AlPcS_{2a}$, Clp, 1 J); BLM 4 or 8 mg/kg was injected i.p. twice daily for 3 days

11.2.4 PCI-Mediated Drug Delivery

The limited efficacy of chemotherapy in the treatment of gliomas is caused by many factors, but two important ones are: (1) the blood brain barrier (BBB) which prevents chemotherapeutic agents from entering the brain and (2) limited endosomal escape of many drugs leading to their inactivation. Chemotherapeutics need to pass the blood brain barrier (BBB) and then enter into cells through the cell plasma membrane, which limits chemotherapeutic agents to mostly lipophilic or low molecular weight compounds that passively diffuse into the cell cytoplasm. In contrast, many highly effective chemotherapeutic agents are large and water-soluble and therefore do not easily penetrate plasma membranes but are actively transported into cells by endocytosis [25]. Their poor ability to escape from the resulting intracellular endosomes leads to their inactivation. Therefore, in combination with modalities leading to increased endosomal escape, the therapeutic effect of these agents would be significantly increased. As outlined above, we have previously shown that selective site-specific opening of the BBB could be obtained in the rat brain by the PCI-mediated potentiation of the effects of known BBB-disrupting agents [19]. BLM administered to animals with targeted BBB opening results in a significant increase in survival compared to drug-only controls. We have also examined the second factor limiting the efficacy of BLM chemotherapy, i.e., endosomal entrapment in in vitro experiments employing multicell tumor spheroids (MTS) formed from human gliomas cells. In comparison to monolayer cultures, a significant advantage of MTS is that their micro-environment more closely mimics the in vivo situation and therefore gene expression and the biological behavior of the cells are likely similar to that encountered in tumor cells in situ. The oxygen gradients characteristic of MTS produce a heterogeneous population of cells that differ in their response to oxygen-dependent therapies such as ionizing radiation, PDT, and chemotherapy. In addition to oxygenation status, tumor response to these therapies is controlled by a number of parameters including intercellular contact and

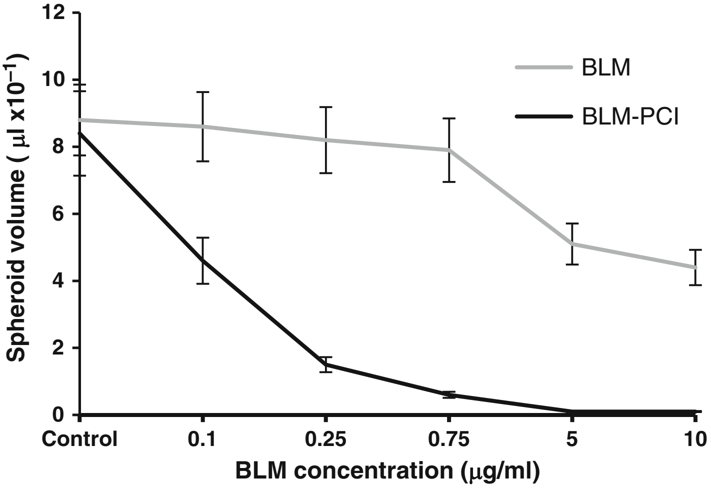

Fig. 11.7 Effects of BLM, and BLM PCI on human glioma MTS growth. Average spheroid volume measured following 4 weeks of incubation as a function of BLM concentration, 0.1–10 μg/mL. 1 μg/mL $\mathrm{AlPcS_{2a}}$ incubation for 18 h. Wavelength of 670 nm: radiant exposure of 1.5 $\mathrm{J/cm^2}$; irradiance of 5 $\mathrm{mW/cm^2}$. Each data point represents the mean of 3 experiments. Error bars denote standard errors

communication and susceptibility to apoptosis. The anti-cancer agent bleomycin (BLM) was employed since the effects of BLM have been shown to be increased by PCI on a number of cell types, but its potential use for the treatment of gliomas has not been established [26]. The toxic effects on spheroid volume growth, evaluated after 4 weeks in culture, of PCI BLM were compared to the effects of BLM alone over a concentration range of 0.1–10 μg/mL (Fig. 11.7). As can be seen, PCI greatly enhanced the effects of the drug and the effects of PCI with 0.1 μg/mL BLM were equivalent to those observed at 10 μg/mL of drug alone.

The number of MTS showing growth after 3 weeks in culture out of a total of 24 replicate cultures in each group is shown in Fig. 11.8. These "survival" data can be used to ascertain if PCI is synergistic or simply additive compared to the results obtained for PDT or drug alone.

Synergism was calculated when analyzing PCI treatments. The equation shown was used to determine if the PCI effect was synergistic, antagonistic, or additive.

$$\alpha = \frac{\mathrm{SF}^{a} \times \mathrm{SF}^{b}}{\mathrm{SF}^{ab}}$$

where $a = \mathrm{PDT}$, $b = \mathrm{BLM}$, and $ab = \mathrm{PCI/BLM}$.

In this scheme SF represents the survival fraction for a specific treatment. If two treatments are to be compared, the survival fractions of each separate treatment are multiplied together and then divided by the survival fraction when both treatments

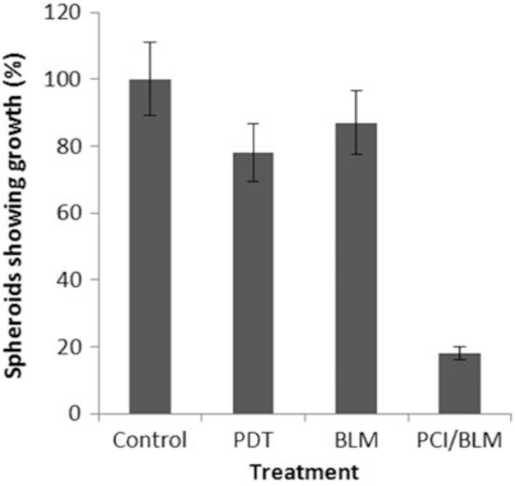

Fig. 11.8 Viability of control and treated human glioma MTS after 4 weeks in culture. 1 μg/mL $AlPcS_{2a}$ incubation for 18 h. Wavelength of 670 nm; radiant exposure of 1.5 J/cm^2, irradiance of 5 mW/cm^2, and 1-hour BLM incubation at a concentration of 0.25 μg/mL. Each data point represents the mean of 3 experiments. Error bars denote standard errors

were applied together. The resulting number (α) describes the cumulative effect. If $\alpha > 1$, the result is synergistic. If $\alpha < 1$, the result is antagonistic, and if $\alpha = 1$ the result is simply additive. The α value for the data shown in Fig. 11.8 was calculated to 3.8, a clearly synergistic effect.

11.2.5 Gene Therapy

Recent research has indicated that mutation or inactivation of tumor suppressor genes in normal neural stem cells (NSC), transforming them into tumor stem cells (TSC), is required and sufficient to induce malignant brain tumors [27]. NSC niches in the brain may harbor TSCs where targeted therapy can be directed [28]. The ability to insert functioning suppressor genes into tumor cells and TSCs would therefore be of considerable interest as a potential treatment modality. Although viral vectors have been used as gene carriers in clinical trials, nonviral vectors offer several advantages. These include flexibility for versatile design, large payloads of genes, and fewer safety concerns. In addition, nonviral vectors have the ability to circumvent the immune response (occurring against viral proteins) allowing iterative administration. One important limitation for cancer gene therapy though is the insurance that the therapeutic gene reaches a sufficient number of tumor cells in a high enough concentration to eliminate the tumor cells and at the same time leave the normal cells unaffected. Since macromolecules, such as DNA plasmids delivered as a complex with cationic polymers, are taken up by cells through endocytosis, they have to penetrate through the membranes of endosomes and into the cytosol in order to exert their full biological effects (see Fig. 11.2). The degradation of "trapped" macromolecules by powerful lysosomal enzymes following

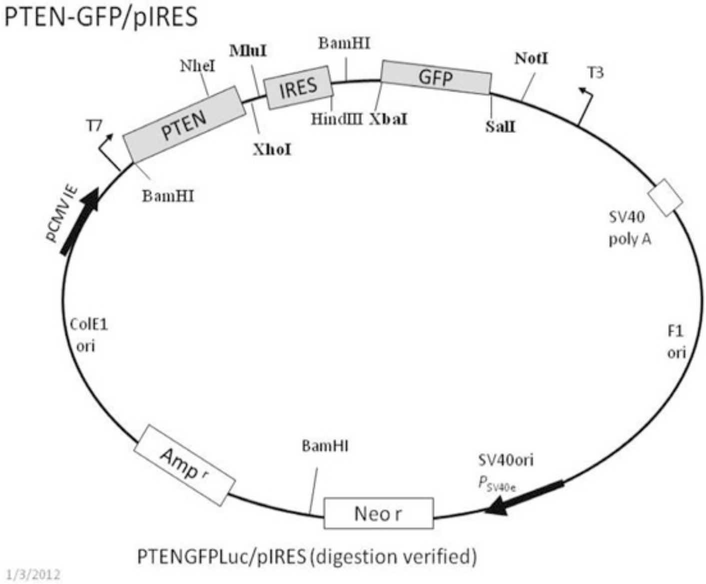

Fig. 11.9 Plasmid PTEN/GFP DNA construct

endosome–lysosome fusion remains a major limitation of gene therapy hindering its therapeutic potential. As previously mentioned, PCI has been shown to be a highly efficient technology for induced endolysosomal escape in a time and site-specific manner for gene therapy by enhanced delivery of various forms of RNA/DNA to the cytosol or nucleus of the targeted cells [29, 30].

PTEN is one of the most commonly lost tumor suppressors in human cancer [31]. Mutations and deletions of PTEN occur that inactivate its enzymatic activity leading to increased cell proliferation and reduced cell death. Frequent genetic inactivation of PTEN occurs in glioblastoma, endometrial cancer, and prostate cancer; and reduced expression is found in many other tumor types such as lung and breast cancer. The glioma cell line U251 MG is known to underexpress the PTEN gene product and can be used to determine the effects of transfection with a functioning PTEN gene. The utility of PCI for the delivery of the GFP indicator gene on the same plasmid as a tumor suppressor gene (PTEN) was investigated in monolayers of U251 human glioma cells. U251 monolayers were incubated in $AlPcS_{2a}$ for 18 h. together with the plasmid and nonviral vectors. In all cases, light treatment was performed with a diode laser at a wavelength of 670 nm. The nonviral transfection agents, branched PEI or protomine sulfate (PS), were used with the plasmid construct (GFP-PTEN: Fig. 11.9).

Since PCI is optimal with a light fluence level that allows 70–80% survival, we performed$AlPcS_{2a}$-mediated PDT at increasing light doses. Live/dead assay of U251 following PDT is shown in Fig. 11.10 for 0, 0.75 and 1.5 J, respectively. Fluence levels of 1.5 J cm^{-2} proved toxic killing more than 50% of the cells. Fluence levels of 0.5–0.75 J cm^{-2} seemed optimal.

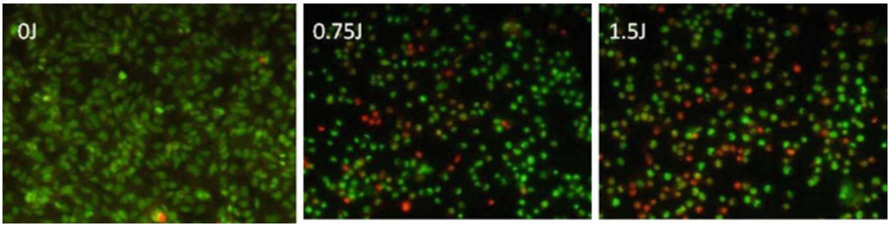

Fig. 11.10 Live-dead assay of U251 cell monolayers following $AlPcS_{2a}$ PDT. *Green* live, *red* dead

11.2.5.1 Effects of PCI on Protamine-Sulfate/DNA Polyplexes

We have investigated utilizing a GFP DNA - protamine-sulfate (PS) polyplex to transfect U251 glioma cells. The polyplexes enter the cell by endocytosis and are sequestered outside the nucleolus in endosomes, resulting in very low transfection rates (Fig. 11.11) [32]. The addition of PCI treatment demonstrated a tenfold increase in transfection rate at optimum PS/DNA concentrations. These results clearly demonstrate the ability of the PCI technique to greatly enhance endosomal escape.

U251 cell monolayers were transfected with the PTEN gene employing the gene carrier bPEI. As seen in Fig. 11.12, the introduction of this tumor suppressor gene inhibited cell growth. The growth inhibitory effect was significantly enhanced by PCI treatment.

These results demonstrate the ability of PCI to increase transfection rates in glioma cells as has been previously reported [33, 34]. Although bPEI is an effective gene carrier, it is highly toxic and is not well suited for in vivo applications. In contrast, PS is relatively non-toxic, but has relatively low transfection efficiency [35, 36]. PCI of PS/DNA polyplexes though could demonstrate a tenfold increase in transfection rate at optimum PS/DNA concentrations (Fig. 11.11). Nevertheless, PS polyplexes enter cells in similar amounts compared to PEI [32]. The difference in transfection efficiency between these two gene carriers is most probably due to increased endosomal escape by PEI/DNA polyplexes. Since PCI greatly enhances endosomal escape, the dramatic effects of PCI shown in Fig. 11.11 for PS/DNA polyplexes support this interpretation. Collectively, the results suggest that $AlPcS_{2a}$-mediated PCI can be used to enhance transfection of tumor suppressor genes in glioma cells or perhaps more importantly into transformed neuro stem cells [27, 28].

11.3 Photothermal Therapy (PTT)

The application of heat to destroy solid tumors (hyperthermia) has been used in cancer treatment for a variety of tumors. Sources for heat generation include microwaves, direct laser light, ultrasound, and near infrared activation of absorbing

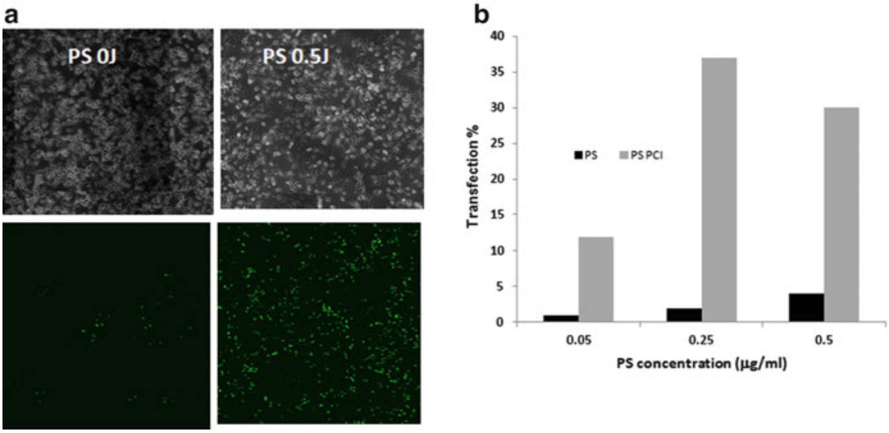

Fig. 11.11 Effects of PCI on GFP gene transfection with protamine-sulfate/DNA polyplexes. DNA complexed with protamine-sulfate, DNA concentration 1 μg mL^{-1}, PDT 0.75 J cm^{-2}. (**a**) Upper panels: phase contrast images showing cell densities; lower panels: two-photon fluorescence images, (**b**) % of cells expressing GFP

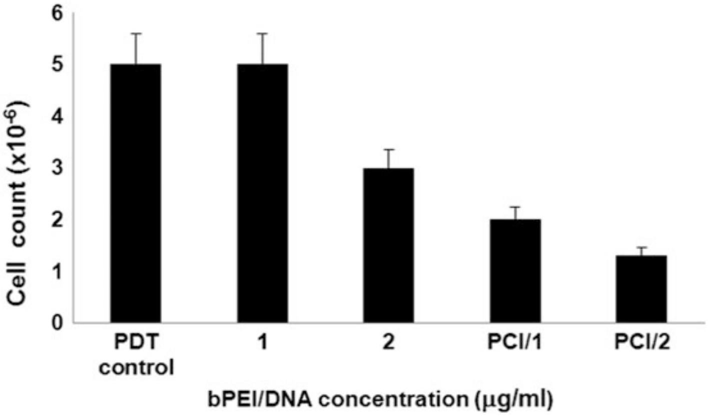

Fig. 11.12 U251 cell growth measured 48 h. following PTEN gene transfection. bPEI/DNA concentration 1 or 2 μg mL^{-1}, PDT 0.75 J cm^{-2}

agents. The latter, called photothermal therapy (PTT), will be discussed briefly in this portion of the chapter. A more detailed review of nanoparticle-mediated PTT can be found in Chap. 10. Unfortunately, the majority of hyperthermia techniques destroy both normal as well as diseased tissue limiting its usefulness. To overcome this limitation, nanoparticles can be used as exogenous energy absorbers to provide specific delivery of heat selectively to tumors. Particles delivered i.v. accumulate to a degree in the tumor by virtue of the enhanced permeability and retention effect (EPR) due to poorly organized and fenestrated vasculature as well as reduced lymphatic drainage [37, 38].

Nanoparticles are structures less than 500 nm in size which has sparked interest with their novel properties (optical, magnetic, and thermal). Gold nanoshells (NS) represent one class of photo-absorbing nanoparticles [39, 40]. They consist of a spherical dielectric silica core (50–500 nm) surrounded by a thin (5–20 nm) gold layer and have a tunable optical absorption within the visible and infrared regions. Since nanoshells are roughly one million times more efficient at converting NIR light into heat than conventional dyes such as indocyanine green, once localized to the tumor and exposed to NIR light, they can generate sufficient heat to induce cell death by mechanisms such as protein denaturation and rupture of cellular membranes via thermal ablation**.**

As gliomas grow, their centers are largely necrotic, due to the rapid proliferation of malignant cells within the core of the tumor at increasingly larger distances from their nearest capillaries. Although this isolation of cells renders the hypoxic areas of gliomas inaccessible to nanoparticle-based therapies where delivery into the tumor is based on the EPR effect, this portion of the tumor is resected during surgery. It is in the resection margins, partially protected by the blood brain barrier, that it is desirable for the nanoparticles to accumulate. Since the vasculature in this region can be more or less normal, the EPR effect will be insufficient to allow the concentration of nanoshells, necessary for hyperthermia, to be reached. One method to overcome this limitation would be to use cells such as stem cells or macrophages to act as vectors.

Tumor-associated macrophages (TAMs) are frequently found in and around glioblastomas in both experimental animals and patient biopsies [41, 42]. This would indicate local synthesis of chemo attractive factors in gliomas and that inflammatory cells can pass through an intact BBB. Monocyte trafficking into the CNS occurs in a highly regulated fashion and is dependent on cell–cell interactions that involve endothelial cells and astrocytes, as well as the local release of factors that promote BBB permeability. Intravenously injected macrophages loaded with iron oxide nanoparticles have been shown to target experimental brain tumors [43]. This would indicate local synthesis of chemo attractive factors in gliomas and that inflammatory cells can pass through an intact BBB. Monocytes or macrophages loaded with drugs, nanoparticles, or photosensitizers could therefore be used to target tumors [44]. The use of macrophages loaded with gold nanoshells for thermal ablation of GBM tumors is potentionally an attractive, relatively safe treatment modality that is worth studying.

We have investigated the effects of exposure to laser NIR in vitro on multicell human glioma spheroids infiltrated with empty (containing no nanoshells) or nanoshell-loaded macrophages [45, 46]. The gold nanoshells (NS) used in this study consisted of a 120 nm silica core with a 12–15 nm gold shell (Nanospectra Biosciences, Inc., Houston, Texas). The resultant optical absorption peak was between 790 and 820 nm for both bare and PEGylated particles. PEGylated nanoshell solutions as supplied by the manufacturer are shown in Fig 11.13.

Gold nanoshells are often PEGylated to prevent their rapid uptake and removal from circulation by the reticulo-endothelial system. The % uptake of PEGylated nanoshells in murine macrophages was lower (3.96%) than that of bare nanoshells

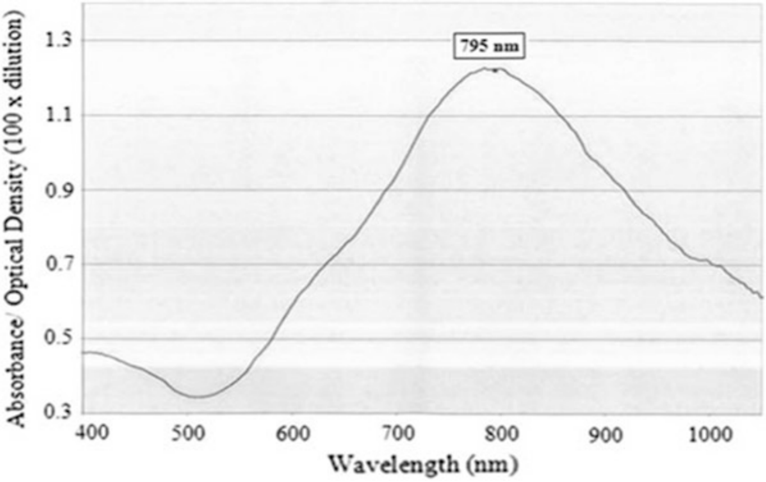

Fig. 11.13 Absorbance curves of PEGylated nanoshell solutions

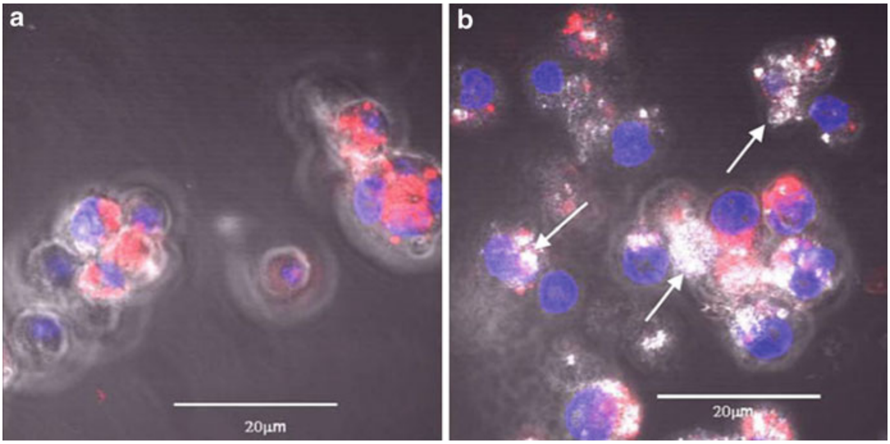

Fig. 11.14 Two-photon fluorescence micrograph of (**a**) empty or (**b**) nanoshell-loaded Ma. Cell nucleus stained with Hoechst 33342 (*blue*), Cytoplasm stained with PKH26 Red Fluorescent (*red*), nanoshell aggregates inside Ma shown by white reflectance (*white arrows*)

(15.74%). However, the PEGylated nanoshell solution was available in a much higher concentration since they have a much lower tendency to aggregate compared to bare nanoshells. Comparison was therefore between the respective numbers of nanoshells taken up by a given number of macrophages. The total amount of PEGylated nanoshells taken up by the macrophages was more than eight times that of bare nanoshells. As seen in Fig. 11.14, macrophages could efficiently take up PEGylated gold NS

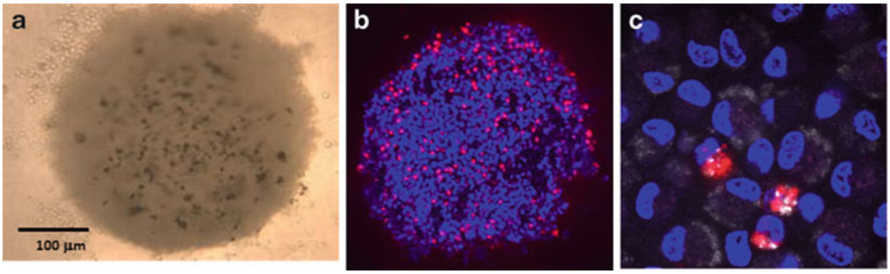

Fig. 11.15 Light and two-photon micrographs of 48 h co-culture of human tumor spheroid and NS-loaded labeled Ma. The Ma (*red*) are seen to migrate throughout the tumor cells (*blue*) making up the spheroid. (**a**) Light microscope ×10, (**b**) two photon ×10, (**c**) two photon ×40

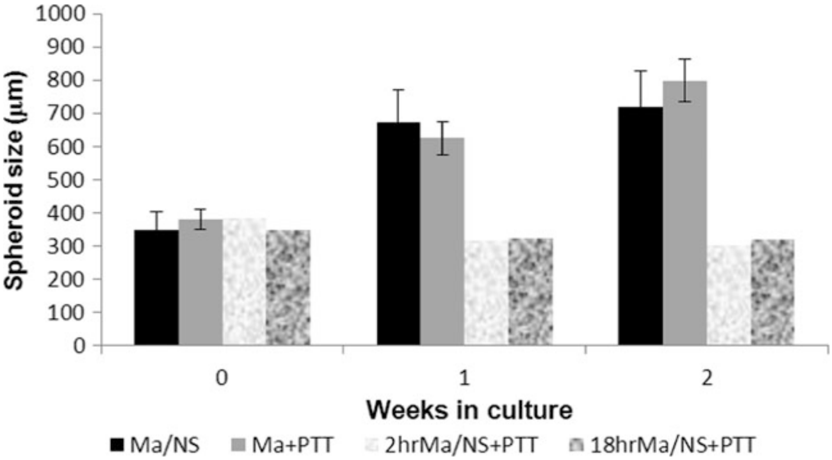

Fig. 11.16 Kinetics of spheroid growth following PTT. Spheroids were formed containing 5×10^3 tumor cells. 48 h after formation, individual spheroids were co-incubated with 2×10^4 empty Ma or NS-loaded Ma for 2 or 18 h. PTT: 14 W cm^{-2}, 10 min. Ma/NS: nanoshell-loaded macrophages—no PTT; Ma +PTT: empty macrophages +PTT

The ability of NS-loaded Ma to infiltrate into multicellular tumor spheroids is clearly illustrated in Fig. 11.15. The monocytes were labeled with a red fluorescent dye and are shown in Fig. 11.15 at two magnifications developed by two-photon microscopy. Mo/Ma were seen to be distributed through the spheroid. This is most probably caused by chemoatractive agents produced by the tumor cells acting on the Ma. NS-loaded macrophages infiltrated into glioma spheroids to the same or, in some cases, to a greater degree than empty Ma [45].

NIR laser irradiation of spheroids incorporating NS-loaded macrophages resulted in complete growth inhibition in an irradiance-dependent manner, while spheroids infiltrated with empty macrophages had growth curves identical to untreated controls following PTT treatment (Fig. 11.16).

11.4 Conclusions

Tumor resection is usually the first modality employed in the treatment of gliomas. With the improved surgical techniques now available, the incidence of gross tumor resection, as defined by a negative post operative MRI, has greatly increased [47, 48]. Nevertheless, the great majority of glioma patients do suffer a recurrence of their tumors leading to their poor prognosis. The therapeutic goal following surgical resection therefore is the elimination of infiltrating tumor cells remaining in the margins of the resection cavity, where most tumors recur, while minimizing damage to normal brain. One of the many obstacles to effective treatment of malignant brain tumors is limited transport of anti-tumor agents through both brain and brain tumor capillaries due to the BBB and the blood–brain tumor barrier (BBTB), the latter which retains many BBB characteristics. We have explored a number of methods, as described in this chapter, for enhancing both drug delivery and efficacy across the BBB and into tumors. Additionally, the ability of macrophages to migrate and accumulate within, and at the periphery, of brain tumors renders them attractive vehicles for the delivery of anti-tumor agents including nanoparticles.

In a clinical setting, light delivered directly into the wall of the tumor resection cavity is required for PCI, PDT, and PTT. Laser light applied through an indwelling balloon applicator filling the resection cavity could meet this requirement [49, 50].

References

1. Wallner KE, Galicich JH, Krol G, Arbit E, Malkin MG (1989) Patterns of failure following treatment for glioblastoma multiforme and anaplastic astrocytoma. Int J Radiat Oncol Biol Phys 16:1405–9
2. Brem H, Piantadosi S, Burger PC et al (1995) Placebo-controlled trial of safety and efficacy of intraoperative controlled delivery by biodegradable polymers of chemotherapy for recurrent gliomas. Lancet 345(8956):1008–12
3. Johannesen TB, Watne K, Lote K, Norum J, Tvera K, Hirschberg H (1999) Intracavity fractionated balloon brachytherapy in glioblastoma. Acta Neurochir 141:127–33
4. Boekelheide K, Eveleth J, Tatum A, Winkelman J (1987) Microtubule assembly inhibition by porphyrins and related-compounds. Photochem Photobiol 46:657–661
5. Dadosh N, Shaklai N (1987) Effect of protoporphyrin-IX on red blood-cell membrane cytoskeleton. J Muscle Res Cell Motil 9:86–92
6. Nelson J, Liaw L, Berns M (1987) Tumor destruction in photodynamic therapy. Photochem Photobiol 46:829–835
7. Sporn L, Foster T (1992) Photofrin and light induces microtubule depolymerization in cultured human endothelial-cells. Cancer Res 52:3443–3448
8. Chen B, Pogue BW, Luna JM et al (2006) Tumor vascular permeabilization by vascular-targeting photosensitization: effects, mechanism, and therapeutic implications. Clin Cancer Res 12:917–923
9. Berg K, Selbo PK, Prasmickaite L et al (1999) Photochemical internalization: a novel technology for delivery of macromolecules into cytosol. Cancer Res 59(6):1180–83

10. Dietze A, Peng Q, Selbo PK et al (2005) Enhanced photodynamic destruction of a transplantable fibrosarcoma using photochemical internalization of gelonin. Br J Cancer 92:2004–9
11. Selbo PK, Kaalhus O, Sivam G, Berg K (2001) 5- aminolevulinic acid-based photochemical internalization of the immunotoxin MOC31-gelonin generates synergistic cytotoxic effects in vitro. Photochem Photobiol 74:303–10
12. Selbo PK, Sivam G, Fodstad Ø, Sandvig K, Berg K (2000) Photochemical internalization increases the cytotoxic effect of the immunotoxin MOC31 gelonin. Int J Cancer 87:853–9
13. Prasmickaite L, Høgset A, Selbo PK et al (2002) Photochemical disruption of endocytic vesicles before delivery of drugs: a new strategy for cancer therapy. Br J Cancer 86:652–7
14. Selbo PK, Weyergang A, Høgset A et al (2010) Photochemical internalization provides time- and space-controlled endolysosomal escape of therapeutic molecules. J Control Release 148(1):2–12
15. Berg K, Bommer J, Moan J (1989) Evaluation of sulfonated aluminum phthalocyanines for use in photochemotherapy. Cellular uptake studies. Cancer Lett 44:7–15
16. Maman N, Dhami S, Phillips D, Brault D (1999) Kinetic and equilibrium studies of incorporation of di-sulfonated aluminum phthalocyanine into unilamellar vesicles. Biochim Biophys Acta 1420:168–178
17. Vykhodtseva N, McDannold N, Hynynen K (2008) Progress and problems in the application of focused ultrasound for blood–brain barrier disruption. Ultrasonics 48:279–96
18. Hirschberg H, Uzal FA, Chighvinadze D, Zhang MJ, Peng Q, Madsen SJ (2008) Disruption of the blood–brain barrier following ALA-mediated photodynamic therapy. Lasers Surg Med 40:535–41
19. Hirschberg H, Zhang MJ, Gach HM et al (2009) Targeted delivery of bleomycin to the brain using photo-chemical internalization of Clostridium perfringens epsilon prototoxin. J Neurooncol 95(3):317–29
20. Murphy LJ, Hachey DL, Oates JA et al (2000) Metabolism of bradykinin in vivo in humans: identification of BK1-5 as a stable plasma peptide metabolite. J Pharmacol Exp Ther 294 (1):263–9
21. Worthington R, Mulders M (1975) The effect of Clostridium perfringens epsilon toxin on the blood–brain barrier of mice. Onderstepoort J Vet Res 42:25–31
22. Nagahama M, Sakurai J (1991) Distribution of labeled Clostridium perfringens epsilon toxin in mice. Toxicon 29:211–7
23. Dorca-Arevalo J, Soler-Jover A, Gibert M et al (2008) Binding of epsilon toxin from Clostridium perfringens in the nervous system. Vet Microbiol 131:14–20
24. Madsen SJ, Angell-Petersen E, Spetalen S, Carper SW, Ziegler SA, Hirschberg H (2006) Photodynamic therapy of newly implanted glioma cells in the rat brain. Lasers Surg Med 38:540–548
25. Pron G, Mahrour N, Orlowski S (1999) Internalization of the bleomycin molecules responsible for bleomycin toxicity: a receptor-mediated endocytosis mechanism. Biochem Pharmacol 57:45–56
26. Berg K, Dietze A, Kaalhus O, Hogset A (2005) Site-specific drug delivery by photochemical internalization enhances the antitumor effect of bleomycin. Clin Cancer Res 11(23):8476–85
27. Alcantara L, Laguno S et al (2009) Malignant astrocytomas originate from neural stem/ progenitor cells in a somatic tumor suppressor mouse model. Cancer Cell 15(1):45–56
28. Evers P, Lee PP et al (2010) Irradiation of the potential cancer stem cell niches in the adult brain improves progression free survival of patients with malignant gliomas. BMC Cancer 10:384–9
29. Hogset A, Ovstebo Engesaeter B, Prasmickaite L et al (2002) Light induced adenovirus gene transfer, an efficient and specific gene delivery technology for cancer gene therapy. Cancer Gene Ther 9:365–371
30. Ndoye A, Dolivet G, Hogset A et al (2006) Eradication of p53-mutated head and neck squamous cell carcinoma xenografts using nonviral p53 gene therapy and photochemical internalization. Mol Ther 13(6):1156–62

31. Knobbe CB, Merlo A, Reifenberger G (2002) Pten signaling in gliomas. Neuro Oncol 4(3):196–211
32. Cho SK, Kwon YJ (2011) Polyamine/DNA polyplexes with acid-degradable polymeric shell as structurally and functionally virus-mimicking nonviral vectors. J Control Release 150:287–297
33. Chou CH, Sun CH, Zhou YH, Madsen SJ and Hirschberg H (2011) Enhanced transfection of brain tumor suppressor genes by photochemical internalization. Proceedings SPIE, photonic therapeutics and diagnostics, vol 7883, p 3U
34. Hirschberg H, Mathews MB, Shih EC, Madsen SJ, Kwon YJ (2012) Enhanced gene transfection by photochemical internalization of protomine sulfate/DNA complexes. Proceedings SPIE, Photonic therapeutics and diagnostics, vol 8207, p S1
35. Tsuchiya Y, Ishti T, Okahata Y, Sato T (2006) Characterization of protamine as a transfection accelerator for gene delivery. J Bioact Compat Polym 21:519–537
36. Liu J, Guo S, Li Z, Liu L, Gu J (2009) Synthesis and characterization of stearyl protamine and investigation of their complexes with DNA for gene delivery. Colloids Surf B Biointerfaces 73(1):36–41
37. Maeda H (2001) The enhanced permeability and retention (EPR) effect in tumor vasculature: the key role of tumor-selective macromolecular drug targeting. Adv Enzyme Regul 41:189–207
38. Maeda H, Fang J, Inutsuka T, Kitamoto Y (2003) Vascular permeability enhancement in solid tumor: various factors, mechanisms involved and its implications. Int Immunopharmacol 3:319–328
39. Huang X, Qian W, El-Sayed IH, El-Sayed MA (2007) The potential use of the enhanced nonlinear properties of gold nanospheres in photothermal cancer therapy. Lasers Surg Med 39(9):747–753
40. Schwartz JA, Shetty AM, Price RE, Stafford RJ, Wang JC, Uthamanthil RK et al (2009) Feasibility study of particle-assisted laser ablation of brain tumors in orthotopic canine model. Cancer Res 69(4):1659–1667
41. Badie B, Schartner JM (2000) Flow cytometric characterization of tumor associated macrophages in experimental gliomas. Neurosurgery 46:957–61 discussion 61–2
42. Roggendorf W, Strupp S, Paulus W (1996) Distribution and characterization of microglia/macrophages in human brain tumors. Acta Neuropathol 92:288–93
43. Valable S, Barbier EL, Bernaudin M, Roussel S, Segebarth C, Petit E et al (2008) In vivo MRI tracking of exogenous monocytes/macrophages targeting brain tumors in a rat model of glioma. Neuroimage 40(2):973–983
44. Choi MR, Stanton-Maxey KJ, Stanley JK et al (2007) A cellular Trojan Horse for delivery of therapeutic nanoparticles into tumors. Nano Lett 7(12):3759–3765
45. Baek SK, Makkouk AR, Krasieva T, Sun CH, Madsen SJ, Hirschberg H (2011) Photothermal treatment of glioma; an in vitro study of macrophage-mediated delivery of gold nanoshells. J Neurooncol 104(2):439–48
46. Madsen SJ, Baek SK, Makkouk AK, Krasieva T, Hirschberg H (2012) Macrophages as cell-based delivery systems for nanoshells in photothermal therapy. Ann Biomed Eng 40 (2):507–15
47. Hirschberg H, Samset E, Hole PK, Lote K (2006) Impact of intraoperative MRI on the results of surgery for high grade gliomas. J Min Inv Neurosurg 48:77–84
48. Stummer W, Pichlmeier U, Meinel T, Wiestler OD, Zanella F, Reulen HJ (2006) Fluorescence-guided surgery with 5-aminolevulinic acid for resection of malignant glioma: a randomized controlled multicentre phase III trial. Lancet Oncol 7:392–401
49. Madsen SJ, Sun CH, Tromberg BJ, Hirschberg H (2001) Development of a novel balloon applicator for optimizing light delivery in photodynamic therapy. Lasers Surg Med 29:406–10
50. Madsen SJ, Svaasand LO, Tromberg BJ, Hirschberg H (2001) Characterization of optical and thermal distributions from an intracranial balloon applicator for photodynamic therapy. Proc SPIE 4257:41

Index

A
Absorption, 1–8, 16, 18, 23, 25–44, 46, 58–61, 64–67, 70, 72, 76, 77, 79, 82, 88, 89, 91, 99, 104, 108, 121, 137, 138, 144–147, 149–151, 154, 165, 177, 183, 184, 192, 218, 219, 226, 236–240, 244, 246, 266
Absorption coefficient, 1–3, 6–8, 16, 17, 30, 33–35, 37, 43, 61, 65, 70, 72, 77, 91, 99, 108, 138, 149, 151, 154
Acoustic-resolution photoacoustic microscopy (AR-PAM), 142–143, 147
5-ALA. *See* 5-Aminolevulinic acid (5-ALA)
Albedo, 4, 5, 76
Aluminum phthalocyanine disulfonate ($AlPcS_{2a}$), 222, 254–256, 259–264
Aminolevulinic acid, 173–197, 214, 216
5-Aminolevulinic acid (5-ALA), 173, 174, 178–183, 187, 189–194, 196, 216
AuroLase®, 248
Autofluorescence, 77, 182–184, 186, 188, 192, 220

B
BAT. *See* Brain-adjacent-to-tumor (BAT)
BBB. *See* Blood-brain barrier (BBB)
BBTB. *See* Blood-brain tumor barrier (BBTB)
Beer-Lambert law, 26, 32–35, 66
Biodistribution of gold nanoparticles, 241–243
Bleomycin, 227, 261
Blood-brain barrier (BBB), 177, 178, 180–182, 212, 214, 216, 223, 227, 241, 242, 253, 254, 256–260, 266, 269
Blood-brain tumor barrier (BBTB), 243, 269
Blood flow, 31, 32, 38, 41, 42, 46, 57, 90, 100–103, 110, 117–133, 138, 147, 158, 162, 166–170, 177, 218, 242
Blood oxygenation, 31, 34, 35, 45, 46, 57–59, 110, 147, 148, 177
Boltzmann transport equation, 1
Brain-adjacent-to-tumor (BAT), 253
Brain aneurysms, 164, 165
Brain connectivity, 162
Brain function, 43, 58, 60, 68, 88, 90, 105, 253
Brain imaging, 24, 26–28, 38–47, 57–83, 87–111, 138, 146–149, 152–154, 157–170
Brain shift, 175, 190, 196
Brain tumor resection, 126, 178
Brain tumors, 10, 11, 14, 15, 17, 126, 173, 174, 176–178, 186, 192, 194–196, 207–214, 216, 222, 223, 225, 227–229, 235–248, 253–269

C
Cardiac (ECG) filtering, 129–133
CBF. *See* Cerebral blood flow (CBF)
CCD/CMOS camera, 104, 105, 121
Cerebral blood flow (CBF), 100–103, 117–133, 147, 168
Cerebral edema, 151–152
Cerebral metabolic rate of oxygen, 100, 138
Clinical study, 45, 87, 126, 128, 133, 165, 176, 191, 220–222
Clinical trial, 174, 187, 192, 197, 207, 213, 217, 219–221, 229, 248, 262
Clostridium perfringens, 258
Coherent light source, 121
Contionious-wave (CW), 14, 26, 28, 38–43, 46, 57–83, 88, 89, 92, 98, 104–105, 140, 226
Contrast agent, 87, 89, 118, 126, 133, 137, 149–151, 180, 182, 238

S.J. Madsen (ed.), *Optical Methods and Instrumentation in Brain Imaging and Therapy*, Bioanalysis: Advanced Materials, Methods, and Devices 3,
DOI 10.1007/978-1-4614-4978-2,

Correlation time, 120, 121, 125, 129–133
Cortical hemodynamics, 144–145, 166
Cortical microvasculature, 138, 144, 148, 168
Cytochrome oxidase, 18, 59, 68

D
DCS. *See* Diffuse correlation spectroscopy (DCS)
Deoxyhemoglobin, 17, 26, 27, 31, 32, 35, 88, 98, 137, 148
Differential pathlength factor, 14, 34, 59, 66, 67, 69, 82
Diffuse correlation spectroscopy (DCS), 32, 41–42, 46, 100
Diffuse optical imaging (DOI), 24, 25, 30, 31, 43–47, 104–105
Diffuse optical imaging instrumentation, 104–105
Diffuse optical spectroscopy (DOS), 23–47, 88, 98, 100
Diffuse optical tomography (DOT), 24, 25, 57–83, 87–111, 154
Diffuse reflectance, 5–7, 13, 14, 18
Diffusion approximation, 3, 37, 58, 69, 70, 76, 78, 79, 83, 91
Diffusion coefficient, 72–75, 77, 82, 91
Diffusion equation, 3, 18, 38, 70–72, 77–79, 92, 96
Diode lasers, 58, 61, 62, 89, 104, 121, 122, 127, 218, 219, 225, 263
Direction of flow, 124
DOI. *See* Diffuse optical imaging (DOI)
Doppler effect, 118, 138
Doppler optical coherence tomography (D-OCT), 157–169
  for imaging brain hemodynamics, 166
Doppler shift, 162
DOS. *See* Diffuse optical spectroscopy (DOS)
DOT. *See* Diffuse optical tomography (DOT)

E
EEG. *See* Electroencephalography (EEG)
Effective attenuation coefficient, 5
Effective penetration depth, 5
Elastix, 132
Electroencephalography (EEG), 47, 106–108, 110
Endocytic vesicles, 227, 254–256
Energy radiance, 2
Enhanced permeability and retention (EPR), 241, 242, 265, 266
Epilepsy, 90, 100, 106, 117, 163, 164
Epilepsy lesion delineation with OCT, 163, 164
EPR. *See* Enhanced permeability and retention (EPR)
Evans blue, 144
Ex vivo measurements, 33

F
F98 glioma, 258
FGR. *See* Fluorescence guided resection (FGR)
Finite element (FE) methods, 92, 98, 103
Fluence, 2, 7, 8, 79, 80, 244, 256, 258, 259, 263
Fluence rate, 1–3, 5, 8, 36, 37, 70, 72, 73, 75, 77–79, 91, 138, 154, 209, 214, 219, 224, 244, 254
Fluorescein, 176, 177
Fluorescence guided resection (FGR), 174, 181–192, 194–197, 211, 214, 215, 222, 224, 228
fMRI. *See* Magnetic resonance imaging (fMRI)
Foscan®, 214
Fourier domain optical coherence tomography (FD-OCT), 159–161, 163
Frequency domain photon migration, 13, 14, 18
Frequency-modulated (FM), 39–41, 43, 46
Full-ring transducer array, 139
Functional brain imaging, 43–47, 67, 146
Functional imaging, 87–89, 146
Functional near-infrared spectroscopy (fNIRS), 16, 18, 24, 69

G
GBM. *See* Glioblastoma multiforme (GBM)
Gene therapy, 222, 228, 229, 262–264
Glioblastoma multiforme (GBM), 173–175, 184–189, 196, 211, 214, 243, 244, 253, 266
Gliomas, 11, 14, 15, 17, 173, 174, 176, 177, 180–182, 186–196, 207, 208, 210–212, 214, 216, 217, 219–225, 227, 238, 242–246, 253, 254, 258, 260–264, 266, 268, 269
Gold-gold sulfide (GGS) nanoparticles, 236, 237
Gold nanocages, 237, 248
Gold nanorods, 236, 239–241, 243
Gold nanoshells (NS), 238–242, 244, 246, 248, 266, 267
Gold-silica nanoshells, 236, 237, 239, 242
Gross total resection, 174–178

H
HbO_2. *See* Oxyhemoglobin (HbO_2)
Head probe, 61, 63–64
Hematoporphyrin derivative (HpD), 213, 214, 216, 219–223
Hemodynamics, 18, 57, 61, 83, 100, 106, 144, 146, 148, 166
Hemoglobin, 16–18, 25–27, 29, 31–35, 42, 57–59, 67, 82, 87, 88, 98, 100–102, 121, 137, 146–148, 213
Hemoglobin absorption spectrum, 16, 58, 59, 88
Hemoglobin concentration, 18, 57, 101, 102, 137, 146
HpD. *See* Hematoporphyrin derivative (HpD)
Hypericin, 214
Hyperoxia, 147, 148
Hyperthermia, 238, 244, 248, 264–266
Hypoxia, 26, 46, 147, 148

I
ICG. *See* Indocyanine green (ICG)
ICGA. *See* Indocyanine green angiography (ICGA)
Image-guided spectroscopy, 88
Image reconstruction methods, 90–103
Image registration, 129, 131–133
Indocyanine green (ICG), 31, 118, 149, 177, 236, 239, 266
Indocyanine green angiography (ICGA), 118, 123, 126, 133, 177
Integrating sphere, 6, 9–11
Intra-operative confocal endomicroscopy, 176
Intraoperative imaging, 122, 126–128, 182, 191, 212, 229
Intrinsic signal optical imaging (ISI), 165, 166
Inverse adding-doubling (IAD) method, 4
Inverse problems, 81, 83, 88, 91, 93–96, 99
In vivo measurements, 5, 7, 8, 19, 129
ISI. *See* Intrinsic signal optical imaging (ISI)

K
Kubelka-Munk model, 3–4

L
Laser diode, 58, 61, 62, 89, 104, 121, 122, 127, 218, 219, 225, 263
Laser Doppler, 100, 118, 166
Laser power, 122, 141, 142, 238, 257
Lasers, 7, 24, 57, 88, 117, 137, 159, 214, 237, 256
Laser speckle contrast imaging (LSCI), 100, 118, 121–128, 132, 133, 199
Light emitting diodes (LED), 61, 216, 218, 219, 225
Light propagation, 1–3, 5, 7, 28, 31, 37, 39, 63, 65, 66, 88, 91
Linear analysis, 57–83
Linear modeling, 58, 64, 80–81
Longitudinal wave, 143, 153
LSCI. *See* Laser speckle contrast imaging (LSCI)

M
Magnetic resonance imaging (fMRI), 31, 46, 47, 89, 100, 118, 166, 178
Malignant gliomas, 174, 181, 182, 187–189, 191, 192, 194–196, 207, 208, 211, 214, 221, 222, 254
MBLL. *See* Modified Beer-Lambert law (MBLL)
Meningioma, 11, 17, 193–196, 210
Metastasis, 192
Metastatic brain tumors, 222
Metronomic PDT, 223–226
Mie scattering, 17, 31, 60, 99
Modified Beer-Lambert law (MBLL), 26, 33–35, 42, 58, 59, 64, 66–68, 70, 78–80, 82, 83
Molecular brain imaging, 149–150, 153
Monkey brain imaging, 152, 153
Monocytes, 242, 266, 268
Monte Carlo (MC) modeling, 2
Motion artifact, 44, 122, 129–133, 141
Multicell tumor spheroids (MTS), 260–262
Multi-modality imaging method, 91, 97

N
Nanoparticles, 137, 149, 178, 223, 235–248, 265, 266, 269
  toxicity, 243
Nanoshell-loaded macrophages, 242, 246, 247, 266, 268
Near-infrared spectroscopy (NIRS), 16, 24, 40, 57, 58, 61–70, 77–79, 82–83, 87–89, 91, 96, 98
Neuroendovascular OCT, 164
Neuroimaging, 57, 89–90, 104
Neurometabolic coupling, 90, 110, 111
Neuronavigation, 175, 176, 186, 189–191

Neurovascular coupling, 138
NIRS. *See* Near-infrared spectroscopy (NIRS)
Normoxia, 27, 147

O
Optical absorption, 23, 25, 26, 29, 36, 38–40, 91, 108, 137, 138, 144–146, 149, 154, 236, 239, 266
Optical coherence tomography (OCT), 157–170, 176
  endovascular catheter, 165
  for functional brain activation, 165
Optical fibers, 37, 61, 63, 104, 106, 143, 216–219, 225, 226, 239, 258
Optical pathlength, 66, 77–80, 159, 218
Optical properties of the brain, 16–19
Optical-resolution photoacoustic microscopy,
Optical scattering, 28, 31–32
Optics fibers, 43, 44, 47, 58, 63, 195
Optode, 38, 44, 61, 63–64, 81–83
Organic dye, 137, 149, 237, 239
Oxygenation saturation,
Oxygen consumption, 100–103
Oxygen saturation, 16, 26, 27, 29, 88, 98, 101–103, 137, 148, 177
Oxyhemoglobin (HbO_2), 16, 25, 31, 35, 58, 59, 67, 68, 98, 99, 101, 102, 104, 106, 108–111, 137, 146, 147, 150

P
PACT. *See* Photoacoustic computed tomography (PACT)
PAM. *See* Photoacoustic microscopy (PAM)
Partial pathlength, 80
PCI. *See* Photochemical internalization (PCI)
PDT. *See* Photodynamic therapy (PDT)
Penetration depth, 5, 8, 17, 19, 23, 44, 100, 138, 143, 144, 157, 163, 166, 223, 239
Phase resolved optical coherence tomography (PR-OCT), 157
Photoacoustic computed tomography (PACT), 138–142, 144–147, 149–152, 154
Photoacoustic microscopy (PAM), 139, 141–144, 147, 148, 154
Photoacoustic tomography, 137–154
Photochemical internalization (PCI), 227, 253–265, 269
Photodiode, 58, 61–63, 89, 104, 143
Photodynamic therapy (PDT), 2, 13, 16, 88, 168, 169, 180, 192, 195, 197, 207–229, 254, 256, 258, 260, 261, 263, 265, 269
Photofrin, 213–216, 220–222, 224, 227
Photon migration, 13, 14, 18
Photon transport in biological tissues, 1, 2
Photosensitizers, 191, 197, 207–210, 212–216, 218–224, 226–229, 254–225, 266
Photothermal therapy (PTT), 235–248, 264–269
Photothrombosis, 124
Phthalocyanines, 20, 227, 254, 255
Physiology parameters, 98–99, 157
Planar transducer array,
Polarization sensitive optical coherence tomography (PC-OCT), 157
Porphyrins, 26, 178, 181, 213
Positron emission tomography (PET), 44–47, 89, 100, 163, 166, 175, 178, 182, 189–191, 196, 248
PpIX. *See* Protoporphyrin IX (PpIX)
Protamine-sulfate/DNA polyplexes, 264, 265
Protoporphyrin IX (PpIX), 173, 178–197, 214, 216, 220, 222–224
PTEN, 227, 263–265
PTT. *See* Photothermal therapy (PTT)
Pulse-oximetry, 24, 26, 28, 30

R
Radiation transport equation (RTE), 1–2, 4, 5, 58, 69–77, 83, 91
Radiative transport, 36, 58, 70, 78
Rayleigh scattering, 17, 31, 60
Relative blood flow, 121, 123, 125
Repetitive PDT, 195
RTE. *See* Radiation transport equation (RTE)

S
Scattering, 1, 23, 60, 88, 118, 137, 157, 217, 237
Scattering anisotropy, 1, 3
Scattering coefficient, 1–6, 16, 17, 30, 32, 35, 36, 38, 40, 42, 43, 61, 70, 74, 77, 88, 89, 91, 219
Scattering phase function, 4–6, 75–76
Selective blood-brain barrier (BBB) disruption, 178, 257, 258
Shear wave, 143, 153
Siegert relation, 120
Singlet oxygen, 209, 210, 256
SLD. *See* Superluminescent diode (SLD)
Somatosensory, 90, 100, 147, 157, 166

Spatial resolution, 23–25, 44, 89–91, 104, 118, 120, 124, 137, 150, 152, 154, 160, 163, 164, 166, 167, 170
Spectroscopy, 14, 16, 18, 23–47, 58, 59, 62, 69, 87–90, 98, 100, 104, 166, 177, 178, 187, 190, 192–196, 209, 212, 216, 220, 224
SPR. *See* Surface plasmon resonance (SPR)
Superluminescent diode (SLD), 159
Surface plasmon resonance (SPR), 239, 240
Surgical microscope, 127, 173, 176, 182, 184, 185, 189, 191–193, 195, 196

T
TAMs. *See* Tumor-associated macrophages (TAMs)
Temporal resolution, 57, 63, 90, 118, 144
Three-dimensional (3D) brain imaging, 163
Time resolved diffuse reflectance spectroscopy, 17
Time resolved (TR) spectroscopy, 18
Tissue parenchyma, 131, 133
Total attenuation coefficient, 4–6, 70, 72, 74
Total hemoglobin concentration, 101, 137
Transport equations, 1–3, 36, 38, 58, 70–72, 91
Transport scattering coefficient, 4
Tumor-associated macrophages (TAMs), 243, 266
Tumor spheroids, 242, 243, 246, 260, 268
Tumor suppressor genes, 227, 262–264
Tumor vasculature, 150, 237, 240
Two-photon PDT, 265

U
U87 glioblastoma tumor, 150
Ultrasound attenuation, 153

V
Vessel occlusion, 124

W
Wash-in (rise time), 123
Whisker stimulation, 146